

FUNCTIONAL POLYESTERS FOR BIOMEDICAL AND INDUSTRIAL APPLICATIONS

Katelyn R. Houston

A dissertation submitted to the faculty at the University of North Carolina at Chapel Hill in partial fulfillment of the requirements for the degree of Doctor of Philosophy in the Department of Chemistry in the College of Arts and Sciences.

Chapel Hill
2016

Approved by:

Valerie Sheares Ashby

Maurice S. Brookhart

Yueh Z. Lee

Frank A. Leibfarth

Wei You

©2016
Katelyn R. Houston
ALL RIGHTS RESERVED

ABSTRACT

Katelyn R. Houston: Functional Polyesters for Biomedical and Industrial Applications
(Under the direction of Valerie Sheares Ashby and Wei You)

Advances in polymer science impact a range of materials applications, from medical technology to commodity plastics. This dissertation describes the development of radiopaque biomaterials and supramolecular engineering polymers accomplished *via* synthesis, characterization, and elucidation of the structure-property relationships of functionalized polyesters.

Computed tomography (CT) generates detailed images for diagnosing diseases and monitoring implants. While metallic implants are easily visualized by CT, polymeric implants, absent of high Z elements, lack radiocontrast. Nevertheless, replacing metal-based implants with polymeric materials has many advantages: biodegradability, increased biocompatibility, and tunable thermal and mechanical properties. Additionally, blood pool imaging utilizes CT contrast agents, which are rapidly excreted and renally toxic. Designing polymeric biomaterials capable of long-lasting x-ray contrast could lead to safer, more effective implants and contrast agents.

In Chapters 2 and 3, a single iodinated monomer was used to synthesize and evaluate a variety of aliphatic, radiopaque polyesters. These polymers exhibited high radiocontrast, tunable thermal and mechanical properties, low cytotoxicity, and they were easily processed into both nanoparticles and thermosets. The nanoparticles showed good continual contrast with no uptake

into the kidneys. Additionally, copolymer thermosets served as stable, biocompatible and degradable, inherently radiopaque shape memory materials.

While the functionalization of a unique monomer was highlighted in the first part, Chapter 4 focuses on polyester endgroup functionalization. The benefits of supramolecular polymers include recyclability, self-healing, and processability. While the effect of the supramolecular ureidopyrimidinone (UPy) endgroup has been investigated on many low-performing polymers, this moiety has not been broadly investigated with higher performance materials. High molecular weight engineering plastics have excellent mechanical properties, but they can be difficult to process. By end-functionalizing low molecular weight engineering polymers with a supramolecular moiety, issues involving processability could be overcome while maintaining robust mechanical properties. Herein, the structure-property relationships of end-functionalized glycol-modified poly(ethylene terephthalate) (PETG) of various molecular weights were investigated using the UPy group and various linkers. By taking advantage of the unique thermal properties of PETG, this system serves as the first example of a supramolecular engineering polymer with enhanced thermal and mechanical properties that also shows improved melt viscosity at temperatures suitable for non-degradative processing.

To Bernice M. Modzel

ACKNOWLEDGEMENTS

First, I would like to thank my advisor, Valerie Sheares Ashby. With her guidance and dedication, I grew as a scientist and a professional throughout my graduate career. With regard to the work outlined in Chapter 2, I would like to thank Sarah Brosnan, Yueh Lee, Laurel Burk, and Judith Nielsen. Chris Luft performed the cytotoxicity studies and the UNC Biomedical Research Imaging Center performed the CT imaging outlined in Chapters 2 and 3. With regard to the work outlined in Chapter 3, I want to thank Linden Allison and Melissa Topping, my summer REU students from Juniata College. With regard to the work outlined in Chapter 4, special thanks goes to Ross Yost, William Daniel, Doug Carico, and Damon Billodeaux. I especially want to thank Annie Jackson and Howard Carman for their input and for their support of the work summarized in Chapter 4. Thanks goes to the Chapel Hill Analytical and Nanofabrication Laboratory, particularly to Carrie Donley for performing XPS and for our helpful conversations (also for involving me in organizing the 2016 Scientific Art Competition). Amar Kumbhar performed the EDS experiments. Special thanks also goes to Joe DeSimone and Wei You, both of whom stepped in to act as co-advisors to me at different times during my graduate career. Without the help of the people acknowledged above, none of my projects would have come to fruition. The work herein was supported by the National Science Foundation Graduate Research Fellowship under Grant No. DGE-1144081 as well as NSF DMR-0418499, NSF-MIRT DMR-1122483, and Eastman Chemical Company.

I would also like to thank the UNC Materials Research Society for supporting me as a leader and for all of the hard work they do fostering interdisciplinary research and relationships

throughout the Research Triangle. Special thanks goes to the Ackland Art Museum for supporting my interests in science and art and trusting me as I curated the exhibition, *Evidence & Expertise*.

In addition, particular thanks goes to my family, friends (especially my NCSU/Raleigh crew), and previous teachers and professors from West Branch Area and Juniata College. My parents, Mark and Julie Houston, deserve the utmost thanks; their love has helped me realize my own potential. I also want to thank my sister, Abby Houston, all of my grandparents: Roper and Marcia Houston, Ronald and Debbie Ruggiero, and Kenneth and Rosemary Shuey, as well as Sue Kerestan. Finally, I want to thank my loving and supportive partner, Cameron Stevens. The input, reassurance, and environment you provide give me strength through all of my failures and successes.

TABLE OF CONTENTS

LIST OF FIGURES	xiv
LIST OF SCHEMES	xviii
LIST OF TABLES	xix
LIST OF ABBREVIATIONS AND SYMBOLS	xx
CHAPTER 1: INTRODUCTION TO FUNCTIONAL POLYESTERS FOR BIOMEDICAL AND INDUSTRIAL APPLICATIONS	1
1.1 Overview.....	1
1.2 Introduction to Radiopaque Biomaterials	1
1.2.1 Computed Tomography	1
1.2.2 Computed Tomography Contrast Agents	3
1.2.2.a Traditional Contrast Agents.....	3
1.2.2.b Metal-based Nanoparticles as Contrast Agents	4
1.2.2.c Iodinated Nano-carriers and Nanoparticles.....	7
1.2.3 Radiopaque Polymers	9
1.2.3.a Polymer Mixtures.....	9
1.2.3.b Inherently Radiopaque Polymers.....	10
1.2.4 Radiopaque Shape Memory Biomaterials	13
1.2.4.a The Shape Memory Cycle.....	13
1.2.4.b Traditional Shape Memory Biomaterials.....	15
1.2.4.c Radiopaque Shape Memory Polymers	16

1.2.5. Summary	17
1.3 Supramolecular Engineering Polyesters	18
1.3.1 Supramolecular Chemistry <i>via</i> Ureidopyrimidinone Endgroup Functionalization.....	18
1.3.2 Engineering Polyesters.....	21
1.3.3 Summary	23
REFERENCES	24
CHAPTER 2: IODINATED HOMOPOLYMERS AS A VERSATILE PLATFORM FOR RADIOPAQUE BIOMATERIALS AND NANOPARTICLES	32
2.1 Introduction.....	32
2.2 Experimental Methods	34
2.2.1 Materials	34
2.2.2 Characterization	34
2.2.3 Synthesis	35
2.2.3.a Synthesis of 2,2-bis(iodomethyl)-1,3-propanediol ^{30,31}	35
2.2.3.b Typical Polymerizations with 2,2-bis(iodomethyl)-1,3-propanediol and Diacids.....	35
2.2.3.c Poly(2,2-bis(iodomethyl)-1,3-propylene succinate)	36
2.2.3.d Poly(2,2-bis(iodomethyl)-1,3-propylene adipate)	36
2.2.3.e Poly(2,2-bis(iodomethyl)-1,3-propylene sebacate).....	36
2.2.3.f Polymer End-capping with 2-Isocyanatoethyl Methacrylate	36
2.2.3.g End-capped Poly(2,2-bis(iodomethyl)-1,3-propylene succinate).....	36
2.2.3.h End-capped Poly(2,2-bis(iodomethyl)-1,3-propylene adipate)	37
2.2.3.i End-capped Poly(2,2-bis(iodomethyl)-1,3-propylene sebacate)	37
2.2.4 Thermoset Fabrication	37

2.2.5 Preliminary Thermoset Degradation by Hydrolysis	37
2.2.6 Typical Liposomal-nanoprecipitation	37
2.2.6.a Core-crosslinking	38
2.2.7 Nanoparticle Stability Tests	39
2.2.7.a Nanoparticle Stability at Body Temperature	39
2.2.7.b Whole Blood and Serum Aggregation Studies	39
2.2.8 Cytotoxicity	39
2.2.9 <i>In Vitro</i> X-ray Images and Projections	40
2.2.10 <i>In Vivo</i> CT Imaging	40
2.3 Results and Discussion	41
2.3.1 Monomer Synthesis	41
2.3.2 Polymer Synthesis and Evaluation	42
2.3.2.a Prepolymers	42
2.3.2.b Thermosets	44
2.3.3 Bulk Polymer Radiopacity	45
2.3.4 Nanoparticle Synthesis and Evaluation	47
2.3.4.a Modified Liposomal-nanoprecipitation Formulation	47
2.3.4.b Evaluation of the Lipid-polymer Hybrid Nanoparticles	48
2.3.4.c Nanoparticle Stability at Body Temperature	49
2.3.4.d Nanoparticle Crosslinking	50
2.3.5 <i>In Vitro</i> Cytotoxicity	51
2.3.6 Nanoparticle Radiopacity	53
2.3.6.a <i>In Vitro</i> Radiopacity	53

2.3.6.a In Vivo Radiopacity	53
2.4 Conclusions	57
REFERENCES	59
CHAPTER 3: RADIOPAQUE SHAPE MEMORY MATERIALS <i>VIA</i> IODINATED COPOLYESTERS	62
3.1 Introduction	62
3.2 Experimental Methods	64
3.2.1 Materials	64
3.2.2 General Characterization	64
3.2.3 Synthesis of poly(2,2-bis(iodomethyl)-1,3-propanediol-co- 1,8-octanediol adipate).....	65
3.2.3.a Polymer containing 15 mole percent 2,2-bis(iodomethyl)-1,3-propanediol (15%I).....	65
3.2.3.b Polymer containing 20 mole percent 2,2-bis(iodomethyl)-1,3-propanediol (20%I).....	65
3.2.3.c Polymer containing 25 mole percent 2,2-bis(iodomethyl)-1,3-propanediol (25%I).....	66
3.2.3.d Polymer containing 35 mole percent 2,2-bis(iodomethyl)-1,3-propanediol (35%I).....	66
3.2.4 End-capping poly(2,2-bis(iodomethyl)-1,3-propanediol-co- 1,8-octanediol adipate) with 2-Isocyanatoethyl Methacrylate.....	66
3.2.5 Thermoset Fabrication	66
3.2.6 Thermoset Cytotoxicity	66
3.2.7 Preliminary Thermoset Degradation by Hydrolysis	67
3.2.8 Dynamic Mechanical Analysis and Shape Memory Testing.....	67
3.3 Results and Discussion	68
3.3.1 Polymer Synthesis and Evaluation.....	68

3.3.1.a Prepolymer Synthesis.....	68
3.3.1.b Iodinated Copolymer Thermosets.....	71
3.3.2 Thermoset Cytotoxicity	73
3.3.3 Thermoset Radiopacity	74
3.3.3.a Long-term Radiopacity	75
3.3.4 Shape Memory	76
3.4 Conclusions.....	78
REFERENCES	80
CHAPTER 4: SUPRAMOLECULAR ENGINEERING POLYESTERS: ENDGROUP FUNCTIONALIZATION OF GLYCOL MODIFIED PET WITH UREIDOPYRIMIDINONE	83
4.1 Introduction.....	83
4.2 Experimental Methods	86
4.2.1 Materials	86
4.2.2 Characterization.....	86
4.2.2.a General Characterization.....	86
4.2.2.b Characterization of Melt-pressed Discs	87
4.2.2.c Characterization of Drop-cast Films	87
4.2.2.d Characterization of Solvent-cast Films.....	88
4.2.3 Synthesis	88
4.2.3.a Synthesis of 1-((3-(Isocyanatomethyl)cyclohexyl)methyl)- 3-(6-methyl-4-oxo-1,4-dihydropyrimidin-2-yl)urea (CH-UPy)	88
4.2.3.b Synthesis of PETG _{2k} Functionalized with CH-UPy (PETG _{2k} -CH-UPy).....	88
4.2.3.c Synthesis of Ureidopyrimidinone Functionalized PETG _{2k} with Dicyclohexyl Linker (PETG _{2k} -D-UPy)	89

4.2.4 Sample Fabrication	90
4.2.4.a Melt-Pressed Discs.....	90
4.2.4.b Drop-cast Films.....	90
4.2.4.c Solvent-cast Films.....	90
4.3 Results and Discussion	91
4.3.1 Synthesis and Characterization of UPy Functionalized PETG.....	91
4.3.1.a UPy Functionalization Using Multiple Linkers	91
4.3.1.b H-UPy Functionalized PETG of Various Molecular Weights.....	93
4.3.2 Thermal, Mechanical, and Viscoelastic Properties of PETG-H-UPy of Various Molecular Weights.....	94
4.3.2.a Thermal Characterization.....	94
4.3.2.b Relationship Between Physical, Mechanical, and Surface Properties	98
4.3.2.c Viscosity in the Melt	102
4.3.2.d Tensile Testing.....	106
4.4 Conclusions.....	107
REFERENCES	109
APPENDIX A: SUPPLEMENTARY INFORMATION FOR CHAPTER 2	111
APPENDIX B: SUPPLEMENTARY INFORMATION FOR CHAPTER 3.....	130
APPENDIX C: SUPPLEMENTARY INFORMATION FOR CHAPTER 4.....	155
APPENDIX D: SUPPLEMENTARY INFORMATION FOR CHAPTER 4— COMMERCIAL COMPARISONS	188

LIST OF FIGURES

Figure 1.1 Chemical structures of well-known iodinated contrast agents: iopromide (ULTRAVIST®), iohexol (OMNIPAQUE®), and the dimer, iodixanol (VISIPAQUE®). ^{3,4,6-8}	3
Figure 1.2 This figure was adapted and used from reference 12. CT images in a rat hepatoma model following injection PEG-coated AuNPs: a) before injection, b) 5 minute-mark (directly after injection of the AuNPs), c) 1 hour, d) 2 hours, e) 4 hours, and f) 12 hours after injection. Large arrows indicate the hepatoma regions. The numbers shown in brackets in the upper right-hand corner of the images indicate the HU values of the hepatoma regions (left) and the surrounding normal liver parenchyma (right). ¹²	5
Figure 1.3 This figure was adapted from reference 19. Schematic of tantalum oxide nanoparticles functionalized with PEG and a fluorescent marker (RITC-APTES) (left). TEM images (right) showing size control and small size of the nanoparticles. ¹⁹	7
Figure 1.4 Figure taken from reference 37. Synthetic scheme for core-shell nanoparticles made by Kong <i>et al.</i> ³⁷	8
Figure 1.5 <i>N</i> -(2,6-diiodocarboxyphenyl)-3,4,5-triiodobenzamide was used to functionalize a radiolucent polyurethane. ⁶³	11
Figure 1.6 A variety of iodinated monomers developed for radiopaque methacrylate-based polymerizations: A) triiodophenyl methacrylate, ⁶⁵ B) 2-methacryloyloxyethyl(2,3,5-triiodobenzoate), ^{38,66,67} C) 3-(methacryloylamidoacetamido)-2,4,6-triiodobenzoic acid, ⁶⁸ D) 2-(2'-iodobenzoyl)-ethyl methacrylate, ⁶⁹ E) 2-(4'-iodobenzoyloxy)-ethylmethacrylate. ⁷⁰	12
Figure 1.7 Iodine-containing polyesters made <i>via</i> ring opening polymerization. ⁷¹	12
Figure 1.8 The Shape Memory Cycle: The sample is first cured into its permanent shape. 1. The sample is heated to melt all crystallites. 2. The sample is deformed, in this case extended, using a force. 3. While under this force, the sample is cooled to produce crystallites that secure the temporary shape. 4. The force is released. 5. Upon heating above the T_m , the crystallites melt, and the sample returns to the permanent shape.	14
Figure 1.9 Shape memory biomaterials adapted from references 83 and 94: A) self-tying suture, ⁸² and B) deployable stent. ⁹³	15
Figure 1.10 Radiopaque shape memory device from figures adapted from reference 101. A) Schematic of the shape memory polymer. This shape memory system consists of a PLGA composite core coated with a crosslinked PEG hydrogel.	

Recovery of the initial shape was achieved when the hydrogel swelled in the presence of water, the stimulus. B) X-ray image of a radiopaque shape memory embolic plug prototype (red arrow) using a micro-catheter (yellow arrow) in a rabbit model. As the hydrogel swelled, vascular embolization was achieved (left to right). ¹⁰⁰	17
Figure 1.11 The quadruple hydrogen bonding dimerization of the ureidopyrimidinone (UPy) moiety. R can represent attachment to a small molecule, direct attachment to a polymer, or attachment to a linker unit, which attaches the UPy unit to a polymer.	18
Figure 1.12 Figure taken from reference 114. Poly(ethylene butylene) with hydroxyl endgroups (left) compared to poly(ethylene butylene) with UPy endgroups (right). ¹¹⁴	19
Figure 1.13 Figure adapted from reference 115: TEM images of thin films made from PEB functionalized with various endgroups at both termini. Chemical structure of the endgroups are depicted next to each TEM image. ¹¹⁵	20
Figure 1.14 A) PCT, B) PETG (m = major component) or PCTG (n = major component), C) PCTA when m ≤ 50 mol%. ¹³⁵⁻¹³⁷	22
Figure 2.1 Comparison of the weight percent of iodine using ¹ H NMR and EDS before and after crosslinking.....	46
Figure 2.2 CT images of iodinated polyester materials. From left to right: sebacic (Se), adipic (Ad), and succinic (Su) acid based thermosets implanted in porcine liver and in air (insets).....	47
Figure 2.3 Nanoparticle formulation method using a modified liposomal-nanoprecipitation method.....	48
Figure 2.4 Analysis of the size and shape of the lipid-polymer hybrid nanoparticles. A) Dynamic light scattering results from the liposomal-nanoprecipitation method showing that the lipid-polymer hybrid nanoparticles were of similar size and PDI for all of the iodinated polymers. B) TEM image depicting the nanoparticles made using the adipic acid based polymer, Ad-NP (scale bar = 200 nm).	49
Figure 2.5 The nanoparticles were formulated in the same batch (RT = room temperature and BT = body temperature, 37 °C). The hydrodynamic diameter of the nanoparticles were analyzed using DLS before and after incubation at 37 °C and also compared with nanoparticles stored at room temperature.....	50
Figure 2.6 ¹ H NMR spectra of A) Nanoparticle suspension that was successfully crosslinked (argon purged and UV irradiated), B) Nanoparticle suspension that was not crosslinked (no purge prior to irradiation), and C) Control nanoparticle	

suspension that had no addition of photoinitiator or UV exposure.	51
Figure 2.7 Cytotoxicity of crosslinked films after 3 days of incubation.	52
Figure 2.8 Cytotoxicity of nanoparticles at different concentrations.	52
Figure 2.9 X-ray projections of succinic, adipic, and sebacic acid based nanoparticles of different concentrations (roughly 150 to 450 mg/mL).	53
Figure 2.10 Graph displaying contrast comparison against a control (no contrast injected) for the heart, liver, spleen, and kidneys.	55
Figure 2.11 CT images of mice injected with no contrast (control, top), a clinically used contrast agent (Omnipaque®, middle) and with the adipic acid based nanoparticles (Ad-NP, bottom). The red arrows indicate significant contrast in the bladder and kidneys for the commercial contrast agent.....	56
Figure 2.12 Micrograph showing aggregation in serum. Circles drawn in to indicate where aggregation took place.	57
Figure 3.1 The melting temperature found by DSC and storage modulus at 25 °C using DMA for each crosslinked copolymer film.....	72
Figure 3.2 EDS of the iodinated prepolymers and crosslinked thermosets.	73
Figure 3.3 Cytotoxicity of the crosslinked thermosets after 3 days of incubation examining the effect of sample size (1-3 spacers) on cell viability.....	74
Figure 3.4 A) CT images of an aluminum bar (A), the iodinated thermosets from 35%I to 15%I (B, C, D, E, respectively), and PCL (F). B) Attenuation units of the iodinated thermosets compared to aluminum and PCL.	75
Figure 3.5 Week 4 CT image of the thermosets that were incubated in PBS buffer solution at 37 °C	76
Figure 3.6 Third shape-memory cycle for each crosslinked copolymer. Step 1: The polymer is heated and mechanically deformed into its temporary position. Step 2: The polymer is cooled below its transition temperature under a constant mechanical stress. Step 3: The polymer is unloaded, releasing the applied stress. Step 4: The polymer is heated past its transition temperature and returns to its permanent shape.....	77
Figure 4.1 DSC spectra (second heating cycle, 10 °C min ⁻¹) of PETG and PETG functionalized with H-UPy A) directly after synthesis, and B) after melt processing.	95

Figure 4.2 GPC traces A) of the raw powder run directly after synthesis, and B) of the melt-pressed materials (CHCl_3 at $25\text{ }^\circ\text{C}$ and 1.0 mL min^{-1} using polystyrene standards).	97
Figure 4.3 Dynamic oscillatory shear measurements of the tan delta as the material goes through cooling and heating cycles, where the peak signifies the T_g of A) H-UPy functionalized materials and B) unfunctionalized PETG (1 Hz, 0.1% strain, parallel plate fixture with plate diameter of 8 mm and gap length of $1000\text{ }\mu\text{m}$).	98
Figure 4.4 The peak of the tan delta plotted against inverse molecular weight (lines added to clearly present trends).	98
Figure 4.5 Photograph comparing PETG _{2k} (left) to PETG _{2k} -H-UPy (right).....	99
Figure 4.6 Dynamic oscillatory shear measurements depicting the G' and G'' of the materials through cooling and heating cycles (1 Hz, 0.1% strain, parallel plate fixture with plate diameter of 8 mm and gap length of $1000\text{ }\mu\text{m}$).	100
Figure 4.7 RMS surface roughness of PETG before and after H-UPy functionalization. RMS surface roughness obtained from AFM images ($20 \times 20\text{ }\mu\text{m}$) using Nanoscope 6.14R1 software.....	101
Figure 4.8 Effect of H-UPy endgroup structure and molecular weight on melt viscosity. Rheological characterization of PETG and PETG-H-UPy at 2000, 3800, and 6800 g mol^{-1} (shear rate 0.05 s^{-1} , parallel plate fixture with plate diameter of 8 mm and gap length of $1000\text{ }\mu\text{m}$).	103
Figure 4.9 Rheological characterization of commercial PETG (shear rate 0.05 s^{-1} , parallel plate fixture with plate diameter of 8 mm and gap length of $1000\text{ }\mu\text{m}$).	103
Figure 4.10 Variable temperature ^1H NMR spectra of PETG _{6.8k} -H-UPy in TCE- d_2 ($c = 5\text{ mM}$, 600 s equilibrium allowed at each temperature). The box outlines peaks that signify the presence of intermolecular H-bonding of UPy endgroups.	104
Figure 4.11 A) Stress–strain curves of PETG and PETG-H-UPy of 2000, 3800, and 6800 g mol^{-1} at 10 mm min^{-1} , and B) average strain at break of the materials over five samples.	107

LIST OF SCHEMES

Scheme 2.1 Synthesis of 2,2-bis(iodomethyl)-1,3-propanediol.....	41
Scheme 2.2 Synthesis of iodinated polyesters followed by photo-crosslinking to yield iodinated thermosets.	43
Scheme 3.1 Synthesis of iodinated copolymers followed by photo-crosslinking to yield iodinated thermosets.	69
Scheme 4.1 UPy functionalized PETG of 2000 g mol ⁻¹ utilizing either a hexamethylene (H), cyclohexyl (CH), or dicyclohexyl (D) linker unit (R).....	91
Scheme 4.2 Endgroup synthesis utilizing different diisocyanates.....	92
Scheme 4.3 One-pot synthesis of UPy functionalized PETG of 2000 g mol ⁻¹ utilizing a dicyclohexyl linker group.	92

LIST OF TABLES

Table 2.1 Properties of 2,2-Bis(iodomethyl)-1,3-propanediol.....	41
Table 2.2 Iodinated Polymer Properties.....	43
Table 2.3 Thermoset Properties.....	45
Table 2.4 EDS Results for the Crosslinked Bulk Materials and Nanoparticles.....	46
Table 2.5 Nanoparticle Size Before and After Injection.....	54
Table 3.1 Iodinated Copolymer Properties.....	70
Table 3.2 Iodinated Copolymer Thermoset Properties.....	71
Table 3.3 Mass Loss of Crosslinked Films After 4 Weeks at 37 °C in PBS Buffer Solution.....	76
Table 3.4 Strain Fixity and Recovery Over Three Shape Memory Cycles.....	78
Table 4.1 Properties of PETG and UPy Functionalized PETG of 2000 g mol ⁻¹	93
Table 4.2 Properties of PETG and H-UPy Functionalized PETG of 3800 and 6800 g mol ⁻¹	94
Table 4.3 Viscosity Change from 90 °C to 120 °C at 600 s ⁻¹	106

LIST OF ABBREVIATIONS AND SYMBOLS

Ad	adipic acid
AFM	atomic force microscopy
ATR FT-IR	attenuated total reflectance Fourier transform spectroscopy
AuNPs	gold nanoparticles
BaSO ₄	barium sulfate
Bi ₂ S ₃	bismuth(III) sulfide
BPA	Bisphenol-A
b.v.	by volume
b.w.	by weight
CaH ₂	calcium hydride
CDCl ₃	deuterated chloroform
CHCl ₃	chloroform
CH ₂ Cl ₂	dichloromethane
CHDM	<i>cis/trans</i> -1,4-cyclohexanedimethanol
CH-UPy	1-((3-(Isocyanatomethyl)cyclohexyl)methyl)-3-(6-methyl-4-oxo-1,4-dihydropyrimidin-2-yl)urea
CIN	contrast medium-induced nephrotoxicity
CME	critical molecular weight for entanglements
CO ₂	carbon dioxide
COOH	carboxylic acid moiety
CT	computed tomography
Đ	dispersity
DBTDL	dibutyltin dilaurate
DI	distilled

DLS	dynamic light scattering
DMA	dynamic mechanical analysis
DMF	dimethylformamide
DNA	deoxyribonucleic acid
DOPA	3,4-dihydroxyphenylalanine
DSC	differential scanning calorimeter
DSPE-PEG	1,2-distearoyl- <i>sn</i> -glycero-3-phosphoethanolamine- <i>N</i> -[amino(polyethylene glycol)-2000] (ammonium salt)
E	Young's modulus
E1/E2	elimination reaction
EDS	energy dispersive x-ray spectrometer
FDA	U.S. Food and Drug Administration
G'	storage modulus
G''	loss modulus
GPC	gel permeation chromatography
H-bond	hydrogen bond
HDI	hexamethylene diisocyanate
HDMI	4,4'-methylenebis(cyclohexyl isocyanate)
HPLC	high performance liquid chromatography
HU	Hounsfield unit
Δ HU	change in HU from control
H-UPy	2(6-isocyanatohexylaminocarbonylamino)-6-methyl-4[1H]pyrimidinone
<i>I</i>	intensity of the transmitted x-rays
<i>I</i> ₀	intensity of the incident x-rays
IACUC	Institutional Animal Care and Use Committee
I-BPA	iodinated Bisphenol-A

I.D.	injected dose
K	integer constant
LyP-1	peptide used to target 4T1 breast cancer tumors
m_f	final mass
m_i	initial mass
MIS	2-amino-4-hydroxy-6-methylpyrimidine
ML	mass loss
M_n	number-average molecular weight
M_w	weight-average molecular weight
MW	molecular weight
N_2	nitrogen
NMR	nuclear magnetic resonance spectroscopy
NP	nanoparticle
PBS	phosphate buffered saline
PBT	poly(butylene terephthalate)
PCL	poly(caprolactone)
PCT	poly(1,4-cyclohexylenedimethylene terephthalate)
PCTA	polymer based on CHDM, terephthalic acid and isophthalic acid
PCTG	glycol (CHDM) modified PET, CHDM repeat unit as major component
PDI	polydispersity index
PDMS	polydimethylsiloxane
PEB	poly(ethylene butylene)
PEG	polyethylene glycol
PEO/PPO	poly(ethylene oxide) and poly(propylene oxide) block co-polymers
PET	poly(ethylene terephthalate)

PETG	glycol (CHDM) modified PET, ethylene glycol repeat unit as major component
PETG _{2k}	PETG of 2000 g mol ⁻¹
PETG _{3.8k}	PETG of 3800 g mol ⁻¹
PETG _{6.8k}	PETG of 6800 g mol ⁻¹
PETG _{2k} -CH-UPy	PETG _{2k} functionalized with CH-UPy
PETG _{2k} -D-UPy	ureidopyrimidinone functionalized PETG _{2k} with HDMI
PETG-H-UPy	PETG polymers functionalized with the H-UPy endgroup
PEU	polyether urethane
Ph ₃ Bi	triphenylbismuth
PLGA	poly(lactic-co-glycolic acid)
Pluronic	poly(ethylene glycol)-poly(propylene glycol)-poly(ethylene glycol)
polyTHF	polytetrahydrofuran
PS	polystyrene
R _f	strain fixity
RITC-APTES	fluorescent marker
R _r	strain recovery
RT	room temperature
SAXS	small-angle x-ray scattering
Sc(OTf) ₃	scandium(III) triflate
Se	sebacic acid
SEM	emission scanning electron microscope
SH-PEG	thiol modified PEG
SN1/SN2	nucleophilic substitution reaction
Sn(Oct) ₂	tin(II) ethylhexanoate
Su	succinic acid

T	temperature
$\tan\delta$	tan delta
TCE- d_2	deuterated 1,1,2,2-tetrachloroethane
TEM	transmission electron microscopy
T_g	glass transition temperature
TGA	thermogravimetric analyzer
THF	tetrahydrofuran
T_m	melting temperature
TPU	thermoplastic polyurethane
UPy	ureidopyrimidinone
UV	ultraviolet
VT-NMR	variable temperature ^1H NMR
Wt%	weight percent
w/w	ratio of weight/weight
XPS	x-ray photoelectron spectroscopy
Z	atomic number
ϵ_m	temporal strain after deformation
ϵ_p	permanent strain after heat induced recovery
ϵ_u	strain after unloading the force
η^*	complex viscosity
$\Delta\eta^*$	difference in viscosity
μ	mass attenuation coefficient
3D	three-dimensional
15%I	polymer containing 15 mole percent 2,2-bis(iodomethyl)-1,3-propanediol
20%I	polymer containing 20 mole percent 2,2-bis(iodomethyl)-1,3-propanediol

25%I polymer containing 25 mole percent 2,2-bis(iodomethyl)-1,3-propanediol
35%I polymer containing 35 mole percent 2,2-bis(iodomethyl)-1,3-propanediol

CHAPTER 1: INTRODUCTION TO FUNCTIONAL POLYESTERS FOR BIOMEDICAL AND INDUSTRIAL APPLICATIONS

1.1 Overview

This dissertation describes the synthesis, characterization, and elucidation of the structure-property relationships of functionalized polyesters for biomedical and industrial applications. Iodine functionalized polyesters were designed to achieve radiopaque biomaterials. Section 1.2 reviews important information pertaining to the development of radiopaque biopolymers for use as computed tomography nanoparticle contrast agents and inherently radiopaque, smart biomaterials. Section 1.3 provides background information explaining the promising field of functionalized engineering polyesters. In this thesis, endgroup functionalization of low molecular weight engineering polyesters was implemented in the development of robust plastics that have low melt viscosities.

1.2 Introduction to Radiopaque Biomaterials

1.2.1 Computed Tomography

Computed tomography (CT) is one of the most widely applied imaging technologies in diagnostic medicine. Sir Godfrey Hounsfield, a British engineer, invented the first CT scanner. Hounsfield went on to receive the 1979 Nobel Prize in Medicine, only seven years after the first clinical trial.¹ Today, CT is broadly accessible and cost efficient, with more than 85 million CT procedures performed annually in the United States.²

CT relies on x-ray penetration and attenuation to generate images. An x-ray tube is rotated around the patient, generating thin cross-sectional images at each angle. These thin slices

are then reconstructed to determine the attenuation in each voxel, where attenuation is defined as the decrease in intensity of transmitted x-rays due to absorption or scattering:

$$I = I_0^{-\mu x} \dots\dots\dots \text{(equation 1.1).}$$

I is the intensity of the transmitted x-rays, I_0 is the intensity of the incident x-rays, μ is the mass attenuation coefficient of the object, and x is the thickness of the object being imaged.^{3,4} It is important to note that μ is proportional to the third power of the atomic number (Z) of the imaged material,^{3,5} and the quality of the developed image is dependent on the electron densities of the object being imaged and the surrounding medium.

The attenuation coefficient for each voxel can then be converted to its CT number, called a Hounsfield unit (HU):

$$HU = K \cdot \frac{(\mu_{\text{voxel}} - \mu_{\text{water}})}{\mu_{\text{water}}} \dots\dots\dots \text{(equation 1.2).}$$

K is an integer constant, typically 1000. For example, the attenuation number of water is 0 HU. Air ($\mu_{\text{air}} \approx 0$) results in a CT number of approximately -1000 HU, and dense bone ($\mu \approx 2\mu_{\text{water}}$) is approximately +1000 HU.¹ Soft tissues have densities similar to water (typically between 40-80 HU) and are hard to distinguish by CT; whereas, the density of bone compared to its surrounding muscle tissue is easy to visualize.⁵

Three-dimensional (3D) images are obtained with high spatial resolution from reconstructed image slices using CT. Anatomic details are interpreted using these 3D CT images for diagnosing diseases and deciphering treatment options.³ Furthermore, CT has high temporal resolution (<50 ms for a complete scan), making CT preferable for tasks such as cardiac motion imaging.¹ Oftentimes, contrast agents, which contain atoms of high Z , are used to enhance the visibility of soft tissue areas. According to the 2012 IMV Medical Information Division CT survey, of the 85.3 million CT procedures performed in the U.S. in 2011, over half (53%)

utilized contrast agents, amounting to over eight million liters of traditional contrast media consumed each year.^{2,6}

1.2.2 Computed Tomography Contrast Agents

1.2.2.a Traditional Contrast Agents

Clinically used contrast agents are small molecules derived from 1,3,5-triiodobenzene (Figure 1.1).^{3,4,6-8} These compounds are utilized due to the high Z of iodine. To increase the biocompatibility of the aromatic base structure, functional groups such as alcohols and amides were added.^{3,6} Although several small molecule contrast agents exist, the pharmacokinetics and potential negative effects are similar for all categories.⁶

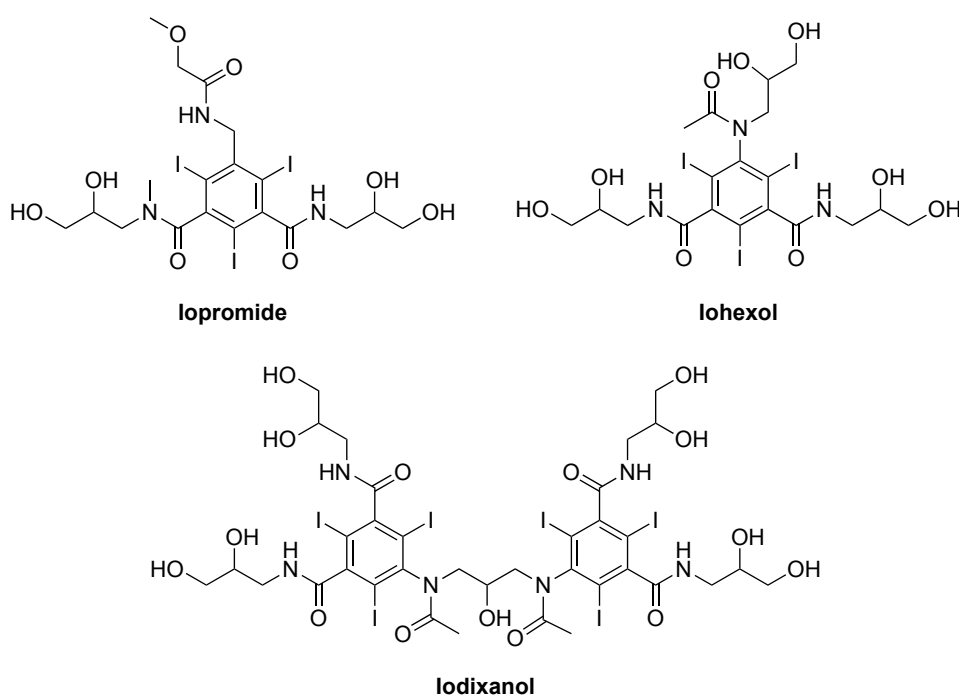


Figure 1.1 Chemical structures of well-known iodinated contrast agents: iopromide (ULTRAVIST®), iohexol (OMNIPAQUE®), and the dimer, iodixanol (VISIPAQUE®).^{3,4,6-8}

The most common and serious side effect of traditional, intravascular CT contrast agents is contrast medium-induced nephrotoxicity (CIN), which is one of the most common causes of

hospital-acquired kidney failure.⁹ Risk factors for nephrotoxicity from CT contrast agents include existing poor renal function (particularly seen in elderly patients), diabetes, kidney disease, and chemotherapy use.^{10,11} In a study by Rudnick *et al.*, patients with preexisting renal insufficiency demonstrated a 21.2 times greater risk for nephrotoxicity than patients without renal insufficiencies.⁸ Moreover, clinical studies of CIN in “high risk” patients include strict enrollment criteria. In many studies, patients with compromised renal function due to disease or illness (i.e., diabetes or cancer) were not eligible. These studies also ensured that patients were optimally hydrated; therefore, real-life clinical incidences of CIN may be even greater.⁸ Difficulties, such as CIN, have reduced the utility of CT and its medical diagnostic capabilities. The development of novel contrast agents that are safe and effective for patients with renal dysfunction is critical.

Additional limitations of traditional contrast agents include vascular permeation and non-specific biodistribution, which limits microvascular and targeting performance.^{12,13} Also, the rapid excretion (blood half-life of <10 minutes) of small molecule contrast agents restricts imaging times.¹² The utilization of nanotechnology could allow increased circulation times, targeted imaging, and avoidance of the kidneys by size exclusion.

1.2.2.b Metal-based Nanoparticles as Contrast Agents

Metal-based materials, such as tantalum, gold, and bismuth have high atomic numbers ($Z = 73, 79, 83$, respectively), and thus high x-ray attenuation capabilities. Therefore, metal-based nanoparticles have been extensively studied for use as improved CT contrast agents.^{3,14–23}

Gold nanoparticles (AuNPs) are the most broadly studied metallic nanoparticles.²⁴ Although bare AuNPs showed detailed anatomical images, these nanoparticles were excreted through the kidneys due to their small size (1.9 nm) and easily aggregated *in vivo*.²⁵ Therefore,

AuNPs were synthesized *via* the Turkevich method, which utilizes the reduction of H₂AuCl₄ with citrate in aqueous conditions.^{12,25} Citrate-stabilized AuNPs are readily modified with surface coatings, such as SH-PEG or the mussel-inspired adhesive, 3,4-dihydroxyphenylalanine (DOPA).^{12,15,26} PEG functionalized AuNPs were biocompatible (nontoxic), accumulated in phagocyte-rich organs, such as the liver and spleen, and displayed long circulation times.¹²

Figure 1.2 displays PEG functionalized AuNPs injected *via* tail-vein into a rat. The nanoparticles allowed visualization of the liver and clearly revealed a hepatoma.¹²

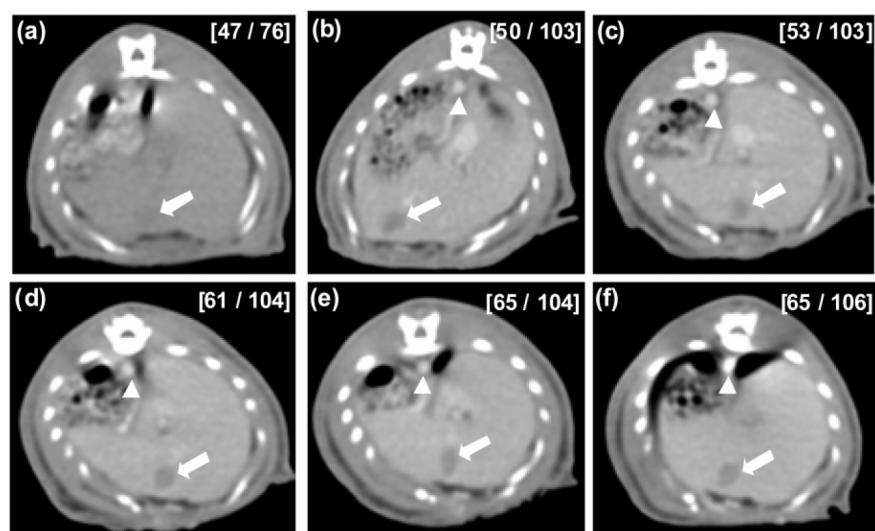


Figure 1.2 This figure was adapted and used from reference 12. CT images in a rat hepatoma model following injection PEG-coated AuNPs: a) before injection, b) 5 minute-mark (directly after injection of the AuNPs), c) 1 hour, d) 2 hours, e) 4 hours, and f) 12 hours after injection. Large arrows indicate the hepatoma regions. The numbers shown in brackets in the upper right-hand corner of the images indicate the HU values of the hepatoma regions (left) and the surrounding normal liver parenchyma (right).¹²

Although AuNPs have been studied extensively and show great promise, they are too expensive for sustainable translation to a hospital setting.^{6,25} Research utilizing bismuth and tantalum hopes to address the impending costs of gold-based contrast agents. Elemental bismuth

is inherently toxic, and Bi_2S_3 nanocrystals show a safety profile similar to traditional iodinated contrast agents.²⁵ Therefore, Bi_2S_3 nanoparticles coated with polyvinylpyrrolidone, PEG, or phospholipids were developed.^{13,22,27} Polymer-coated Bi_2S_3 nanoparticles showed higher x-ray absorption than iodinated contrast agents, but their size, shape, and stability remained a challenge.^{12,15,28} In one example by Sailor and coworkers, Bi_2S_3 nanoparticles were coated using DSPE-PEG *via* noncovalent bonding and labeled using the LyP-1 peptide (used to target 4T1 breast cancer tumors) to produce 28 nm particles.²⁸ The particles provided sufficient contrast for detailed CT images of targeted tumors, and they were mainly cleared by the liver and spleen. Approximately 4% of the nanoparticles were cleared by the kidneys, and a small amount of agglomeration occurred (evident in the lungs), suggesting degradation into ionic bismuth *in vivo*.²⁸

Tantalum and tantalum oxide are widely used in clinical applications as radiographic markers and implants.¹⁹ Tantalum oxide nanoparticles have been synthesized with various silane-modified surfaces that allow easy immobilization of a PEG corona.^{18–20} These particles show improvements over traditional contrast agents, such as long circulation times and the potential for multimodal imaging.^{19,20} In the work of Hyeon and coworkers, a fluorescent dye was introduced to PEG functionalized tantalum oxide nanoparticles, allowing bimodal visualization of the lymph nodes using CT and fluorescence imaging (Figure 1.3).¹⁹ Due to the small size of tantalum-based nanoparticles (5-19 nm), excretion through the kidneys remains a concern.^{5,18}

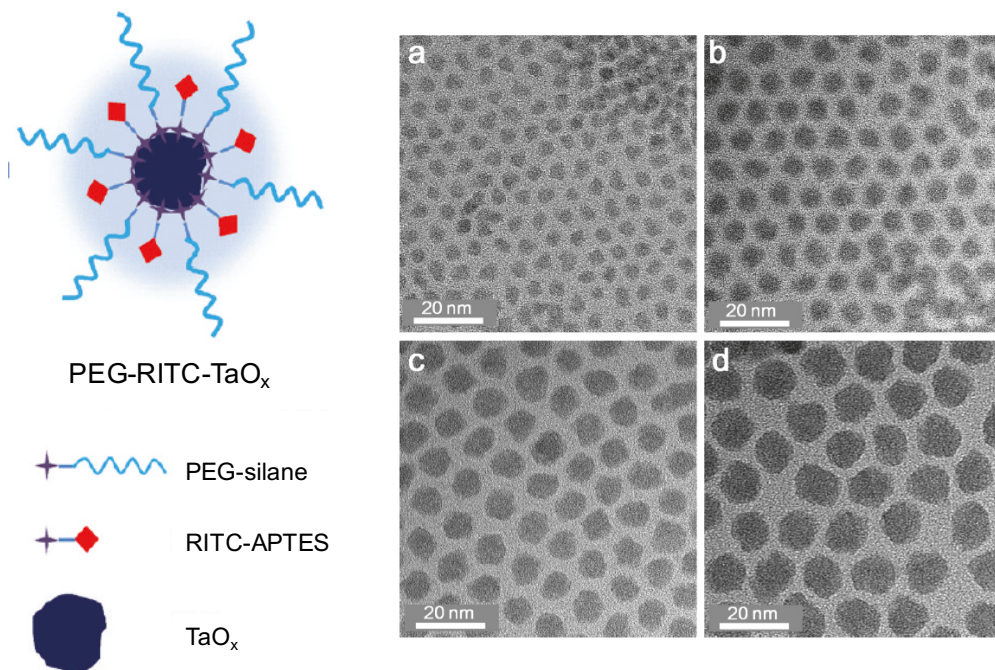


Figure 1.3 This figure was adapted from reference 19. Schematic of tantalum oxide nanoparticles functionalized with PEG and a fluorescent marker (RITC-APTES) (left). TEM images (right) showing size control and small size of the nanoparticles.¹⁹

1.2.2.c Iodinated Nano-carriers and Nanoparticles

Iodine-based nano-carriers, such as nano-emulsions, micelles, and liposomes, were developed to circumvent the limitations of traditional, small molecule contrast media.^{13,29–32} Polymeric micelles can have CMCs up to 1000-fold lower than those of surfactant-based nano-emulsions and micelles.³³ De Vries *et al.* formulated emulsions using radiopaque oils derived from the 2,3,5-triodobenzoate moiety. Emulsions using either phospholipids or amphiphilic polymers were tested *in vivo* as CT blood pool contrast agents. The phospholipid-based emulsion was unstable and caused acute lung embolism and mouse death, presumably as a result of low colloidal stability. Conversely, the polymer-stabilized emulsion showed a long blood circulation half-life (3 hours), exhibited no noticeable signs of toxicity, and was metabolized by the liver.²⁹

In another example, liposome-encapsulated iodixanol (a traditional contrast agent, Figure 1.1) was tested in a clinical trial. While x-ray attenuation was significantly enhanced, side effects such as backache, chills, and flu-like symptoms were considered too pronounced for clinical use.³⁰ A similar liposomal system encapsulating iopromide (Figure 1.1) also showed enhanced attenuation (>60 HU from baseline). However, when testing the mean lethal dose of this liposomal system against free iopromide, the free agent was better tolerated.³¹ Poor stability of micellar and liposomal systems, including aggregation and leakage of encapsulated agents, remains a concern.^{32,33}

To circumvent the stability issues of nano-carriers, polymeric core-shell nanoparticles and new polymer systems were researched.³⁴⁻³⁷ As depicted in Figure 1.4, Kong *et al.* synthesized nano-capsules of crosslinked poly(ethylene glycol)-poly(propylene glycol)-poly(ethylene glycol) (Pluronic) encasing Lipiodol®, an iodinated derivative of poppy seed oil.³⁷ These 150 nm core-shell particles were stable and noncytotoxic. Furthermore, the particles enhanced attenuation for 4 hours and accumulated in the liver and spleen. After histological analysis, however, slight aggregation due to protein adsorption was observed.³⁷

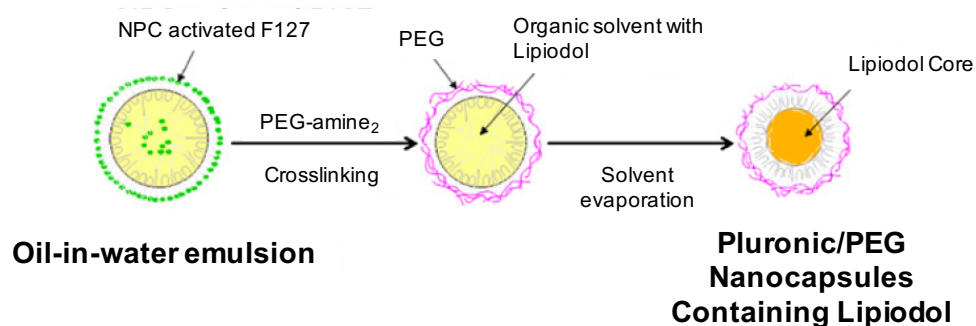


Figure 1.4 Figure taken from reference 37. Synthetic scheme for core-shell nanoparticles made by Kong *et al.*³⁷

New polymer systems utilized aromatic ring-bound iodine in methacrylates,^{38,39} styrenics,⁴⁰ anhydride esters,⁴¹ and cellulose.⁴² For example, the emulsion polymerization of 2-methacryloyloxyethyl(2,3,5-triiodobenzoate) formed nanoparticles of approximately 25.5 nm. These nanoparticles showed elevated visibility of the blood pool for 30 minutes after injection and were removed by the mononuclear phagocyte system.³⁴

All of the contrast agents described to this point utilized metals or aromatic ring-bound iodine. While aromatic ring-bound iodine is likely employed to increase the stability of the covalently bound iodine, the precursors are expensive, toxic, and poorly biodegradable. An ideal contrast agent should be radiopaque, cost-effective, biocompatible, long-circulating, safely excreted, and easily formulated.

1.2.3 Radiopaque Polymers

1.2.3.a Polymer Mixtures

Typical organic polymer biomaterials are radiolucent due to their lack of high Z elements. In many cases, however, radiopacity is necessary for monitoring implantation; for example, radiolucent stents run the risk of improper placement.^{43,44} For this reason, many polymeric implants include metallic markers made of platinum, gold, or titanium.^{43,45-47}

Heterogeneous polymer mixtures utilizing inorganic salts or metallic particles were also developed to induce radiopacity.⁴⁸⁻⁵³ For example, bone cements are typically made from PMMA composites comprising barium sulfate, zirconium dioxide, or tantalum oxide.^{48,54-58} Drawbacks of heterogeneous polymer mixtures include incompatibility with the polymer matrix (e.g., negative effects on physical, thermal, or mechanical properties) and leaching of the radiopaque additives. Leaching can result in the loss of radiopacity of the implant, additive aggregation (aggregates can obstruct implantation pathways, such as the small lumen of a

catheter), or toxicity.^{44,59} Inorganic radiopaque agents and radiocontrast-inducing additives can also cause undesirable discoloration, which limits the pigment options of the material in its final form.⁶⁰

Homogeneous mixtures were made by chelating heavy metal salts with polymers.^{53,61,62} In an example by Smid and coworkers, organobismuth (e.g., Ph₃Bi) was incorporated with PMMA, PVC, and polystyrene. In all cases, the addition of only 1.3% by weight (b.w.) of the organobismuth additive plasticized the polymers and lowered the T_g; however, a minimum of 24% b.w. of the additive was necessary to match the radiopacity of an aluminum control.⁶²

1.2.3.b Inherently Radiopaque Polymers

Inherently radiopaque polymers, utilizing covalently bound iodine, supersede many of the issues involved with heterogeneous and homogeneous polymer mixtures, such as inhomogeneity, leaching of additives, and thermomechanical property variations. One approach to designing inherently radiopaque polymers involves post-functionalization of high molecular weight polymers with iodinated molecules. Post-functionalization has been demonstrated on cellulose esters,⁴² polyurethanes,⁶³ and poly(organophosphazenes).⁶⁴ Allcock and coworkers post-functionalized poly(dichlorophosphazene) to create 3,5-diiodotyrosine ethyl ester or 4-iodophenylalanine ethyl ester side groups.⁶⁴ In another example, James *et al.* functionalized a commercially available polyurethane (Tecoflex 80 A) with triiodobenzoyl chloride or *N*-(2,6-diiodocarboxyphenyl)-3,4,5-triiodo benzamide (Figure 1.5) *via* urethane linkages on the polymer backbone.⁶³

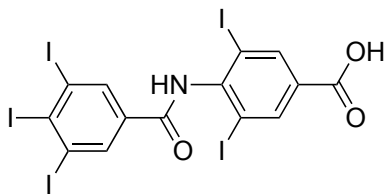


Figure 1.5 *N*-(2,6-diiodocarboxyphenyl)-3,4,5-triiodobenzamide was used to functionalize a radiolucent polyurethane.⁶³

Another approach to making inherently radiopaque polymers involves the use of iodinated monomers in polymerization. As briefly described in Section 1.2.2.c, several methacrylate-based iodinated polymers have been developed (Figure 1.6),^{38,65–70} additionally, radiopaque TPUs and polyesters were designed.^{50,59,63,71–73} All of these polymers incorporate aromatic iodinated monomers. For example, many radiopaque TPUs utilize an iodinated Bisphenol-A (I-BPA).^{59,73} These I-BPA-based TPUs had various properties and degradation profiles; however, BPA is a controversial monomer that has been banned from certain applications by the FDA.⁷⁴

In a unique example by Rode *et al.*, 2,2-bis(hydroxyl-methyl)propane-1,3-diyl-bis(2,3,5-triiodobenzoate) was synthesized using 2,3,5-triiodobenzoic acid and 2,2-dimethyl-(1,3-dioxane-5,5-diyl)dimethanol. This molecule was then used to make polyesters and polyester urethanes by ring opening polymerization (Figure 1.7 depicts the polyester). These polyesters and TPUs were hydrolytically biodegradable; however, the radiopacity of the polymers over the course of degradation was not analyzed.⁷¹

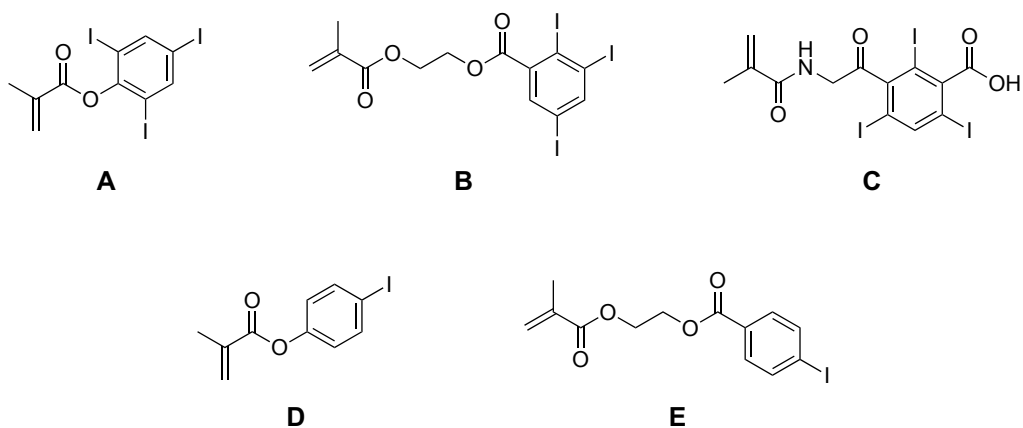


Figure 1.6 A variety of iodinated monomers developed for radiopaque methacrylate-based polymerizations: A) triiodophenyl methacrylate,⁶⁵ B) 2-methacryloyloxyethyl(2,3,5-triiodobenzoate),^{38,66,67} C) 3-(methacryloylamidoacetamido)-2,4,6-triiodobenzoic acid,⁶⁸ D) 2-(2'-iodobenzoyl)-ethyl methacrylate,⁶⁹ E) 2-(4'-iodobenzoyloxy)-ethylmethacrylate.⁷⁰

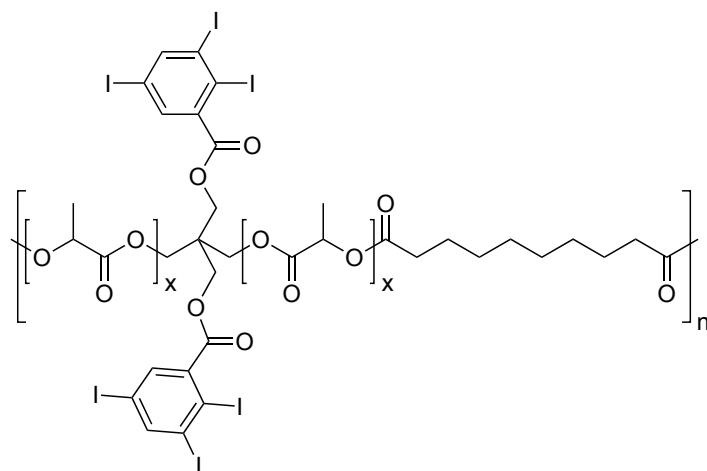


Figure 1.7 Iodine-containing polyesters made *via* ring opening polymerization.⁷¹

Only two examples utilizing nonaromatic iodine (iodine that is not attached to aryl moieties) were found in the literature. One of these aliphatic polymers was designed primarily for flame retardant purposes and contained a significant amount of the brominated precursor.⁷⁵ The other example involved the synthesis of α -iodo- ϵ -caprolactone to make iodinated poly(ϵ -caprolactone) (PCL); post-functionalization of PCL to make poly(α -iodo- ϵ -caprolactone)

was also implemented.⁷⁶⁻⁷⁸ The secondary iodine in poly(α -iodo- ϵ -caprolactone) presumably allows side-reactions, such as SN1, SN2, E1 and E2.

1.2.4 Radiopaque Shape Memory Biomaterials

1.2.4.a The Shape Memory Cycle

Shape memory polymers are a class of smart materials that can be programmed into a permanent and a temporary shape. These polymers are typically elastomers; therefore, the permanent shape is programmed by chemical crosslinks, referred to as permanent netpoints. The temporary shape is programmed by the application of a stimulus, such as heat or light, and a force. In the case of thermal shape memory, semicrystalline polymers are often utilized. Crystallites provide physical netpoints that preserve the temporary shape after the force is removed and until the material is recovered by exposing the material to the stimulus, heat. Once the material, in its temporary shape, is heated above its T_m , it will return to its entropically preferred permanent shape, which was encoded by chemical crosslinks.⁷⁹⁻⁸¹ Figure 1.8 depicts the shape memory cycle.

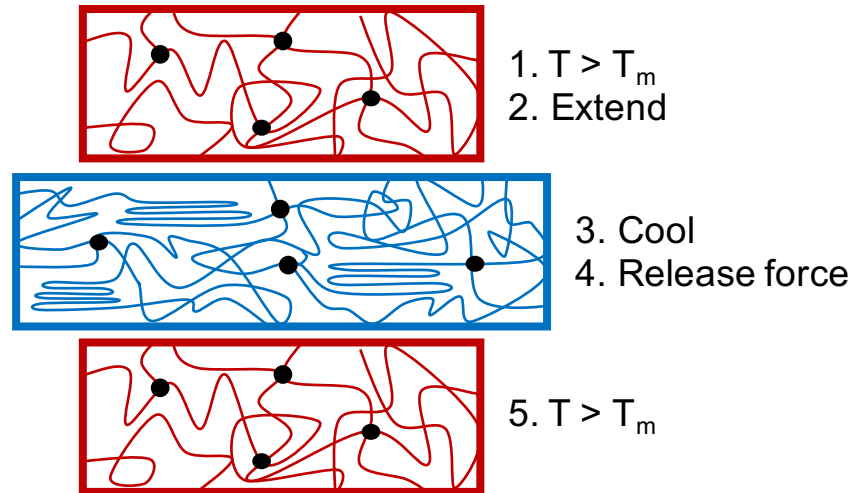


Figure 1.8 The Shape Memory Cycle: The sample is first cured into its permanent shape. 1. The sample is heated to melt all crystallites. 2. The sample is deformed, in this case extended, using a force. 3. While under this force, the sample is cooled to produce crystallites that secure the temporary shape. 4. The force is released. 5. Upon heating above the T_m , the crystallites melt, and the sample returns to the permanent shape.

The effectiveness of the material to perform shape memory is quantified by strain fixity (R_f) and strain recovery (R_r), as shown in equations 1.3 and 1.4. Fixity refers the sample's ability to maintain its temporary shape after the force is released, and recovery quantifies the sample's ability to transition back to the permanent shape upon reheating. In equations 1.3 and 1.4, ϵ_u represents strain after unloading the force, ϵ_m represents temporal strain after deformation, and ϵ_p represents the permanent strain after heat induced recovery.⁸¹

$$R_f (\%) = \frac{\epsilon_u}{\epsilon_m} \cdot 100 \dots \dots \dots \text{(equation 1.3)}$$

$$R_r (\%) = \frac{(\epsilon_u - \epsilon_p)}{(\epsilon_m - \epsilon_p)} \cdot 100 \dots \dots \dots \text{(equation 1.4)}$$

1.2.4.b Traditional Shape Memory Biomaterials

Shape memory polymers have shown particular value as biomaterials; further, many biocompatible polymers have innate shape memory properties. Shape memory polymers include PCL,^{82,83} poly(lactic acid),⁸⁴ polyurethanes,^{85–87} polyethylene,^{88,89} and variations of poly(octylene adipate).^{90–92} Biomedical applications of shape memory polymers include self-tying sutures,⁸² deployable stents,^{93,94} and mechanically active scaffolds.^{52,95} Thus, shape memory biomaterials can significantly lower the invasiveness of implantation.⁸² Figure 1.9A displays a self-tying suture made using oligo(ϵ -caprolactone)diol and oligo(*p*-dioxanone)diol copolymers developed by Lendlein and Langer.⁸² In Figure 1.9A, the copolymer self-ties over a period of 20 seconds at $T > T_m$. In Figure 1.9B, Gall and coworkers developed a deployable stent using crosslinked networks of *tert*-butyl acrylate, di(ethylene glycol) dimethacrylate, and poly(ethylene glycol) dimethacrylate.⁹³

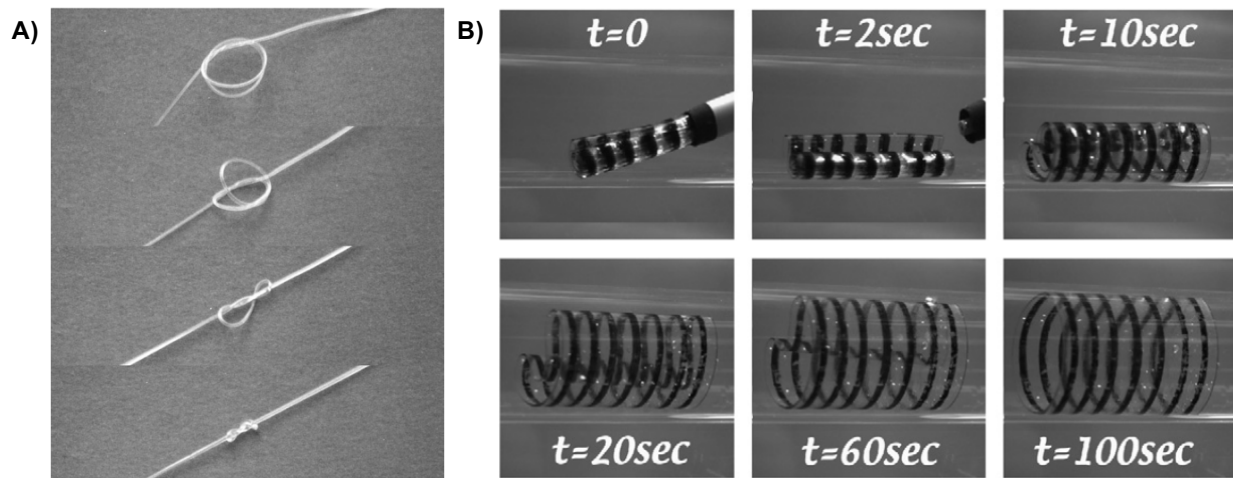


Figure 1.9 Shape memory biomaterials adapted from references 83 and 94: A) self-tying suture,⁸² and B) deployable stent.⁹³

1.2.4.c Radiopaque Shape Memory Polymers

Shape memory polymers have shown great utility in the biomedical field, where radiopacity is of specific interest. The first examples of materials with x-ray and shape memory properties were radiopaque shape memory alloys. Shape memory alloys are provided radiocontrast through fabrication with expensive elements, such as platinum or erbium;^{96–98} therefore, the addition of radiopacity to shape memory polymers would be beneficial for cost and environmental reasons.⁹⁹ Although none of the polymers depicted in Section 1.2.3.b were tested for “smart” capabilities, such as shape memory, inherently radiopaque polymers in the form of TPUs and semicrystalline polyesters (e.g., PCL) should be capable of performing shape memory.

To date, all of the polymers specifically tested for shape memory were provided radiocontrast through impregnation using inorganic salts and particles or contrast agents.^{52,95,100–102} In an example by Wong *et al.*, PLGA/PEG copolymers showed shape memory properties and were provided radiopacity using filament compounds based on barium, bismuth, and tantalum (Figure 1.10).¹⁰⁰ In this example, the shape memory effect was triggered by water by taking advantage of the solubility of PEG. This radiopaque shape memory device was tested *in vivo* in a rabbit model as an embolization plug for temporary vascular occlusion. Other examples of radiopaque shape memory composites involve BaSO₄ impregnation of polyether urethanes for active tissue engineering scaffolds.^{52,95} These examples are heterogeneous polymer mixtures, and therefore, possess the potential disadvantages outlined in Section 1.1.3.a.

An ideal radiopaque shape memory polymer should be provided radiopacity through covalently bound, stable iodine. The iodinated precursors and subsequent polymers should be nontoxic, biocompatible, and biodegradable. Additionally, in the case of thermal shape memory, the polymer should have a T_m slightly above body temperature and have long-lasting radiopacity.

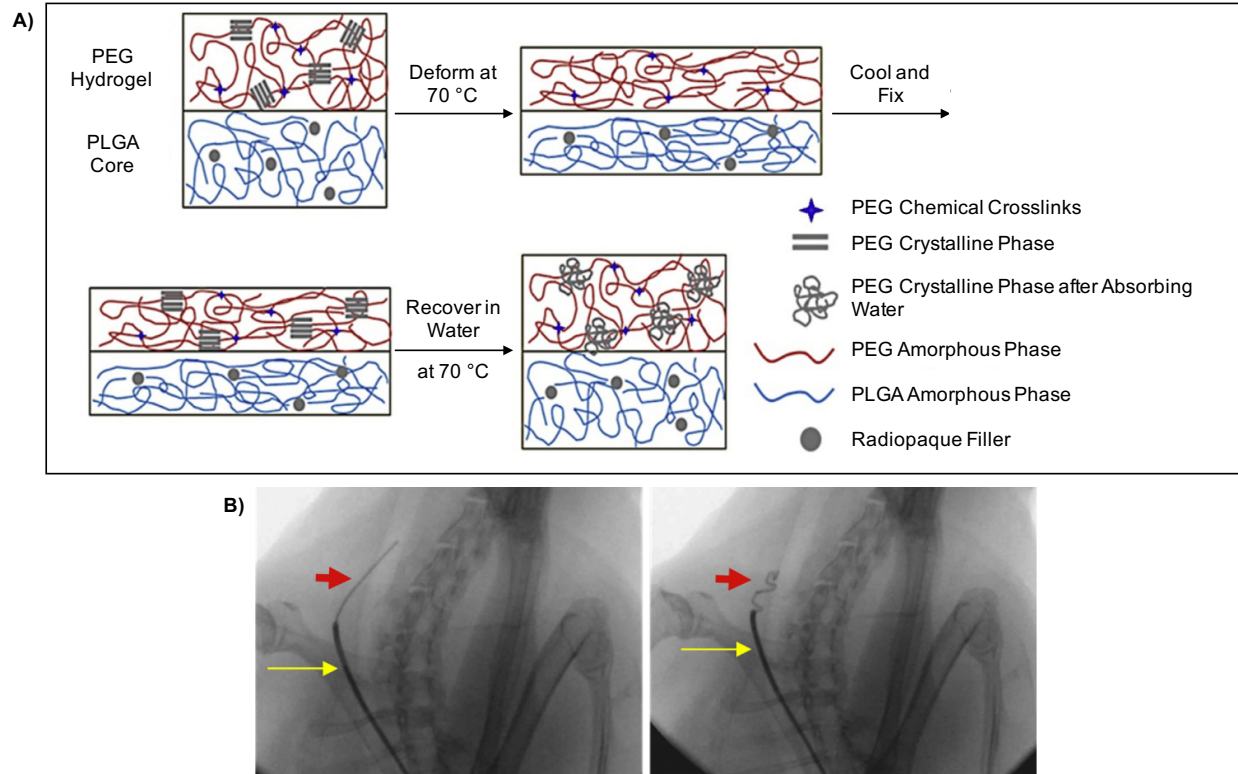


Figure 1.10 Radiopaque shape memory device from figures adapted from reference 101. A) Schematic of the shape memory polymer. This shape memory system consists of a PLGA composite core coated with a crosslinked PEG hydrogel. Recovery of the initial shape was achieved when the hydrogel swelled in the presence of water, the stimulus. B) X-ray image of a radiopaque shape memory embolic plug prototype (red arrow) using a micro-catheter (yellow arrow) in a rabbit model. As the hydrogel swelled, vascular embolization was achieved (left to right).¹⁰⁰

1.2.5. Summary

The development of new, radiopaque materials could augment procedures performed in the biomedical and radiology fields. In this dissertation, radiopaque polyesters were synthesized using a unique, aliphatic, iodinated monomer. These polymers were fabricated into nanoparticles as improved CT contrast agents (Chapter 2) and thermosets as inherently radiopaque shape memory materials (Chapter 3). The work outlined in Chapter 2 has been

submitted for publication, and the work outlined in Chapter 3 is currently in preparation for submission.

1.3 Supramolecular Engineering Polyesters

1.3.1 Supramolecular Chemistry *via* Ureidopyrimidinone Endgroup Functionalization

Supramolecular chemistry takes place due to non-covalent bonds, such as pi-pi stacking,¹⁰³ ionomers,^{104,105} metal-ligand,¹⁰⁶⁻¹⁰⁸ and host-guest complexes.¹⁰⁹ Materials incorporating hydrogen bonding moieties are the most well-studied of the supramolecular polymer families. These supramolecular interactions have been displayed in the form of weak H-bonding (e.g., -COOH)¹¹⁰ or in the form of multiple H-bonding (e.g., DNA).¹¹¹ Multiple hydrogen bonds *via* the quadruple H-bonding ureidopyrimidinone (UPy) group (Figure 1.11) are known to produce superior, thermally reversible supramolecular assemblies that dramatically alter the properties of the initial molecule or polymer.¹¹²⁻¹¹⁶

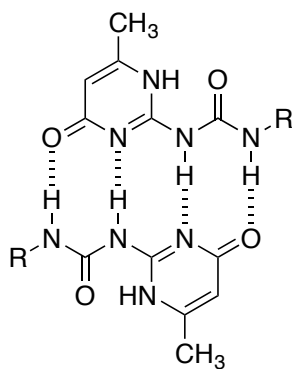


Figure 1.11 The quadruple hydrogen bonding dimerization of the ureidopyrimidinone (UPy) moiety. R can represent attachment to a small molecule, direct attachment to a polymer, or attachment to a linker unit, which attaches the UPy unit to a polymer.

Although H-bonds are directionally selective, the UPy group is self-complimentary; thus, stoichiometry does not affect the degree of supramolecular polymerization.¹¹² Therefore, the

supramolecularly enhanced molecular weight of UPy functionalized polymers leads to increased mechanical properties, like elasticity (Figure 1.12).^{114,115} This enhancement, in part, is due to the strength of the H-bonds in a UPy dimer, which falls between that of a single H-bond (5-65 kJ mol⁻¹) and a covalent bond (350 kJ mol⁻¹).^{104,117} Nevertheless, the quadruple H-bonds shown in Figure 1.11 while strong, are also dynamic. Thus, low melt viscosities can be achieved as a result of the thermal reversibility of UPy-UPy aggregation.^{114,115} The combination of apparently orthogonal properties *via* UPy functionalization is beneficial in the application of self-healing,^{118,119} recyclable,¹²⁰ and adhesive materials.¹²¹

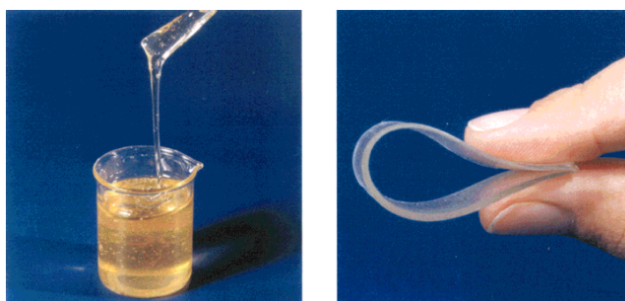


Figure 1.12 Figure taken from reference 114. Poly(ethylene butylene) with hydroxyl endgroups (left) compared to poly(ethylene butylene) with UPy endgroups (right).¹¹⁴

Polymer functionalization using the UPy group is extremely versatile. UPy groups can be attached to polymers using a variety of synthetic techniques. The most common approach utilizes isocyanate-functionalized isocyanates with a choice of several nucleophiles at the polymer termini (e.g., hydroxyl or amine).^{114,115,122,123} Modification of the R group (Figure 1.11) can alter the strength and extent of UPy aggregation and polymerization. For example, modifying the type of linker attaching the UPy unit to the polymer termini can allow lateral stacking in addition to the dimerization depicted in Figure 1.11.^{115,124} Kautz *et al.* functionalized

the termini of poly(ethylene butylene) (PEB) with a variety of endgroups (Figure 1.13).¹¹⁵ Direct functionalization of PEB with the UPy moiety did not lead to fiber formation or an apparent T_m (Figure 1.13a). When the UPy group was attached to PEB *via* a hexamethylene with two urea groups (Figure 1.13d), micrometer long fibers formed as well as a clear T_m at 129 °C. PEB with linear bisurea-functionalized termini showed aggregation in the form of small fibers (Figure 1.13b), thus providing evidence that the linker attaching the UPy end-unit to the polymer plays a major role in fiber formation and UPy-UPy “crystallization”.¹¹⁵ A study by Appel *et al.* indicated that the driving force of fiber formation is phase separation of the endgroup clusters from the polymer backbone, and this phase separation was only achievable with oligomers of low T_g (PEB has a T_g of -57 °C and no inherent T_m).¹²⁴

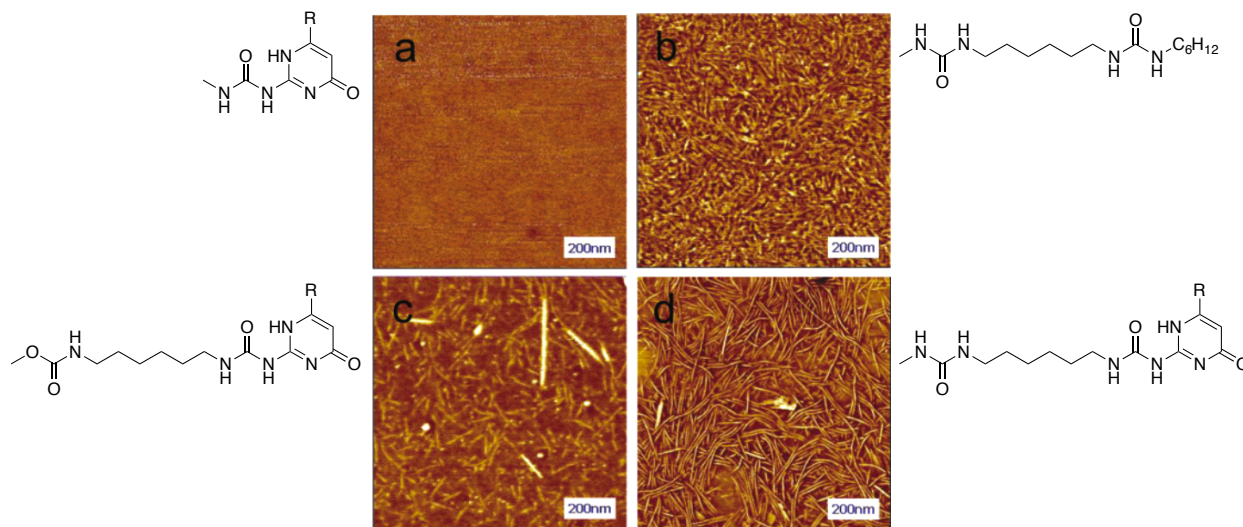


Figure 1.13 Figure adapted from reference 115: TEM images of thin films made from PEB functionalized with various endgroups at both termini. Chemical structure of the endgroups are depicted next to each TEM image.¹¹⁵

The vast majority of supramolecular polymers are low performing, such as PEO/PPO,¹¹² PDMS,¹²³ PEB,^{113–115} polyTHF,^{116,122} PCL,^{122,125,126} and aliphatic polycarbonates.^{116,127}

Hydrogen bonding moieties were also applied to polymers with higher glass transition temperatures, such as polystyrene.¹²⁸⁻¹³¹ For example, Rotello and coworkers presented styrenic polymers with triple H-bonding moieties.¹²⁸⁻¹³⁰ However, the UPy moiety has had limited investigation with more robust glassy or semi-crystalline polymers.

Long and coworkers attached the UPy moiety to polystyrene and poly(butylene terephthalate).^{131,132} In one case, polystyrene, polyisoprene and poly(styrene-*b*-isoprene) were UPy functionalized. All of the materials were analyzed by DSC, TGA, and GPC. Notably, the degradation temperature of the polymers decreased and the T_g increased as a result of UPy functionalization. Only functionalized polyisoprene and poly(styrene-*b*-isoprene) were studied further using rheology and TEM.¹³¹

1.3.2 Engineering Polyesters

The development of high molecular weight, semi-aromatic polyesters, specifically poly(ethylene terephthalate) (PET), was first reported the late 1940s by Whinfield and Dickson.¹³⁴ Since these early developments, engineering polyesters have become some of the most important and ubiquitous polymers for a number of applications. Engineering polyesters are used for computers, televisions, kitchen appliances, agriculture equipment, medical devices, and packaging (e.g., medical, food, specialty). For example, PET is the foremost engineering polyester used in the production of synthetic fibers for applications like tire reinforcement and clothing, with more than 17,000 kilotons produced each year.¹³⁵ As polymer science advanced, the demands of industrial manufacturers and consumers raised; therefore, a variety of other semi-aromatic and aromatic engineering polyesters and copolyesters were designed.

In the late 1950s, Eastman Kodak patented poly(1,4-cyclohexylenedimethylene terephthalate) (PCT) and *cis/trans*-1,4-cyclohexanedimethanol (CHDM) modified variations of

PET (Figure 1.14).^{136,137} During processing, polymers with high melting temperatures, like PCT ($T_m \sim 290\text{ }^\circ\text{C}$), can thermally and hydrolytically degrade. Although injection molding crystalline plastics is advantageous for some end-use applications (e.g., glass fiber reinforced formulations), lowering (or eliminating) the T_m is desired to decrease processing and crystallization temperatures.¹³⁵

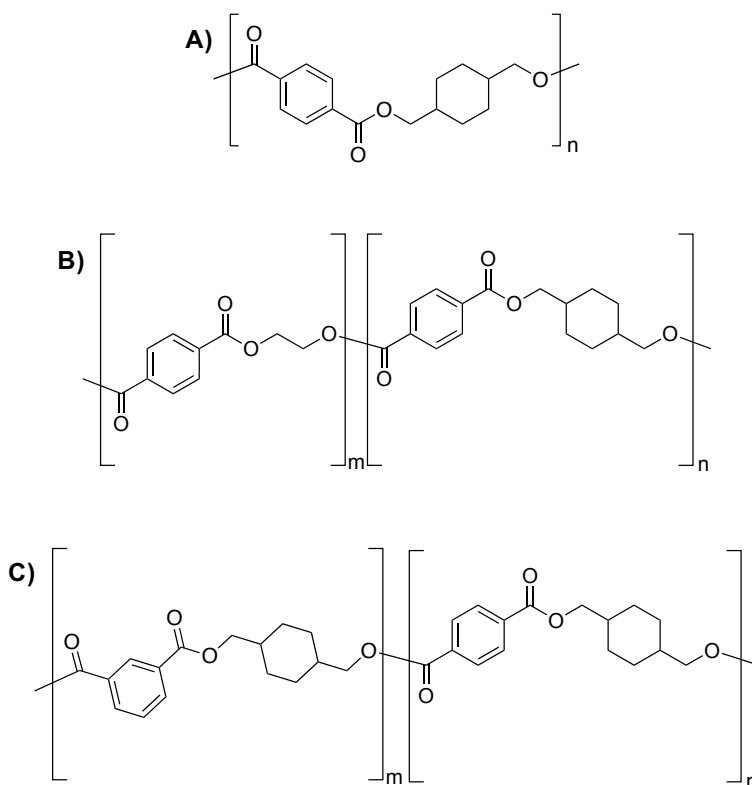


Figure 1.14 A) PCT, B) PETG ($m = \text{major component}$) or PCTG ($n = \text{major component}$), C) PCTA when $m \leq 50\text{ mol}\%$.¹³⁵⁻¹³⁷

CHDM-based copolymers (e.g., PETG, PCTG, and PCTA in Figure 1.14) were designed for the manufacture of more aesthetic injection molded or blow molded objects by modifying the comonomer make-up to suit the desired end-use. The increased amorphous character of CHDM copolymers revealed improved clarity, impact strength, and dye uptake.¹³⁵ For example, PETG

is the most widely used of the CHDM-based polyesters found in Figure 1.14. PETG has no T_m by DSC and remains amorphous after processing; as a result, PETG is used for specialty packaging (e.g., cosmetics) where high clarity and impact toughness are important.^{135,138}

1.3.3 Summary

The next step in the advancement of supramolecular chemistry should involve terminal UPy functionalization and thorough characterization of engineering and high performance oligomers. Thorough examination of supramolecular engineering polymers would potentially open a new field of supramolecular chemistry. This work would deepen the current understanding of supramolecular systems.¹³³ In Chapter 4 of this dissertation, the synthesis and characterization of UPy functionalized PETG oligomers is summarized. UPy functionalized PETG serves as the first example of a supramolecular engineering polymer with enhanced thermal, mechanical, and viscoelastic properties at pertinent use and processing temperatures. The work reviewed in Chapter 4 was published in RSC Polymer Chemistry (DOI: 10.1039/c6py01421f).¹³³

REFERENCES

- (1) Goldman, L. W. *J. Nucl. Med. Technol.* **2007**, *35*, 115.
- (2) *IMV 2013 CT Market Outlook Report*; 2013.
- (3) Lee, N.; Choi, S. H.; Hyeon, T. *Adv. Mater.* **2013**, *25*, 2641.
- (4) Yu, S. B.; Watson, A. D. *Chem. Rev.* **1999**, *99*, 2353.
- (5) Shilo, M.; Reuveni, T.; Motiei, M.; Popovtzer, R. *Nanomedicine* **2012**, *7*, 257.
- (6) Katzberg, R. W.; Haller, C. *Kidney Int.* **2006**, *69*, S3.
- (7) Chalmers, N.; Jackson, R. W. **1999**, *72*, 701.
- (8) Rudnick, M. R.; Goldfarb, S.; Wexler, L.; Ludbrook, P. A.; Murphy, M. J.; Halpern, E. F.; Hill, J. A.; Winniford, M.; Cohen, M. B.; Vanfossen, D. B. *Kidney Int.* **1995**, *47*, 254.
- (9) Heinrich, M. C.; Haberle, L.; Muller, V.; Bautx, W.; Uder, M. *Radiology* **2009**, *250*, 68.
- (10) Wang, A. Z.; Langer, R.; Farokhzad, O. C. *Annu. Rev. Med.* **2012**, *63*, 185.
- (11) Corsonello, A.; Pedone, C.; Corica, F.; Mussi, C.; Carbonin, P.; Antonelli Incalzi, R. *Arch. Intern. Med.* **2005**, *165*, 790.
- (12) Kim, D.; Park, S.; Lee, J. H.; Jeong, Y. Y.; Jon, S. *J. Am. Chem. Soc.* **2007**, *129*, 7661.
- (13) Hyafil, F.; Cornily, J.-C.; Feig, J. E.; Gordon, R.; Vucic, E.; Amirbekian, V.; Fisher, E. A.; Fuster, V.; Feldman, L. J.; Fayad, Z. A. *Nat. Med.* **2007**, *13*, 636.
- (14) Sun, I.-C.; Eun, D.-K.; Koo, H.; Ko, C.-Y.; Kim, H.-S.; Yi, D. K.; Choi, K.; Kwon, I. C.; Kim, K.; Ahn, C.-H. *Angew. Chemie* **2011**, *50*, 9348.
- (15) Sun, I.-C.; Eun, D.-K.; Na, J. H.; Lee, S.; Kim, I.-J.; Youn, I.-C.; Ko, C.-Y.; Kim, H.-S.; Lim, D.; Choi, K.; Messersmith, P. B.; Park, T. G.; Kim, S. Y.; Kwon, I. C.; Kim, K.; Ahn, C.-H. *Chemistry* **2009**, *15*, 13341.
- (16) Sharma, P.; Singh, A.; Brown, S. C.; Bengtsson, N.; Walter, G. A.; Grobmyer, S. R.; Iwakuma, N.; Santra, S.; Scott, E. W.; Moudgil, B. M. In *Cancer Nanotechnology: Methods in Molecular Biology*; Grobmyer, S. R., Moudgil, B. M., Eds.; Springer International Publishing, 2010; pp 67–81.
- (17) Eck, W.; Nicholson, A. I.; Zentgraf, H.; Semmler, W.; Bartling, S. *Nano Lett.* **2010**, *10*, 2318.
- (18) Bonitatibus, P. J.; Torres, A. S.; Kandapallil, B.; Lee, B. D.; Goddard, G. D.; Colborn, R. E.; Marino, M. E. *ACS Nano* **2012**, *6*, 6650.

- (19) Oh, M. H.; Lee, N.; Kim, H.; Park, S. P.; Piao, Y.; Lee, J.; Jun, S. W.; Moon, W. K.; Choi, S. H.; Hyeon, T. *J. Am. Chem. Soc.* **2011**, *133*, 5508.
- (20) Xiao, Q.; Bu, W.; Ren, Q.; Zhang, S.; Xing, H.; Chen, F.; Li, M.; Zheng, X.; Hua, Y.; Zhou, L.; Peng, W.; Qu, H.; Wang, Z.; Zhao, K.; Shi, J. *Biomaterials* **2012**, *33*, 7530.
- (21) Fang, Y.; Peng, C.; Guo, R.; Zheng, L.; Qin, J.; Zhou, B.; Shen, M.; Lu, X.; Zhang, G.; Shi, X. *Analyst* **2013**, *138*, 3172.
- (22) Kinsella, J. M.; Jimenez, R. E.; Karmali, P. P.; Rush, A. M.; Kotamraju, V. R.; Gianneschi, N. C.; Ruoslahti, E.; Stupack, D.; Sailor, M. J. *Angew. Chemie* **2011**, *50*, 12308.
- (23) Rabin, O.; Manuel Perez, J.; Grimm, J.; Wojtkiewicz, G.; Weissleder, R. *Nat. Mater.* **2006**, *5*, 118.
- (24) Anselmo, A. C.; Mitragotri, S. *AAPS J.* **2015**, *17*, 1041.
- (25) He, W.; Ai, K.; Lu, L. *Sci. China Chem.* **2015**, *58*, 753.
- (26) Dalsin, J. L.; Hu, B.-H.; Lee, B. P.; Messersmith, P. B. *J. Am. Chem. Soc.* **2003**, *125*, 4253.
- (27) Pan, D.; Roessl, E.; Schlomka, J. P.; Caruthers, S. D.; Senpan, A.; Scott, M. J.; Allen, J. S.; Zhang, H.; Hu, G.; Gaffney, P. J.; Choi, E. T.; Rasche, V.; Wickline, S. A.; Proksa, R.; Lanza, G. M. *Angew. Chemie* **2010**, *49*, 9635.
- (28) Kinsella, J. M.; Jimenez, R. E.; Karmali, P. P.; Rush, A. M.; Kotamraju, V. R.; Gianneschi, N. C.; Ruoslahti, E.; Stupack, D.; Sailor, M. J. *Angew. Chemie* **2011**, *50*, 12308.
- (29) de Vries, A.; Custers, E.; Lub, J.; van den Bosch, S.; Nicolay, K.; Grull, H. *Biomaterials* **2010**, *31*, 6537.
- (30) Leander, P.; Höglund, P.; Børseth, A.; Kloster, Y.; Berg, A. *Eur. Radiol.* **2001**, *11*, 698.
- (31) Leike, J. U.; Sachse, A.; Rupp, K. *Invest. Radiol.* **2001**, *36*, 303.
- (32) Montet, X.; Pastor, C. M.; Vallée, J.-P.; Becker, C. D.; Geissbuhler, A.; Morel, D. R.; Meda, P. *Invest. Radiol.* **2007**, *42*, 652.
- (33) Hallouard, F.; Anton, N.; Choquet, P.; Constantinesco, A.; Vandamme, T. *Biomaterials* **2010**, *31*, 6249.
- (34) Aviv, H.; Bartling, S.; Kiesling, F.; Margel, S. *Biomaterials* **2009**, *30*, 5610.
- (35) Bae, K. H.; Lee, Y.; Park, T. G. *Biomacromolecules* **2007**, *8*, 650.
- (36) Hallouard, F.; Briançon, S.; Anton, N.; Li, X.; Vandamme, T.; Fessi, H. *Pharm. Res.*

2013, 30, 2023.

- (37) Kong, W. H.; Lee, W. J.; Cui, Z. Y.; Bae, K. H.; Park, T. G.; Kim, J. H.; Park, K.; Seo, S. W. *Biomaterials* **2007**, 28, 5555.
- (38) Galperin, A.; Margel, S. *Biomacromolecules* **2006**, 7, 2650.
- (39) Galperin, A.; Margel, D.; Baniel, J.; Dank, G.; Biton, H.; Margel, S. *Biomaterials* **2007**, 28, 4461.
- (40) Galperin, A.; Margel, D.; Margel, S. *J. Biomed. Mater. Res. Part A* **2006**, 79, 545.
- (41) Carbone, A. L.; Song, M.; Uhrich, K. E. *Biomacromolecules* **2008**, 9, 1604.
- (42) Mottu, F.; Rüfenacht, D. A.; Laurent, A.; Doelker, E. *Biomaterials* **2002**, 23, 121.
- (43) Serruys, P. W.; Ormiston, J. A.; Onuma, Y.; Regar, E.; Gonzalo, N.; Garcia-Garcia, H. M.; Nieman, K.; Bruining, N.; Dorange, C.; Miquel-Hébert, K.; Veldhof, S.; Webster, M.; Thuesen, L.; Dudek, D. *Lancet* **2009**, 373, 897.
- (44) Agusti, G.; Jordan, O.; Andersen, G.; Doelker, E.; Chevalier, Y. *J. Appl. Polym. Sci.* **2014**, 132, 41791.
- (45) Ormiston, J. A.; Serruys, P. W. S. *Circ. Cardiovasc. Interv.* **2009**, 2, 255.
- (46) Escorsell, A.; Bosch, J. *Gastroenterol. Res. Pract.* **2011**, 2011, 1.
- (47) Hubmann, R.; Bodlaj, G.; Czompo, M.; Benko, L.; Pichler, P.; Al-Kathib, S.; Kiblböck, P.; Shamyieh, A.; Biesenbach, G. *Endoscopy* **2006**, 38, 896.
- (48) Kurtz, S. M.; Villarraga, M. L.; Zhao, K.; Edidin, A. A. *Biomaterials* **2005**, 26, 3699.
- (49) Constant, M. J.; Keeley, E. M.; Cruise, G. M. *J. Biomed. Mater. Res. B. Appl. Biomater.* **2009**, 89, 306.
- (50) Kiran, S.; James, N. R.; Jayakrishnan, A.; Joseph, R. *J. Biomed. Mater. Res. Part A* **2012**, 100, 3472.
- (51) Kim, H.-C.; Chung, Y. S. *Fibers Polym.* **2013**, 14, 292.
- (52) Cui, J.; Kratz, K.; Heuchel, M.; Hiebl, B.; Lendlein, A. *Polym. Adv. Technol.* **2011**, 22, 180.
- (53) Rawls, H. R.; Starr, J.; Kasten, F. H.; Murray, M.; Smid, J.; Cabasso, I. *Dent. Mater.* **1990**, 6, 250.
- (54) Moszner, N.; Salz, U. *Prog. Polym. Sci.* **2001**, 26, 535.
- (55) Boelen, E. J. H.; Lewis, G.; Xu, J.; Slots, T.; Koole, L. H.; Van Hooy-Corstjens, C. S. J. J.

- Biomed. Mater. Res. Part A* **2008**, *86*, 76.
- (56) Heini, P.; Berlemann, U. *Eur. Spine J.* **2001**, *10*, 205.
- (57) Vázquez, B.; Ginebra, M. P.; Gil, F. J.; Planell, J. A.; López Bravo, A.; San Román, J. *Biomaterials* **1999**, *20*, 2047.
- (58) Mitchell, W.; Matthews, J. B.; Stone, M. H.; Fisher, J.; Ingham, E. *Biomaterials* **2003**, *24*, 737.
- (59) Kiran, S.; James, N. R.; Joseph, R.; Jayakrishnan, A. *Biomaterials* **2009**, *30*, 5552.
- (60) Carbone, A. L.; Song, M. J.; Uhrich, K. E. *Biomacromolecules* **2008**, *9*, 1604.
- (61) Rawls, H. R.; Granier, R. J.; Smid, J.; Cabasso, I. *J. Biomed. Mater. Res.* **1996**, *31*, 339.
- (62) Delaviz, Y.; Zhang, Z.-X.; Cabasso, I.; Smid, J. *J. Appl. Polym. Sci.* **1990**, *40*, 835.
- (63) James, N. R.; Philip, J.; Jayakrishnan, A. *Biomaterials* **2006**, *27*, 160.
- (64) Hindenlang, M. D.; Soudakov, A. A.; Imler, G. H.; Laurencin, C. T.; Nair, L. S.; Allcock, H. R. *Polym. Chem.* **2010**, *1*, 1467.
- (65) Davy, K. W. M.; Anseau, M. R.; Odlyha, M.; Foster, G. M. *Polym. Int.* **1997**, *43*, 143.
- (66) Saralidze, K. S.; Aldenhoff, B. J.; Knetsch, L. W.; Koole, L. H. *Biomacromolecules* **2003**, *4*, 793.
- (67) Benzina, A.; Kruft, M. A. B.; van der Veen, F. H.; Bar, F. H.; Blezer, R.; Lindhour, T.; Koole, L. H. *J. Biome Mater Res* **1996**, *32*, 359.
- (68) Horak, D.; Metalova, M.; Rypacek, F. *J Biomed Mater Res* **1997**, *34*, 183.
- (69) Kruft, M. a; van der Veen, F. H.; Koole, L. H. *Biomaterials* **1996**, *18*, 31.
- (70) Aldenhoff, Y. B. J.; Kruft, M.-A. B.; Pijpers, a P.; van der Veen, F. H.; Bulstra, S. K.; Kuijer, R.; Koole, L. H. *Biomaterials* **2002**, *23*, 881.
- (71) Rode, C.; Schmidt, A.; Wyrwa, R.; Weisser, J.; Schmidt, K.; Moszner, N.; Gottlöber, R.-P.; Heinemann, K.; Schnabelrauch, M. *Polym. Int.* **2014**, *63*, 1732.
- (72) Kiran, S.; Joseph, R. *J. Biomed. Mater. Res. Part A* **2014**, *102*, 3207.
- (73) Sang, L.; Wei, Z.; Liu, K.; Wang, X.; Song, K.; Wang, H.; Qi, M. *J. Biomed. Mater. Res. Part A* **2014**, *102*, 1121.
- (74) Tavernise, S. *The New York Times*. 2012, p A15.
- (75) Larsen, E. R. Radiopaque Thermoset Polymer, 1986.

- (76) Habnoui, S. El; Blanquer, S.; Darcos, V.; Coudane, J. *J. Polym. Sci. Part A Polym. Chem.* **2009**, *47*, 6104.
- (77) Habnoui, S. El; Darcos, V.; Coudane, J. *Macromol. Rapid Commun.* **2009**, *30*, 165.
- (78) Nottelet, B.; Coudane, J.; Vert, M. *Biomaterials* **2006**, *27*, 4948.
- (79) Wu, L.; Jin, C.; Sun, X. *Biomacromolecules* **2011**, *12*, 235.
- (80) Lendlein, A.; Langer, R. *Science* **2002**, *296*, 1673.
- (81) Mather, P. T.; Luo, X.; Rousseau, I. A. *Annu. Rev. Mater. Res.* **2009**, *39*, 445.
- (82) Lendlein, A.; Langer, R. *Science* **2002**, *296*, 1673.
- (83) Zhu, G.; Liang, G.; Xu, Q.; Yu, Q. *J. Appl. Polym. Sci.* **2003**, *90*, 1589.
- (84) Yuan, D.; Chen, Z.; Xu, C.; Chen, K.; Chen, Y. *ACS Sustain. Chem. Eng.* **2015**, *3*, 2856.
- (85) Saad, G. R.; Lee, Y. J.; Seliger, H. *Macromol. Biosci.* **2001**, *1*, 91.
- (86) Takahashi, T.; Hayashi, N.; Hayashi, S. *J. Appl. Polym. Sci.* **1996**, *60*, 1061.
- (87) Kim, B. K.; Shin, Y. J.; Cho, S. M.; Jeong, H. M. *J. Polym. Sci. Part B* **2000**, *38*, 2652.
- (88) Muto, K.; Osaka Works Sumitomo Elec. Ind. Ltd. Osaka-shi, O. Polyethylene Heat Shrinkable Tube. 02254977.8, 2003.
- (89) Chernous, D. A.; Shil'ko, S. V.; Pleskachevshii, Y. M. *J. Eng. Phys. Thermophys.* **2004**, *77*, 6.
- (90) Li, Q.; Zhou, J.; Vatankhah-Varnoosfaderani, M.; Nykypanchuk, D.; Gang, O.; Sheiko, S. *S. Macromolecules* **2016**, *49*, 1383.
- (91) Jackson, A. M. S.; Sheiko, S. S.; Ashby, V. S. *Langmuir* **2015**, *31*, 5489.
- (92) Turner, S. A.; Zhou, J.; Sheiko, S. S.; Ashby, V. S. *ACS Appl. Mater. Interfaces* **2014**, *6*, 8017.
- (93) Yakacki, C. M.; Shandas, R.; Lanning, C.; Rech, B.; Eckstein, A.; Gall, K. *Biomaterials* **2007**, *28*, 2255.
- (94) Wache, H. M.; Tartakowska, D. J.; Hentrich, A.; Wagner, M. H. *J Mater Sci Mater Med* **2003**, *14*, 109.
- (95) Cui, J.; Kratz, K.; Lendlein, a. *Smart Mater. Struct.* **2010**, *19*, 65019.
- (96) Tuissi, A.; Carr, S.; Butler, J.; Gandhi, A. A.; O'Donoghue, L.; McNamara, K.; Carlson, J. M.; Lavelle, S.; Tiernan, P.; Biffi, C. A.; Bassani, P.; Tofail, S. A. M. *Shape Mem.*

Superelasticity **2016**, *2*, 196.

- (97) Wang, S.; Guo, F. M.; Jiang, D. Q.; Liu, Y.; Cui, L. S. *Scr. Mater.* **2014**, *81*, 4.
- (98) Lin, B.; Gall, K.; Maier, H. J.; Waldron, R. *Acta Biomater* **2009**, *5*, 257.
- (99) Ebara, M.; Uto, K.; Idota, N.; Hoffman, J. M.; Aoyagi, T. *Adv. Mater.* **2012**, *24*, 273.
- (100) Wong, Y. S.; Salvekar, A. V.; Zhuang, K. Da; Liu, H.; Birch, W. R.; Tay, K. H.; Huang, W. M.; Venkatraman, S. S. *Biomaterials* **2016**, *102*, 98.
- (101) Langer, R. S.; Lendlein, A.; Annette, S.; Grublowitz, H. Biodegradable Shape Memory Polymers. 6160084, 2000.
- (102) Langer, R.; Lendlein, A. Shape Memory Polymers. US 6388043 B1, 2002.
- (103) Burattini, S.; Merino, D. H.; Weng, W.; Seppala, J.; Colquhoun, H. M.; Hayes, W.; Mackay, M. E.; Hamley, I. W.; Rowan, S. J. *J. Am. Chem. Soc.* **2010**, *132*, 12051.
- (104) Faul, B. C. F. J.; Antonietti, M. *Adv. Mater.* **2003**, *15*, 673.
- (105) Craig, S. L. *Angew. Chemie* **2009**, *48*, 2645.
- (106) Li, H.; Wu, L. *Soft Matter* **2014**, *10*, 9038.
- (107) Fox, J. D.; Rowan, S. J. *Macromolecules* **2009**, *42*, 6823.
- (108) Beck, J. B.; Ineman, J. M.; Rowan, S. J. *Macromolecules* **2005**, *38*, 5060.
- (109) Dong, S.; Zheng, B.; Wang, F.; Huang, F. *Acc. Chem. Res.* **2014**, *47*, 1982.
- (110) Lillya, C. P.; Baker, R. J.; Hutte, S.; Winter, H. H.; Lin, Y.-G.; Shi, J.; Dickinson, L. C.; Chien, J. C. W. *Macromolecules* **1992**, *25*, 2076.
- (111) Khakshoor, O.; Wheeler, S. E.; Houk, K. N.; Kool, E. T. *J. Am. Chem. Soc.* **2012**, *134*, 3154.
- (112) Sijbesma, R. P.; Beijer, F. H.; Brunsveld, L.; Folmer, B. J. B.; Hirschberg, J. H. K. K.; Lange, R. F. M.; Lower, J. K. L.; Meijer, E. W. *Science* **1997**, *278*, 1601.
- (113) Keizer, H. M.; van Kessel, R.; Sijbesma, R. P.; Meijer, E. W. *Polymer.* **2003**, *44*, 5505.
- (114) Folmer, B. J. B.; Sijbesma, R. P.; Versteegen, R. M.; van der Rijt, J. a. J.; Meijer, E. W. *Adv. Mater.* **2000**, *12*, 874.
- (115) Kautz, H.; van Beek, D. J. M.; Sijbesma, R. P.; Meijer, E. W. *Macromolecules* **2006**, *39*, 4265.
- (116) Keizer, H. M.; Sijbesma, R. P.; Jansen, J. F. G. A.; Pasternack, G.; Meijer, E. W.

- Macromolecules* **2003**, *36*, 5602.
- (117) Söntjens, S. H. M.; Sijbesma, R. P.; Van Genderen, M. H. P.; Meijer, E. W. *J. Am. Chem. Soc.* **2000**, *122*, 7487.
- (118) Faghihnejad, A.; Feldman, K. E.; Yu, J.; Tirrell, M. V.; Israelachvili, J. N.; Hawker, C. J.; Kramer, E. J.; Zeng, H. *Adv. Funct. Mater.* **2014**, 2322.
- (119) Bastings, M. M. C.; Koudstaal, S.; Kieltyka, R. E.; Nakano, Y.; Pape, a. C. H.; Feyen, D. a M.; van Slochteren, F. J.; Doevendans, P. a.; Sluijter, J. P. G.; Meijer, E. W.; Chamuleau, S. a J.; Dankers, P. Y. W. *Adv. Healthc. Mater.* **2014**, *3*, 70.
- (120) Agnaou, R.; Capelot, M.; Tencé-Girault, S.; Tournilhac, F.; Leibler, L. *J. Am. Chem. Soc.* **2014**, *136*, 11268.
- (121) Biyani, M. V; Foster, E. J.; Weder, C. *ACS Macro Lett.* **2013**, *2*, 236.
- (122) Shokrollahi, P.; Mirzadeh, H.; Huck, W. T. S.; Scherman, O. A. *Polymer.* **2010**, *51*, 6303.
- (123) Botterhuis, N. E.; van Beek, D. J. M.; Gemert, G. M. L.; Bosman, A. W.; Sijbesma, R. P. *J. Polym. Sci. Part A Polym. Chem.* **2008**, *46*, 3877.
- (124) Appel, W. P. J.; Portale, G.; Wisse, E.; Dankers, P. Y. W.; Meijer, E. W. *Macromolecules* **2011**, *44*, 6776.
- (125) van Beek, D. J. M.; Spiering, A. J. H.; Peters, G. W. M.; Te Nijenhuis, K.; Sijbesma, R. P. *Macromolecules* **2007**, *40*, 8464.
- (126) van Beek, D. J. M.; Gillissen, M. A. J.; Van As, B. A. C.; Palmans, A. R. A.; Sijbesma, R. P. *Macromolecules* **2007**, *40*, 6340.
- (127) Dankers, P. Y. W.; Zhang, Z.; Wisse, E.; Grijpma, D. W.; Sijbesma, R. P.; Feijen, J.; Meijer, E. W. *Macromolecules* **2006**, *39*, 8763.
- (128) Deans, R.; Ilhan, F.; Rotello, V. M. *Macromolecules* **1999**, *32*, 4956.
- (129) Ilhan, F.; Galow, T. H.; Gray, M.; Clavier, G.; Rotello, V. M. *J. Am. Chem. Soc.* **2000**, *122*, 5895.
- (130) Ilhan, F.; Gray, M.; Rotello, V. M. *Macromolecules* **2001**, *34*, 2597.
- (131) Yamauchi, K.; Lizotte, J. R.; Hercules, D. M.; Vergne, M. J.; Long, T. E. *J. Am. Chem. Soc.* **2002**, *124*, 8599.
- (132) Yamauchi, K.; Kanomata, A.; Inoue, T.; Long, T. E. *Macromolecules* **2004**, *37*, 3519.
- (133) Houston, K. R.; Jackson, A.-M. S.; Yost, R. W.; Carman, H. S.; Ashby, V. S. *Polym. Chem.* No. PY-ART-08-2016-001421.R1.

- (134) Whinfield, J. R.; Dickson, J. T. Polymeric Linear Terephthalic Esters. 2465319, 1949.
- (135) Sheirs, J.; Long, T. E. *Modern Polyesters*; John Wiley & Sons, Ltd.: West Sussex, 2003.
- (136) Kodak; Kibler, C. J.; Bell, A.; Smith, J. G. Improvements in Linear Polyesters and Polyesteramides. 818157, 1956.
- (137) Kodak, E.; Kibler, C. J.; Bell, A.; Smith, J. G. Linear Polyesters and Polyester-amides from 1,4-cyclohexanedimethanol. 2901466, 1959.
- (138) Turner, S. R. *J. Polym. Sci. Part A Polym. Chem.* **2004**, *42*, 5847.

CHAPTER 2: IODINATED HOMOPOLYMERS AS A VERSATILE PLATFORM FOR RADIOPAQUE BIOMATERIALS AND NANOPARTICLES

2.1 Introduction

Computed tomography (CT) is a critical tool of modern diagnostic medicine. CT generates detailed images used for diagnosing diseases and health conditions and for monitoring implants over the course of their lifetime.¹⁻³ Therefore, polymeric implantable biomaterials that are capable of high x-ray contrast without sacrificing their thermal and mechanical properties are not only desirable but also critical for the ever-expanding scope of implantable biomaterials.^{12,13}

The conspicuity of implants in the acquired CT image is dependent on the electron density of the surrounding medium. Replacing electron-dense metal-based implants with polymeric materials has many advantages: tunable biodegradability, increased biocompatibility, and improved or adaptable mechanical properties. However, these advantages sacrifice the ability to monitor an implant over the course of its lifetime because these biomaterials often lack radiocontrast with respect to the surrounding tissue. This challenge has been overcome traditionally by the addition of metallic tags,^{4,5,14} the development of composites,¹⁵⁻¹⁷ or the covalent attachment of iodine-containing molecules to the polymer structure.^{9,10,18-28} For example, polymer-based medical devices, such as stents, incorporate gold or platinum metallic markers,^{4,5,14} thus directly contradicting the overall goal of complete device biodegradability.

Diagnostic radiology often requires general blood pool imaging of low-contrast soft tissues, such as the liver or bowel; thus, contrast agents containing barium or iodine are regularly utilized.³ However, traditional CT contrast agents suffer from limitations including rapid

excretion (typical distribution half-life of approximately 10 minutes), unspecific biodistribution, and renal toxicity.^{3,6} The production of radiopaque polymeric biomaterials could allow the realization of safer, more effective implants and CT contrast agents.

Current research attempts to circumvent the complications connected to traditional contrast agents through the development of new iodinated liquids or mixtures,² coordination polymers,⁷ copolymers and polymers based on methacrylates,⁸ anhydride esters,⁹ cellulose,¹⁰ liposomes,³ and nanoparticles.⁶ Aviv *et al.* showed that polymer nanoparticles produced by the emulsion polymerization of 2-methacryloyloxyethyl(2,3,5-triiodobenzoate) provided significant contrast enhancement after 30 minutes and allowed for easy visualization of a cancerous mouse liver.⁸ While most of these developed materials are capable of satisfactory contrast, stability and toxicity remain problematic in some cases.^{3,11}

Though there is variance in the structure and delivery method of contrast agents, almost all iodine-based contrast materials described in the literature utilize aromatic ring-bound iodine.^{9,18,21,29} Many of these precursors are expensive and toxic; however, they presumably increase the stability of the bound iodine. Few examples of aliphatic iodinated polymers exist;^{25–27} new, aliphatic iodinated polymers could provide improved stability, safety (i.e., nontoxic), and biodegradability. Herein, a novel, aliphatic, iodinated biomaterial platform is reported. This platform exhibits: stability, radiopacity, low cost, versatile thermal and mechanical properties, and no cytotoxicity. Furthermore, these materials can be processed into thermosets and lipid-polymer hybrid nanoparticles. The fabrication of nanoparticle contrast agents has the potential to increase the utility of x-ray computed tomography as a diagnostic and disease management tool for all patient populations.

2.2 Experimental Methods

2.2.1 Materials

All materials were purchased from Sigma-Aldrich, Fisher Scientific, or VWR International. Water was filtered using a Milli-Q Advantage A10 Ultrapure Water Purification System for aqueous solutions and washings. Millipore (Amicon Ultra) Centrifugal Filters with a 100 kDa MWCO were used to purify and concentrate nanoparticle suspensions.

Dichloromethane (CH_2Cl_2) was dried over CaH_2 and distilled immediately before use.

2.2.2 Characterization

The monomers and prepolymers were characterized using a Bruker 400 AVANCE (^1H and ^{13}C NMR), a TA Instruments Q200 differential scanning calorimeter (DSC), a Perkin Elmer Pyris 1 thermogravimetric analyzer (TGA). Gel permeation chromatography (GPC) was performed on a Waters 2695 Separations Module relative to polystyrene standards to characterize the prepolymers. All films were characterized by DSC, TGA, and Instron Model 5566 equipped with a 500 N load cell. Elemental analysis was performed using an Oxford instruments, INCA PentaFET energy dispersive x-ray spectrometer (EDS) on a Hitachi S-4700 cold cathode field emission scanning electron microscope (SEM), through Midwest Microlab LLC (monomer and polymers), and using a Kratos Axis Ultra DLD X-ray Photoelectron Spectrometer (XPS). Nanoparticles were characterized using a Malvern Instruments nano ZS zetasizer dynamic light scattering (DLS) instrument, a JEOL 100 CX II transmission electron microscope (TEM), and a TA instruments Q5000 TGA. DLS was performed at 25 °C and allowed to equilibrate for 120 seconds unless otherwise noted.

2.2.3 Synthesis

2.2.3.a Synthesis of 2,2-bis(iodomethyl)-1,3-propanediol^{30,31}

In a nitrogen-purged flask equipped with a reflux condenser, 2,2-bis(bromomethyl)-1,3-propanediol (50.0 g, 0.190 mmol) was added with sodium iodide (286 g, 1.90 mmol), followed by the addition of 1 L of acetone. The reaction was refluxed for 3 days. Once the reaction had gone to completion, the solvent was removed, and the product was extracted with ethyl acetate (thrice) and DI water with 5% sodium thiosulfate (thrice). The product was recrystallized in a solvent mixture of dichloromethane (400 mL) and acetone (<200 mL) to produce large white crystals, yield 56.5 g (83%). ¹H NMR, acetone-d₆, δ (ppm) 4.08 (t, *J* = 5 Hz, 2H), 3.59 (d, *J* = 4 Hz, 4H) and 3.34 (s, 4H). ¹³C NMR, acetone-d₆, δ (ppm) 63.10 and 13.04. Elemental analysis, calculated 16.86 %C, 2.83 %H, 71.31 %I, 8.99 %O; found 16.97 %C, 2.83 %H, 70.55 %I, 9.04 %O.

2.2.3.b Typical Polymerizations with 2,2-bis(iodomethyl)-1,3-propanediol and Diacids

Various polymers were prepared *via* the polycondensation of 2,2-bis(iodomethyl)-1,3-propanediol and the corresponding diacids: succinic, adipic, and sebacic acid. In a typical run using sebacic acid as the diacid, a dry flask was charged with 2,2-bis(iodomethyl)-1,3-propanediol (3.250 g, 9.131 mmol), sebacic acid (1.776 g, 8.780 mmol), and scandium triflate (0.090 g, 0.182 mmol). The flask was nitrogen purged before heating the reaction to 135 °C. After 1-2 hours, the temperature was lowered to 100 °C, and vacuum was reduced to 30 torr at a rate of 80 torr per hour. This pressure was maintained for 24 hours, after which the vacuum was reduced to 0.3 torr for another 24 hours. The polymerization was terminated by cooling the reaction mixture to room temperature, dissolving the polymer in CHCl₃, and precipitating into cold methanol (-78 °C) and cold diethyl ether (-78 °C).

2.2.3.c *Poly(2,2-bis(iodomethyl)-1,3-propylene succinate)*

^1H NMR, CDCl_3 , δ (ppm) 4.16 (s, 4H), 3.57 (s, 0.23H), 3.30 (s, 4H), and 2.68 (s, 4H).

^{13}C NMR, CDCl_3 , δ (ppm) 171.40, 64.73, 40.05, 29.05, and 9.94.

2.2.3.d *Poly(2,2-bis(iodomethyl)-1,3-propylene adipate)*

^1H NMR, CDCl_3 , δ (ppm) 4.11 (s, 4H), 3.56 (s, 0.23H), 3.29 (s, 4H), 2.37 (m, 4H), and 1.68 (m, 4H). ^{13}C NMR, CDCl_3 , δ (ppm) 172.37, 64.26, 39.93, 33.76, 24.36, and 9.49.

2.2.3.e *Poly(2,2-bis(iodomethyl)-1,3-propylene sebacate)*

^1H NMR, CDCl_3 , δ (ppm) 4.09 (s, 4H), 3.47 (s, 0.1H), 3.28 (s, 4H), 2.32 (t, $J = 7.4$ Hz, 4H), 1.61 (t, $J = 6.1$, 4H), and 1.3 (s, 8H). ^{13}C NMR, CDCl_3 , δ (ppm) 172.82, 64.00, 39.78, 34.10, 29.03, 24.88, and 9.38.

2.2.3.f *Polymer End-capping with 2-Isocyanatoethyl Methacrylate*

In a typical run, a dry round bottom flask was charged with the iodinated polymer (4.0 g, 0.96 mmol), and purged with nitrogen before the addition of dry CH_2Cl_2 (24 mL). The 2-isocyanatoethyl methacrylate (0.57 mL, 3.8 mmol) was added, followed by the dropwise addition of tin(II) ethylhexanoate (20 μL , 0.05 mmol). The reaction was stirred for 24 hours at room temperature. The reaction was terminated by precipitation into cold methanol (-78 $^\circ\text{C}$) or cold ether (-78 $^\circ\text{C}$). The prepolymer was dried *in vacuo* at room temperature for 24 hours before use and stored at 4 $^\circ\text{C}$.

2.2.3.g *End-capped Poly(2,2-bis(iodomethyl)-1,3-propylene succinate)*

^1H NMR, CDCl_3 , δ (ppm) 6.13 (m, 0.18H), 5.61 (m, 0.18H), 4.23 (m, 0.66H), 4.15 (s, 4H), 3.49 (m, 0.38H), 3.30 (s, 4H), 2.67 (s, 4H), and 1.95 (d, $J = 8$ Hz, 0.56H).

2.2.3.h End-capped Poly(2,2-bis(iodomethyl)-1,3-propylene adipate)

¹H NMR, CDCl₃, δ (ppm) 6.13 (m, 5.60 (m, 0.23H), 5.60 (m, 0.21H), 4.23 (m, 0.48H), 4.10 (s, 4H), 3.50 (m, 0.41H), 3.28 (s, 4H), 2.37 (m, 4H), 1.97 (d, *J* = 8 Hz, 0.72H), and 1.67 (m, 4H).

2.2.3.i End-capped Poly(2,2-bis(iodomethyl)-1,3-propylene sebacate)

¹H NMR, CDCl₃, δ (ppm) 6.18 (s), 5.64 (s), 4.29 (t, *J* = 6 Hz), 4.24 (m), 4.09 (s, 4H), 3.56 (t, *J* = 8 Hz), 3.51 (m), 3.28 (s, 4H), 2.32 (t, *J* = 7.4 Hz, 4H), 1.95 (s), 1.61 (t, *J* = 6.1, 4H), and 1.3 (s, 8H).

2.2.4 Thermoset Fabrication

A prepolymer solution (2 g mL⁻¹ in CHCl₃) containing approximately 2% b.w. diethoxyacetophenone was cast into a mold or onto a glass slide. The mold was then placed in a UV chamber (ELC-500 Light Exposure System) for 10 minutes under a flow of N₂. The film was placed in a vacuum oven at 70 °C for 24 hours under high vacuum.

2.2.5 Preliminary Thermoset Degradation by Hydrolysis

Films of known weight were placed in 1 mL of 10 mM pH 7.4 phosphate buffered saline (PBS) solution at 37 °C. The films were removed from the buffer solution at prescribed intervals and dried under vacuum for 24 hours before their masses were measured. Each measurement was performed on three separate samples. Mass loss (ML) was calculated according to the following equation, where *m_i* is the initial mass and *m_f* is the final mass:

$$ML = \frac{m_i - m_f}{m_i} \times 100 \dots\dots\dots \text{(equation 2.1).}$$

2.2.6 Typical Liposomal-nanoprecipitation

Stock solutions of PEG-monostearate (n=55) and lecithin were prepared separately at concentrations of 2 mg mL⁻¹ and 1 mg mL⁻¹ in 4% b.v. ethanol aqueous solutions, respectively.

Stock solutions of prepolymer were prepared at a concentration of 2.5 mg mL^{-1} in HPLC-grade DMF. PEG-monostearate (21.68 mL) and lecithin (1.25 mL) solutions were then added to 228 mL purified water. The photoinitiator, 2,2-diethoxyacetophenone, (0.0116 g, 0.0557 mmol) was added to 43.4 mL of the polymer solution, which was then poured into the aqueous phospholipid/lipid-PEG solution, such that the ratio of polymer to phospholipid/lipid-PEG was equal to 2.4:1. Once the prepolymer solution was added, water (206 mL) was promptly added to the mixture, so that the final volume ratio of pure water to organic solution was 10:1. The resulting mixture was sonicated for 10 minutes using a Branson 1510 bath sonicator at a frequency of 42 kHz and power of 70 W. The particles were then irradiated with UV light for at least 20 minutes. The nanoparticle suspensions were purified and concentrated by centrifugation using Millipore filters and were stored at $4 \text{ }^{\circ}\text{C}$. The method described was used in the majority of the experiments described in this thesis. Other formulations varied the ratios of solutions or the concentration of either the aqueous or organic solutions. In some cases, DSPE-PEG was used instead as the lipid conjugated PEG. This general method was used in traditional nanoprecipitation methods without the addition of a lipid-PEG or stabilizer to the aqueous phase.

2.2.6.a Core-crosslinking

A nanoparticle suspension was charged to a round bottom flask then sealed. Argon was bubbled through the suspension for 30 minutes to purge any oxygen present. The suspension was then placed in a broad spectrum UV chamber (ELC-500 Light Exposure System) for 10 minutes under a steady flow of N_2 (to maintain the temperature at approximately $25 \text{ }^{\circ}\text{C}$). After exposure to UV radiation, the suspension was lyophilized and dissolved in CDCl_3 for ^1H NMR.

2.2.7 Nanoparticle Stability Tests

2.2.7.a Nanoparticle Stability at Body Temperature

Nanoparticle suspensions (100 nm, PDI = 0.14) at concentrations of 1.0 mg mL⁻¹ and 3.4 mg mL⁻¹ were incubated in a 37 °C water bath. DLS was performed at 37 °C (300 second soak) after 1 hour of incubation (1.0 mg mL⁻¹: 99 nm, PDI = 0.11; 3.4 mg mL⁻¹: 100 nm, PDI = 0.11) and 1 day of incubation (1.0 mg mL⁻¹: 98 nm, PDI = 0.10; 3.4 mg mL⁻¹: 100 nm, PDI = 0.10). TEM was performed on the more concentrated nanoparticles after 1 day of incubation and compared to a sample of unheated nanoparticles made from the same formulation batch at the same concentration.

2.2.7.b Whole Blood and Serum Aggregation Studies

A nanoparticle suspension (82 mg mL⁻¹) was added to both serum and whole blood at ratios of 1:1, 1:10, and 1:100. For the ratio of 1:1 (nanoparticle suspension to whole blood/serum), the liquids were mixed on a slide and viewed under the microscope immediately. Ratios of 1:10 and 1:100 were mixed in Eppendorf tubes and viewed approximately 2 minutes after mixing.

2.2.8 Cytotoxicity

To assess the biocompatibility of the crosslinked films, 20,000 murine alveolar macrophages (ATCC CCL-2019) were seeded into 24 well plates in 1mL of complete RPMI 1640 containing 0.05mM 2-mercaptoethanol and 10% fetal bovine serum per well. Cells were allowed to adhere for 24 hours and subsequently incubated with the crosslinked films, which were placed into Falcon cell culture inserts containing a 3µm pore size. One milliliter of complete medium was added to each insert and cells/crosslinked films were incubated for an additional 72 hours in a 37°C, 5% CO₂ incubator. After the 72-hour incubation period, cell

culture inserts were removed and all medium was aspirated off cells. 300 μ L of fresh medium was added back to each well followed by the addition of 300 μ L CellTiter-Glo[®] Luminescent Cell Viability Assay reagent (Promega, Madison WI). Plates were placed on a microplate shaker for 2 minutes, incubated at RT for 10 minutes to stabilize luminescent signal. The luminescent signal was recorded on a Molecular Dynamics SpectraMax M5 plate reader. Cell viability was expressed as a percentage of the luminescent signal of cells grown in the absence of crosslinked film (cells only in complete medium). Each measurement was performed in triplicate with three independently prepared batches of polymeric material.

2.2.9 *In Vitro* X-ray Images and Projections

X-ray projections and images were taken with a novel carbon-nanotube cathode x-ray source with a tungsten anode and 0.2 mm Be and 0.5 mm Al filtration, at 50 kVp energy.³² For the in-air experiments, polymer films with dimensions of approximately 30 x 3 x 3 mm were used. For the in-tissue experiments, polymer films (4 x 2 x 2 mm) were implanted into porcine liver segments (15 mm cubes). Nanoparticles were suspended in water at different concentrations (150 to 450 mg mL⁻¹) to obtain x-ray projections.

2.2.10 *In Vivo* CT Imaging

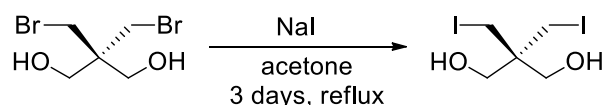
In vivo imaging was performed under the permission of The University of North Carolina at Chapel Hill Institutional Animal Care and Use Committee (IACUC), protocol number 12-184.0B. Female Balb/C mice were purchased from Charles River (5-7 weeks old). CT images were performed using a Gamma Medica, Inc. eXplore CT-120 (70 kVp, 50 mA) prior to the tail vein injection of nanoparticles (120 μ L, 130 mg I/mL). Another mouse was administered OMNIPAQUE[®] 300 (iohexol, 120 μ L, diluted with saline to 150 mg I/mL). Time points were taken immediately followed by 5 minute intervals until reaching 30 minutes. The mouse

administered the nanoparticles was imaged again 1 hour after injection. The mice were anesthetized and maintained using inhalation anesthesia (1.5% isoflurane in 1:2 O₂/N₂). The mouse administered with OMNIPAQUE® 300 was sacrificed 30 minutes after the imaging procedure, and the mouse administered the nanoparticles was sacrificed upon completion of the 60-minute imaging procedure. Images were processed using ImageJ software.

2.3 Results and Discussion

2.3.1 Monomer Synthesis

The key to the synthesis of the materials described herein is the aliphatic iodine component, 2,2-bis(iodomethyl)-1,3-propanediol (Scheme 2.1). This monomer is resistant to thermal degradation, which is evident through its high thermal degradation of 5% b.w. at 201 °C (Table 2.1). Furthermore, 2,2-bis(iodomethyl)-1,3-propanediol can be stored at ambient temperatures without special UV protection.



Scheme 2.1 Synthesis of 2,2-bis(iodomethyl)-1,3-propanediol.

Table 2.1 Properties of 2,2-Bis(iodomethyl)-1,3-propanediol.

T _m (°C) ^a	ΔH (J g ⁻¹) ^a	5% (°C) ^b	10% (°C) ^b	Calculated %I	Experimental %I ^c
130.7	93.0	201	216	71.36	71.16

^a DSC, first heat 10 °C min⁻¹; ^b Decomposition measured by TGA 20 °C min⁻¹; ^c Measured by elemental analysis.

Most aliphatic iodinated compounds degrade easily at room temperature, when exposed to light, or in the presence of nucleophiles, thus yielding far more stable elimination or

substitution products. 2,2-Bis(iodomethyl)-1,3-propanediol is resistant to elimination products (loss of iodine to produce an alkene) because the resulting molecule would have a fifth, forbidden bond to carbon. Furthermore, substitution as a side reaction is suppressed as a result of steric hindrance. This is evident, as the simple Finkelstein reaction utilized to produce 2,2-bis(iodomethyl)-1,3-propanediol took several days at reflux to reach full conversion (Scheme 2.2). Recrystallization yielded monomer of high purity (determined by elemental analysis, Table 2.1 and Table A1-A2 from Appendix A). These properties permit the manufacture of polymers at various temperatures (80 to 140 °C) without degradation of the starting materials.

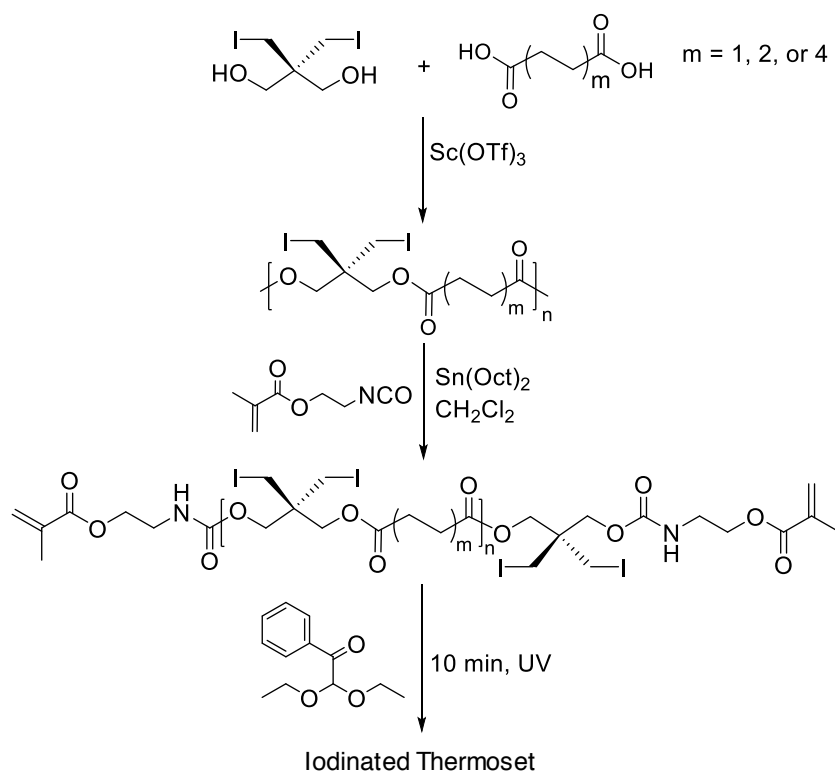
2.3.2 Polymer Synthesis and Evaluation

2.3.2.a Prepolymers

The iodinated monomer was polymerized with succinic, adipic, and sebacic acids (Scheme 2.2). For convenience, the iodinated polymers will be identified by their respective diacid co-monomers (i.e., succinic (Su), adipic (Ad), and sebacic (Se) acid). Scandium(III) triflate, which is insensitive to halogens, was utilized as the catalyst.³³ More traditional catalysts, such as lipases and tin(II) ethylhexanoate, were ineffective due to limitations of reaction temperature (i.e., lipases), polymer molecular weight, or purity. By utilizing scandium(III) triflate, polyesters with number-average molecular weights between 4400 and 5700 g mol⁻¹ and dispersity of 1.4 - 1.5 (\bar{M}_w/\bar{M}_n lower than 2 due to fractionation upon purification) were produced, as shown in Table 2.2.

The prepolymers were amorphous, with glass transition temperatures between -3 and -45 °C (Table 2.2). The thermal degradation temperatures of these materials matched the expected degradation temperatures of typical aliphatic polyesters.³⁴ The iodinated monomer had a significantly lower degradation temperature (5% weight loss at 201 °C, Table 2.1) than the

polymers (5% weight loss at 210-290 °C). The increase in thermal stability of the iodinated monomer indicates that the monomer was stabilized upon incorporation into the polymer chain.



Scheme 2.2 Synthesis of iodinated polyesters followed by photo-crosslinking to yield iodinated thermosets.

Table 2.2 Iodinated Polymer Properties.

Polymer (by diacid)	M_n (g mol^{-1}) ^a	$\langle M_n \rangle$ (g mol^{-1}) ^b	$\langle M_w \rangle$ (g mol^{-1}) ^b	\mathcal{D}^b	5% (°C) ^c	T_g (°C) ^d
Succinic	4400	5500	7700	1.4	290	-3
Adipic	5600	5900	9000	1.5	270	-30
Sebacic	5700	7800	11000	1.5	210	-45

^a Measured by ^1H NMR (400 MHz in CDCl_3). ^b Measured by GPC in THF using polystyrene standards. ^c Measured by TGA. ^d Measured by DSC, mid-point of the second heat.

2.3.2.b Thermosets

Because the prepolymers were viscous liquids at room temperature, they were end-functionalized with a methacrylate group to yield macromonomers. These macromonomers were UV crosslinked into thermoset elastomers to impart improved mechanical properties (Table 2.3). The sebacic acid and adipic acid based polymers had high maximum strains (>100%) and low moduli (between 0.6 and 5 MPa). The succinic acid based polymer had a much higher modulus (55 MPa) and a lower maximum strain. Facile crosslinking of the polymers was of particular interest because crosslinking could potentially produce stabilized nanoparticles. Although nanoparticle fabrication was the ultimate goal, the properties of the elastomers were analyzed thoroughly.

In addition to improved mechanical properties, the glass transition temperatures of the polymers increased as a result of crosslinking. The thermal properties of the elastomers varied depending on the diacid used and on the molecular weight of the prepolymers (Table 2.3). Similar to the trend observed in the prepolymers, the T_g of the elastomers decreased as the hydrocarbon spacer of the diacid comonomer increased ($m = 1, 2, \text{ or } 4$; Scheme 2.2), varying from -1 to -16 °C. Glass transition temperatures as high as 16 °C were achieved when the succinic acid based polymer molecular weight was increased to $7,000 \text{ g mol}^{-1}$ (Table A3, Appendix A).

The hydrolytic degradation of the adipic acid based thermoset was tested over the course of 20 days in a solution of PBS at 37 °C. Only 2.3% mass loss was observed. The slow hydrolytic degradation of this polymer is most likely due to a combination of chemical crosslinks and the hydrophobicity and steric effects of the iodinated monomer.³⁵ The incorporation of a PEG copolymer allowed for a slight increase in mass loss (approximately 5% mass loss over 20

days). Further studies are necessary to confirm that this mass loss was due to polymer degradation and was not due to the leaching of small molecules or oligomers.

Table 2.3 Thermoset Properties.

Polymer (by diacid)	T_g (°C)^a	5% (°C)^b	E (MPa)^{c,*}	Strain (%)^{c,*}
Succinic	-1	290	55.4	21
Adipic	-11	340	4.9	140
Sebacic	-16	370	0.6	222

^a DSC, second heat 10 °C min⁻¹. ^b Decomposition measured by TGA. ^c Measured by Instron, Young's modulus (E) and strain at break at 25 °C at 10 mm min⁻¹. * Measured using polymers in Table A3 of Appendix A.

2.3.3 Bulk Polymer Radiopacity

Because radiopacity is directly related to iodine content, the amount of iodine incorporated into the polymers was analyzed. ¹H NMR was used to determine the iodine content of the prepolymers before crosslinking. Peaks associated with the iodinated unit were compared with peaks associated with the diacid unit (Appendix A, Figures A3-A5). After UV crosslinking, the thermosets were analyzed by EDS. The thermosets exhibited very high iodine contents by EDS (>60%, Table 2.4). Minimal iodine loss was apparent when comparing the EDS results after UV crosslinking (a semi-quantitative technique) to the weight percent of iodine calculated by ¹H NMR prior to crosslinking (Figure 2.1). Furthermore, the crosslinked thermosets exhibited little to no color change, thus indicating minimal iodine loss (Appendix A, Figure A15).³⁶ The lack of color change and the high iodine values measured by EDS suggest that iodine content does not differ significantly as a result of UV exposure.

Table 2.4 EDS Results for the Crosslinked Bulk Materials and Nanoparticles.

Element	Wt% Element in Sample			
	Se	Ad	Su	Ad-NP
C	24	17	17	35
I	68	72	72	52

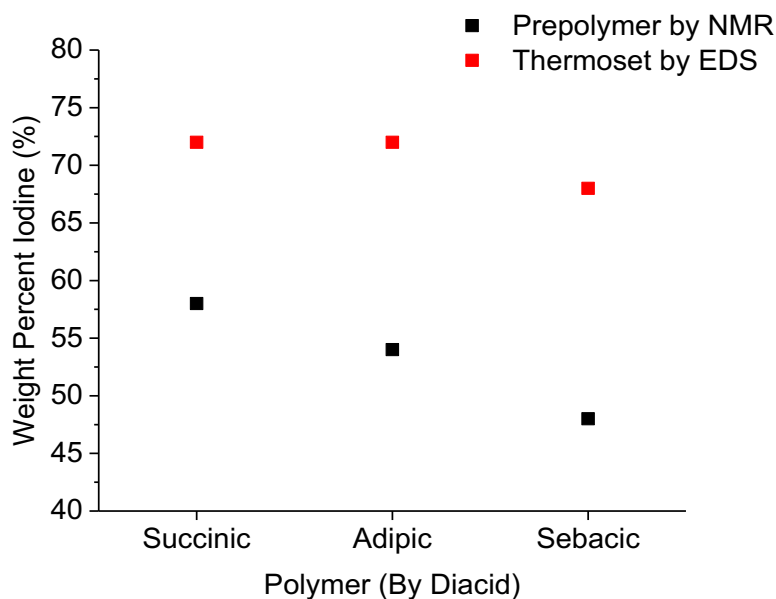


Figure 2.1 Comparison of the weight percent of iodine using ^1H NMR and EDS before and after crosslinking.

The high iodine content of these materials was visually apparent in CT images. Figure 2.2 shows CT images of crosslinked rods of each iodinated material in air (inset). To illustrate that these materials are easily visualized within tissue, they were implanted into cut segments of porcine liver and imaged (Figure 2.2). The contrast of these materials decreases only slightly upon implantation.

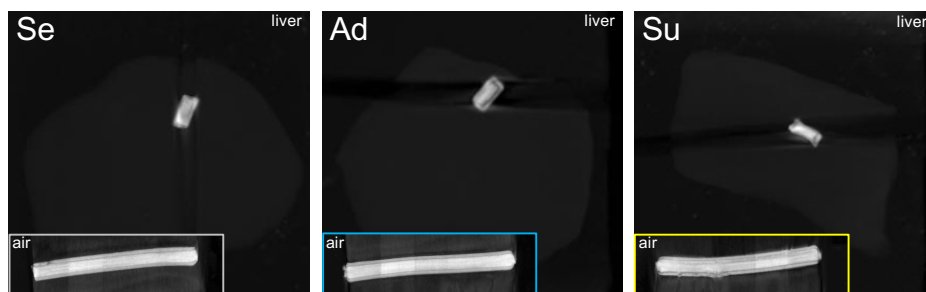


Figure 2.2 CT images of iodinated polyester materials. From left to right: sebacic (Se), adipic (Ad), and succinic (Su) acid based thermosets implanted in porcine liver and in air (insets).

2.3.4 Nanoparticle Synthesis and Evaluation

2.3.4.a Modified Liposomal-nanoprecipitation Formulation

Nanoparticles were synthesized using a modified liposomal-nanoprecipitation method (Figure 2.3).^{37,38} This method was selected to coat the hydrophobic nanoparticle core with PEG, which is well known to increase *in vivo* circulation times and potentially reduce the amount of iodine needed for good contrast (permitting a lower injection dose, I.D.).^{11,39} Nanoparticles were also made using a traditional nanoprecipitation method without PEG. While highly monodisperse nanoparticles could be formulated without PEG (PDIs of 0.01-0.07), they were too large (>400 nm) and easily aggregated in water (Table A4). Thus, the PEG corona also allowed easy dispersion of the nanoparticles in water.^{37,38}

To make the lipid-polymer hybrid nanoparticles, a solution of iodinated polymer in DMF was added to an aqueous solution containing a lipid-conjugated PEG (i.e., monostearate) and lecithin, a phospholipid stabilizer. As the DMF mixed with the water, the hydrophobic polymer chains collapsed into nanoparticles. The resulting mixture was sonicated for 10 minutes to allow kinetic self-assembly of the lipids on the surface of the precipitated polymeric particles.

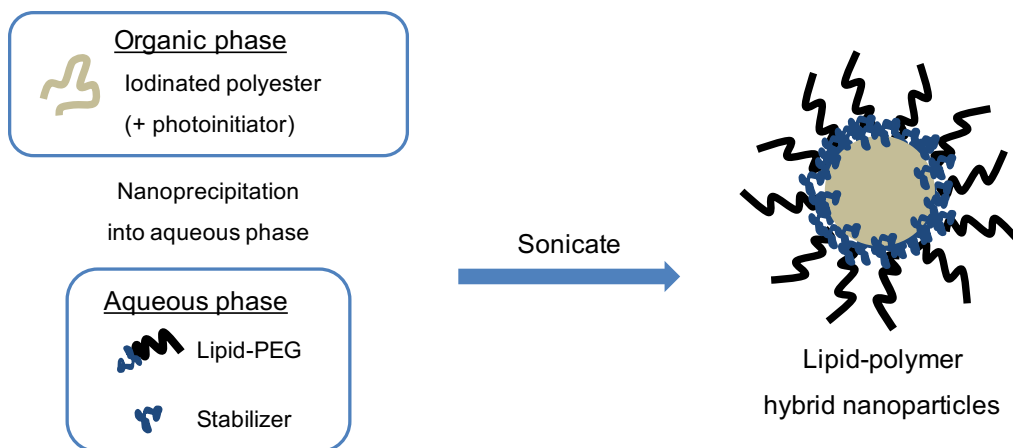


Figure 2.3 Nanoparticle formulation method using a modified liposomal-nanoprecipitation method.

2.3.4.b Evaluation of the Lipid-polymer Hybrid Nanoparticles

Nanoparticles between 50 and 150 nm were targeted because particles within this size range are typically removed by the liver and spleen rather than by the kidneys.⁴⁰ The modified, liposomal-nanoprecipitation procedure resulted in nanoparticles of approximately 75 nm with an average PDI of 0.11 for the succinic acid based particles (Su-NP), 82 nm with an average PDI of 0.11 for the adipic acid based particles (Ad-NP), and 89 nm with an average PDI of 0.12 for the sebacic acid based particles (Se-NP), as seen in Figure 2.4. EDS analysis of the particles showed high concentrations of iodine, only slightly lower than the bulk materials (Table 2.4). The slight decrease in weight percent iodine provides evidence that the nanoparticles remained coated in lipid-PEG after purification.

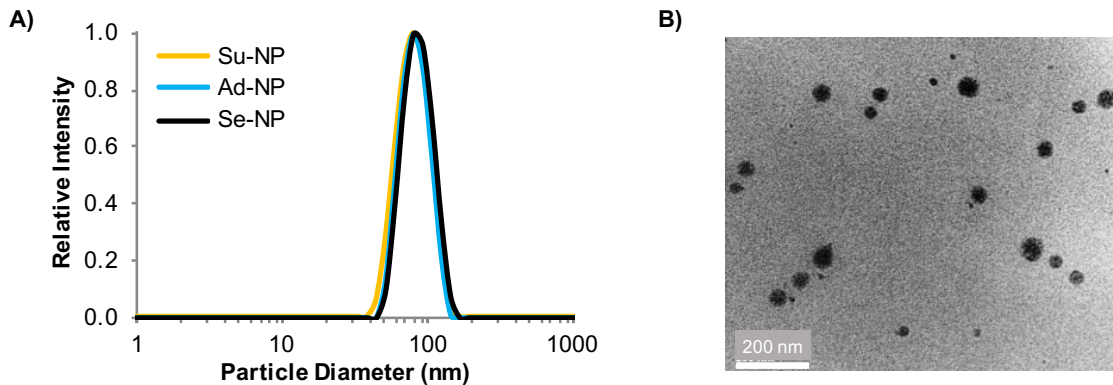


Figure 2.4 Analysis of the size and shape of the lipid-polymer hybrid nanoparticles. A) Dynamic light scattering results from the liposomal-nanoprecipitation method showing that the lipid-polymer hybrid nanoparticles were of similar size and PDI for all of the iodinated polymers. B) TEM image depicting the nanoparticles made using the adipic acid based polymer, Ad-NP (scale bar = 200 nm).

2.3.4.c Nanoparticle Stability at Body Temperature

To evaluate the stability of the nanoparticles, Ad-NP samples were incubated at 37 °C, and particle characteristics (size and PDI) were measured using DLS at time points of 1 hour and 24 hours to monitor if aggregation would occur. As shown in Figure 2.5, no significant change in size or PDI was noted during the incubation period, suggesting that the nanoparticles were stable when heated to body temperature. The particles remained at approximately 100 nm with PDIs of 0.1 over the course of 24 hours.

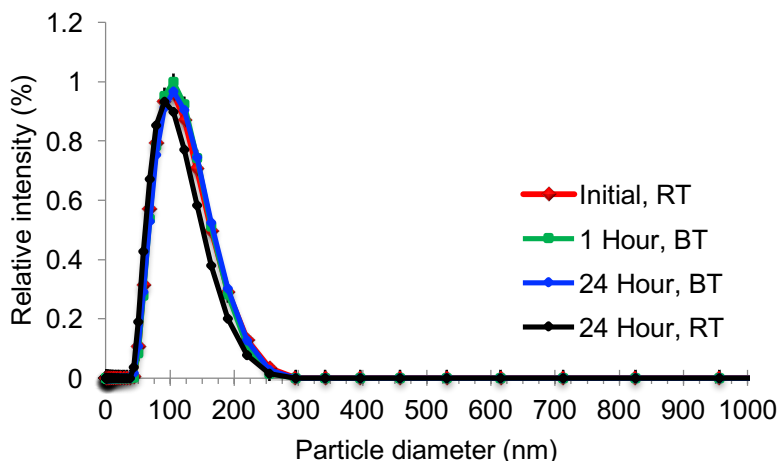


Figure 2.5 The nanoparticles were formulated in the same batch (RT = room temperature and BT = body temperature, 37 °C). The hydrodynamic diameter of the nanoparticles were analyzed using DLS before and after incubation at 37 °C and also compared with nanoparticles stored at room temperature.

2.3.4.d Nanoparticle Crosslinking

The nanoparticles reported to this point were not successfully crosslinked; however, crosslinking of the polymer core was of interest. Three Ad-NP suspensions were prepared using the same stock solutions of polymer, lipid-PEG, and lecithin. The photoinitiator was not added to one of the formulation batches as a control, and the resulting nanoparticles were stored away from light until further characterization was performed. In another batch, the photoinitiator was added to the nanoparticle suspension, and the suspension was exposed to UV light for 10 minutes. The ^1H NMR spectrum showed that this initial crosslinking method was not effective, presumably due to oxygen in the system, which prevented any radical reactions from occurring (Figure 2.6). As depicted in Figure 2.6, these nanoparticles showed the same ^1H NMR peak shifts and integrations as the formulation that had no UV exposure. To rectify this problem, another Ad-NP suspension was made with the addition of photoinitiator; this suspension was purged with argon in an airtight container (30 minutes for a 50 mL suspension). Crosslinking occurred after exposure to UV light for 10 minutes. Crosslinking was verified by ^1H NMR based

on the disappearance of the methylene peaks at 6.13 and 5.61 ppm (Figure 2.6). ^1H NMR of the Ad-NP suspension that was argon purged and irradiated showed only the expected spectral peaks of the lipid-PEG/stabilizer portion of the nanoparticles because the crosslinked polymer was not soluble in CDCl_3 .⁴¹

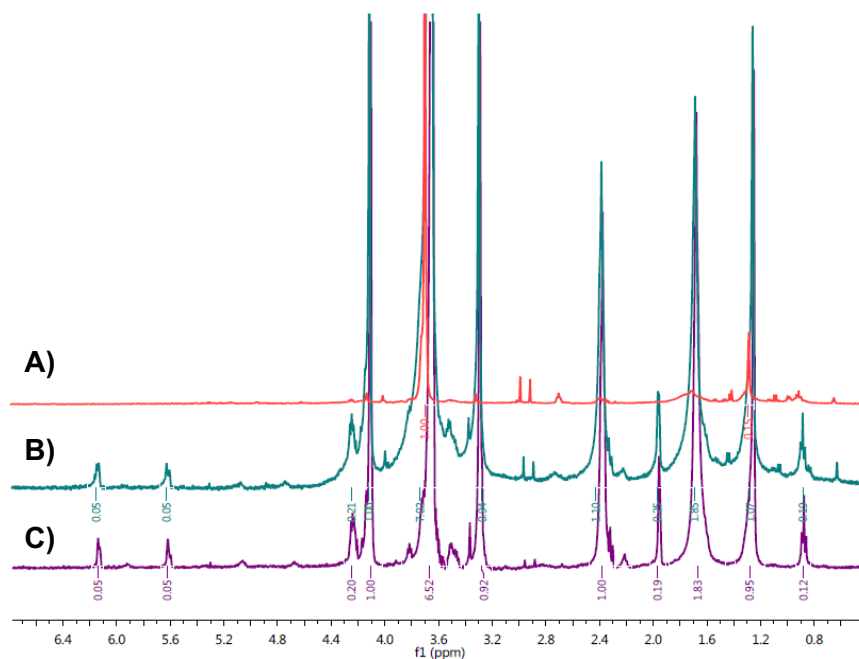


Figure 2.6 ^1H NMR spectra of A) Nanoparticle suspension that was successfully crosslinked (argon purged and UV irradiated), B) Nanoparticle suspension that was not crosslinked (no purge prior to irradiation), and C) Control nanoparticle suspension that had no addition of photoinitiator or UV exposure.

2.3.5 *In Vitro* Cytotoxicity

The cytotoxicity of the crosslinked films and lipid-polymer hybrid nanoparticles is shown in Figures 2.7 and 2.8. No cytotoxicity was found for the bulk crosslinked films, and the nanoparticles showed no cytotoxicity up to $400\ \mu\text{g mL}^{-1}$. The cytotoxicity of these nanoparticles compares favorably against liquid contrast agents such as Fenestra VC, which displays significant cytotoxicity at $<100\ \mu\text{g mL}^{-1}$.⁴² The nanoparticles in this study do not show

cytotoxicity until $\geq 100 \mu\text{g mL}^{-1}$. The percent viability was found using a CellTiter-Glo[®] luminescent cell viability kit to determine the amount of bioluminescent ATP present in the cells after 3 days of incubation. Each measurement was performed in triplicate, with three independently prepared batches of polymeric material.

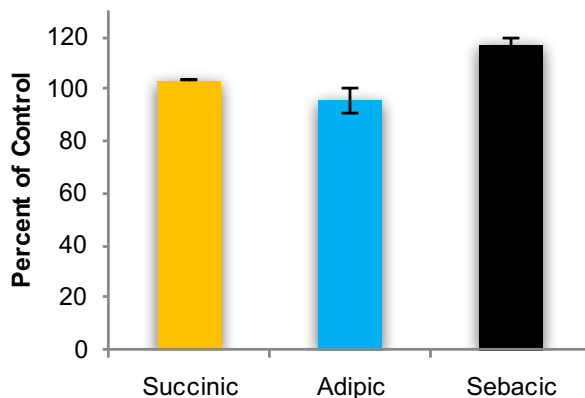


Figure 2.7 Cytotoxicity of crosslinked films after 3 days of incubation.

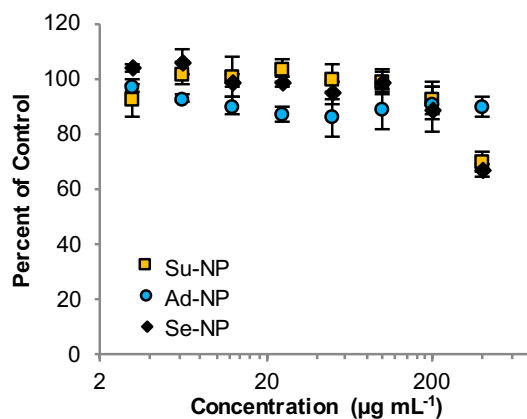


Figure 2.8 Cytotoxicity of nanoparticles at different concentrations.

2.3.6 Nanoparticle Radiopacity

2.3.6.a In Vitro Radiopacity

The effectiveness of the nanoparticles as general blood pool contrast agents was evaluated. CT images of nanoparticle dispersions showed high contrast when compared to DI water and a commercial contrast agent, Omnipaque® 300 (Figure 2.9). The attenuation was dependent on both concentration and particle type. As expected, the particles incorporating the succinic acid based polymer (highest iodine content) showed the highest contrast, and the contrast increased with increasing concentration of suspended nanoparticles (Figure 2.9).

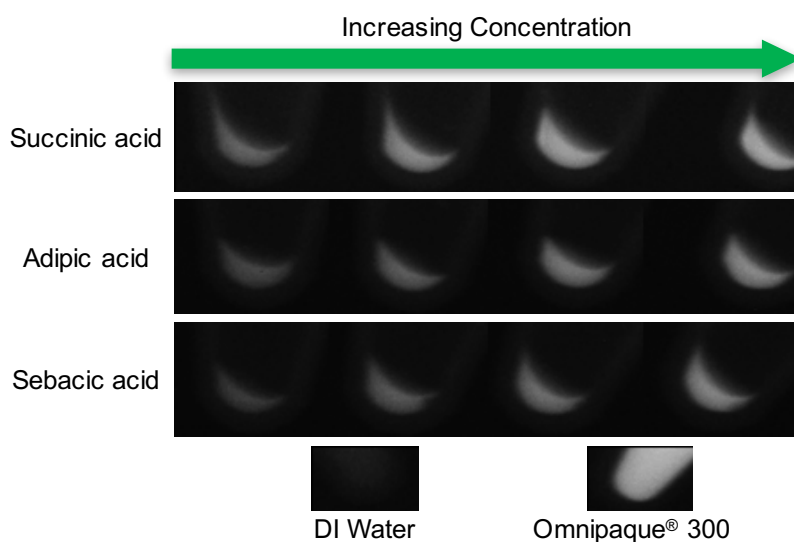


Figure 2.9 X-ray projections of succinic, adipic, and sebacic acid based nanoparticles of different concentrations (roughly 150 to 450 mg/mL).

2.3.6.a In Vivo Radiopacity

The adipic acid based nanoparticles were used in a preliminary *in vivo* study. These nanoparticles were made on a large scale, purified using sterile water, and concentrated to approximately 130 mg I mL⁻¹. Their size was analyzed by DLS prior to injecting the particles into the tail vein of a Balb/C mouse (Table 2.5). The nanoparticles were approximately 94 nm

with a PDI of 0.09, and the sample was prepared such that the I.D. would be 120 μL . One female Balb/C mouse was imaged with no administered contrast agents; the consequent Hounsfield units (HU) values obtained from this negative control were used to find ΔHU when analyzing the CT images of the mice injected with contrast agents. Another mouse was injected with Omnipaque (120 μL I.D., 150 mg I mL^{-1}) as a positive control. CT imaging was performed immediately after injection followed by time points at 5 minute intervals until reaching 30 minutes for both mice (Figure A16-A17, Appendix A), and an additional time point was taken 60 minutes after injection of the mouse administered the nanoparticles.

Table 2.5 Nanoparticle Size Before and After Injection.

Particle	Size (d.nm)	PDI
Ad-NP before injection 1	93.5	0.1
Ad-NP before injection 2	94.0	0.1
Ad-NP before injection 3	93.8	0.1
Ad-NP after injection 1	96.7	0.1
Ad-NP after injection 2	96.9	0.1
Ad-NP after injection 3	97.0	0.1

In Figure 2.10, the nanoparticles (Ad-NP) showed comparable contrast to the clinically used contrast agent at the 30-minute time point, and Ad-NP contrast was long-lasting (observed over 60 minutes). The nanoparticles bypassed the kidneys completely, whereas the commercial agent displayed immediate excretion and high attenuation in the kidneys (Figure 2.10 and Figure 2.11). The enhanced contrast observed in the mouse administered the nanoparticles suggests that nanoparticle contrast agents made from the iodinated polyesters synthesized herein have the potential to greatly increase blood pool attenuation and circulation.

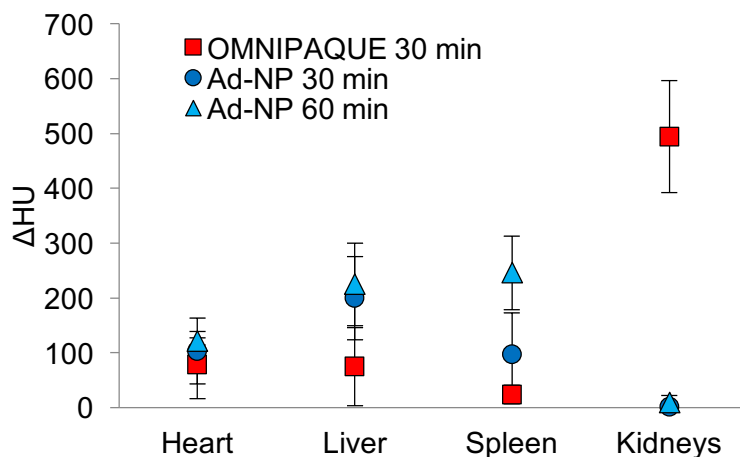


Figure 2.10 Graph displaying contrast comparison against a control (no contrast injected) for the heart, liver, spleen, and kidneys.

Although the mouse administered Ad-NPs showed healthy vital signs through the course of the imaging experiment, aggregation in the lungs was apparent (Figure A17, Appendix A). Aggregation can lead to acute lung embolism; therefore, the study was ended after one hour. The mice were sacrificed and organs were dissected for pathology. A histological analysis implied the development of acute pulmonary edema (Figure A18, Appendix A). Nanoparticle aggregation is a common challenge in the field.^{43,44} This aggregation presumably depends on the interplay between characteristics, such as hydrophobicity of the nanoparticle interior and the kinetic stability of the lipid-PEG corona. To ensure that the aggregation occurred due to interactions within the murine body and not as a result of the injection process, DLS was performed on nanoparticles taken from the same batch and ejected with a syringe of the same gauge as the *in vivo* study. The nanoparticles were only an average of 3 nm larger (approximately 97 nm), and there was no change in the PDI as a result of injection (Table 2.5).

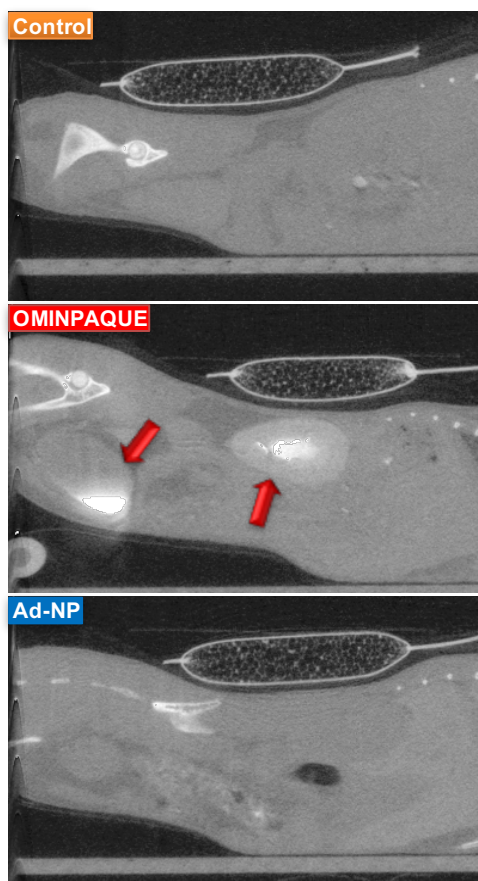


Figure 2.11 CT images of mice injected with no contrast (control, top), a clinically used contrast agent (Omnipaque®), middle) and with the adipic acid based nanoparticles (Ad-NP, bottom). The red arrows indicate significant contrast in the bladder and kidneys for the commercial contrast agent.

The stability of the nanoparticles was tested further in serum and whole blood. This experiment provided valuable information about the potential *in vivo* behavior of the particles. Low kinetic stability of the PEG shell anchored to the hydrophobic polymer core could result in coalescence, particularly for the nanoparticles used *in vivo*, which were not crosslinked.^{44,45} A crosslinked nanoparticle suspension was added to mouse serum and whole blood at ratios of 1:1, 1:10, and 1:100. The mixture consisting of a 1:10 ratio Ad-NP to serum/whole blood most closely simulated the dilution of the particles if they were administered to a mouse with an injected dose of 200 μ L. The mixtures were viewed under a microscope and compared to pure

serum and whole blood samples to see if any visible aggregates would form. Aggregates up to 5x the size of the surrounding red blood cells were observed (Figure 2.12). These aggregates were large enough to cause congestion in the capillary bed of the lungs. Studies have shown that the adsorption of blood plasma proteins increases as particle surface hydrophobicity increases.^{43,46} The observed aggregation in Figure 2.12 suggests that the lipid-PEG shell surrounding the particle was not stable, even after core crosslinking, thus exposing the hydrophobic core *in vivo* and causing proteins to attach.

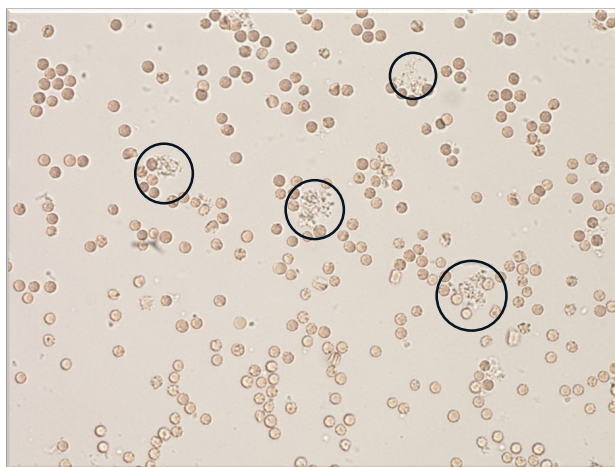


Figure 2.12 Micrograph showing aggregation in serum. Circles drawn in to indicate where aggregation took place.

2.4 Conclusions

A series of iodinated polyesters were synthesized and evaluated. These polyesters have the potential to serve as radiopaque biomaterials and blood pool contrast agents. This versatile platform of wholly aliphatic, highly iodinated materials allows easy processability and tunable chemical and physical properties. These iodinated polymers provided excellent contrast in air and imbedded in tissue (porcine liver). Additionally, these polymers exhibited no cytotoxicity. By using a modified liposomal-nanoprecipitation method to make nanoparticles, these materials

showed great potential as an alternative to standard liquid contrast agents, as they have good attenuation and do not uptake in the kidneys; however, stability remained problematic. The work presented here illustrates a new platform for the development of next-generation radiopaque biomaterials that have: modular physical and chemical properties, high radiopacity, low cost, easy processability, and sound biocompatibility.

REFERENCES

- (1) Bushberg, J. T.; Seibert, J. A.; Leidholdt, E. M.; Boone, J. M. *Essential Physics of Medical Imaging*, 2nd ed.; Williams & Wilkins: Philadelphia, 2002.
- (2) Hyafil, F.; Cornily, J.-C.; Feig, J. E.; Gordon, R.; Vucic, E.; Amirbekian, V.; Fisher, E. A.; Fuster, V.; Feldman, L. J.; Fayad, Z. A. *Nat. Med.* **2007**, *13*, 636.
- (3) Krause, W. *Adv. Drug Deliv. Rev.* **1999**, *37*, 159.
- (4) Escorsell, A.; Bosch, J. *Gastroenterol. Res. Pract.* **2011**, *2011*, 1.
- (5) Ormiston, J. A.; Serruys, P. W. S. *Circ. Cardiovasc. Interv.* **2009**, *2*, 255.
- (6) Kong, W. H.; Lee, W. J.; Cui, Z. Y.; Bae, K. H.; Park, T. G.; Kim, J. H.; Park, K.; Seo, S. W. *Biomaterials* **2007**, *28*, 5555.
- (7) deKrafft, K. E.; Xie, Z.; Cao, G.; Tran, S.; Ma, L.; Zhou, O. Z.; Lin, W. *Angew. Chem. Int. Ed. Engl.* **2009**, *48*, 9901.
- (8) Aviv, H.; Bartling, S.; Kiesling, F.; Margel, S. *Biomaterials* **2009**, *30*, 5610.
- (9) Carbone, A. L.; Song, M. J.; Uhrich, K. E. *Biomacromolecules* **2008**, *9*, 1604.
- (10) Mawad, D.; Mouaziz, H.; Penciu, A.; Méhier, H.; Fenet, B.; Fessi, H.; Chevalier, Y. *Biomaterials* **2009**, *30*, 5667.
- (11) Hallouard, F.; Anton, N.; Choquet, P.; Constantinesco, A.; Vandamme, T. *Biomaterials* **2010**, *31*, 6249.
- (12) Ramakrishna, S.; Mayer, J.; Wintermantel, E.; Leong, K. W. *Compos. Sci. Technol.* **2001**, *61*, 1189.
- (13) Galperin, A.; Margel, D.; Baniel, J.; Dank, G.; Biton, H.; Margel, S. *Biomaterials* **2007**, *28*, 4461.
- (14) Serruys, P. W.; Ormiston, J. A.; Onuma, Y.; Regar, E.; Gonzalo, N.; Garcia-Garcia, H. M.; Nieman, K.; Bruining, N.; Dorange, C.; Miquel-Hébert, K.; Veldhof, S.; Webster, M.; Thuesen, L.; Dudek, D. *Lancet* **2009**, *373*, 897.
- (15) Kurtz, S. M.; Villarraga, M. L.; Zhao, K.; Edidin, A. A. *Biomaterials* **2005**, *26*, 3699.
- (16) Lewis, G. J. *J. Biomed. Mater. Res.* **1997**, *38*, 155.
- (17) Heini, P.; Berlemann, U. *Eur. Spine J.* **2001**, *10*, 205.
- (18) Galperin, A.; Margel, D.; Margel, S. *J. Biomed. Mater. Res. Part A* **2006**, *79*, 545.
- (19) Davy, K. W. M.; Anseau, M. R.; Odlyha, M.; Foster, G. M. *Polym. Int.* **1997**, *43*, 143.

- (20) Jayakrishnan, A.; Chithambara Thanoo, B. *J. Appl. Polym. Sci.* **1992**, *44*, 743.
- (21) Mottu, F.; Rüfenacht, D. A.; Laurent, A.; Doelker, E. *Biomaterials* **2002**, *23*, 121.
- (22) Vázquez, B.; Ginebra, M. P.; Gil, F. J.; Planell, J. A.; López Bravo, A.; San Román, J. *Biomaterials* **1999**, *20*, 2047.
- (23) James, N. R.; Philip, J.; Jayakrishnan, A. *Biomaterials* **2006**, *27*, 160.
- (24) Hindenlang, M. D.; Soudakov, A. A.; Imler, G. H.; Laurencin, C. T.; Nair, L. S.; Allcock, H. R. *Polym. Chem.* **2010**, *1*, 1467.
- (25) Habnoui, S. El; Darcos, V.; Coudane, J. *Macromol. Rapid Commun.* **2009**, *30*, 165.
- (26) Habnoui, S. El; Blanquer, S.; Darcos, V.; Coudane, J. *J. Polym. Sci. Part A Polym. Chem.* **2009**, *47*, 6104.
- (27) Nottelet, B.; Coudane, J.; Vert, M. *Biomaterials* **2006**, *27*, 4948.
- (28) Kiran, S.; James, N. R.; Jayakrishnan, A.; Joseph, R. *J. Biomed. Mater. Res. Part A* **2012**, *100*, 3472.
- (29) Mawad, D.; Poole-Warren, L. A.; Martens, P.; Koole, L. H.; Slots, T. L. B.; van Hooy-Corstjens, C. S. J. *Biomacromolecules* **2008**, *9*, 263.
- (30) Chopin, S.; Delaunay, J.; Cousseau, J. *Tetrahedron Lett.* **2005**, *46*, 373.
- (31) Miyake, H.; Hayashi, K.; Okamura, S. *J. Polym. Sci.* **1965**, *3*, 2731.
- (32) Cao, G.; Calderon-Colon, X.; Wang, P.; Burk, L.; Lee, Y. Z.; Rajaram, R.; Sultana, S.; Lalush, D.; Lu, J.; Zhou, O. *Proceedings of SPIE.* 2009, p 72585Q1-7.
- (33) Takasu, A.; Shibata, Y.; Narukawa, Y.; Hirabayashi, T. *Macromolecules* **2007**, *40*, 151.
- (34) Chrissafis, K.; Paraskevopoulos, K. M.; Bikiaris, D. N. *Polym. Degrad. Stab.* **2006**, *91*, 60.
- (35) Lyu, S.; Untereker, D. *Int J Mol Sci* **2009**, *10*, 4033.
- (36) Aldenhoff, Y. B. J.; Kruft, M.-A. B.; Pijpers, a P.; van der Veen, F. H.; Bulstra, S. K.; Kuijer, R.; Koole, L. H. *Biomaterials* **2002**, *23*, 881.
- (37) Fang, R. H.; Chen, K. N. H.; Aryal, S.; Hu, C.-M. J.; Zhang, K.; Zhang, L. *Langmuir* **2012**, *28*, 13824.
- (38) Fang, R. H.; Aryal, S.; Hu, C.-M. J.; Zhang, L. *Langmuir* **2010**, *26* (22), 16958.
- (39) Otsuka, H.; Nagasaki, Y.; Kataoka, K. *Adv. Drug Deliv. Rev.* **2012**, *64*, 246.

- (40) Shilo, M.; Reuveni, T.; Motiei, M.; Popovtzer, R. *Nanomedicine* **2012**, *7*, 257.
- (41) Hu, X.; Chen, X.; Wei, J.; Liu, S.; Jing, X. *Macromol. Biosci.* **2009**, *9* (5), 456.
- (42) de Vries, A.; Custers, E.; Lub, J.; van den Bosch, S.; Nicolay, K.; Grull, H. *Biomaterials* **2010**, *31*, 6537.
- (43) Gessner, a; Waicz, R.; Lieske, A.; Paulke, B.; Mäder, K.; Müller, R. H. *Int. J. Pharm.* **2000**, *196* (2), 245.
- (44) de Vries, A.; Custers, E.; Lub, J.; van den Bosch, S.; Nicolay, K.; Grull, H. *Biomaterials* **2010**, *31*, 6537.
- (45) Mandal, B.; Bhattacharjee, H.; Mittal, N.; Sah, H.; Balabathula, P.; Thoma, L. a; Wood, G. C. *Nanomedicine* **2013**, *9* (4), 474.
- (46) Green, R. J.; Davies, M. C.; Roberts, C. J.; Tendler, S. J. *Biomaterials* **1999**, *20* (4), 385.

CHAPTER 3: RADIOPAQUE SHAPE MEMORY MATERIALS *VIA* IODINATED COPOLYESTERS

3.1 Introduction

Shape memory polymers are a class of smart materials that can be programmed into a temporary shape by the application of a stimulus and force. The temporary shape will remain until the material is recovered by exposing the material to the stimulus, such as heat or light.¹⁻³ Over the last several decades, shape memory polymers have been developed for biomedical applications, such as self-tying sutures,² deployable stents,^{4,5} and dynamic tissue-engineering scaffolds.⁶⁻⁸ In many cases, however, shape memory polymers lack radiopacity due to the absence of high Z elements. Therefore, although shape memory polymers can significantly lower the invasiveness of implantation,⁹ many are unable to be monitored by imaging technologies, like computed tomography (CT).

The first examples of radiopaque shape memory materials appeared in the fabrication of radiopaque shape memory alloys;^{10,11} however, shape memory polymers are not only less expensive than shape memory alloys but also are considered more environmentally friendly.¹² For example, shape memory alloys are given radiocontrast through fabrication with elements, such as tungsten, platinum, or erbium.^{10,11,13}

Many of the shape memory polymers that also have x-ray contrast proficiency are provided radiocontrast through impregnation using inorganic salts and particles or contrast agents.^{6,7,14-16} For example, a mechanically active, shape memory scaffold was designed by Lendlein and coworkers.⁶ This shape memory material (an aliphatic polyether urethane, PEU)

was impregnated with up to 40% b.w. BaSO₄ microparticles in order to induce radiopacity. The resulting material showed good shape memory capabilities and x-ray contrast; however, the PEU selected for this study was not biodegradable.⁶ Biodegradability was presumably not a desired property of this shape memory system, as leaching of BaSO₄ would cause the polymer to lose its radiopacity prematurely. The leaching of inorganic salts, such as BaSO₄, into the body has been documented as a possible risk due to the toxicity of the metal ions.¹⁷ Furthermore, impregnation using inorganic radiopaque additives can cause undesirable discoloration and limit pigment options of the material in its final form.¹⁸

There are several inherently radiopaque polymers (covalently bound iodine) capable of shape memory; however, none of these materials were studied as “smart” biomaterials. Thermoplastic polyurethanes (TPUs), which utilize chemically bound, aromatic iodine in the crosslinker or in the hard segment of the TPU, are expected to exhibit shape memory capabilities.¹⁹⁻²⁴ These inherently radiopaque TPUs, however, possess some drawbacks. First, many of these polymers utilize monomers that result in non-biodegradable polymer systems. Secondly, several of these systems utilize an iodinated version of bisphenol-A (BPA), which has been banned from use in some applications by the FDA.²⁵ In order to design a biodegradable TPU system, Y. Li and coworkers developed a TPU based on polybutylene succinate. While this material showed radiocontrast and biodegradability, it utilized iodinated BPA in its hard segment.²³

Additionally, an aliphatic iodinated poly(ϵ -caprolactone) (PCL) was synthesized.²⁶⁻²⁸ While this polymer was not tested as a shape memory material, PCL is a well-known shape memory polymer.^{9,29} However, this polymer contains secondary iodides that are capable of SN1, SN2, E1, and E2 side-reactions.

In this report, copolymers incorporating an aliphatic, iodinated monomer were developed. The synthesis of copolymers allowed for the addition of a broad range of materials properties to the existing iodinated polymer platform described in Chapter 1. For example, the thermal, mechanical, and x-ray properties of these copolymers could be fine-tuned by varying the amount of the iodinated component incorporated into the polymer. These copolymers were also noncytotoxic and stable, showing long-lasting radiopacity. Furthermore, these copolymers were tested as “smart” radiopaque biomaterials capable of performing the shape memory cycle several times.

3.2 Experimental Methods

3.2.1 Materials

All materials were purchased from Sigma-Aldrich, Fisher Scientific, or VWR International and used as received. Dichloromethane (CH_2Cl_2) was dried over CaH_2 and distilled immediately before use. 2,2-Bis(iodomethyl)-1,3-propanediol was synthesized as described in Chapter 2, Section 2.2.

3.2.2 General Characterization

The polymers were characterized using a Bruker 400 AVANCE (^1H NMR), a TA Instruments Q200 differential scanning calorimeter (DSC), and a Perkin Elmer Pyris 1 thermogravimetric analyzer (TGA). Gel permeation chromatography (GPC) was performed using a Waters 2695 separations module using THF as the mobile phase (1 mL min^{-1} , $25 \text{ }^\circ\text{C}$) with a Waters 2414 refractive index detector. Average molar mass was derived from a calibration curve based on a series of PS standards ranging from 500 to $100,000 \text{ g mol}^{-1}$. Thermosets were characterized by DSC, TGA, and dynamic mechanical analysis (DMA) on a TA Instruments G2 RSA. Elemental analysis was performed using an Oxford instruments,

INCA PentaFET energy dispersive x-ray spectrometer (EDS) on a Hitachi S-4700 cold cathode field emission scanning electron microscope (SEM) and a Kratos Axis Ultra DLD X-ray Photoelectron Spectrometer (XPS). CT images were performed using a Gamma Medica, Inc. eXplore CT-120 (70 kVp, 50 mA).

3.2.3 Synthesis of poly(2,2-bis(iodomethyl)-1,3-propanediol-co-1,8-octanediol adipate)

Various polymers were prepared *via* the polycondensation of 2,2-bis(iodomethyl)-1,3-propanediol, 1,8-octanediol, and adipic acid. The polymers were varied by modifying the ratio of the diol comonomers. Section 3.2.3.a describes the typical polymerization method used to synthesize all of the polymers.

3.2.3.a Polymer containing 15 mole percent 2,2-bis(iodomethyl)-1,3-propanediol (15%I)

A dry flask was charged with 2,2-bis(iodomethyl)-1,3-propanediol (0.76 g, 2.14 mmol), 1,8-octanediol (1.77 g, 12.12 mmol), adipic acid (2.00 g, 13.69 mmol), and scandium triflate (0.14 g, 0.28 mmol). The flask was nitrogen purged before heating the reaction to 80 °C. After 5 hours, vacuum was applied and reduced to 0.3 torr at a rate of 80 torr per hour. This pressure was maintained for 24 hours. The polymerization was terminated by cooling the reaction mixture to room temperature, dissolving the polymer in CHCl₃, and precipitating the polymer into cold diethyl ether (-78 °C). ¹H NMR, CDCl₃, δ (ppm) 4.06 (m, 1.00H), 3.63 (t, 0.01H), 3.56 (d, 0.03H), 3.26 (m, 0.11H), 2.32 (m, 1.03H), 1.63 (m, 2.17H), 1.32 (s, 1.87H).

3.2.3.b Polymer containing 20 mole percent 2,2-bis(iodomethyl)-1,3-propanediol (20%I)

¹H NMR, CDCl₃, δ (ppm) 4.08 (m, 1.00H), 3.66 (t, 0.02H), 3.58 (d, 0.03H), 3.29 (m, 0.16H), 2.35 (m, 1.00H), 1.68 (m, 2.14H), 1.34 (s, 1.82H).

3.2.3.c Polymer containing 25 mole percent 2,2-bis(iodomethyl)-1,3-propanediol (25%I)

^1H NMR, CDCl_3 , δ (ppm) 4.06 (m, 1.00H), 3.63 (t, 0.01H), 3.56 (s, 0.03H), 3.27 (m, 0.23H), 2.34 (m, 1.03H), 1.61 (m, 2.15H), 1.32 (s, 1.64H).

3.2.3.d Polymer containing 35 mole percent 2,2-bis(iodomethyl)-1,3-propanediol (35%I)

^1H NMR, CDCl_3 , δ (ppm) 4.07 (m, 1.00H), 3.56 (d, 0.05H), 3.27 (m, 0.31H), 2.34 (m, 1.06H), 1.64 (m, 2.03H), 1.32 (s, 1.47H).

3.2.4 End-capping poly(2,2-bis(iodomethyl)-1,3-propanediol-co-1,8-octanediol adipate) with 2-Isocyanatoethyl Methacrylate

In a typical reaction, a dry round bottom flask was charged with the iodinated polymer (2.93 g, 0.42 mmol), and purged with nitrogen before the addition of dry CH_2Cl_2 (18 mL). 2-Isocyanatoethyl methacrylate (0.25 mL, 1.76 mmol) was added, followed by the dropwise addition of tin(II) ethylhexanoate (40 μL , 0.11 mmol). The reaction was stirred for 48 hours at room temperature. The reaction was terminated by precipitation into cold diethyl ether ($-78\text{ }^\circ\text{C}$). The prepolymer was dried *in vacuo* at room temperature for 24 hours before use and stored at $4\text{ }^\circ\text{C}$.

3.2.5 Thermoset Fabrication

A prepolymer solution (2 g mL^{-1} in chloroform) containing approximately 2% b.w. diethoxyacetophenone was cast into a mold or onto a glass slide. The mold was then placed in a UV chamber (ELC-500 Light Exposure System) for 10 minutes under a flow of N_2 . The film was placed in a vacuum oven at $70\text{ }^\circ\text{C}$ for 24 hours under high vacuum.

3.2.6 Thermoset Cytotoxicity

To assess the biocompatibility of the crosslinked films, 20,000 HeLa cells (human epithelial cervical adenocarcinoma cell line, ATCC CCL-2) were seeded into 24 well plates in 1mL of complete MEM (1X) containing [L-glutamine ($.292\text{ g L}^{-1}$) and 10% fetal bovine serum]

per well. Cells were allowed to adhere for 24 hours and subsequently incubated with 1, 2, or 3 pieces of crosslinked films (measured to be 0.75 cm in length, 2 mm high, and 2 mm wide) that were placed into Falcon cell culture inserts containing a 3 μm pore size. One milliliter of complete medium was added to each insert and cells/crosslinked films were incubated for an additional 72 hours in a 37°C, 5% CO₂ incubator. After the 72-hour incubation period, cell culture inserts were removed and all medium was aspirated off cells. 300 μL of fresh medium was added back to each well followed by the addition of 300 μL CellTiter-Glo® Luminescent Cell Viability Assay reagent (Promega, Madison WI). Plates were placed on a microplate shaker for 2 minutes, incubated at RT for 10 minutes to stabilize luminescent signal. The luminescent signal was recorded on a Molecular Dynamics SpectraMax M5 plate reader. Cell viability was expressed as a percentage of the luminescent signal of cells grown in the absence of crosslinked film (cells only in complete medium).

3.2.7 Preliminary Thermoset Degradation by Hydrolysis

Films of known weight were placed in 1 mL of 10 mM pH 7.4 phosphate buffered saline (PBS) solution at 37 °C. The films were removed from the buffer solution at prescribed intervals and dried under vacuum for 72 hours before their masses were measured. Each measurement was performed on three separate samples. Mass loss (ML) was calculated according to equation 2.1.

3.2.8 Dynamic Mechanical Analysis and Shape Memory Testing

An RSA-G2 dynamic mechanical analyzer from TA Instruments was employed for both shape programming and mechanical tests. A typical temperature ramp ranged from 0 to 60 °C at the same heating and cooling rates of 3 °C min⁻¹, where E is the tensile storage modulus measured by DMA at strain of 0.1% and a frequency of 1 Hz. E was analyzed at 25 °C. For shape programming, the sample was heated to 70 °C. The sample was then stretched to a strain

of approximately 20% of the initial length. After stretching, the sample was quenched at 0 °C and annealed at 0 °C for 5 minutes. The instrument was then set to isoforce mode, where the external force was set to be constantly at zero as the sample was heated back to 70 °C. Percent fixity (R_f) and percent recovery (R_r) were calculated (equations 1.3 and 1.4, Chapter 1).

3.3 Results and Discussion

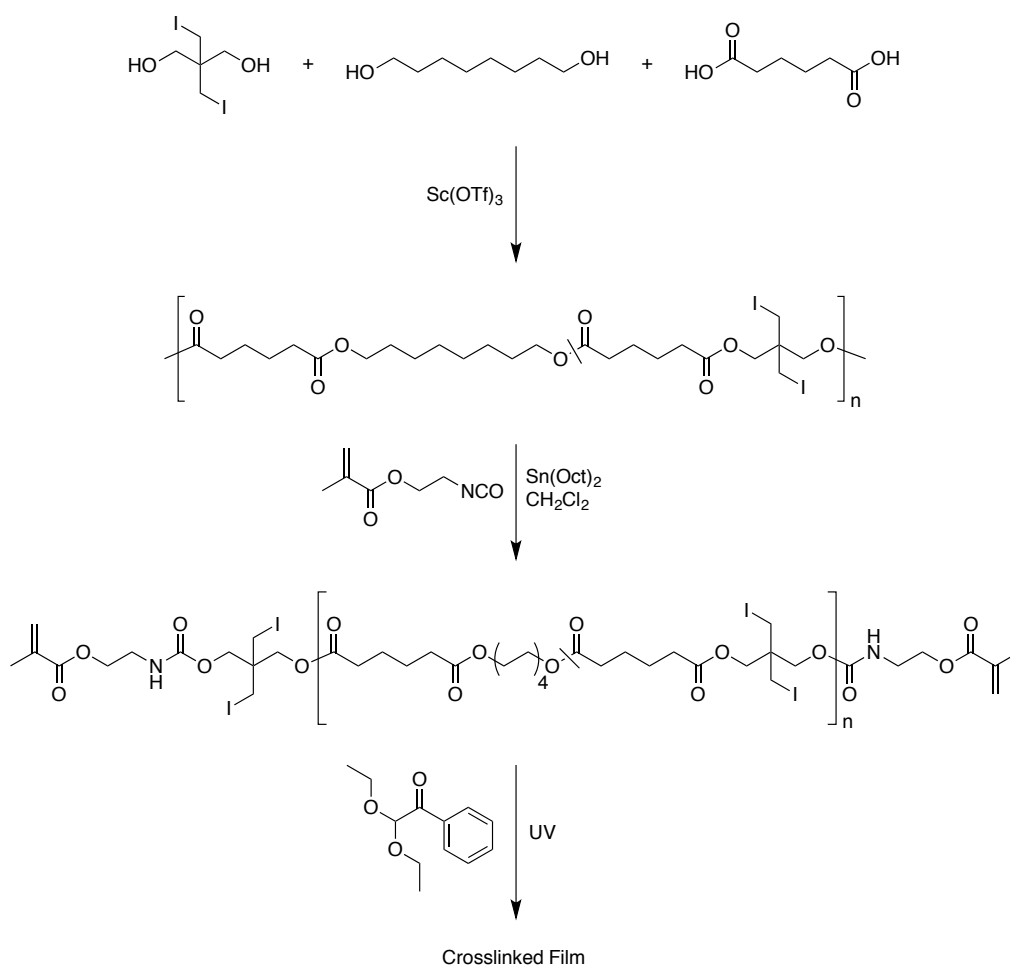
3.3.1 Polymer Synthesis and Evaluation

3.3.1.a Prepolymer Synthesis

Because radiopaque shape memory materials were desired, semicrystallinity was an essential property. Crystallites act as physical net-points, which hold the temporary shape in place.^{3,30} Because the bulky, iodinated units of 2,2-bis(iodomethyl)-1,3-propanediol produced 100% amorphous homopolymers, a linear comonomer, 1,8-octanediol, was selected to induce semicrystallinity into the copolymers. Scheme 3.1 displays the polymerization of poly(2,2-bis(iodomethyl)-1,3-propanediol-co-1,8-octanediol adipate). Four different copolymers were made by varying the ratio of 1,8-octanediol to 2,2-bis(iodomethyl)-1,3-propanediol. The iodine content of the polymers was varied by targeting the incorporation of 15%, 20%, 25%, and 35% 2,2-bis(iodomethyl)-1,3-propanediol by mole into the respective polymers. For convenience, these iodinated copolymers will be identified by the targeted mole percent of 2,2-bis(iodomethyl)-1,3-propanediol incorporated into the polymer; i.e., 15%I will represent the polymer with 15 mole percent of the iodinated monomer incorporated, as seen in the experimental section (Section 3.2.3).

Overall, the synthesis of the copolymers was similar to the method used for the iodinated homopolymers described in Chapter 2 (Scheme 2.2). A much lower reaction temperature was required in the synthesis of the copolymers as compared to the synthesis of the homopolymers

found in Chapter 2. To synthesize the iodinated homopolymers, the reaction temperature started at 135 °C in order to melt 2,2-bis(iodomethyl)-1,3-propanediol, a crystalline solid ($T_m \sim 130$ °C; Appendix B, Table B1 and Figure B1). The reaction temperature could only be lowered once oligomers formed. In the synthesis of the copolymers (Scheme 3.1), the reaction temperature was maintained at 80 °C throughout the course of the synthesis. At 80 °C, 1,8-octanediol is a liquid capable of solubilizing the iodinated diol.



Scheme 3.1 Synthesis of iodinated copolymers followed by photo-crosslinking to yield iodinated thermosets.

The copolymers ranged from 5,500 to 7,700 g mol⁻¹ with dispersities of approximately 1.3 (\mathcal{D} lower than 2 is due to fractionation upon purification; Table 3.1). The iodine content was calculated by ¹H NMR and compared to the targeted mole percent of the iodinated monomer (Table 3.1). Peaks associated with the iodinated monomer were compared with peaks associated with the diacid unit (Appendix B, Figures B3-B6). On average, the polymers incorporated 83% of the intended mole percent of the iodinated monomer.

The T_m of the iodinated prepolymers increased as the amount of 1,8-octanediol increased, from 40 to 58 °C. A T_m slightly greater than 37 °C (body temperature) was desired. The glass transition temperatures increased with decreasing amounts of 1,8-octanediol. While this trend may seem counterintuitive, the trend in T_g is believed to be due to the higher amount of iodinated monomer, which raises the specific volume of the polymer. The bulky iodinated monomer is believed to increase the energy barrier for bond rotation, thus making the T_g increase slightly.³¹ At 35%I, the ratio T_g/T_m (Kelvin temperatures) is exactly 0.75, thus this polymer is asymmetric, and the T_g is dependent on secondary forces and chain mobility (i.e., bond rotation).³² This T_g dependence on iodinated monomer content was also observed in the homopolymers in Chapter 2. The thermal degradation temperatures of these materials matched the expected degradation temperatures of typical aliphatic polyesters.³³

Table 3.1 Iodinated Copolymer Properties.

Polymer (by mol %I)	M_n (g mol ⁻¹) ^a	Actual mol %I monomer ^a	$\langle M_n \rangle$ (g mol ⁻¹) ^b	$\langle M_w \rangle$ (g mol ⁻¹) ^b	\mathcal{D}^b	T_g (°C) ^c	T_m (°C) ^c	5% (°C) ^d
15	7000	11	11000	15000	1.3	-46	58	340
20	5600	16	9000	12000	1.3	-44	54	341
25	7700	23	10000	13000	1.3	-40	48	341
35	5500	31	9800	12000	1.2	-37	40	368

^a Measured by ¹H NMR (400 MHz in CDCl₃). ^b Measured by GPC in THF using polystyrene standards. ^c Measured by TGA. ^d Measured by DSC, mid-point of the second heat.

3.3.1.b Iodinated Copolymer Thermosets

Next, the polymers were endcapped with 2-isocyanatoethyl methacrylate, which formed macromonomers and allowed facile UV crosslinking. To crosslink the prepolymers into thermosets, a 1:1 (b.w.) mixture of prepolymer and chloroform was made followed by the addition of a photoinitiator, diethoxyacetophenone. The mixture was added to a mold and exposed to UV light for 10 minutes under a flow of nitrogen. Chemical crosslinks were incorporated into the polymer network to hold the polymer in its permanent shape (i.e., permanent net-points).^{3,30}

The mechanical and thermal properties of the resulting thermosets varied depending on the ratio of comonomer diols (Table 3.2 and Figure 3.1). The 20%I polymer had a T_m of 41 °C, which was ideal, as it would allow local heating without damaging the surrounding cells in an *in vivo* implantable biomaterial application.³⁴ Increasing the percentage of iodinated monomer resulted in a decrease of the T_m and the storage modulus (E) because the polymer was less crystalline (Table 3.2 and Figure 3.1). The storage moduli of the materials varied from 16 to 143 MPa as the amount of crystalline monomer increased.

Table 3.2 Iodinated Copolymer Thermoset Properties.

Polymer film (by mol%I)	T_g (°C) ^a	T_m (°C) ^a	5% (°C) ^b	E (MPa) ^c
15	-47	47	397	143
20	-45	41	362	66
25	-42	34	382	34
35	-37	33	383	16

^a DSC, second heat 10 °C min⁻¹, ^b Decomposition measured by TGA 20 °C min⁻¹, ^c DMA tensile storage modulus at T = 25 °C.

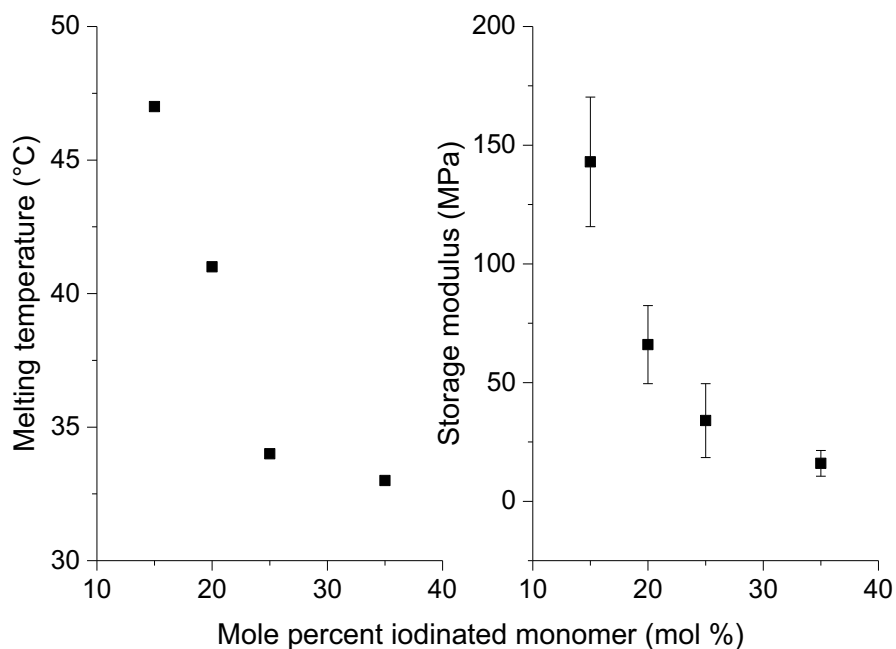


Figure 3.1 The melting temperature found by DSC and storage modulus at 25 °C using DMA for each crosslinked copolymer film.

The impact of UV crosslinking on iodine content was studied by determining the weight percent of iodine in the prepolymers and in the thermosets using EDS. Figure 3.2 shows that the UV crosslinking process had little to no effect on iodine content, an indication of UV stability (Tables B3-B11, Appendix B). Figure B21 in Appendix B also shows that the films had minimal color change as a result of UV exposure, which is indicative of minimal iodine loss.^{18,35} Minimal color change is significant, as traditional inorganic radiopaque agents and radiocontrast-inducing additives can cause undesirable discoloration.¹⁸

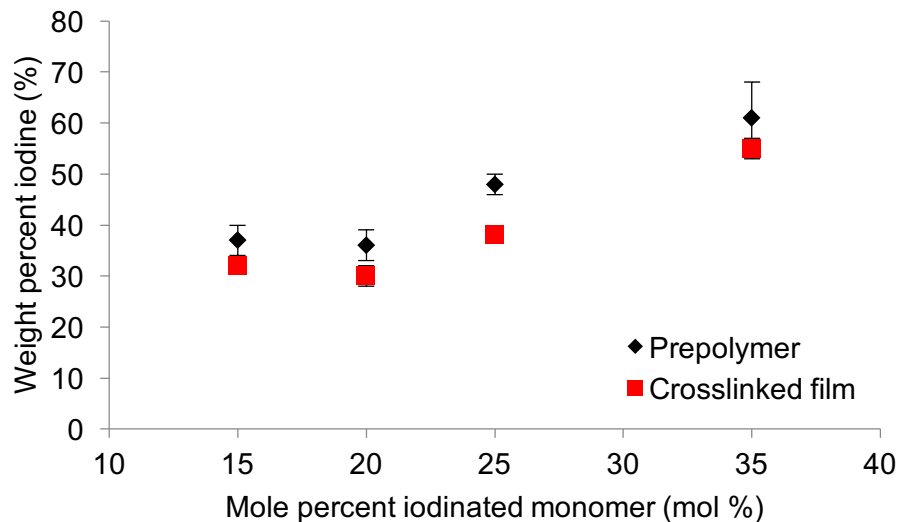


Figure 3.2 EDS of the iodinated prepolymers and crosslinked thermosets.

3.3.2 Thermoset Cytotoxicity

The cytotoxicity of the iodinated copolymers was analyzed by measuring the percent viability of HeLa cells after 3 days of incubation (Figure 3.3). Each experiment was performed on 1, 2, and 3 spacers (dimensions of 0.75 x 2 x 2 mm) to examine how the size of the sample affected cell viability. Almost all of the thermosets showed no cytotoxicity (cell viability $\geq 80\%$). The sample containing three spacers of the 35%I polymer showed cytotoxicity with only 48% cell viability, thus suggesting increased iodine content (by %I and film amount) leads to cytotoxicity.

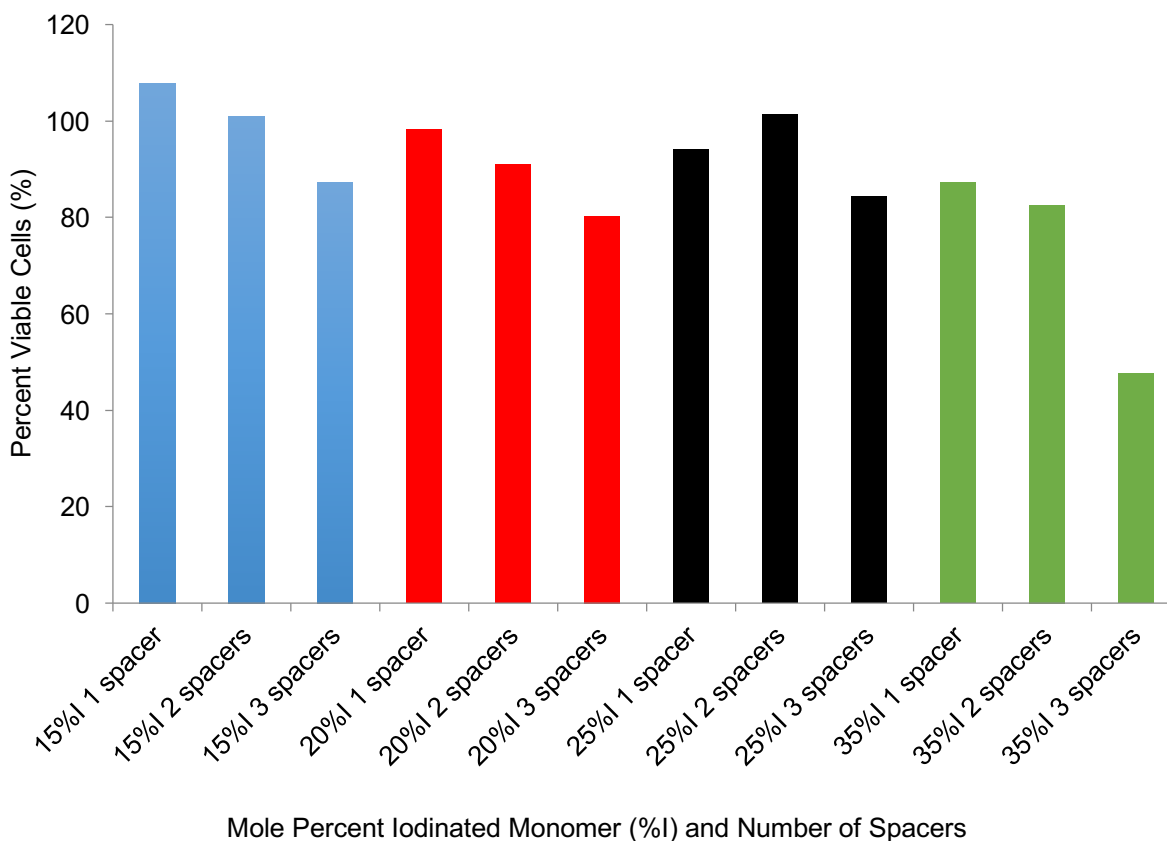


Figure 3.3 Cytotoxicity of the crosslinked thermosets after 3 days of incubation examining the effect of sample size (1-3 spacers) on cell viability.

3.3.3 Thermoset Radiopacity

The radiopacity of the polymers was studied by CT imaging. Figure 3.4A shows CT images of the iodinated thermosets. The high radiocontrast of all of the thermosets was apparent when comparing the CT images to aluminum and polycaprolactone (PCL; Figure 3.4). Figure 3.4A also shows that the radiopacity of the iodinated thermosets are homogenous throughout the entire polymer film. Figure 3.4B displays the attenuation of the aluminum bar, iodinated thermosets, and PCL in attenuation units calculated using ImageJ software. Figure 3.4B clearly shows that the radiopacity of the iodinated thermosets is dependent on iodine content, as the attenuation decreases with decreasing mole percent of the iodinated monomer. Figure 3.4 also

shows the lack of radiocontrast of typical biomaterials, such as PCL (Figure 3.4 F), due to their lack of high Z elements.

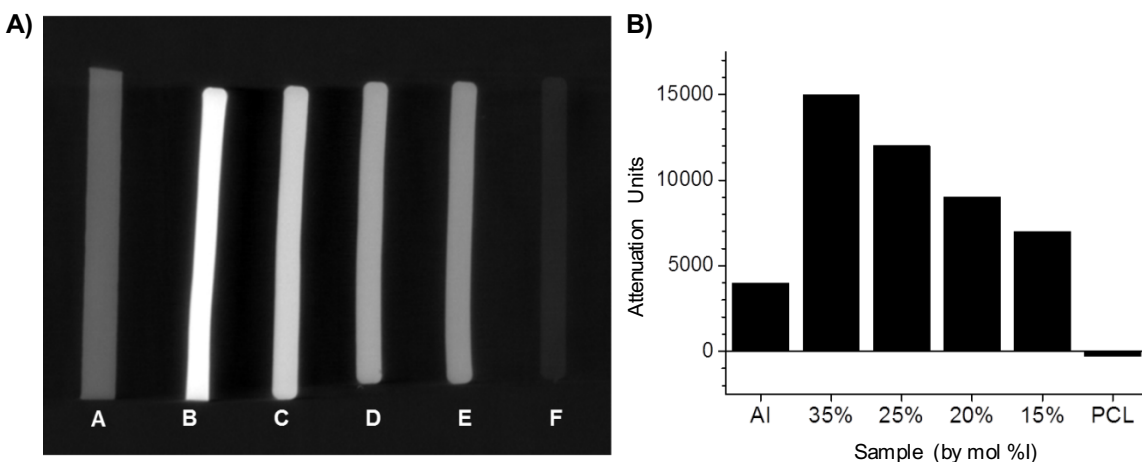


Figure 3.4 A) CT images of an aluminum bar (A), the iodinated thermosets from 35%I to 15%I (B, C, D, E, respectively), and PCL (F). B) Attenuation units of the iodinated thermosets compared to aluminum and PCL.

3.3.3.a Long-term Radiopacity

The thermosets were placed in a PBS solution at 37 °C, removed from the buffer solution at prescribed intervals, and dried under vacuum before further analysis. A CT image was taken at the four-week mark (Figure 3.5), depicting the long-lasting radiopacity of the films. The high cell viability displayed in Figure 3.3 along with the radiocontrast shown in Figure 3.5 indicates minimal leaching of any cytotoxic or radiopaque molecules. The radiocontrast of the thermosets after four weeks of incubation also suggests that any polymer degradation occurred at the ester linkages of the copolymers and was not due to side reactions that would result in a loss of iodine.

Table 3.3 displays the mass loss of each sample over the four-week incubation period (PBS, 37 °C). The high iodine content of these materials makes them very hydrophobic and increases the steric hindrance of water molecules to the ester linkages.³⁶ Furthermore, chemical crosslinks and crystallinity can limit water penetration and hydrolytic degradation.³⁷⁻⁴⁰ Thus, the

polymers showed low mass losses, between 0.7-5.2%. Typical degradable polymers and elastomers can take 6 months to 3 years to degrade,³⁷⁻⁴² therefore, further degradation studies must be carried out to confirm that the mass loss measured in Table 3.3 was due to polymer degradation rather than leaching of small molecules or oligomers. Rapidly degradable polymers could be built by incorporating comonomers or copolymers, such as 3,3'-dithiodipropionic acid or PEG.

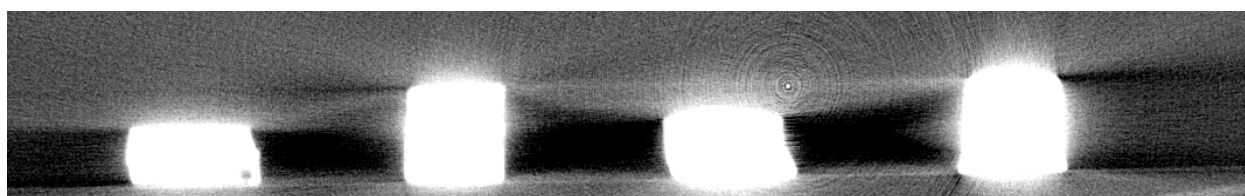


Figure 3.5 Week 4 CT image of the thermosets that were incubated in PBS buffer solution at 37 °C.

Table 3.3 Mass Loss of Crosslinked Films After 4 Weeks at 37 °C in PBS Buffer Solution.

Polymer film (by mol% I monomer)	Mass loss at 4 weeks (%)
15	4.5 ±0.7
20	2.1 ±0.3
25	1.6 ±0.9
35	4.2 ±0.7

3.3.4 Shape Memory

Crosslinking the polymers provided the net-points needed to maintain the polymers' permanent shape during the shape memory cycle. In order to test the shape memory cycle on the iodinated copolymers, DMA was performed. Figure 3.6 shows the third shape memory cycle for each sample, where “1” represents the sample in its initial, permanent shape. At 1, the sample was heated above its T_m to 70 °C. From 1 to 2, the sample was stretched to a strain

approximately 20% higher than the initial length. In the process of going from 2 to 3, the sample was quenched at 0 °C. At 3, the sample was annealed at 0 °C for 5 minutes to allow crystallites to form and act as physical net-points that hold the secondary shape in-place. The transition from 3 to 4 was the result of relaxation that occurred when the instrument was set to maintain an external force of zero. Finally, 4 to 1 represents the process of reheating the sample and inducing shape change back to the original shape as the polymer exceeds the melting temperature.^{3,43} The percent fixity (R_f) and percent recovery (R_r) were calculated using equations 1.3 and 1.4 (Table 3.4). High values of both fixity and recovery were observed for all of the polymers. The highest values were observed in samples that were more crystalline.

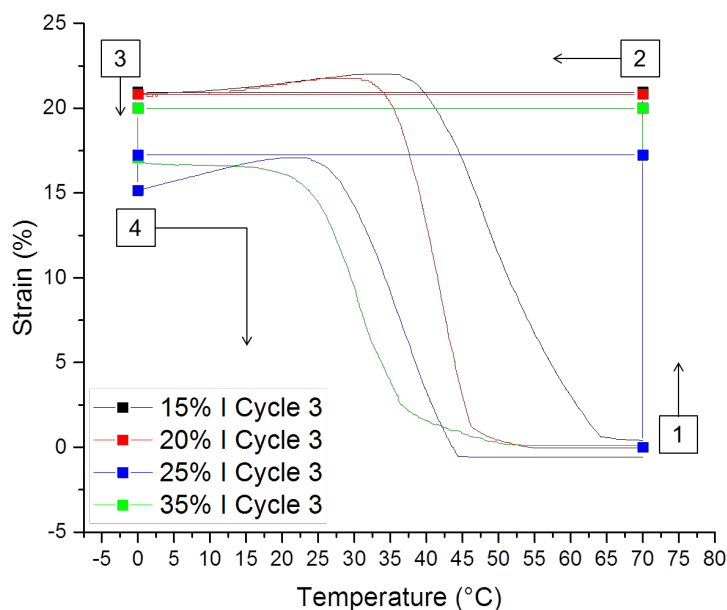


Figure 3.6 Third shape-memory cycle for each crosslinked copolymer. Step 1: The polymer is heated and mechanically deformed into its temporary position. Step 2: The polymer is cooled below its transition temperature under a constant mechanical stress. Step 3: The polymer is unloaded, releasing the applied stress. Step 4: The polymer is heated past its transition temperature and returns to its permanent shape.

Table 3.4 Strain Fixity and Recovery Over Three Shape Memory Cycles.

Polymer film (by mol%I)	R_f (%)	R_r (%)
15	99.8 ±0.2	99.8 ±0.2
20	99.6 ±0.7	99.6 ±0.7
25	89.7 ±1.6	89.8 ±1.3
35	87.2 ±2.1	87.2 ±2.1

3.4 Conclusions

A series of iodinated copolyesters were synthesized and evaluated. By incorporating a linear comonomer diol, 1,8-octanediol, with the signature iodinated diol, 2,2-bis(iodomethyl)-1,3-propanediol, semicrystalline polymers were developed. These polymers were end-functionalized with a photo-crosslinkable methacrylate unit for easy fabrication of thermosets, and the thermosets maintained high iodine contents after UV exposure.

The resulting prepolymers and thermosets had tunable thermal, mechanical, and x-ray capabilities. By modifying the ratio of 1,8-octanediol to 2,2-bis(iodomethyl)-1,3-propanediol, the crystallinity and iodine content of the polymers was altered; this allowed for the design of a polymer with an ideal T_m of 41 °C (just above body temperature) and high radiocontrast. Regardless of the iodine content, all of the polymers were highly radiopaque, which was beneficial, as increasing iodine content and sample amount led to lower percent cell viability and shape memory capability. The polymers of 15%I, 20%I, and 25%I showed no cytotoxicity regardless of sample size. All of the polymers showed high, long-lasting radiopacity.

Additionally, these polymers possessed “smart”, shape memory capabilities. For example, the 20%I polymer not only had an ideal T_m , but also showed R_r and R_f values of >99%. The work presented here further illustrates the versatility of the iodinated polymer platform outlined in Chapter 1. This copolymer platform not only exhibits the properties outlined in

Chapter 1: modular physical and chemical properties, high radiopacity, low cost, easy processability, and sound biocompatibility; but also, this platform has the added benefit of “smart” actuation *via* the thermal shape memory process. Thus, these materials serve as the first example of an inherently radiopaque, aliphatic shape memory polymer with nontoxic, stable, covalently attached iodine.

REFERENCES

- (1) Wu, L.; Jin, C.; Sun, X. *Biomacromolecules* **2011**, *12*, 235.
- (2) Lendlein, A.; Langer, R. *Science* **2002**, *296*, 1673.
- (3) Mather, P. T.; Luo, X.; Rousseau, I. A. *Annu. Rev. Mater. Res.* **2009**, *39*, 445.
- (4) Wache, H. M.; Tartakowska, D. J.; Hentrich, A.; Wagner, M. H. *J Mater Sci Mater Med* **2003**, *14*, 109.
- (5) Yakacki, C. M.; Shandas, R.; Lanning, C.; Rech, B.; Eckstein, A.; Gall, K. *Biomaterials* **2007**, *28*, 2255.
- (6) Cui, J.; Kratz, K.; Heuchel, M.; Hiebl, B.; Lendlein, A. *Polym. Adv. Technol.* **2011**, *22*, 180.
- (7) Cui, J.; Kratz, K.; Lendlein, a. *Smart Mater. Struct.* **2010**, *19*, 65019.
- (8) Neuss, S.; Blumenkamp, I.; Stainforth, R.; Boltersdorf, D.; Jansen, M.; Butz, N.; Perez-Bouza, A.; Knüchel, R. *Biomaterials* **2009**, *30*, 1697.
- (9) Lendlein, A.; Langer, R. *Science* **2002**, *296*, 1673.
- (10) Tuissi, A.; Carr, S.; Butler, J.; Gandhi, A. A.; O'Donoghue, L.; McNamara, K.; Carlson, J. M.; Lavelle, S.; Tiernan, P.; Biffi, C. A.; Bassani, P.; Tofail, S. A. M. *Shape Mem. Superelasticity* **2016**, *2*, 196.
- (11) Wang, S.; Guo, F. M.; Jiang, D. Q.; Liu, Y.; Cui, L. S. *Scr. Mater.* **2014**, *81*, 4.
- (12) Ebara, M.; Uto, K.; Idota, N.; Hoffman, J. M.; Aoyagi, T. *Adv. Mater.* **2012**, *24*, 273.
- (13) Lin, B.; Gall, K.; Maier, H. J.; Waldron, R. *Acta Biomater* **2009**, *5*, 257.
- (14) Wong, Y. S.; Salvekar, A. V.; Zhuang, K. Da; Liu, H.; Birch, W. R.; Tay, K. H.; Huang, W. M.; Venkatraman, S. S. *Biomaterials* **2016**, *102*, 98.
- (15) Langer, R. S.; Lendlein, A.; Annette, S.; Grablowitz, H. Biodegradable Shape Memory Polymers. 6160084, 2000.
- (16) Langer, R.; Lendlein, A. Shape Memory Polymers. US 6388043 B1, 2002.
- (17) Jayakrishnan, A.; Chithambara Thanoo, B. *J. Appl. Polym. Sci.* **1992**, *44*, 743.
- (18) Carbone, A. L.; Song, M. J.; Uhrich, K. E. *Biomacromolecules* **2008**, *9*, 1604.
- (19) Kiran, S.; James, N. R.; Jayakrishnan, A.; Joseph, R. *J. Biomed. Mater. Res. Part A* **2012**, *100*, 3472.

- (20) Kiran, S.; James, N. R.; Joseph, R.; Jayakrishnan, A. *Biomaterials* **2009**, *30*, 5552.
- (21) James, N. R.; Philip, J.; Jayakrishnan, A. *Biomaterials* **2006**, *27*, 160.
- (22) Kiran, S.; Joseph, R. *J. Biomed. Mater. Res. Part A* **2014**, *102*, 3207.
- (23) Wei, Z.; Song, P.; Sang, L.; Liu, K.; Zhou, C.; Wang, Y.; Li, Y. *Polymer*. **2014**, *55*, 2751.
- (24) Qu, W.; Weijuan, X.; Feng, C.; Tuo, X.; Qui, T. *J. Polym. Sci. Part A* **2011**, *49*, 2191.
- (25) Tavernise, S. *The New York Times*. 2012, p A15.
- (26) Habnoui, S. El; Blanquer, S.; Darcos, V.; Coudane, J. *J. Polym. Sci. Part A Polym. Chem.* **2009**, *47*, 6104.
- (27) Habnoui, S. El; Darcos, V.; Coudane, J. *Macromol. Rapid Commun.* **2009**, *30*, 165.
- (28) Nottelet, B.; Coudane, J.; Vert, M. *Biomaterials* **2006**, *27*, 4948.
- (29) Zhu, G.; Liang, G.; Xu, Q.; Yu, Q. *J. Appl. Polym. Sci.* **2003**, *90*, 1589.
- (30) Liu, C.; Qin, H.; Mather, P. T. *J. Mater. Chem.* **2007**, *17*, 1543.
- (31) Sheirs, J.; Long, T. E. *Modern Polyesters*; John Wiley & Sons, Ltd.: West Sussex, 2003.
- (32) Odian, G. In *Principles of Polymerization*; John Wiley & Sons, I., Ed.; John Wiley & Sons, Inc.: Hoboken, 2004; pp 29–32.
- (33) Chrissafis, K.; Paraskevopoulos, K. M.; Bikiaris, D. N. *Polym. Degrad. Stab.* **2006**, *91*, 60.
- (34) Dill, K. A.; Ghosh, K.; Schmit, J. D. *Proc. Natl. Acad. Sci.* **2011**, *108*, 17876.
- (35) Aldenhoff, Y. B. J.; Kruft, M.-A. B.; Pijpers, a P.; van der Veen, F. H.; Bulstra, S. K.; Kuijer, R.; Koole, L. H. *Biomaterials* **2002**, *23*, 881.
- (36) Lyu, S.; Untereker, D. *Int J Mol Sci* **2009**, *10*, 4033.
- (37) Bigg, D. M. *Adv. Polym. Technol.* **2005**, *24*, 69.
- (38) Vert, M.; Mauduit, J.; Li, S. *Biomaterials* **1994**, *15*, 1209.
- (39) Olson, D. a.; Gratton, S. E. a; DeSimone, J. M.; Sheares, V. V. *J. Am. Chem. Soc.* **2006**, *128* (41), 13625.
- (40) Nicolau, S. E.; Davis, L. L.; Duncan, C. C.; Olsen, T. R.; Alexis, F.; Whitehead, D. C.; Van Horn, B. A. *J. Polym. Sci. Part A Polym. Chem.* **2015**, *53*, 2421.
- (41) McMullin, E.; Rebar, H. T.; Mather, P. T. *Macromolecules* **2016**, *49*, 3769.

- (42) Miyajima, M.; Koshika, A.; Okada, J.; Kusai, A.; Ikeda, M. *Int. J. Pharm.* **1998**, *169*, 255.
- (43) Xie, T. *Polymer*. **2011**, *52*, 4985.

CHAPTER 4: SUPRAMOLECULAR ENGINEERING POLYESTERS: ENDGROUP FUNCTIONALIZATION OF GLYCOL MODIFIED PET WITH UREIDOPYRIMIDINONE

4.1 Introduction

Modification of polymer properties through post-polymerization functionalization is of significant interest, specifically through the use of supramolecular chemistry.¹⁻⁴ Functionalization of polymer endgroups with supramolecular units (e.g. hydrogen bonding units) results in noncovalent bonds that dramatically alter the properties of the initial polymer.⁵⁻⁹ In particular, terminal functionalization using the quadruple hydrogen bonding ureidopyrimidinone (UPy) group produces superior, thermally reversible polymer assemblies that merge orthogonal properties, such as low melt viscosity and enhanced elasticity.^{7,8} The UPy motif has been extensively applied to low molecular weight, aliphatic polymers. Systems including PEO/PPO,⁵ PDMS,¹⁰ PEB,⁶⁻⁸ polyTHF,^{9,11} PCL,¹¹⁻¹³ and aliphatic polycarbonates^{9,14} have been explored. Additionally, utilization of different linker units attaching the UPy endgroup to the virgin polymer have led to dramatic differences in fiber formation and stress-relaxation.⁸ Thermoplastic elastomers,^{7,15} recyclable materials,¹⁶ adhesives,¹⁷ and bioactive scaffolds¹⁸ have been developed using UPy terminated, low-performing polymers. These polymers generally have glass transition temperatures significantly lower than the reported dissociation temperature of UPy-UPy aggregates (approximately 80 °C).¹⁹ Hydrogen bonding moieties have also been applied to polymers with higher glass transition temperatures, such as polystyrene.²⁰⁻²² However, the UPy moiety has had limited investigation with more robust glassy or semi-crystalline polymers. The reversible bonding of UPy assemblies, and thus reversible decrease of

molecular weight, could be of great use if applied to high performance and engineering polymers.

High performance and engineering polymers are often manufactured into shaped objects in the polymer melt state.^{23,24} Because these polymers are ubiquitous in everyday life, the design of engineering polymers with robust mechanical properties at room temperature and low viscosity at elevated temperatures is greatly desired. The combination of these properties into one polymeric system is particularly challenging because processability is lost as performance is enhanced.²³ A great deal of work has been dedicated to the development of easily processable engineering polymers through the synthesis of new monomers and polymerization of novel copolymers; however, this work is costly and arduous.^{23,25,26} The design of mechanically robust, highly processable engineering polymers *via* modification of existing polymers would be significant.

The melt viscosity of low molecular weight engineering polymers is much lower than that of high molecular weight polymers; despite their excellent processability, the mechanical properties of these low molecular weight materials are greatly diminished due to a lack of entanglements.^{3,16} By utilizing thermally reversible, noncovalent bonds, the mechanical properties of low molecular weight engineering plastics could be improved at room temperature while maintaining their processability. In a seminal study, Long and coworkers reported UPy functionalization of low molecular weight poly(butylene terephthalate) (PBT), an industrial engineering polymer.¹⁹ This material displayed high tensile strength and toughness. The viscosity at 235 °C was more than ten times lower than the viscosity of high molecular weight PBT. However, the processing temperature remained problematic, as the temperature at which these viscoelastic improvements were observed also approached the decomposition temperature

of the UPy end-unit (onset of weight loss at 200 °C).^{22,27} Furthermore, the improvement in viscosity was dependent on the inherent T_m of PBT (225 °C). This study clearly revealed the importance of the thermal properties of the virgin material.

Herein, the first example of a supramolecular engineering polymer with enhanced thermal and mechanical properties that also shows improved melt viscosity at temperatures well below the decomposition temperature of the UPy moiety is reported. Glycol modified poly(ethylene terephthalate) (PETG) was carefully selected for end-functionalization due to its unique thermal properties. High molecular weight PETG has a T_g of 80 °C; therefore, low molecular weight PETG displays glass transition temperatures below the UPy-UPy dissociation temperature. Furthermore, incorporation of a cyclohexyl diol comonomer induces slow crystallization kinetics (halftime >1000 minutes), thus producing an amorphous copolyester.²⁵ The relationship between endgroup structure and polymer structure along with physical performance (thermal, mechanical, rheological) were investigated. This system serves as evidence that the improvement of the thermal, mechanical, and melt-viscoelastic properties of an engineering polymer through endgroup modification with supramolecular binding units can be achieved. The terminal functionalization of this class of engineering polyesters with various endgroup linkers, along with thorough characterization, deepens the current understanding of supramolecular chemistry with respect to robust polymer systems and demonstrates that supramolecular chemistry could be applied more broadly for the improvement of industrially relevant, high performing polymers.

4.2 Experimental Methods

4.2.1 Materials

PETG of various molecular weights, 2000, 3800, and 6800 g mol⁻¹ (PETG_{2k}, PETG_{3.8k}, PETG_{6.8k}) were provided by Eastman Chemical Company (molecular weight verified by inherent viscosity) and dried *in vacuo* at 50 °C for 24 hours before use. 2-Amino-4-hydroxy-6-methylpyrimidine (MIS) (98%), hexamethylene diisocyanate (HDI) (≥99%), and dibutyltin dilaurate (DBTDL) (95%) were used as received from Aldrich. 4,4'-Methylenebis(cyclohexyl isocyanate) (HDMI) (mixture of isomers, >97%) and 1,3-bis(isocyanatomethyl)cyclohexane (cis- and trans- mixture, >99%) were used as received from TCI America. Pentanes, sand (sea washed), and silica gel were used as received from Fisher Scientific. Chloroform (99.9%, stabilized with amylenes, extra dry) was purchased from Acros and filtered over a column of aluminum oxide (Brockmann I) and stored over molecular sieves. 1,2,4-Trichlorobenzene (99%) and pyridine (≥99%) were purchased from Acros and dried over molecular sieves. 2(6-Isocyanatohexylaminocarbonylamino)-6-methyl-4[1H]pyrimidinone (H-UPy) and all polymers functionalized with the H-UPy endgroup were synthesized as previously reported (PETG-H-UPy).⁷

4.2.2 Characterization

4.2.2.a General Characterization

¹H NMR spectra were recorded on a Bruker 400 AVANCE (400 MHz) using CDCl₃. Variable temperature ¹H NMR spectra were recorded on a Bruker 500 AVANCE (500 MHz) using 1,1,2,2-tetrachloroethane-*d*₂ (TCE-*d*₂). The temperature was calibrated using ethylene glycol, and a 600 s soak time was allowed at each temperature (25-100 °C). Thermal properties were measured using a TA Instruments Q200 DSC (heating rate of 10 °C min⁻¹) and a TA

Instruments Q5000 TGA (25-550 °C). GPC was performed using a Waters 2695 separations module using chloroform as the mobile phase (1 mL min⁻¹, 25 °C) with a Waters 2414 refractive index detector. Average molar mass was derived from a calibration curve based on a series of PS standards ranging from 500 to 100,000 g mol⁻¹. ATR FT-IR spectra were recorded on a Bruker ALPHA or a Perkin-Elmer Spectrum II instrument with a diamond crystal ATR accessory.

4.2.2.b Characterization of Melt-pressed Discs

Rheological measurements were performed on a TA Instruments ARES-G2 rheometer using an 8 mm parallel plate fixture and 1000 μm gap. Dynamic oscillatory shear measurements were used to calculate the G', G'' and tanδ at 1 Hz and 0.1% strain with temperatures from 160-35 °C at a ramp rate of 3 °C min⁻¹. Samples were first heated to 160 °C (300 s soak), and then measured over both a cooling and a heating cycle. Each measurement was performed on three samples, and the average curve was calculated using OriginPro software. Frequency sweeps were measured from 1-600 rad s⁻¹ (1 Hz, 0.1% strain) at 90 and 120 °C. Viscosity was measured over temperatures from 160 °C to approximately 90 °C at 3 °C min⁻¹ and 0.05 s⁻¹ shear rate. The lowest temperature was dependent on the amount of torque applied to the fixture as the material approached its T_g. The materials of 2000 g mol⁻¹ were only heated to 140 °C due to their low viscosities. Each measurement was performed on three samples, and the average curve was calculated using OriginPro software.

4.2.2.c Characterization of Drop-cast Films

AFM was performed using an Asylum Research MFP3D Atomic Force Microscope in tapping mode at a scan rate of 1 Hz. Tap300Al-G rotated monolithic silicon probes with 30 nm aluminum reflectivity coating, resonant frequency of 300 kHz, spring constant of 40 N m⁻¹,

length of 125 μm , width of 30 μm , and nominal tip radius of curvature less than 10 nm were used. Images were displayed and analyzed using Nanoscope 6.14R1 software.

4.2.2.d Characterization of Solvent-cast Films

Tensile tests were performed on an Instron Model 5566 equipped with a 500 N load cell. The samples (3 mm strips) were extended at a rate of 10 mm min^{-1} at room temperature until failure. Static water-in-air contact angles were measured with a KSV instrument and imaging using the goniometer/static sessile drop method (with at least 3 different spots on one film).

4.2.3 Synthesis

4.2.3.a Synthesis of 1-((3-(Isocyanatomethyl)cyclohexyl)methyl)-3-(6-methyl-4-oxo-1,4-dihydropyrimidin-2-yl)urea (CH-UPy)

MIS (0.50 g, 3.99 mmol) was charged to a dry three-neck round-bottomed flask fitted with a reflux condenser. 1,3-Bis(isocyanatomethyl)cyclohexane (4.79 mL, 27.17 mmol) was charged, and the mixture was heated to 100 $^{\circ}\text{C}$ under nitrogen atmosphere. After 24 hours, the reaction mixture was allowed to cool to room temperature, and then washed two times with pentanes to remove excess 1,3-bis(isocyanatomethyl)cyclohexane. The product was dissolved in chloroform and precipitated into cold pentanes. The white product was filtered and dried *in vacuo* at 40 $^{\circ}\text{C}$ overnight (yield 65%). $^1\text{H NMR}$ (400 MHz, CDCl_3) δ : 13.08 (N–H, 1H), 11.90 (N–H, 1H), 10.23 (N–H, 1H), 5.82 (s, 1H), 3.15 (m, 4H), 2.23 (s, 3H), 1.95 (m, 1H), 1.81 (m, 4H), 1.37 (m, 1H), 1.27 (m, 1H), 0.90 (m, 2H), 0.69 (q, 1H). FT-IR (ATR): $\nu = 2920 \text{ cm}^{-1}$ (ureido N–H), 2259 cm^{-1} (–NCO), 1662 cm^{-1} (ureido C=O), 1521 cm^{-1} (ureido N–H).

4.2.3.b Synthesis of PETG_{2k} Functionalized with CH-UPy (PETG_{2k}-CH-UPy)

PETG_{2k} (2000 g mol^{-1} , 1.68 g, 0.84 mmol), CH-UPy (0.80 g, 2.52 mmol), and 85 mL chloroform were charged to a dry round-bottomed flask equipped with a reflux condenser. The reaction mixture was heated to 65 $^{\circ}\text{C}$ under nitrogen, and then DBTDL (0.20 mL, 0.34 mmol)

was added. After 16 hours, 2 g silica gel was charged to the reaction mixture along with DBTDL (0.10 mL, 0.17 mmol), and the reaction stirred at 65 °C for 2 hours. The hot solution was filtered over a short column of sand to remove the silica gel. The chloroform was removed by rotary evaporation and the resulting polymer was dried *in vacuo* at 60 °C. ¹H NMR (400 MHz, CDCl₃) δ: 13.10 (N–H, 0.02H), 11.84 (N–H, 0.02H), 10.17 (N–H, 0.02H), 8.12 (s, 1H), 5.83 (s, 0.02H), 4.72 (s, 0.57H), 4.53 (s, 0.09H), 4.41 (s, 0.08H), 4.31 (d, 0.12H), 4.21 (d, 0.24H), 4.00 (s, 0.02H), 3.90 (s, 0.04H), 3.24 (m, 0.03H), 3.08 (d, 0.14H), 2.23 (s, 0.10H), 1.96 (q, 0.53H), 1.68 (m, 0.18H), 1.27 (s, 0.16H), 1.18 (m, 0.26H), 0.88 (m, 0.11H), 0.63 (m, 0.04H). FT-IR (ATR): $\nu = 1715\text{ cm}^{-1}$ (PETG C=O), 1662 cm^{-1} (ureido C=O), 1521 cm^{-1} (ureido N–H).

4.2.3.c Synthesis of Ureidopyrimidinone Functionalized PETG_{2k} with Dicyclohexyl Linker (PETG_{2k}-D-UPy)

HDMI (0.46 mL, 1.9 mmol), chloroform (5 mL), and DBTDL (0.20 mL, 0.34 mmol) were charged to a dry three-neck round-bottomed flask. In a separate, dry flask, a solution of PETG_{2k} (2000 g mol⁻¹, 1.5 g, 0.75 mmol) in chloroform (10 mL) was prepared. The PETG_{2k} solution was added to the HDMI solution dropwise using an addition funnel. The reaction mixture stirred under nitrogen at room temperature for 24 hours, and then the chloroform was removed by rotary evaporation. Pyridine (10 mL) was charged to reaction flask followed by MIS (0.70 g, 5.6 mmol) and DBTDL (0.20 mL, 0.34 mmol). A reflux condenser was fit to the flask, and the reaction stirred at 120 °C under nitrogen for 24 hours. Pyridine was removed by rotary evaporation, and then the crude product was dissolved in chloroform. Excess MIS was filtered, and the chloroform was removed by rotary evaporation. The resulting polymer was dried *in vacuo* at 60 °C. ¹H NMR (400 MHz, CDCl₃) δ: 13.13 (N–H, 0.02H), 11.93 (N–H, 0.02H), 9.80 (N–H, 0.02H), 8.10 (s, 1H), 5.81 (s, 0.02H), 4.68 (s, 0.58H), 4.49 (s, 0.14H), 4.39 (d, 0.09H), 4.28 (d, 0.11H), 4.18 (s, 0.26H), 3.98 (s, 0.01H), 3.87 (s, 0.03H), 3.77 (s, 0.07H),

3.40 (s, 0.06H), 2.34 (s, 0.01H), 2.20 (s, 0.08H), 1.95 (q, 0.53H), 1.63 (m, 0.88H), 1.13 (s, 1.4H).
FT-IR (ATR): $\nu = 1715 \text{ cm}^{-1}$ (PETG C=O), 1660 cm^{-1} (ureido C=O), 1523 cm^{-1} (ureido N-H).

4.2.4 Sample Fabrication

4.2.4.a Melt-Pressed Discs

Discs were made using a hydraulic melt press at $180 \text{ }^{\circ}\text{C}$ using specially made shims of 1 mm thickness and 8 mm diameter. The samples were allowed to fully melt without pressure for 1-3 minutes, and then 10-15 tons of pressure was applied for 3-4 minutes.

4.2.4.b Drop-cast Films

Polymer solutions were prepared in 1,2,4-trichlorobenzene (1.0 mg mL^{-1} at approximately $120 \text{ }^{\circ}\text{C}$). The solutions were drop-cast onto dry, clean glass slides (cleaned with chloroform and ethanol) using a pipette, and then placed in an oven at $120 \text{ }^{\circ}\text{C}$ overnight.

4.2.4.c Solvent-cast Films

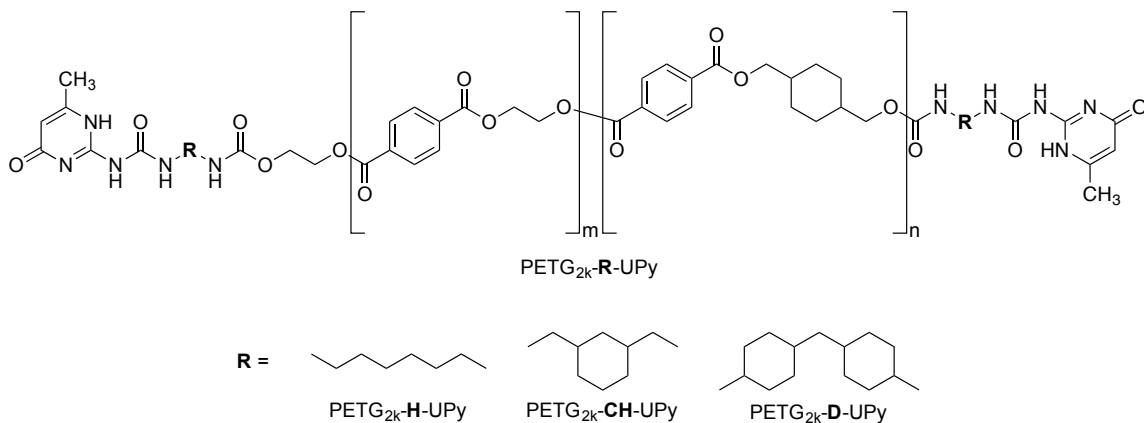
Solvent-cast films were prepared for tensile testing using a micrometer-based doctor-blade. PETG solutions of 25% w/w and PETG-H-UPy solutions of 13% w/w were prepared in 1,2,4-trichlorobenzene at $120 \text{ }^{\circ}\text{C}$. These concentrations produced suitable solution viscosities for fabricating uniform films, noting that the UPy functionalized polymers required a lower concentration due to the increased viscosity of the UPy-UPy aggregated polymers. The solvent evaporated at $120 \text{ }^{\circ}\text{C}$ for 16 hours at ambient pressure, and then the films dried under vacuum for 3 hours, gradually increasing the temperature to $180 \text{ }^{\circ}\text{C}$. The films had an average thickness of $40 \text{ }\mu\text{m}$.

4.3 Results and Discussion

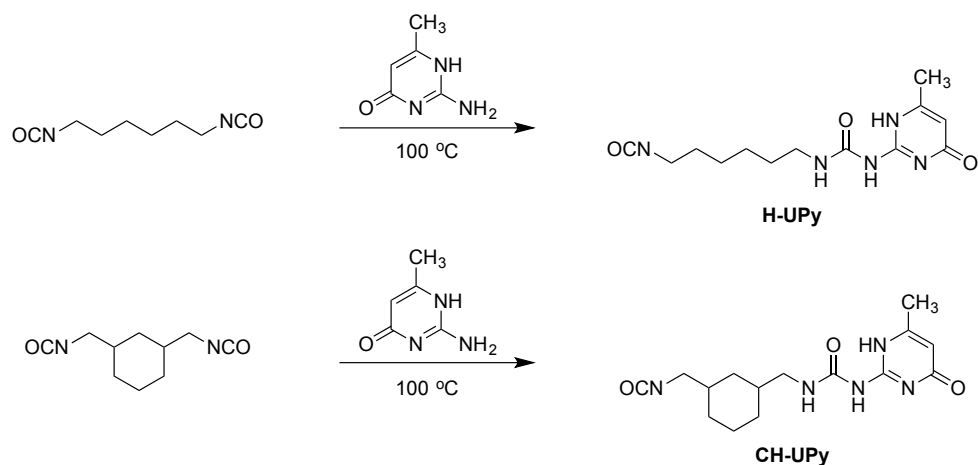
4.3.1 Synthesis and Characterization of UPy Functionalized PETG

4.3.1.a UPy Functionalization Using Multiple Linkers

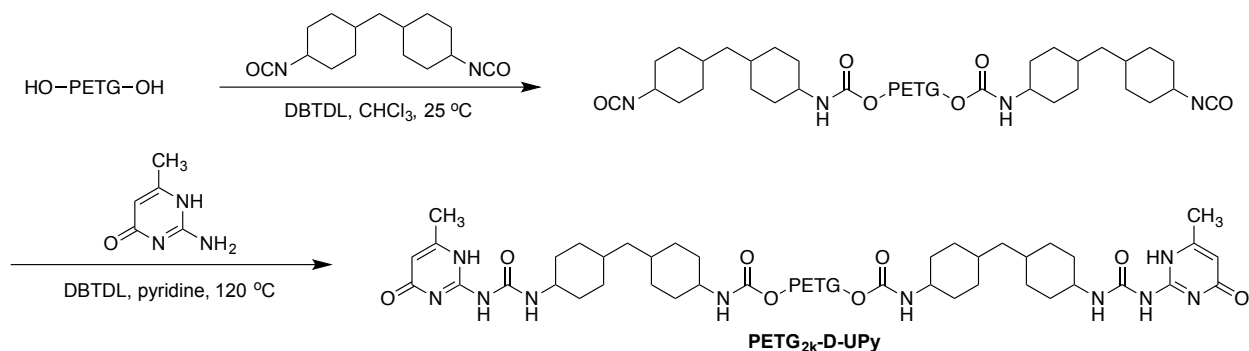
The packing capability of UPy endgroups could be affected by the structure of the linker, which attaches the UPy moiety to the polymer terminus.⁵ Therefore, three endgroup linkers of increasing rigidity were investigated, as depicted in Scheme 4.1. The preparation of PETG_{2k}-H-UPy⁷ and PETG_{2k}-CH-UPy involved separate synthesis of the respective endgroups (Scheme 4.2) followed by functionalization of hydroxyl terminated PETG. While similar approaches were attempted in the synthesis of PETG_{2k}-D-UPy without success, a one-pot synthetic route (Scheme 4.3) was utilized to successfully make the polymer.^{5,22}



Scheme 4.1 UPy functionalized PETG of 2000 g mol⁻¹ utilizing either a hexamethylene (H), cyclohexyl (CH), or dicyclohexyl (D) linker unit (R).



Scheme 4.2 Endgroup synthesis utilizing different diisocyanates.



Scheme 4.3 One-pot synthesis of UPy functionalized PETG of 2000 g mol^{-1} utilizing a dicyclohexyl linker group.

Table 4.1 summarizes the molecular weight, molecular weight distribution, and thermal properties of the resulting polymers. The number average molecular weight obtained by GPC was similar before and after end-functionalization. UPy functionalization caused a slight increase in the overall molecular weight (decreased retention times) of the polymers. Similar increases in molecular weight were observed when comparing PETG_{2k}-H-UPy, PETG_{2k}-CH-UPy and PETG_{2k}-D-UPy, suggesting minimal chain extension occurred during the one-pot synthesis of PETG_{2k}-D-UPy. Endgroup analysis, calculated by ¹H NMR, also confirmed that the degree of polymerization (X_n) did not appreciably change during the synthesis of PETG_{2k}-D-UPy. The

relative integrals associated with the aromatic protons of the repeating unit at 8.10 ppm and the methylene group of the hydroxyl endgroup at 3.98 ppm was similar to the ratio of the integral associated with the repeating unit and the same methylene group after UPy functionalization, which caused a downfield shift to 4.40 ppm (Figures C3 and C4, Appendix C). The ^1H NMR spectra used to determine X_n of PETG_{2k}-CH-UPy and PETG_{2k}-H-UPy are shown in the Appendix C (Figures C5 and C6, respectively).

Table 4.1 Properties of PETG and UPy Functionalized PETG of 2000 g mol⁻¹.

Sample	$\langle M_n \rangle^a$ (g mol ⁻¹)	$\langle M_w \rangle^a$ (g mol ⁻¹)	\bar{D}^a	5% Degradation ^b (°C)	T_g^c (°C)
PETG _{2k}	2600	3900	1.5	378	46
PETG _{2k} -H-UPy	3600	5900	1.6	336	67
PETG _{2k} -CH-UPy	5500	10000	1.9	269	66
PETG _{2k} -D-UPy	5200	10000	2.0	247	61

^aMeasured by GPC in CHCl₃ using polystyrene standards. ^b Measured by TGA. ^c Measured by DSC, mid-point of the second heat.

Table 4.1 also shows the temperature of degradation was analyzed by thermogravimetric analysis. As expected, the UPy functionalized polymers displayed lower degradation temperatures (5% b.w. at 247-336 °C) as compared to PETG_{2k} (5% b.w. at 378 °C) due to decomposition of the isocytosine head.²⁷ End-functionalization with the UPy moiety caused an increase in the T_g as compared with the unfunctionalized PETG, suggesting strong interactions among the quadruple hydrogen bonding endgroups. Thus, supramolecular self-assembly of the UPy endgroups led to an increase in the “operative” molecular weight and T_g of the polymers.

4.3.1.b H-UPy Functionalized PETG of Various Molecular Weights

Full thermal, mechanical, and rheological characterization of PETG of various molecular weights before and after end-functionalization would allow for a thorough study of the effects of the UPy moiety attached to engineering polymers. Due to the ease of synthesis and the fact that

H-UPy functionalization caused the most pronounced increase in T_g , PETG of various molecular weights were functionalized with H-UPy. The critical molecular weight for entanglements (CME) of PETG is approximately 5000 g mol^{-1} ; therefore, molecular weights just below and above the CME, 3800 and 6800 g mol^{-1} (as calculated by inherent viscosity), were selected. The molecular weight, molecular weight distribution, and thermal properties of the higher molecular weight polymers before and after H-UPy functionalization can be found in Table 4.2. GPC and endgroup analysis by ^1H NMR confirmed that the molecular weight and X_n did not appreciably change due to end-functionalization (Table 4.2 and Figures C7-C10, Appendix C, respectively). Furthermore, decreases in the degradation temperatures of the H-UPy functionalized polymers were observed. Analogous to the TGA results displayed in Table 4.1, the lower degradation temperatures found in Table 4.2 are due to early decomposition of the isocytosine head of the UPy end-unit.

Table 4.2 Properties of PETG and H-UPy Functionalized PETG of 3800 and 6800 g mol^{-1} .

Sample	$\langle M_n \rangle^a$ (g mol^{-1})	$\langle M_w \rangle^a$ (g mol^{-1})	\mathcal{D}^a	5% Degradation ^b ($^{\circ}\text{C}$)	T_g^c ($^{\circ}\text{C}$)
PETG _{3.8k}	6100	10000	1.7	387	58
PETG _{3.8k} -H-UPy	10000	16000	1.6	360	71
PETG _{6.8k}	12000	21000	1.8	381	72
PETG _{6.8k} -H-UPy	17000	27000	1.6	371	72

^a Measured by GPC in CHCl_3 using polystyrene standards. ^b Measured by TGA. ^c Measured by DSC, mid-point of the second heat.

4.3.2 Thermal, Mechanical, and Viscoelastic Properties of PETG-H-UPy of Various Molecular Weights

4.3.2.a Thermal Characterization

Figure 4.1A displays the thermal properties of the raw polymer powders with no further processing performed after synthesis. The T_g of PETG_{2k}-H-UPy was $21 \text{ }^{\circ}\text{C}$ higher than the T_g of

PETG_{2k}; whereas, the T_g of PETG_{3.8k}-H-UPy was only 13 °C higher than the T_g of PETG_{3.8k}. If the UPy endgroups of PETG_{2k}-H-UPy aggregated as a simple dimer, the T_g would be expected to be similar to the T_g of PETG_{3.8k}, which is approximately twice its molecular weight. However, the T_g of PETG_{2k}-H-UPy was approximately 10 °C higher than the T_g of PETG_{3.8k}. The relationship between molecular weight and T_g therefore suggests that the UPy endgroups aggregate in a multiple fashion in the melt state (through either multiple end-to-end interactions or pi-pi stacking) when the molecular weight is below the CME.²² There was no difference in T_g before and after H-UPy functionalization when looking at the polymers of 6800 g mol⁻¹ (Figure 4.1A). This result was not surprising, since the polymers are above the CME. Also, because PETG_{6.8k}-H-UPy is of higher molecular weight than PETG_{2k}-H-UPy and PETG_{3.8k}-H-UPy, it has fewer endgroups and a lower concentration of UPy end-units.

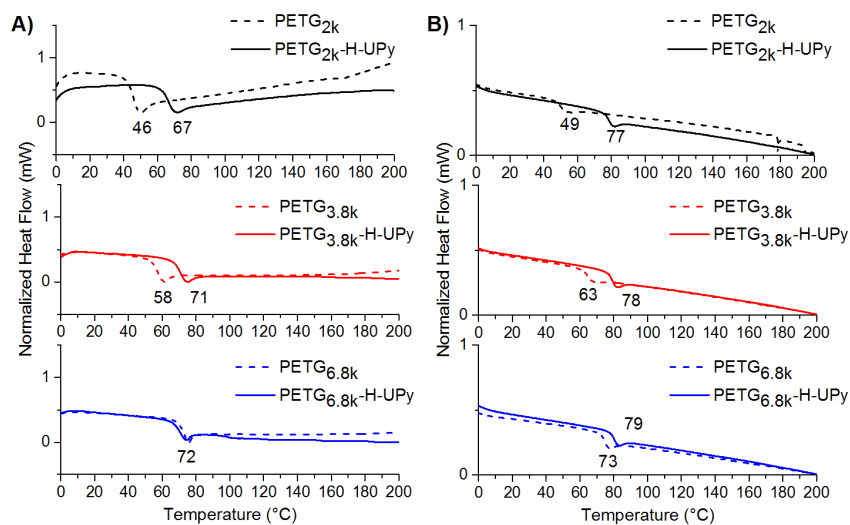


Figure 4.1 DSC spectra (second heating cycle, 10 °C min⁻¹) of PETG and PETG functionalized with H-UPy A) directly after synthesis, and B) after melt processing.

Polymer processing can have a significant impact on properties. Furthermore, the importance of thermal annealing in UPy functionalized systems is well documented.^{15,16,28} The

polymers were melt-pressed into 8 mm diameter circular discs for rheological experiments, and thermal properties were analyzed by DSC after melt processing. Figure 4.1B depicts the DSC spectra of the samples after melt processing. The UPy functionalized polymers revealed more dramatic increases in T_g as compared with the unfunctionalized polymers of the same molecular weight, suggesting that melt processing enhanced UPy aggregation. Importantly, the T_g (by DSC) of high molecular weight, commercial- grade PETG is approximately 80 °C, very close to the T_g of each of the melt processed UPy functionalized polymers. Regardless of base molecular weight, UPy aggregation increased the “operative” molecular weight of the polymers to well above the CME.

Because the increase in T_g of the unfunctionalized materials was not significant, transesterification was not suspected. GPC was performed on the UPy functionalized polymers after processing to ensure T_g increases were due to annealing alone (Figure 4.2). ATR FT-IR as well as ^1H NMR were also used to analyze the polymers before and after processing (Figures C19-C27, Appendix C). This not only eliminated concerns of transesterification but also crosslinking of the urea or urethane linkages into biuret or allophanate units.²⁹

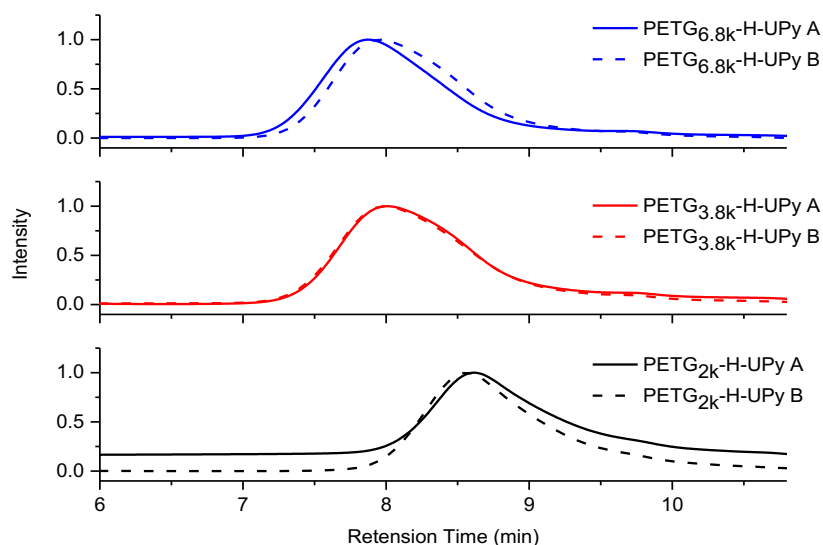


Figure 4.2 GPC traces A) of the raw powder run directly after synthesis, and B) of the melt-pressed materials (CHCl_3 at $25\text{ }^\circ\text{C}$ and 1.0 mL min^{-1} using polystyrene standards).

Dynamic oscillatory shear measurements were performed on the melt-pressed discs over cooling and heating cycles (Figure 4.3). As observed in the DSC spectra, the glass transition temperatures, signified by the peak of the tan delta, of the H-UPy functionalized polymers were much higher than the unfunctionalized PETG, and the increase was most significant when comparing the polymers of 2000 g mol^{-1} . When the peaks of the tan delta were plotted against the inverse of the molecular weight (Figure 4.4), the unfunctionalized polymers corresponded with Fox-Flory theory.³⁰ However, the H-UPy functionalized polymers were not consistent with Fox-Flory theory based on their inherent molecular weights. These polymers all possess “operative” molecular weights well above the CME, which are presumably induced from the supramolecular, noncovalent bonding of the UPy endgroups. Although the effect of UPy functionalization on T_g decreases with increasing molecular weight, the properties are enhanced to levels comparable with the commercial material (Appendix D, Figure D1).

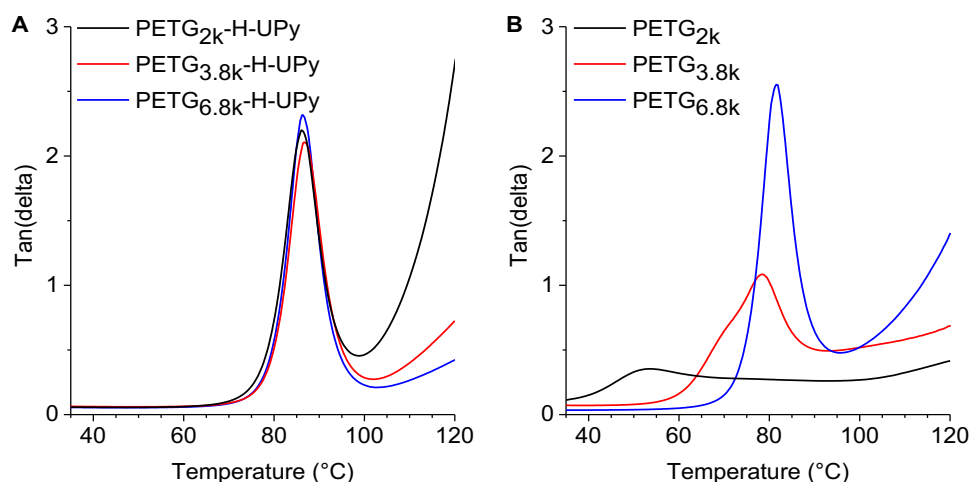


Figure 4.3 Dynamic oscillatory shear measurements of the tan delta as the material goes through cooling and heating cycles, where the peak signifies the Tg of A) H-UPy functionalized materials and B) unfunctionalized PETG (1 Hz, 0.1% strain, parallel plate fixture with plate diameter of 8 mm and gap length of 1000 μm).

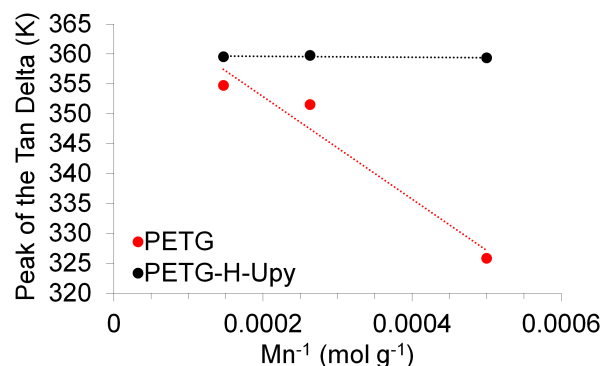


Figure 4.4 The peak of the tan delta plotted against inverse molecular weight (lines added to clearly present trends).

4.3.2.b Relationship Between Physical, Mechanical, and Surface Properties

The physical appearance of PETG_{2k} and PETG_{2k}-H-UPy (Figure 4.5) denotes the differences observed in the mechanical properties (Figure 4.6). PETG_{2k} is a brittle, opaque solid; however, PETG_{2k}-H-UPy is clear and flexible. PETG_{2k} displayed features of a highly crystalline polymer, with a limited glassy plateau and no crossover between G' and G'' in the glass

transition region. PETG_{2k}-H-UPy showed dramatic improvements in mechanical properties, and displayed the overall features of an amorphous plastic. AFM further confirmed the difference between the crystalline and amorphous character of the polymer before and after H-UPy functionalization. Prior to end-functionalization, PETG_{2k} had a surface roughness of 73.4 ± 8.1 nm, while PETG_{2k}-H-UPy had a pristine, smooth surface of 1.2 ± 0.3 nm (Figure 4.7). Furthermore, Figure 4.6 shows the onset of terminal flow at 110 °C for PETG_{2k}-H-UPy, suggesting that UPy-UPy bonds have dissociated and any remaining small crystallites have melted by 150 °C.



Figure 4.5 Photograph comparing PETG_{2k} (left) to PETG_{2k}-H-UPy (right).

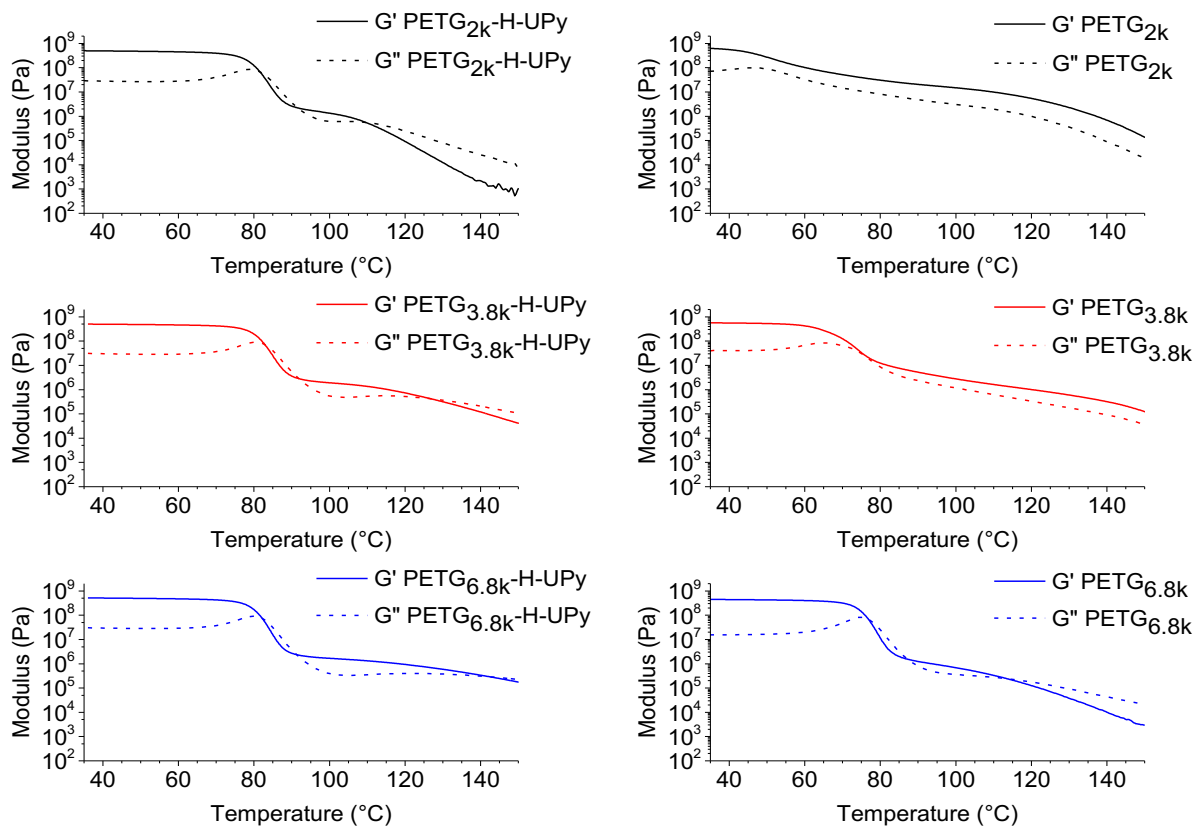


Figure 4.6 Dynamic oscillatory shear measurements depicting the G' and G'' of the materials through cooling and heating cycles (1 Hz, 0.1% strain, parallel plate fixture with plate diameter of 8 mm and gap length of 1000 μm).

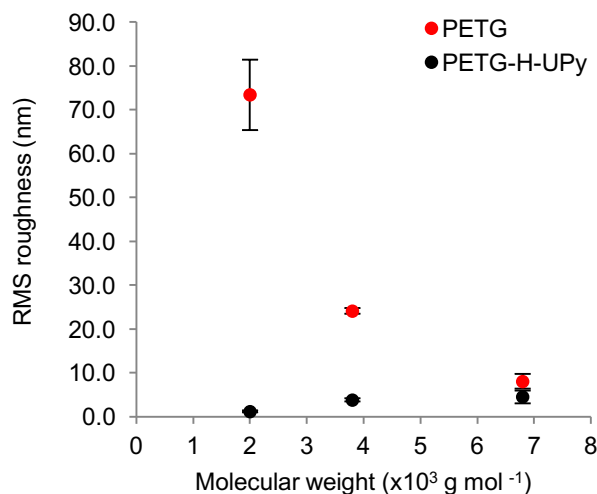


Figure 4.7 RMS surface roughness of PETG before and after H-UPy functionalization. RMS surface roughness obtained from AFM images ($20 \times 20 \mu\text{m}$) using Nanoscope 6.14R1 software.

Dynamic rheology and AFM showed similar, though less pronounced, trends when looking at materials of 3800 and 6800 g mol^{-1} (Figures 4.6 and 4.7, respectively). Because these polymers are of higher molecular weight, they have fewer endgroups and therefore, a lower concentration of UPy groups within the system. Furthermore, because these materials are near the CME, the properties of the unfunctionalized polymers are improved as compared with PETG_{2k}. However, regardless of inherent molecular weight, the elastic moduli of the H-UPy functionalized materials were improved over the moduli of the virgin polymers. The H-UPy functionalized polymers maintained a high elastic modulus over a broad temperature range, comparable to commercial-grade PETG (Appendix D, Figure D2). Interestingly, an extended plateau was observed before reaching the terminal flow regime when looking at PETG_{6.8k}-H-UPy. This behavior is believed to be due to the increased inherent molecular weight of the polymer, causing slower reptation and stress-relaxation.

After H-UPy functionalization of PETG_{3.8k}, which had an RMS surface roughness of $24.2 \pm 0.7 \text{ nm}$, PETG_{3.8k}-H-UPy resulted in a smooth surface with RMS surface roughness of 3.9 ± 0.4

nm. Materials of 6800 g mol^{-1} showed no significant differences in surface roughness because the unfunctionalized material is above the CME.³¹ Furthermore, the surface roughness of the H-UPy functionalized materials were all comparable to that of commercial PETG (Figure D3, Appendix D). Other surface properties, such as static water-in-air contact angle, did not show any significant difference when comparing the functionalized and unfunctionalized materials, suggesting that the UPy endgroups do not aggregate at the surface of the polymer film (Figure C29, Appendix C).

4.3.2.c Viscosity in the Melt

Figure 4.8 displays the effect of the H-UPy endgroup and molecular weight on melt viscosity. The melt viscosity of PETG_{2k}-H-UPy was 34 times higher than that of PETG_{2k} at 87 °C. At 100 °C, the viscosity of PETG_{2k}-H-UPy dramatically decreased, and the viscosity matched the viscosity of PETG_{2k} by 110 °C, confirming dissociation of UPy-UPy aggregates. Furthermore, the viscosity of PETG_{2k}-H-UPy and PETG_{3.8k}-H-UPy was much lower than the viscosity of commercial PETG (Figure 4.9 and Figure D4, Appendix D). At 150 °C, the viscosity of PETG_{2k}-H-UPy (1620 Pa.s) was 56 times lower than commercial PETG (91,200 Pa.s), and PETG_{3.8k}-H-UPy (13,100 Pa.s) was 7 times lower. This is significant, as these materials serve as the first example of engineering polymers with improved thermal and mechanical properties, as well as improved flow characteristics at pertinent temperatures, well below the onset of UPy degradation. Thus, the reduced thermal stability of the UPy endgroup by TGA (Table 4.1 and Table 4.2) does not affect the thermal stability of the final product at temperatures of use or processing.

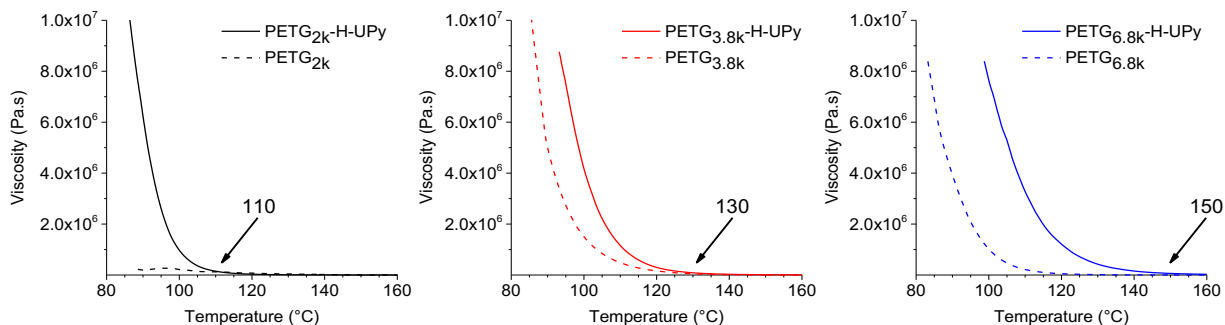


Figure 4.8 Effect of H-UPy endgroup structure and molecular weight on melt viscosity. Rheological characterization of PETG and PETG-H-UPy at 2000, 3800, and 6800 g mol⁻¹ (shear rate 0.05 s⁻¹, parallel plate fixture with plate diameter of 8 mm and gap length of 1000 μm).

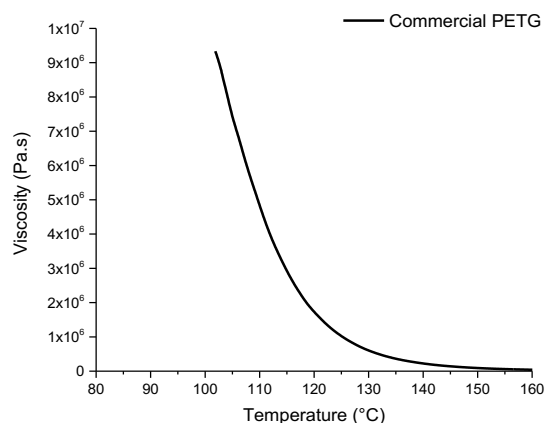


Figure 4.9 Rheological characterization of commercial PETG (shear rate 0.05 s⁻¹, parallel plate fixture with plate diameter of 8 mm and gap length of 1000 μm).

The viscosity of PETG_{3.8k} and PETG_{6.8k} is approximately 25 times greater than the viscosity of PETG_{2k} at 87 °C. Consequently, the viscosity of the H-UPy functionalized materials of higher molecular weight meet the viscosity of the corresponding virgin polymer at a higher temperature than observed in the materials of 2000 g mol⁻¹. This data correlates with the extended rubbery plateau regions observed in Figure 4.6. To confirm that this is due to the slow reptation of the higher molecular weight polymers in the bulk, melt state and not necessarily due to an increase in the UPy-UPy dissociation temperature, variable temperature ¹H NMR (VT-

NMR) was performed on PETG_{6.8k}-H-UPy from 25-100 °C (Figure 4.10). The strength of intermolecular quadruple hydrogen bonding decreased by 65 °C, which was observed through weakened signals at 11.3 and 13.1 ppm. Dissociation occurred circa 80 °C, with complete dissociation occurring by 100 °C as the signals disappeared. The weakening and disappearance of the signals at 11.3 and 13.1 ppm changed at similar temperatures when looking at the VT-NMR spectra of PETG_{2k}-H-UPy, further confirming that the extended rubbery plateau is due to interactions in the bulk, melt state of the higher molecular weight polymer (Figure C30, Appendix C).

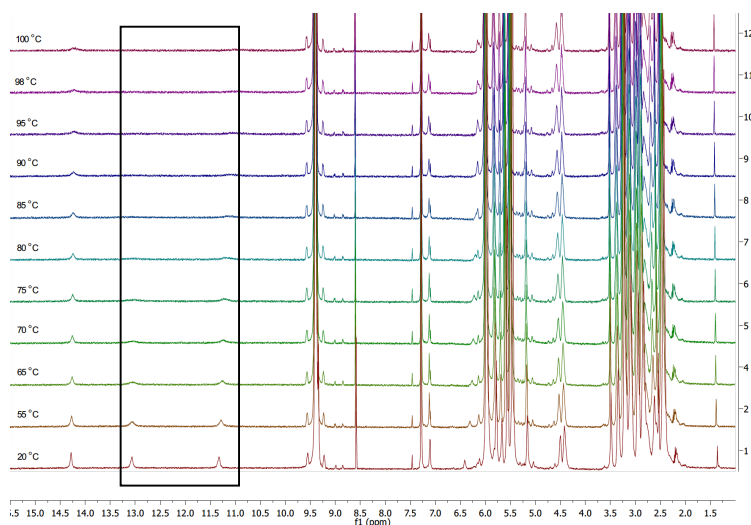


Figure 4.10 Variable temperature ¹H NMR spectra of PETG_{6.8k}-H-UPy in TCE-d₂ (c = 5 mM, 600 s equilibrium allowed at each temperature). The box outlines peaks that signify the presence of intermolecular H-bonding of UPy endgroups.

The viscosity of the materials was observed over several frequencies (1-600 s⁻¹) at temperatures just above the UPy-UPy dissociation temperature, 90 and 120 °C (Table 4.3 and Figures C31-C34 in Appendix C). At these temperatures, the H-UPy functionalized materials experience a dramatic decrease in viscosity, where the difference in viscosity ($\Delta\eta^*$) was

calculated by $(\eta^*_{90\text{ }^\circ\text{C}})/(\eta^*_{120\text{ }^\circ\text{C}})$ at 600 s^{-1} . The materials begin at viscosities that are much higher than the corresponding unfunctionalized precursors, thus the large decrease in viscosity of the H-UPy functionalized materials suggests the dissociation of UPy-UPy aggregates. UPy dissociation is also presumed because the temperature range observed in the experiment was near the dissociation temperature of UPy-UPy aggregates, as reported in previous literature and seen in the VT-NMR experiments in Figure 4.10 and Figure C30 of Appendix C.¹⁹ At $120\text{ }^\circ\text{C}$, the viscosity of the UPy functionalized materials is approximately the same as the viscosity of the unfunctionalized polymers of the same molecular weight (i.e., materials of $3,800\text{ g mol}^{-1}$ and $6,800\text{ g mol}^{-1}$). Surprisingly, the viscosity of PETG_{2k}-H-UPy was much lower than the viscosity of PETG_{2k} at $120\text{ }^\circ\text{C}$. It is suspected, based on the crystalline character of the PETG_{2k} observed in Figures 4.5 and 4.6, that the viscosity of PETG_{2k} remained higher at $120\text{ }^\circ\text{C}$ due to lingering crystallites.

The drop in viscosity of the H-UPy functionalized polymers, however, is similar to the drop in viscosity observed in the commercial material (Table 4.3). Therefore, it is unclear if this drop is due solely to UPy-UPy dissociation or due to the fact that these polymers take on the more amorphous properties of the high molecular weight material. A combination of both rationales is likely, as it is clear that $\Delta\eta^*$ increases in unfunctionalized PETG with increasing molecular weight (i.e., as the polymers approach the CME).

Table 4.3 Viscosity Change from 90 °C to 120 °C at 600 s⁻¹.

Polymer	$\eta^*_{90\text{ }^\circ\text{C}}$	$\eta^*_{120\text{ }^\circ\text{C}}$	$\Delta\eta^*$ (Pa.s)
PETG _{2k}	79,500	20,400	4
PETG _{2k} -H-UPy	163,700	3,000	54
PETG _{3.8k}	45,100	4,000	12
PETG _{3.8k} -H-UPy	172,300	4,000	48
PETG _{6.8k}	56,200	2,800	20
PETG _{3.8k} -H-UPy	199,800	4,000	51
Commercial PETG	217,300	4,000	55

4.3.2.d Tensile Testing

Finally, tensile testing was performed to measure the elongation at break and overall toughness of the engineering plastics. As shown in Figure 4.5 and Figure 4.6, PETG_{2k} had nearly no mechanical integrity and broke almost immediately upon stretching (Figure 4.11). Figure 4.11B more clearly shows the lack of mechanical integrity of PETG_{2k}, since the sample broke almost immediately upon elongation, making it difficult to identify in Figure 4.11A. PETG_{2k}-H-UPy showed dramatic improvements in tensile properties. The strain at break of PETG_{2k}-H-UPy was comparable to PETG_{6.8k} when looking at the average of five samples (Figure 4.11B). In addition to the elongation at break, the tensile strength of PETG_{2k}-H-UPy (48 ±14 MPa at yield) was approximately two times greater than the tensile strength of PETG_{2k} (26 ±8 MPa at yield) and comparable to PETG_{6.8k} (39 ±6 MPa at yield). Thus, PETG_{2k}-H-UPy performed comparably to a polymer at least three times its own base molecular weight (Figure D5, Appendix D). Significant improvements were also seen in the elongation at break of PETG_{3.8k}-H-UPy as compared to PETG_{3.8k}. The improvements observed in the tensile properties of PETG_{2k}-H-UPy and PETG_{3.8k}-H-UPy, along with the viscoelastic improvements observed in Figure 4.8, show that these polymers not only have improved processing capabilities but also have fundamental mechanical robustness.

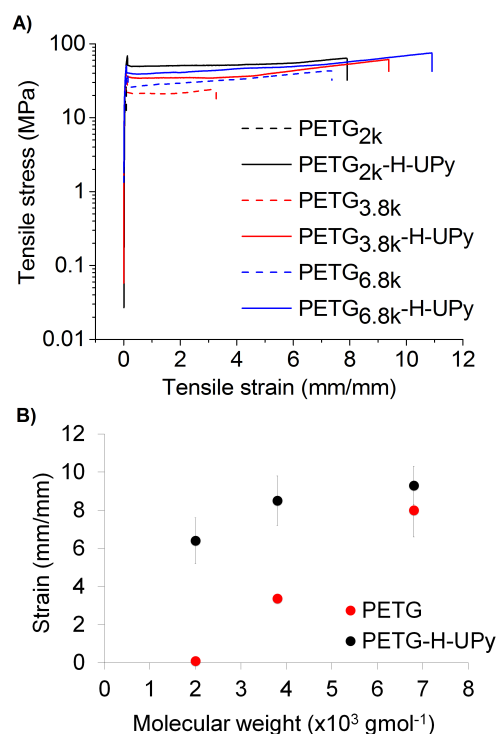


Figure 4.11 A) Stress–strain curves of PETG and PETG-H-UPy of 2000, 3800, and 6800 g mol⁻¹ at 10 mm min⁻¹, and B) average strain at break of the materials over five samples.

4.4 Conclusions

Two synthetic strategies were utilized to end-functionalize engineering polymers with the UPy endgroup, thus delineating the adaptability of supramolecular functionalization of a robust polymer system. The synthetic method was dependent on the rigidity of the linker connecting the UPy moiety to the polymer terminus, varying from linear to bicyclic. An increase in T_g was observed regardless of endgroup structure.

Endgroup functionalization of PETG of different molecular weights was also explored utilizing polymers well below and near the CME. Property changes were most substantial in polymers of the lowest molecular weight (2000 g mol⁻¹). Materials of higher molecular weights (3800 and 6800 g mol⁻¹) showed less pronounced changes in thermal, mechanical, and viscoelastic properties. Notably, however, the higher molecular weight materials properties were

enhanced to levels of performance similar to commercial PETG (comparison of these materials to the commercial polymer can be found in Appendix D, Figures D1-D5).

The enhancement of materials properties of PETG_{2k}-H-UPy were remarkable. The thermal properties of PETG_{2k}-H-UPy were comparable to high molecular weight, commercial-grade PETG, displaying a 28 °C increase in T_g over PETG_{2k} after melt-processing. The tensile performance was comparable to materials greater than three times the base molecular weight of 2000 g mol⁻¹. Furthermore, the melt-viscosity of PETG_{2k}-H-UPy dropped to match the low viscosity of PETG_{2k} at 110 °C. Due to the unique thermal properties of PETG and the utilization of elegant supramolecular chemistry, an engineering polymer was designed to exhibit robust mechanical properties at room temperature and a high T_g , thus an adequate theoretical “use temperature range”. Additionally, this material exhibited a low melt viscosity at a suitable temperature for safe, non-degradative processing. While future endeavors may explore even lower molecular weight prepolymers and other uniquely adequate, high-performing polymer systems, this study gives a practical example of a supramolecularly improved industrially relevant polymer.

REFERENCES

- (1) Lehn, J. M. *Polym. Int.* **2002**, *51* (10), 825.
- (2) Brunsveld, L.; Folmer, B. J. B.; Meijer, E. W.; Sijbesma, R. P. *Chem. Rev.* **2001**, *101*, 4071.
- (3) de Greef, T. F. A.; Meijer, E. W. *Nature* **2008**, *453* (7192), 171.
- (4) Bertrand, A.; Lortie, F.; Bernard, J. *Macromol. Rapid Commun.* **2012**, *33*, 2062.
- (5) Sijbesma, R. P.; Beijer, F. H.; Brunsveld, L.; Folmer, B. J. B.; Hirschberg, J. H. K. K.; Lange, R. F. M.; Lower, J. K. L.; Meijer, E. W. *Science* **1997**, *278*, 1601.
- (6) Keizer, H. M.; van Kessel, R.; Sijbesma, R. P.; Meijer, E. W. *Polymer*. **2003**, *44*, 5505.
- (7) Folmer, B. J. B.; Sijbesma, R. P.; Versteegen, R. M.; van der Rijt, J. a. J.; Meijer, E. W. *Adv. Mater.* **2000**, *12*, 874.
- (8) Kautz, Holger, van Beek, D. J. M., Sijbesma, Rint P., Meijer, E. W. *Macromolecules* **2006**, *39*, 4265.
- (9) Keizer, H. M.; Sijbesma, R. P.; Jansen, J. F. G. A.; Pasternack, G.; Meijer, E. W. *Macromolecules* **2003**, *36*, 5602.
- (10) Botterhuis, N. E.; van Beek, D. J. M.; Gemert, G. M. L.; Bosman, A. W.; Sijbesma, R. P. *J. Polym. Sci. Part A Polym. Chem.* **2008**, *46*, 3877.
- (11) Shokrollahi, P.; Mirzadeh, H.; Huck, W. T. S.; Scherman, O. A. *Polymer*. **2010**, *51*, 6303.
- (12) Van Beek, D. J. M.; Spiering, A. J. H.; Peters, G. W. M.; Te Nijenhuis, K.; Sijbesma, R. P. *Macromolecules* **2007**, *40* (23), 8464.
- (13) van Beek, D. J. M.; Gillissen, M. A. J.; Van As, B. A. C.; Palmans, A. R. A.; Sijbesma, R. P. *Macromolecules* **2007**, *40*, 6340.
- (14) Dankers, P. Y. W.; Zhang, Z.; Wisse, E.; Grijpma, D. W.; Sijbesma, R. P.; Feijen, J.; Meijer, E. W. *Macromolecules* **2006**, *39*, 8763.
- (15) Appel, W. P. J.; Portale, G.; Wisse, E.; Dankers, P. Y. W.; Meijer, E. W. *Macromolecules* **2011**, *44*, 6776.
- (16) Agnaou, R.; Capelot, M.; Tencé-Girault, S.; Tournilhac, F.; Leibler, L. *J. Am. Chem. Soc.* **2014**, *136*, 11268.
- (17) Biyani, M. V; Foster, E. J.; Weder, C. *ACS Macro Lett.* **2013**, *2*, 236.
- (18) Dankers, P. Y. W.; Harmsen, M. C.; Brouwer, L. A.; van Luyn, M. J. A.; Meijer, E. W. *Nat. Mater.* **2005**, *4*, 568.

- (19) Yamauchi, K.; Kanomata, A.; Inoue, T.; Long, T. E. *Macromolecules* **2004**, *37* (10), 3519.
- (20) Deans, R.; Ilhan, F.; Rotello, V. M. *Macromolecules* **1999**, *32*, 4956.
- (21) Ilhan, F.; Galow, T. H.; Gray, M.; Clavier, G.; Rotello, V. M. *J. Am. Chem. Soc.* **2000**, *122*, 5895.
- (22) Yamauchi, K.; Lizotte, J. R.; Hercules, D. M.; Vergne, M. J.; Long, T. E. *J. Am. Chem. Soc.* **2002**, *124*, 8599.
- (23) Scheirs, J.; Long, T. E. *Modern Polyesters: Chemistry and Technology of Polyesters and Copolyesters*; John Wiley & Sons, Ltd.: West Sussex, 2003.
- (24) Kemmish, D. J. *Practical Guide to High Performance Engineering Plastics*; iSmithers Rapra Publishing: Shropshire, 2011.
- (25) Turner, S. R. *J. Polym. Sci. Part A Polym. Chem.* **2004**, *42*, 5847.
- (26) Seymour, R. B.; Kirshenbaum, G. S. *High Performance Polymers: Their Origin and Development*; Elsevier Science Publishing Co., Inc.: New York, 1986.
- (27) Armstrong, G.; Buggy, M. *Mater. Sci. Eng. C* **2001**, *18*, 45.
- (28) Chirle, M.; Hoffmann, I.; Peiper, T.; Kilian, H.-G.; Stadler, R. *Polym. Bull.* **1996**, *36*, 95.
- (29) Delebecq, E.; Pascault, J. P.; Boutevin, B.; Ganachaud, F. *Chem. Rev.* **2013**, *113*, 80.
- (30) Fox, T. G.; Flory, P. J. *J. Appl. Phys.* **1950**, *21*, 581.
- (31) Bu, H.; Gu, F.; Bao, L.; Chen, M. *Macromolecules* **1998**, *31*, 12582.

APPENDIX A: SUPPLEMENTARY INFORMATION FOR CHAPTER 2
IODINATED HOMOPOLYMERS AS A VERSATILE PLATFORM FOR RADIOPAQUE
BIOMATERIALS AND NANOPARTICLES

Table A1. EDS Results from 2,2-Bis(iodomethyl)-1,3-propanediol.

Element	Wt%
C	16.97
H	2.83
I	70.75
O	9.04
N	0.00

Table A2. XPS Results from 2,2-Bis(iodomethyl)-1,3-propanediol.

Element	Atomic Mass	Atomic Concentration (%)	Mass Concentration (%)
C	12.011	66.71	27.15
I	126.904	14.58	62.71
O	15.999	18.70	10.14
Br	79.904	0.00	0.00

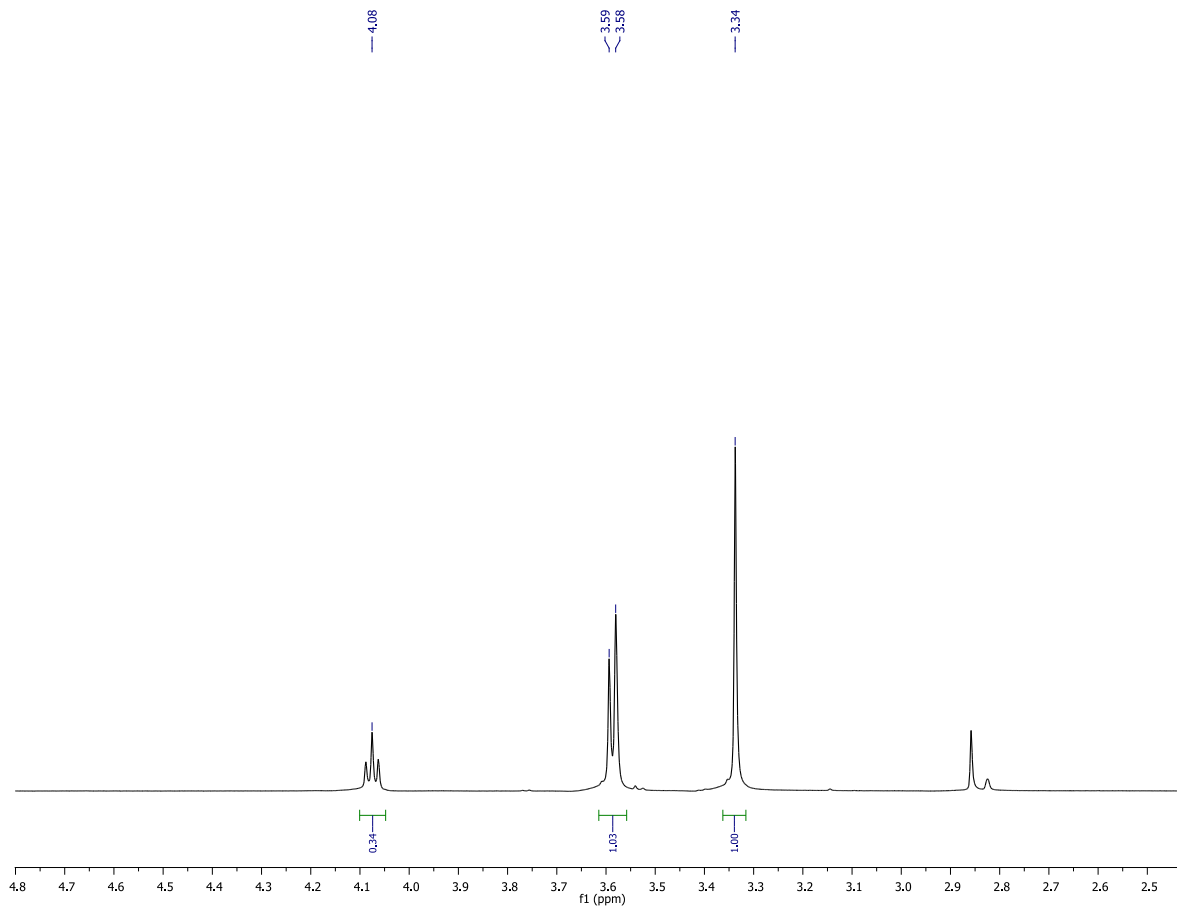


Figure A1. ^1H NMR of 2,2-bis(iodomethyl)-1,3-propanediol (HDO, H_2O residual peaks).

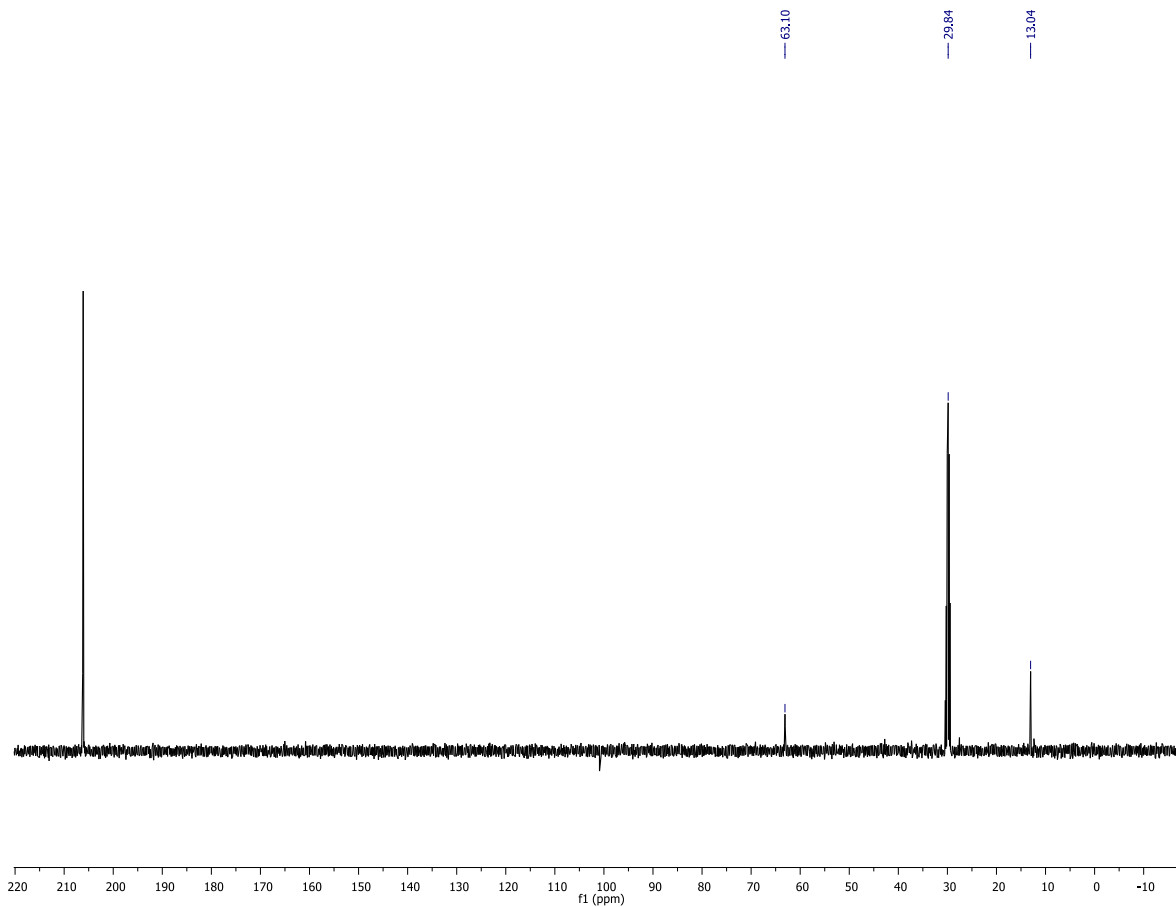


Figure A2. ^{13}C NMR of 2,2-bis(iodomethyl)-1,3-propanediol.

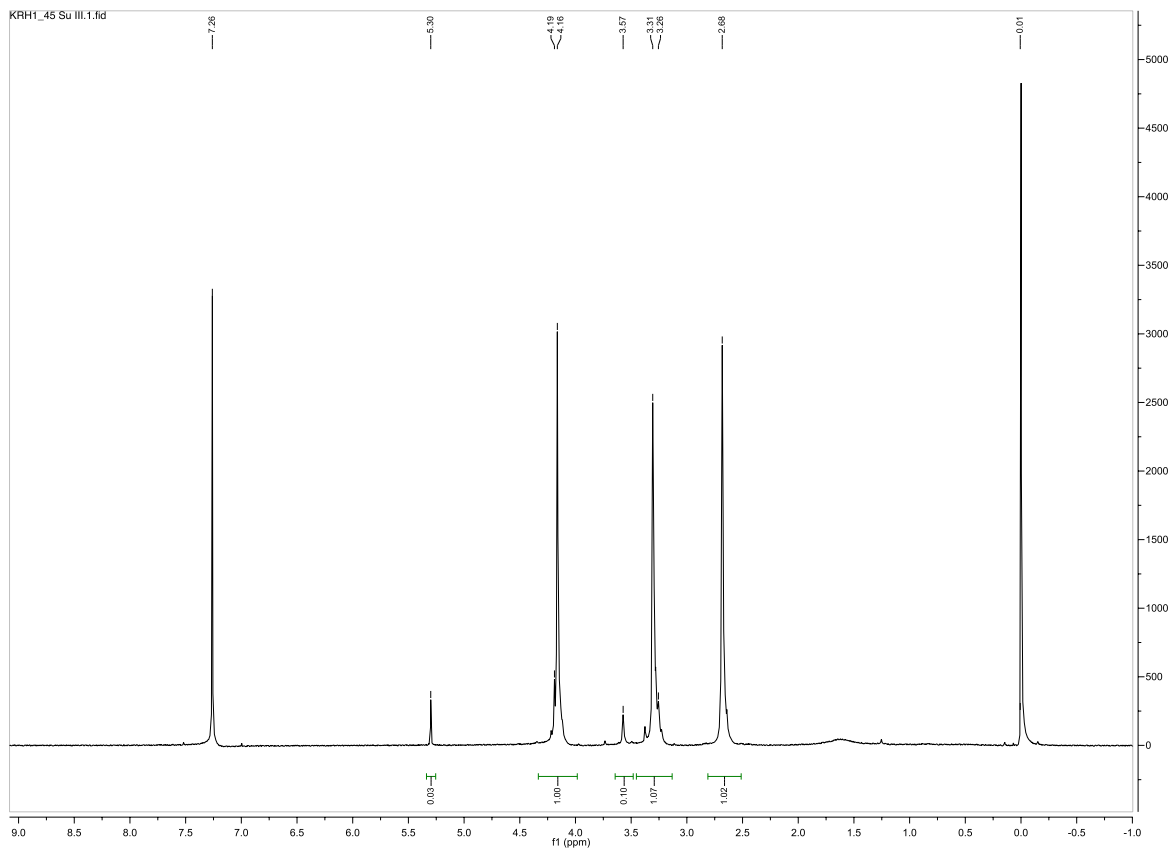


Figure A3. ^1H NMR of the succinic acid based prepolymer.

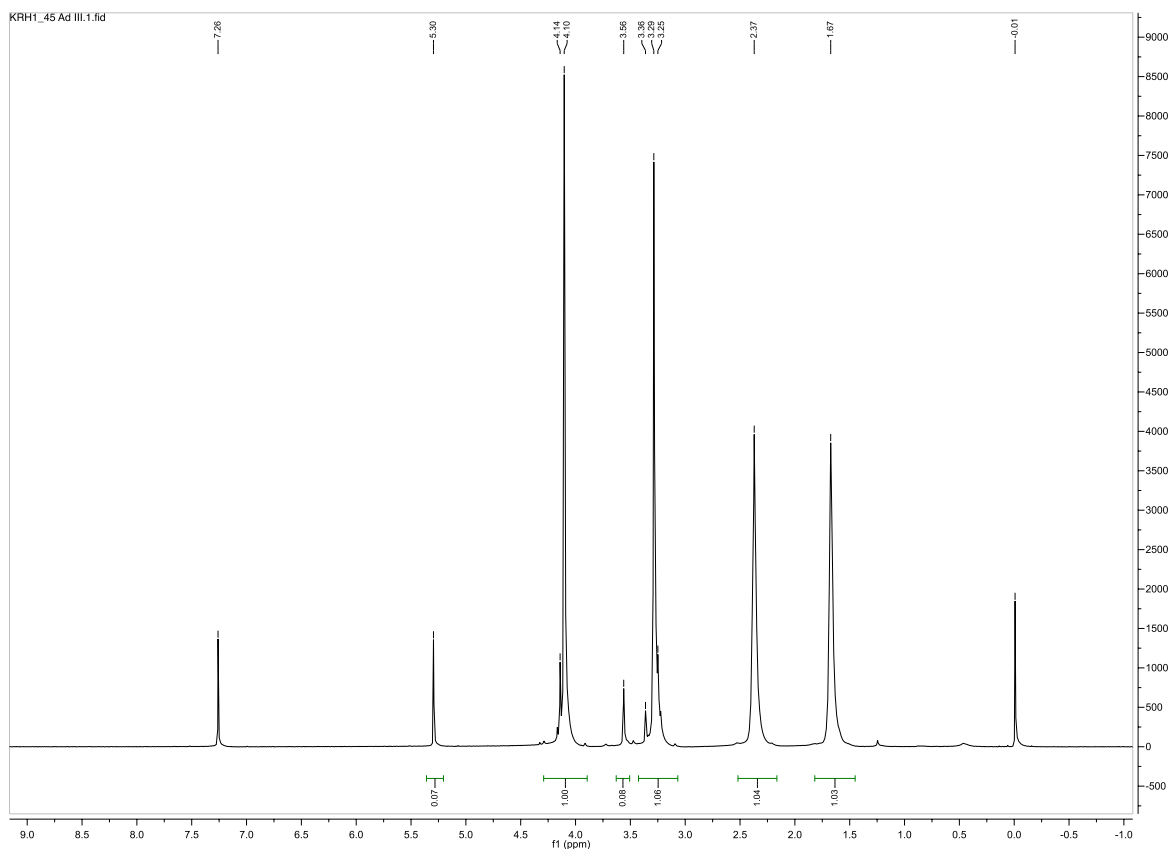


Figure A4. ^1H NMR of the adipic acid based prepolymer.

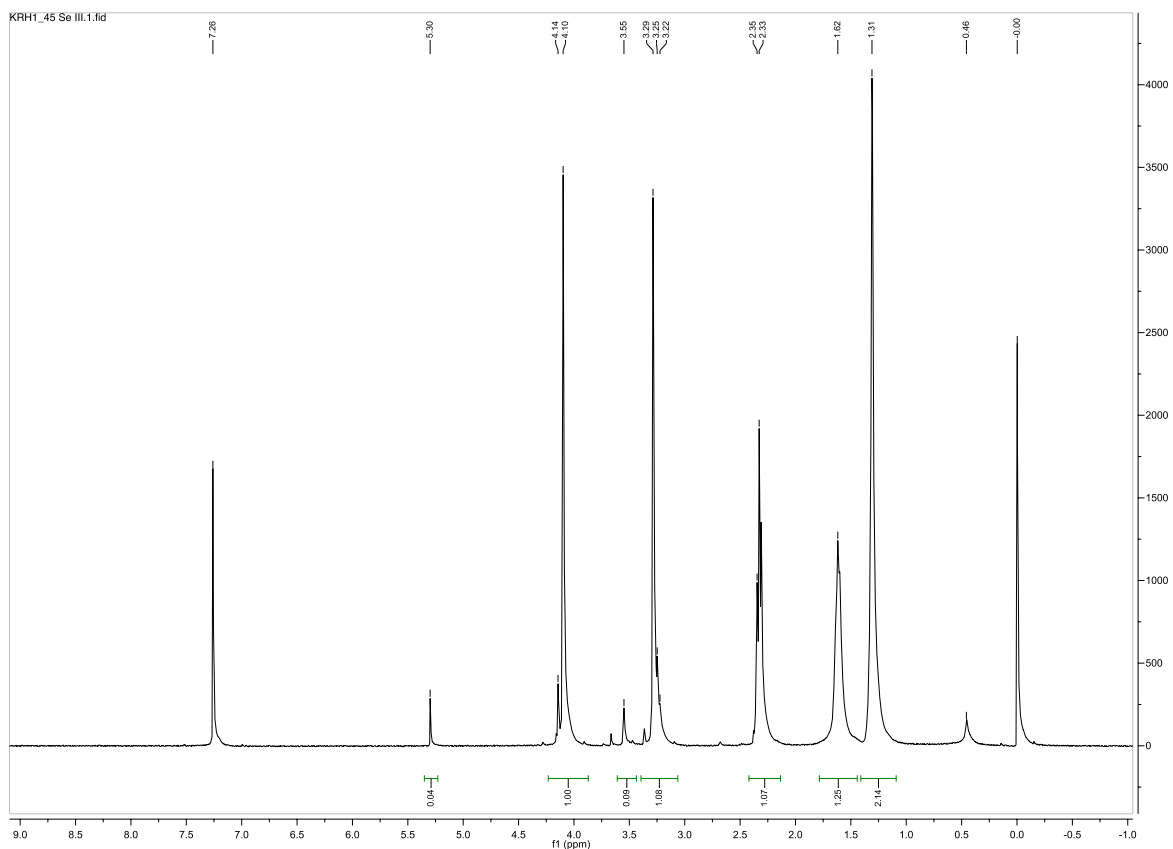


Figure A5. ^1H NMR of the sebacic acid based prepolymer.

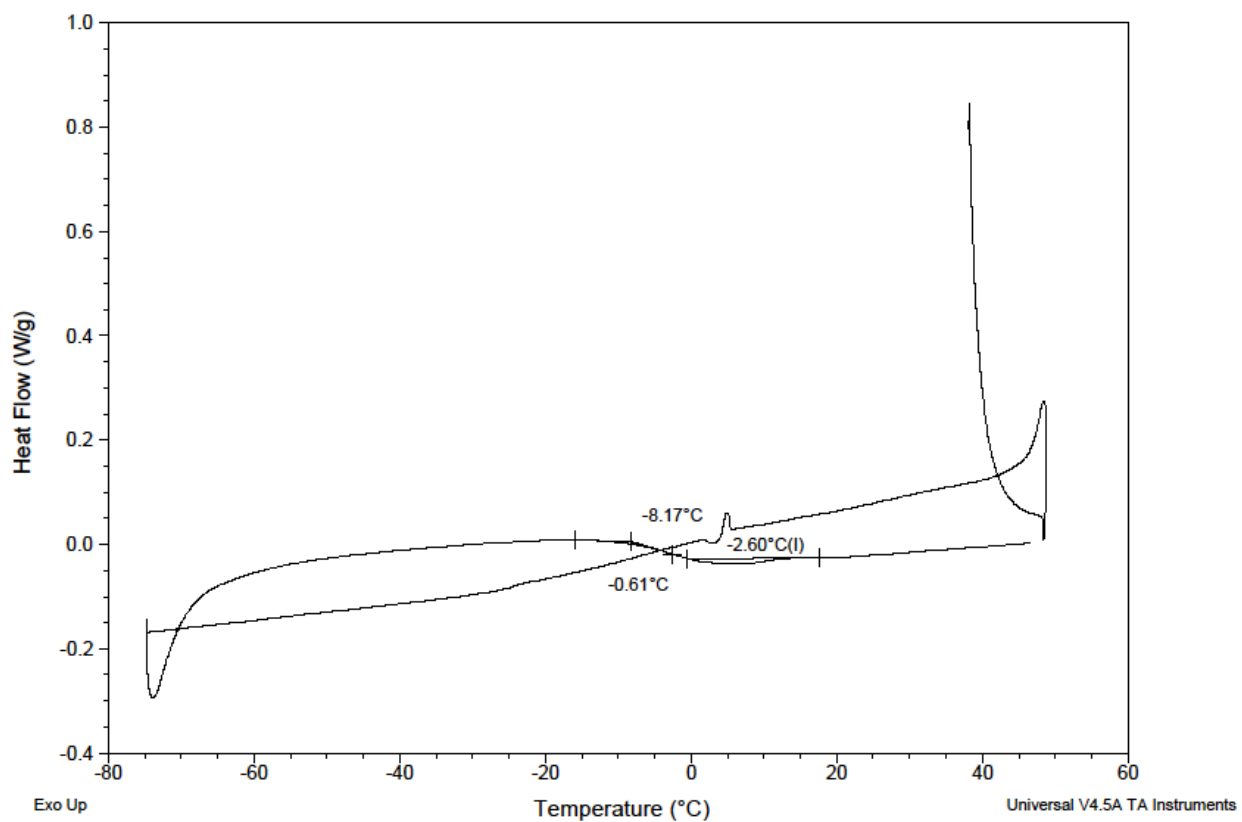


Figure A6. DSC of the succinic acid based prepolymer.

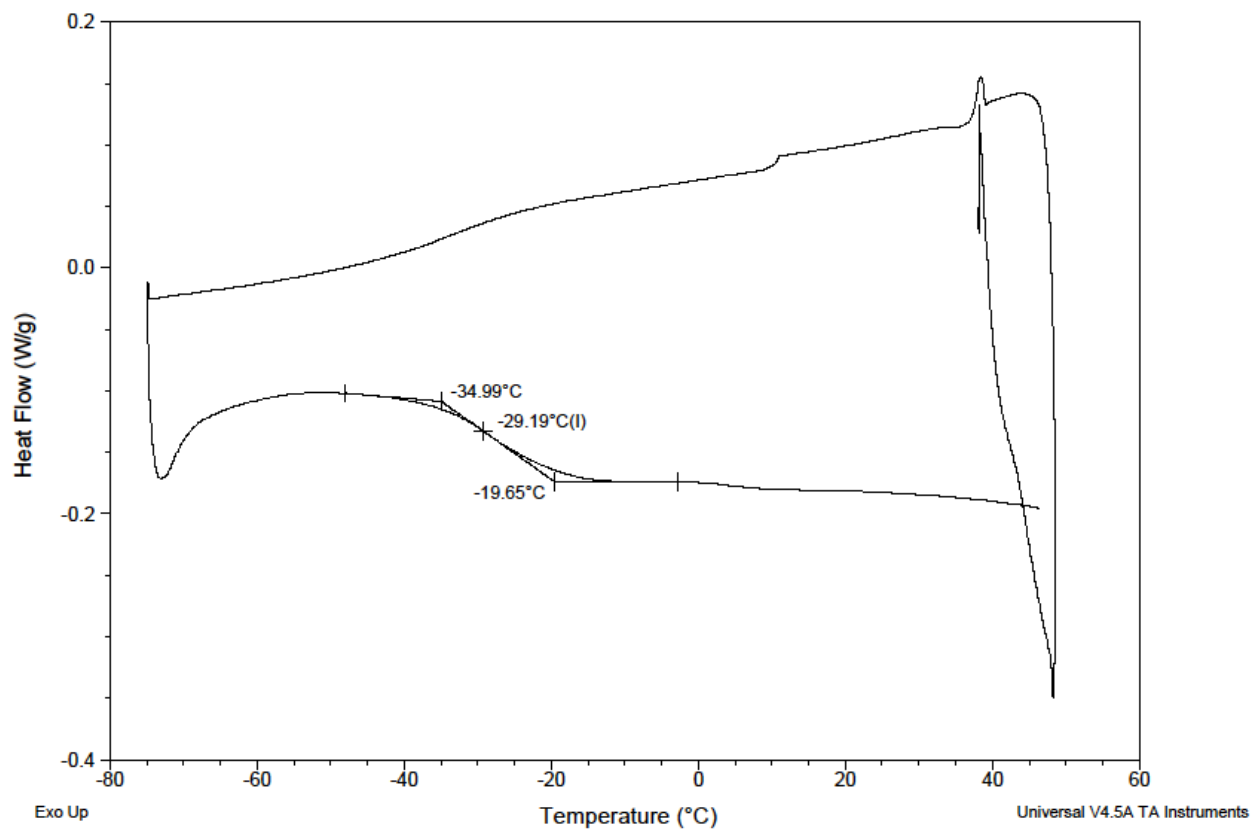


Figure A7. DSC of the adipic acid based prepolymer.

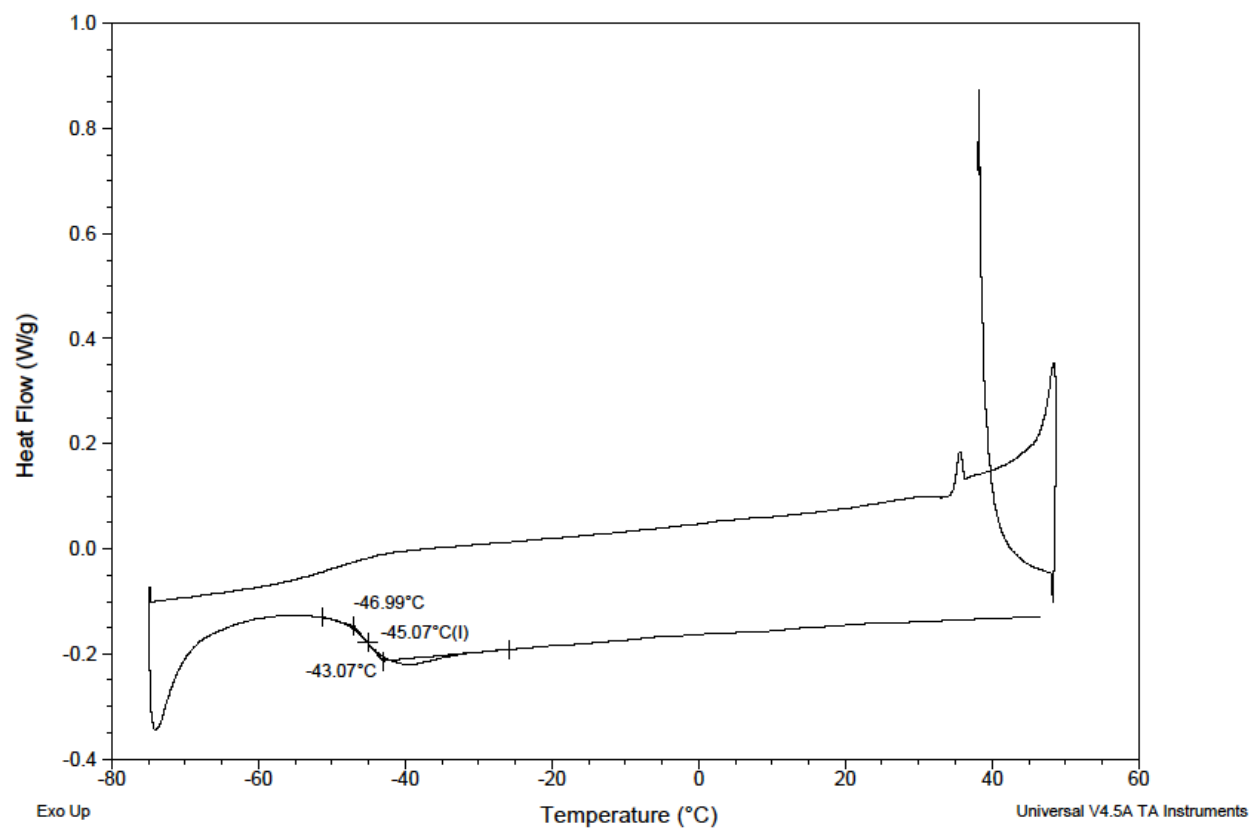


Figure A8. DSC of the sebacic acid based prepolymer.

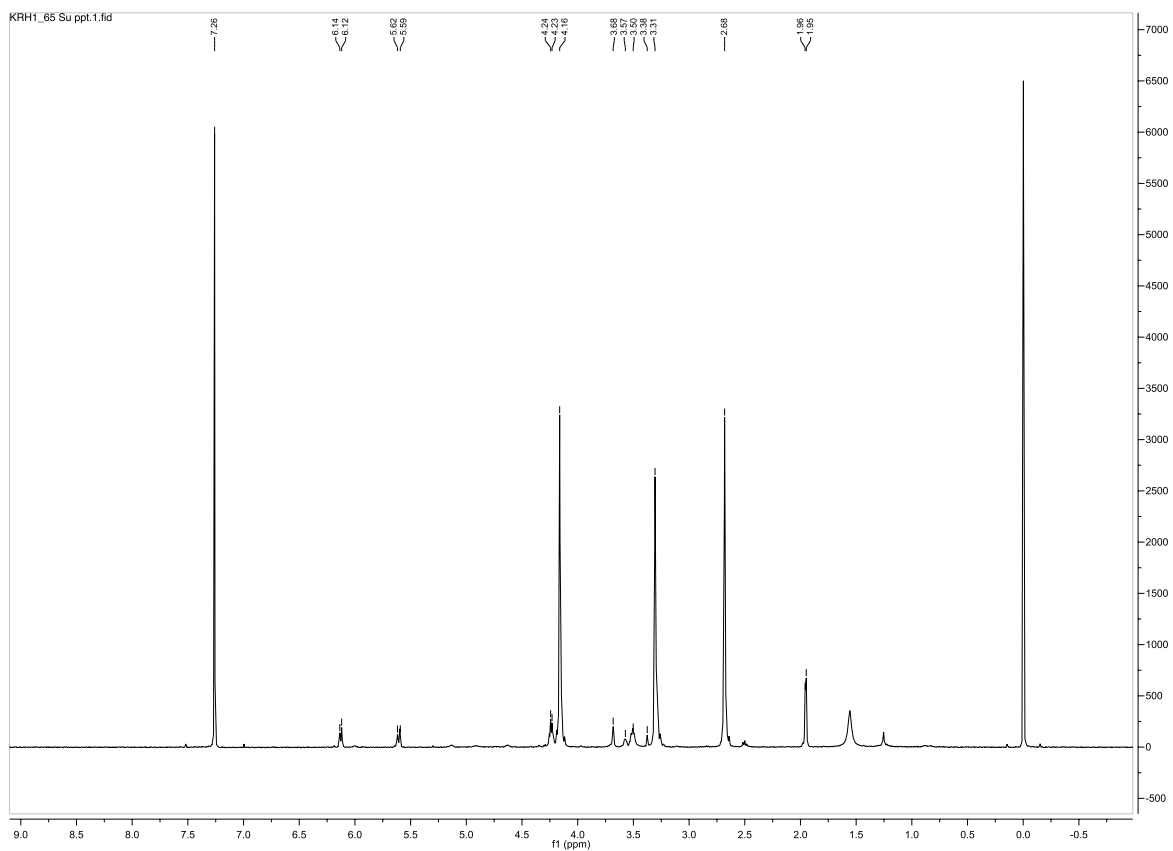


Figure A9. ¹H NMR of the methacrylate endcapped succinic acid based prepolymer.

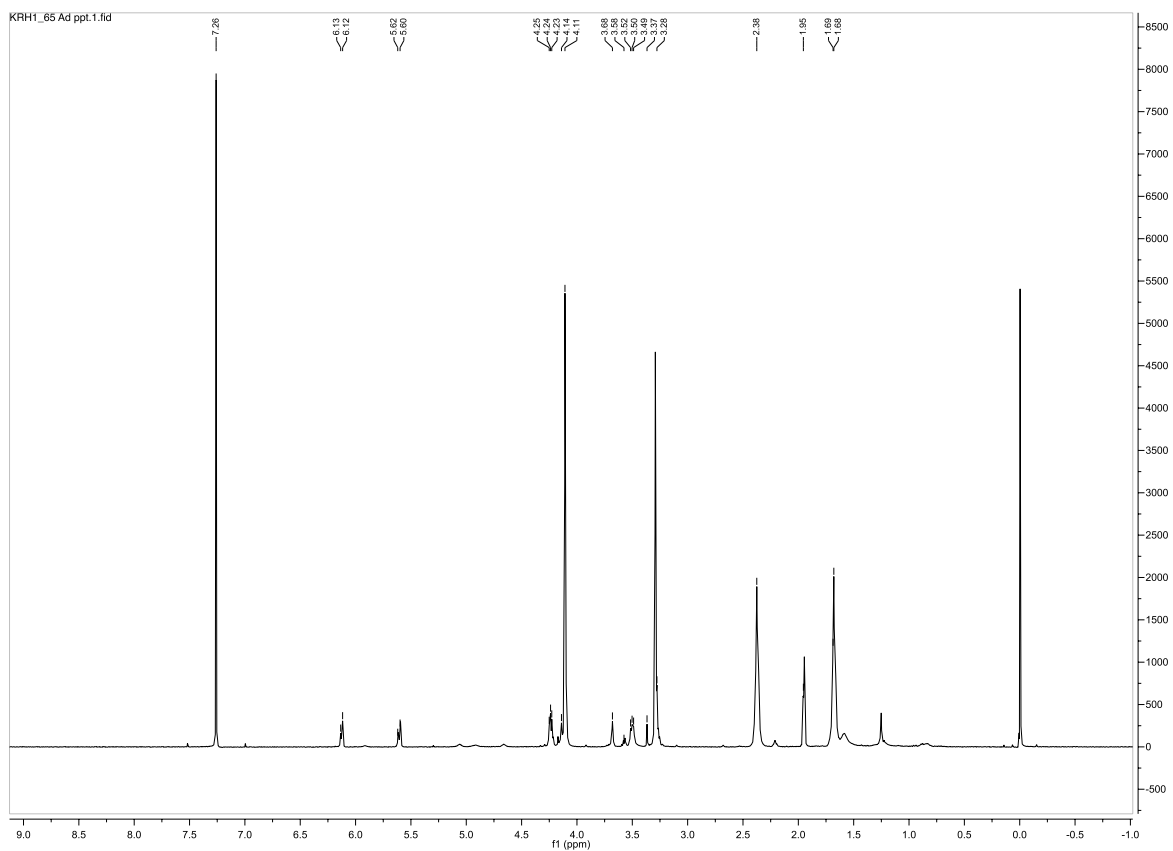


Figure A10. ¹H NMR of the methacrylate endcapped adipic acid based prepolymer.

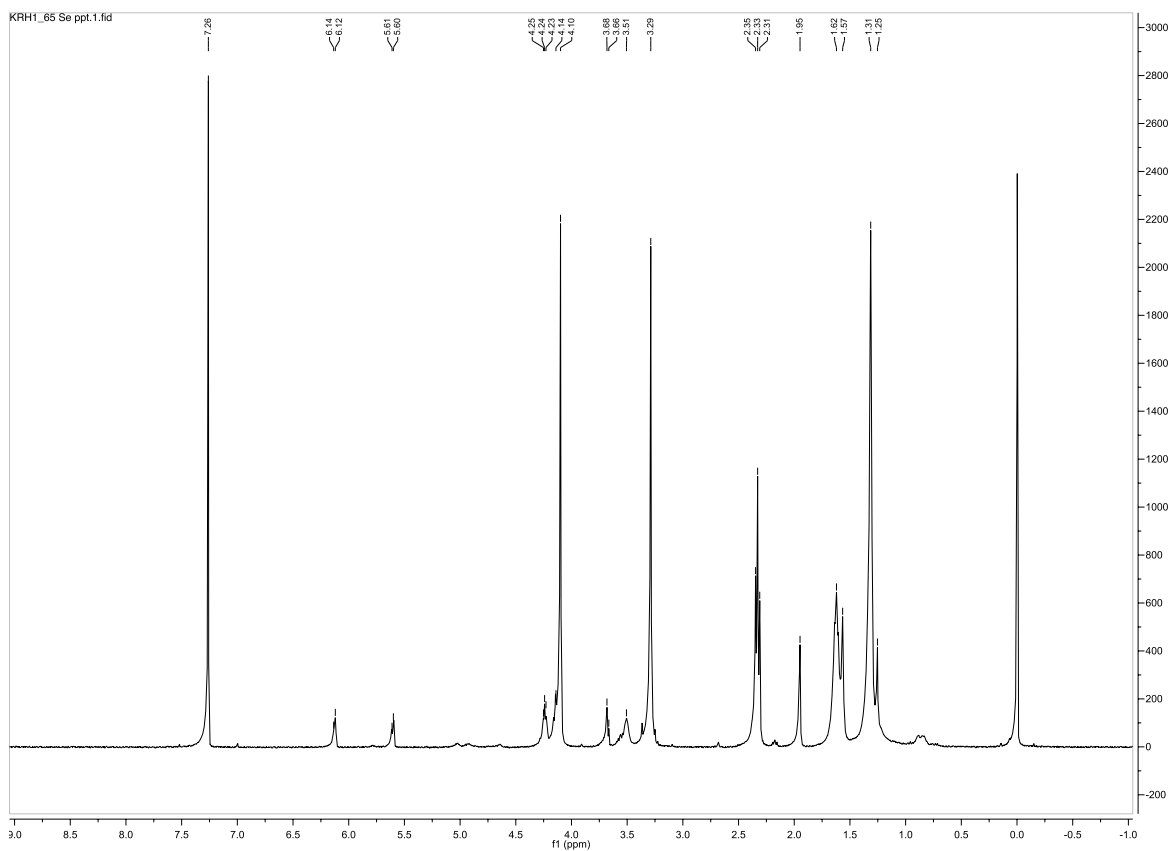


Figure A11. ¹H NMR of the methacrylate endcapped sebacic acid based prepolymer.

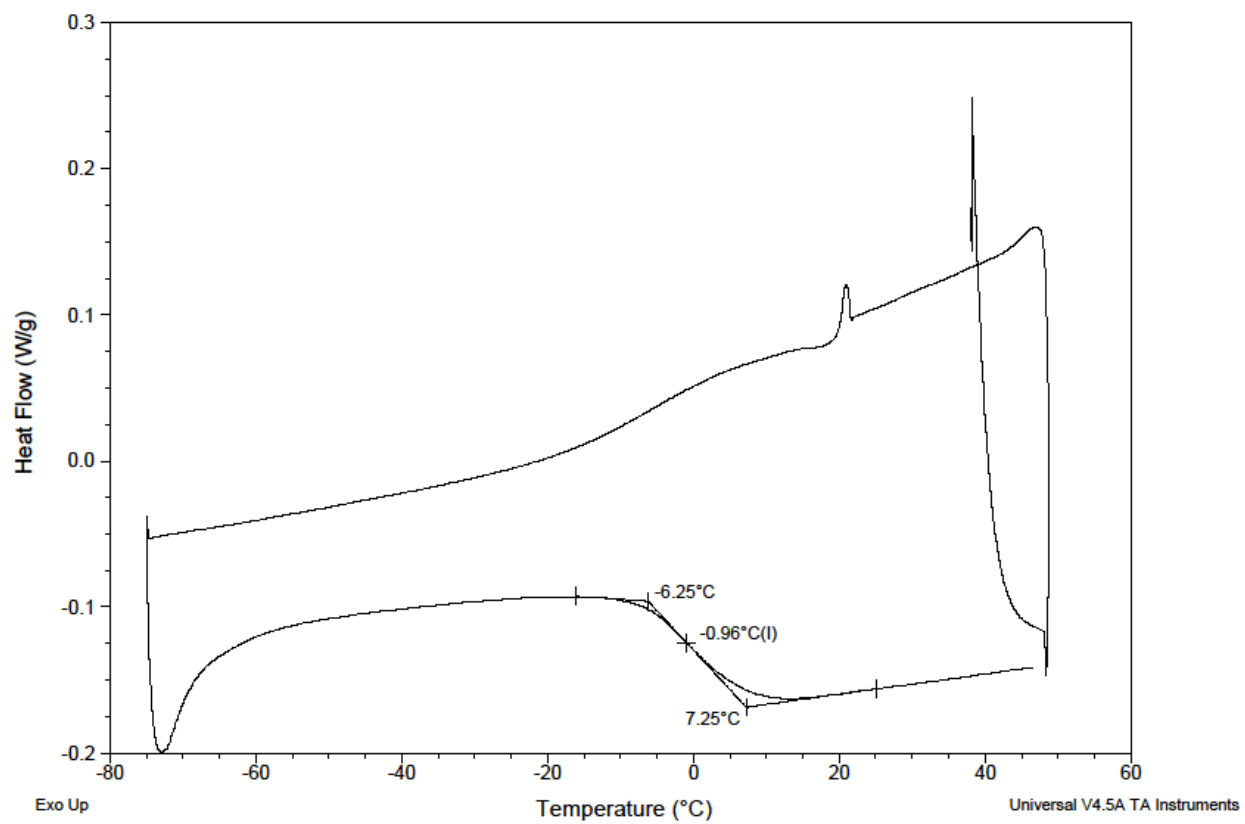


Figure A12. DSC of the succinic acid based thermoset.

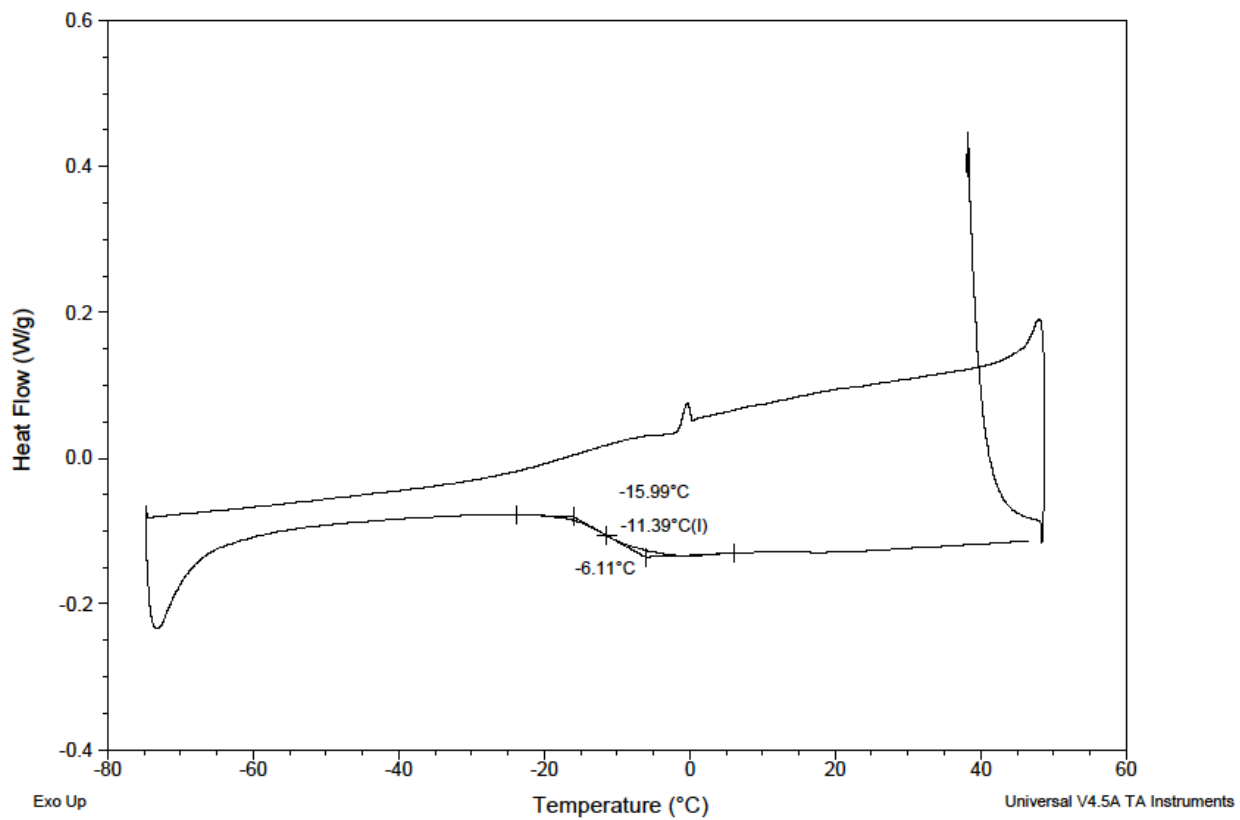


Figure A13. DSC of the adipic acid based thermoset.

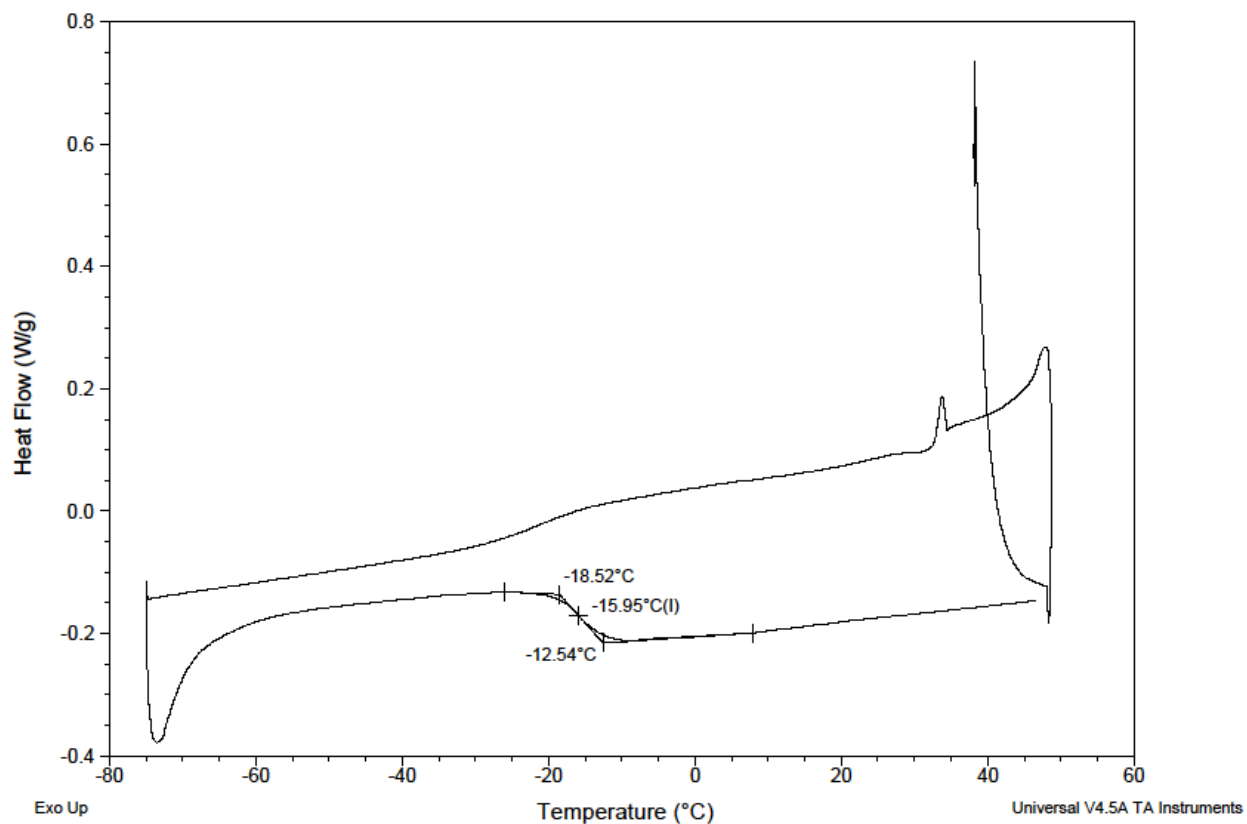
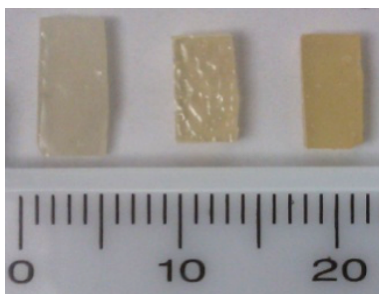


Figure A14. DSC of the sebacic acid based thermoset.

Table A3. Properties of Iodinated Thermosets Used in Instron Experiments.

Polymer (by diacid)	M_n (g mol ⁻¹) ^a	PDI ^b	T_g (°C) ^c	5% (°C) ^d
Succinic	7300	1.38	16.5	284
Adipic	7770	1.49	6.4	280
Sebacic	8700	1.38	-14.0	310

^a Determined by ¹H NMR before crosslinking, ^b Determined by GPC before crosslinking, ^c DSC, second heat 10 °C min⁻¹, ^d Decomposition measured by TGA 20 °C min⁻¹.

**Figure A15.** Photos displaying minimal discoloration after crosslinking the films. Films listed by diacid from left to right: Succinic, Adipic, Sebacic.**Table A4.** DLS Results of Nanoparticles Formulated Without PEG.

Size (d.nm)	PDI
450.3	0.01
434.2	0.02
428.9	0.07

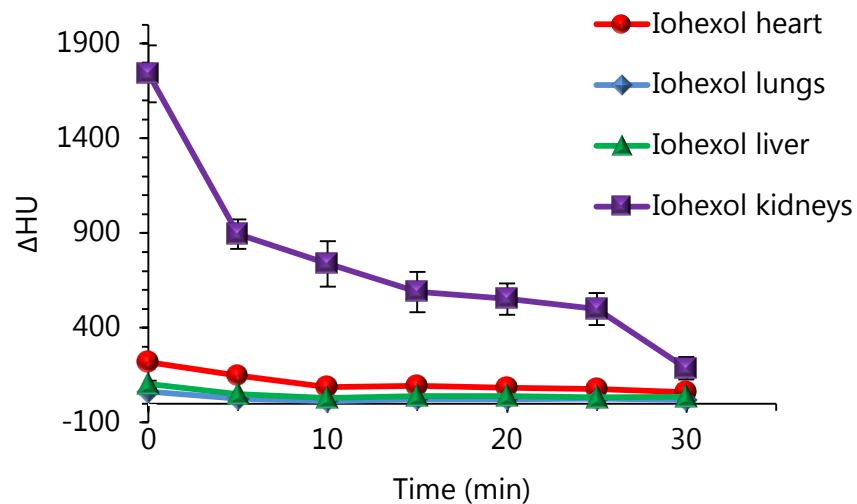


Figure A16. Graph displaying the attenuation measured in the heart, lungs, liver, spleen, and kidneys from the time of injection of Omnipaque® (iohexol) and every 5 minutes until reaching 30 minutes.

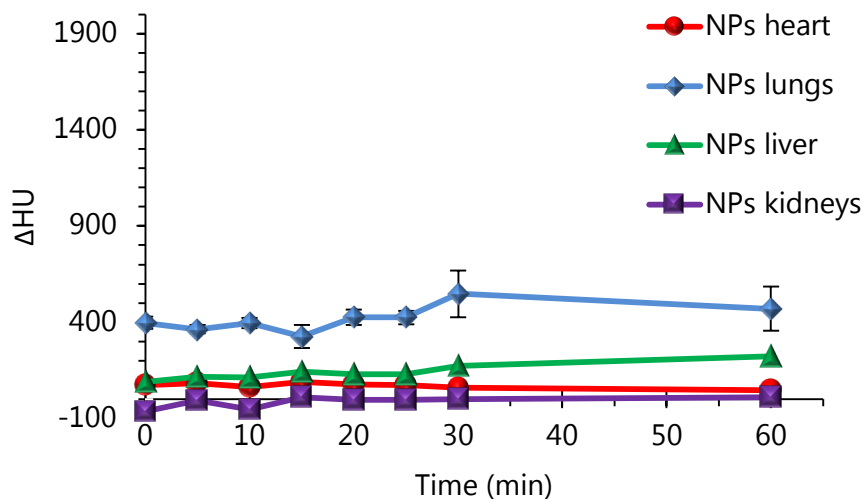


Figure A17. Graph displaying the attenuation measured in the heart, lungs, liver, spleen, and kidneys from the time of injection of the adipic acid based nanoparticles (NPs), every 5 minutes until reaching 30 minutes, and again after 60 minutes.

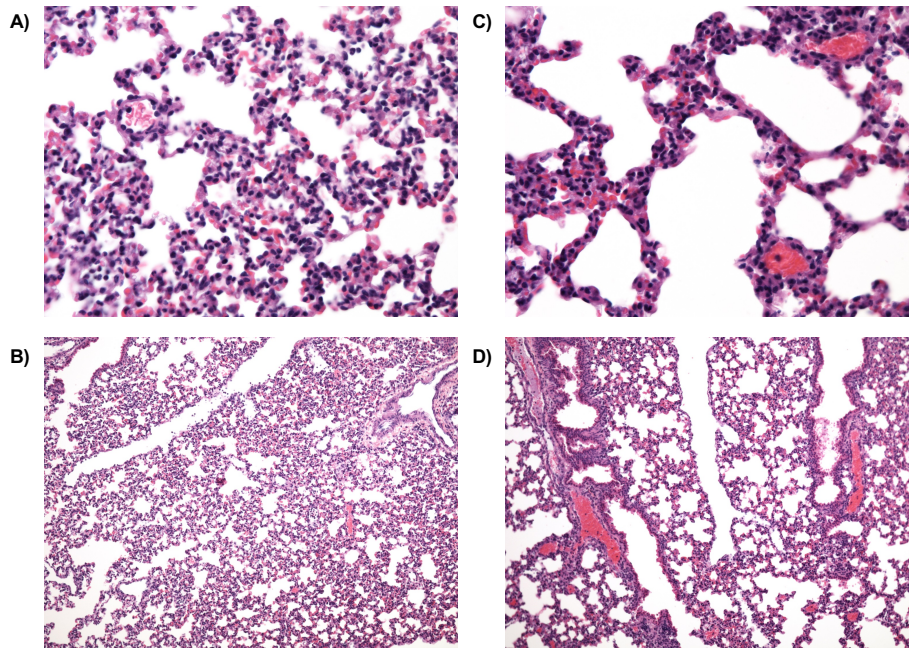
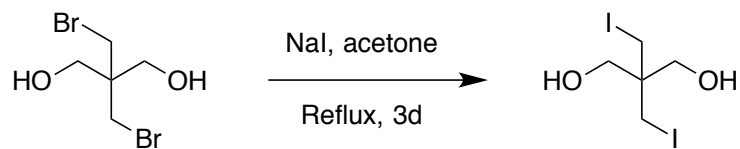


Figure A18. Images obtained from slides made using the lungs of the mouse injected with nanoparticles (A at 10x and B at 40x) and the lungs of the control mouse (no contrast agent injected, C at 10x and D at 40x).

APPENDIX B: SUPPLEMENTARY INFORMATION FOR CHAPTER 3
RADIOPAQUE SHAPE MEMORY MATERIALS VIA IODINATED COPOLYESTERS



Scheme B1. Iodinated monomer, 2,2-bis(iodomethyl)-1,3-propanediol. Yield: 74%; T.Y. 67.6 g; A.Y. 49.9 g

Table B1. Properties of 2,2-Bis(iodomethyl)-1,3-propanediol Determined by DSC and TGA.

T_m (°C)	ΔH (J/g)	5% (°C)	10% (°C)
130	104	201	216

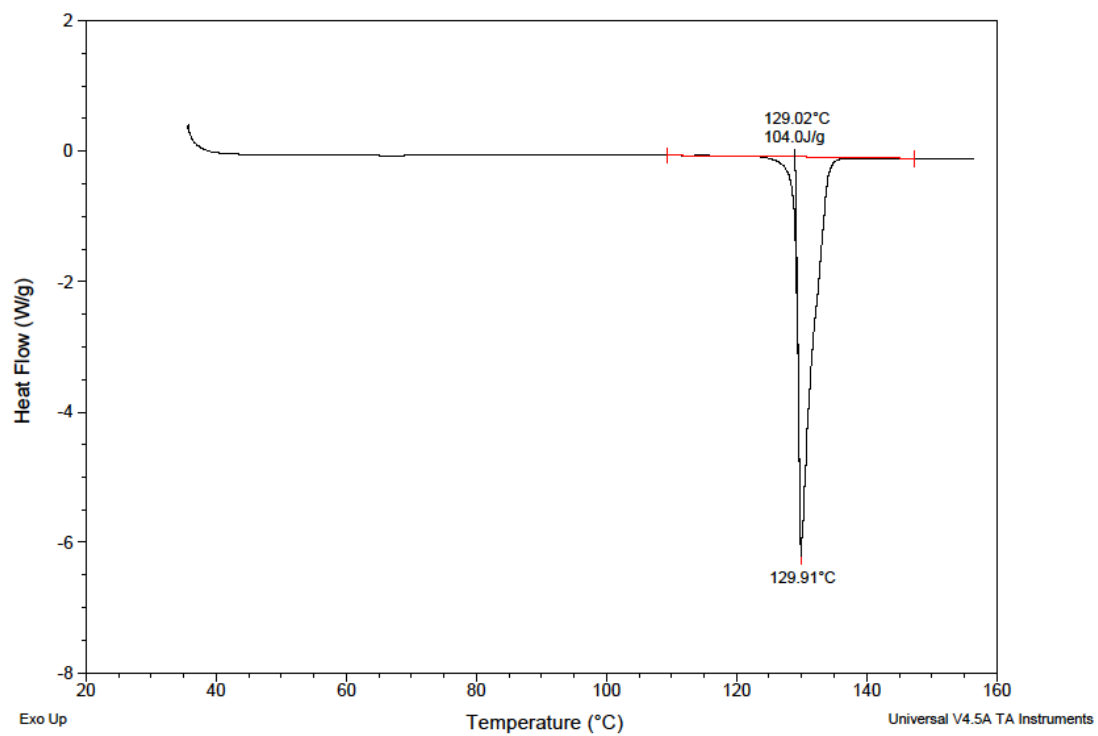


Figure B1. DSC (ramp at 10 °C min⁻¹) spectrum of 2,2-bis(iodomethyl)-1,3-propanediol.

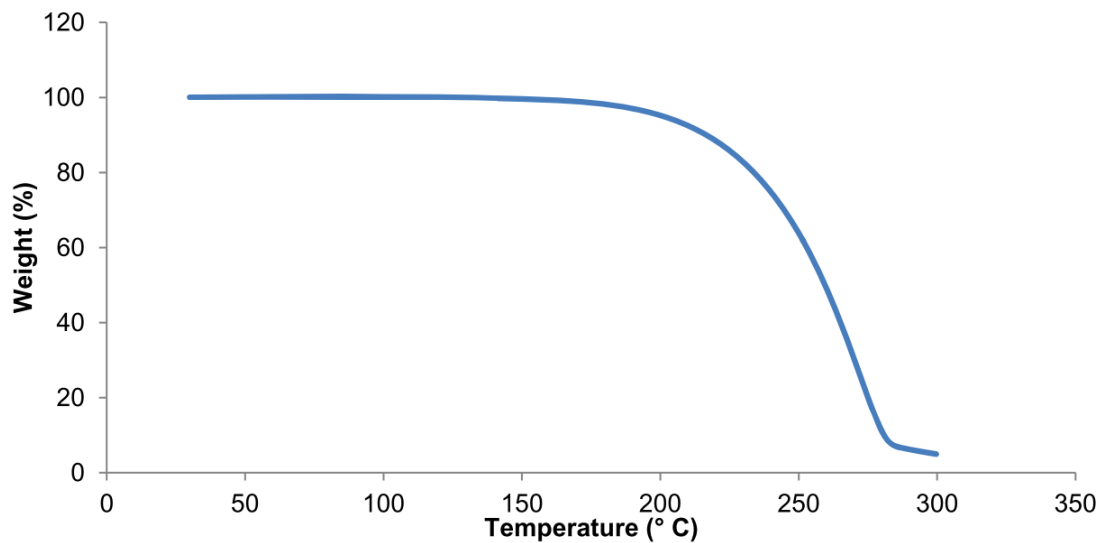


Figure B2. TGA (ramp at 20 °C min⁻¹) spectrum of 2,2-bis(iodomethyl)-1,3-propanediol.

Table B2. Elemental Analysis of 2,2-Bis(iodomethyl)-1,3-propanediol Determined by XPS.

Peak	Mass Concentration (%)	Atomic Concentration (%)
I	60.25	13.26
O	9.89	17.27
C	29.86	69.47
Br	0.00	0.00

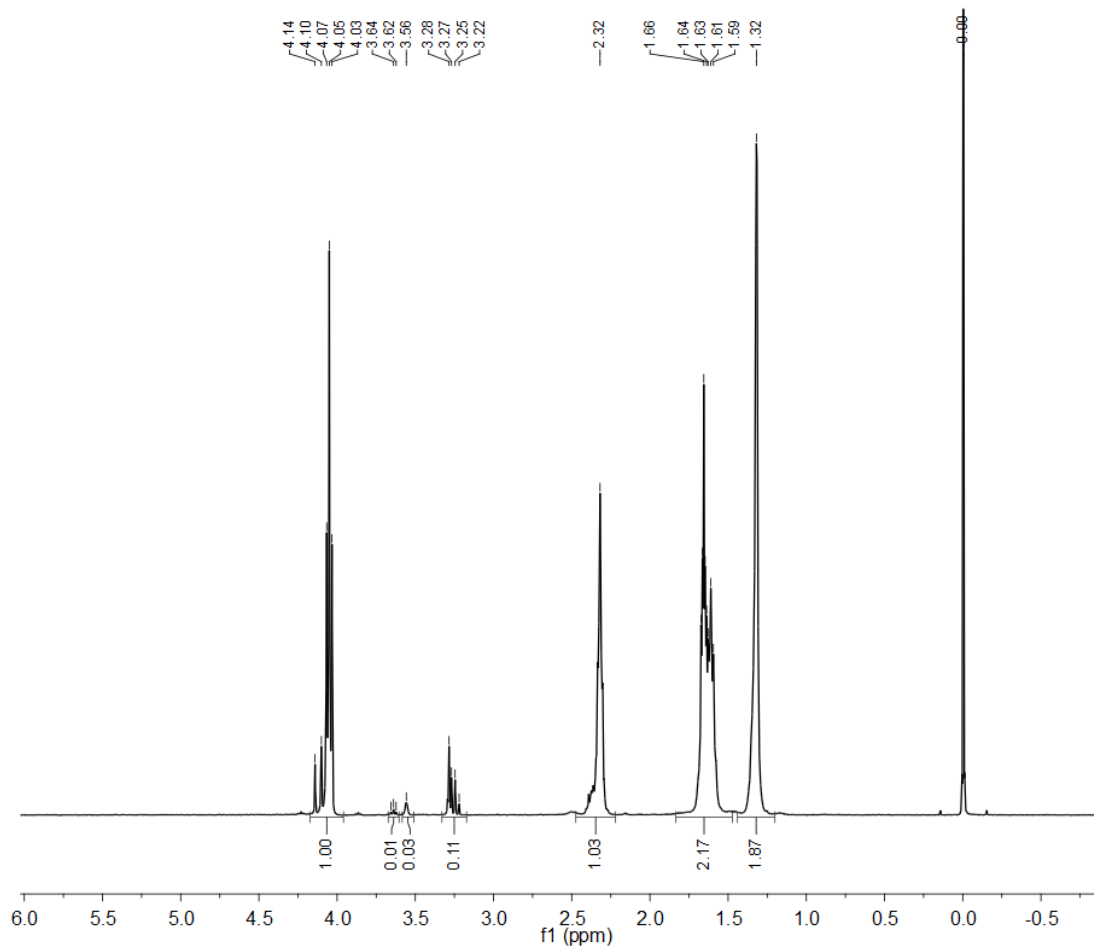


Figure B3. ^1H NMR spectrum of the prepolymer with a target of 15 mole percent iodinated monomer.

Example of how molecular weight is calculated using Figure B3:

$$\begin{aligned}
 & 1.00 / (0.01 + 0.03) = 25 \text{ repeat units} \\
 & 25 * 0.11 = 2.75 \text{ (representative of iodinated repeat units)} \\
 & 2.75 * 466.05 \text{ g mol}^{-1} = 1300 \text{ g mol}^{-1} \text{ (MW of total iodinated units in polymer)} \\
 & 22.25 * 256.34 \text{ g mol}^{-1} = 5700 \text{ g mol}^{-1} \text{ (MW of total octanediol-based units in polymer)} \\
 & 1300 \text{ g mol}^{-1} + 5700 \text{ g mol}^{-1} = 7000 \text{ g mol}^{-1} \text{ (MW of polymer)}
 \end{aligned}$$

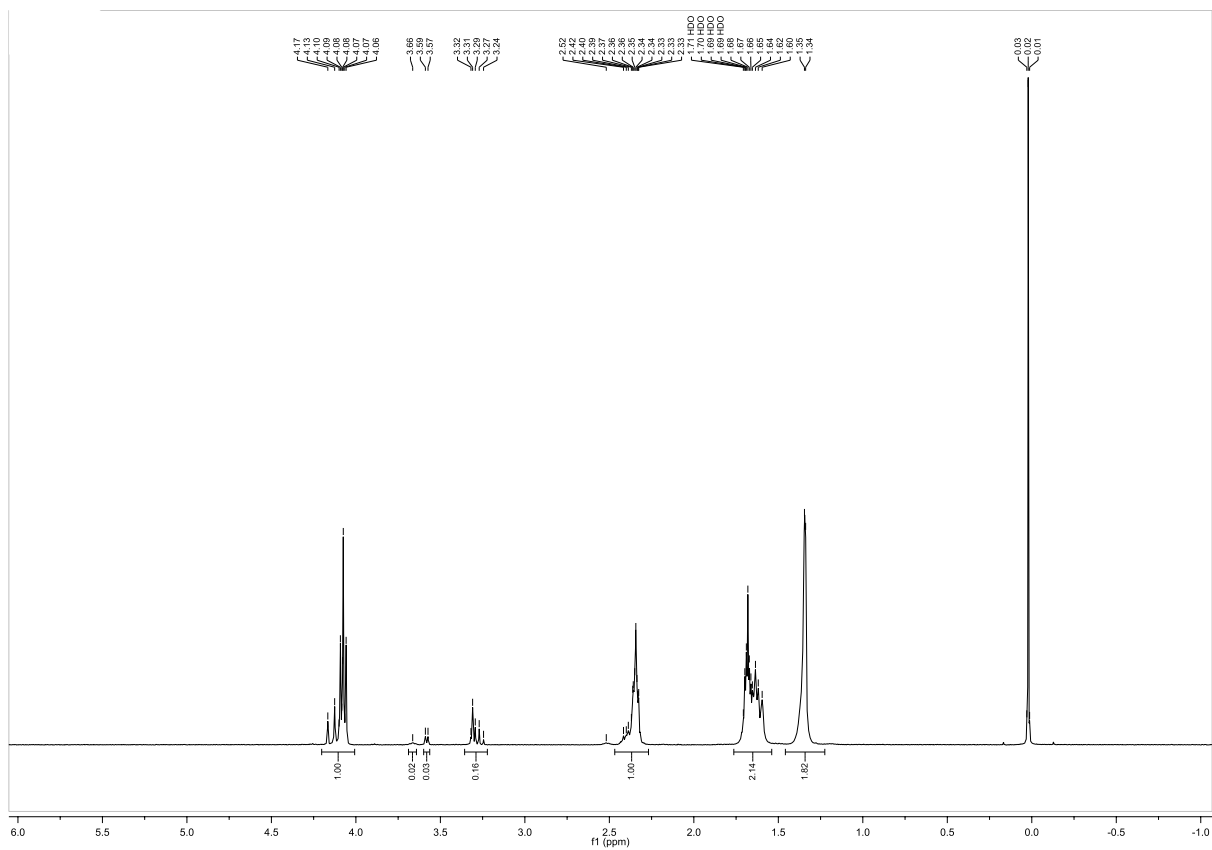


Figure B4. ^1H NMR spectrum of the prepolymer with a target of 20 mole percent iodinated monomer

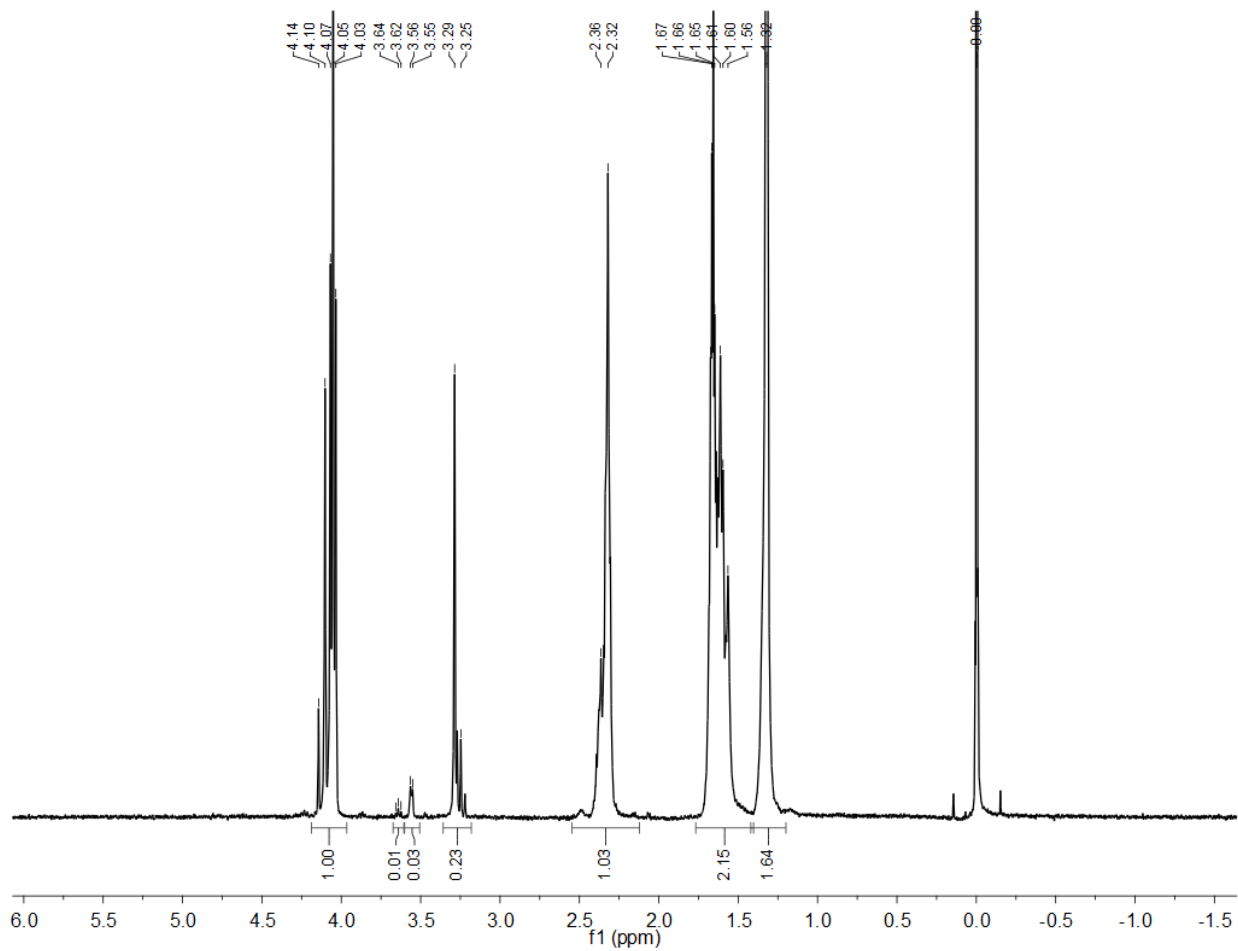


Figure B5. ^1H NMR spectrum of the prepolymer with a target of 25 mole percent iodinated monomer

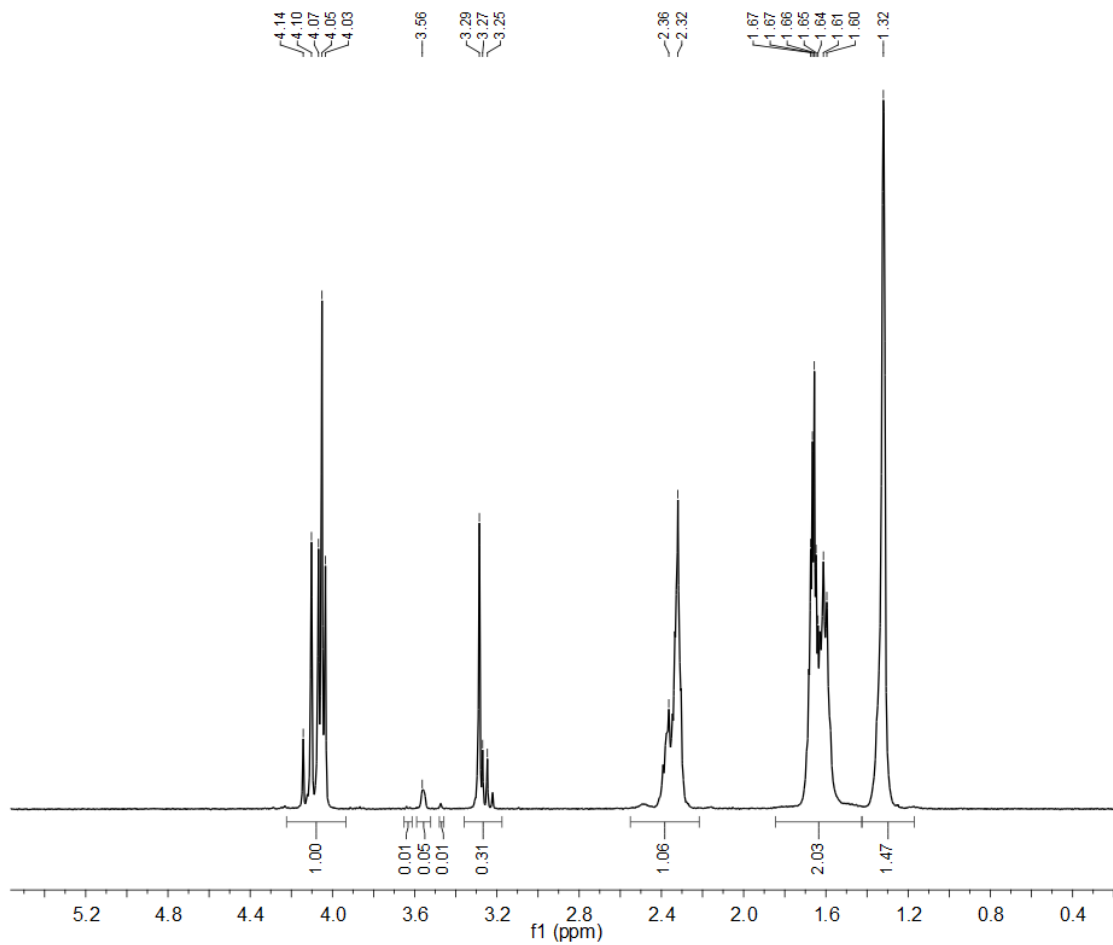


Figure B6. ^1H NMR spectrum of the prepolymer with a target of 35 mole percent iodinated monomer

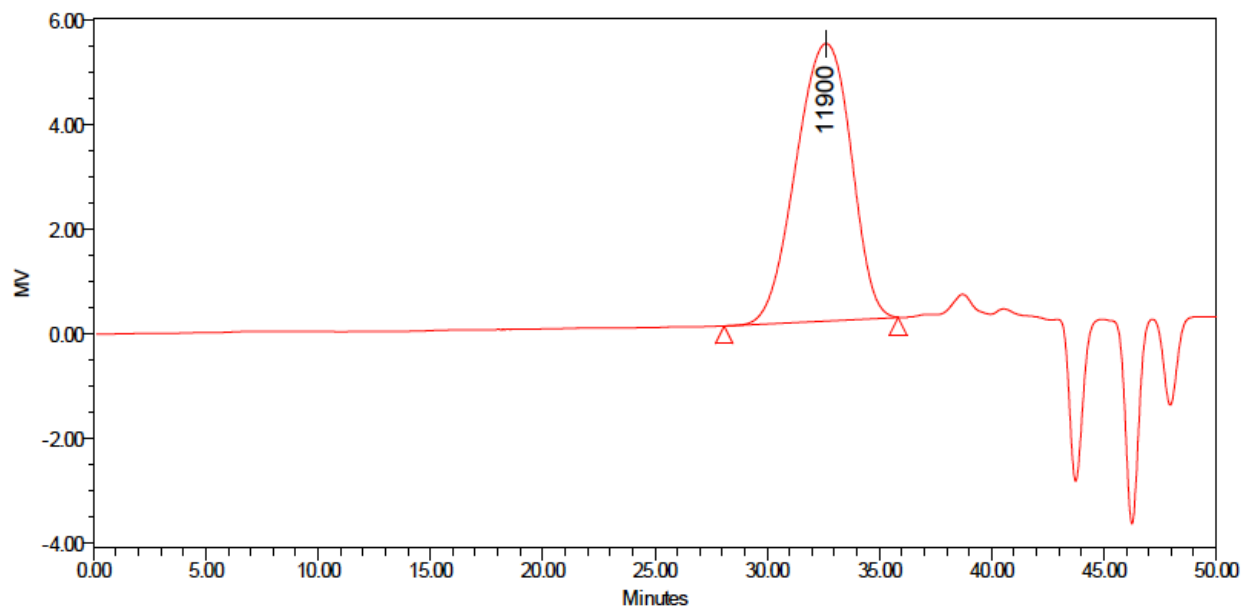


Figure B7. GPC: 15 mol% I (number value depicts $\langle M_p \rangle$).

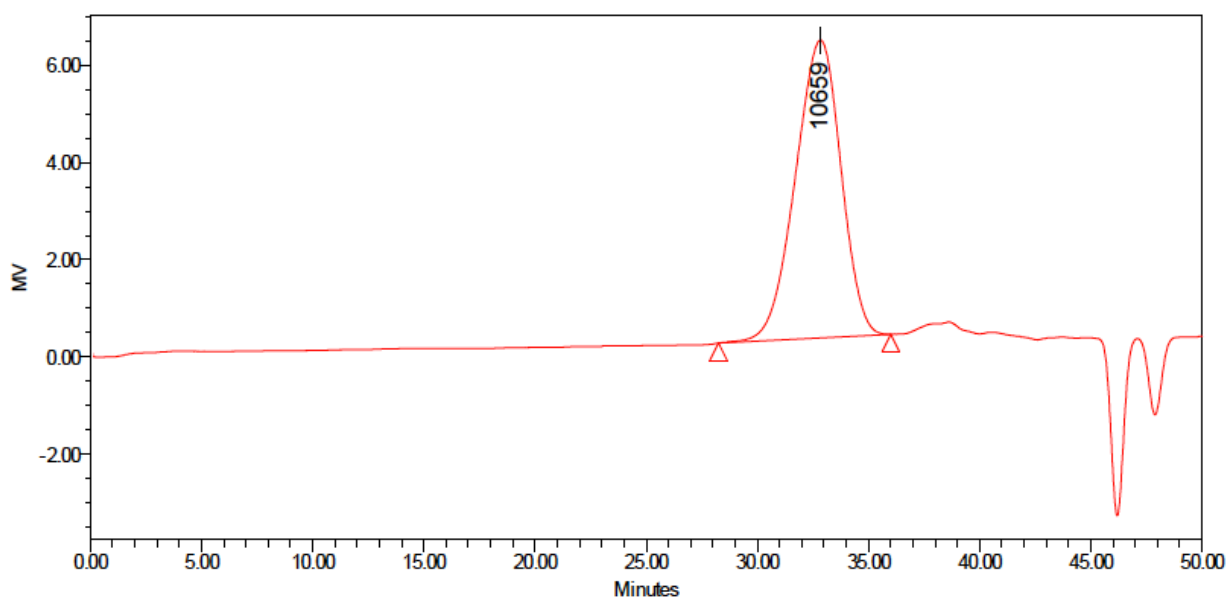


Figure B8. GPC: 20 mol% I (number value depicts $\langle M_p \rangle$).

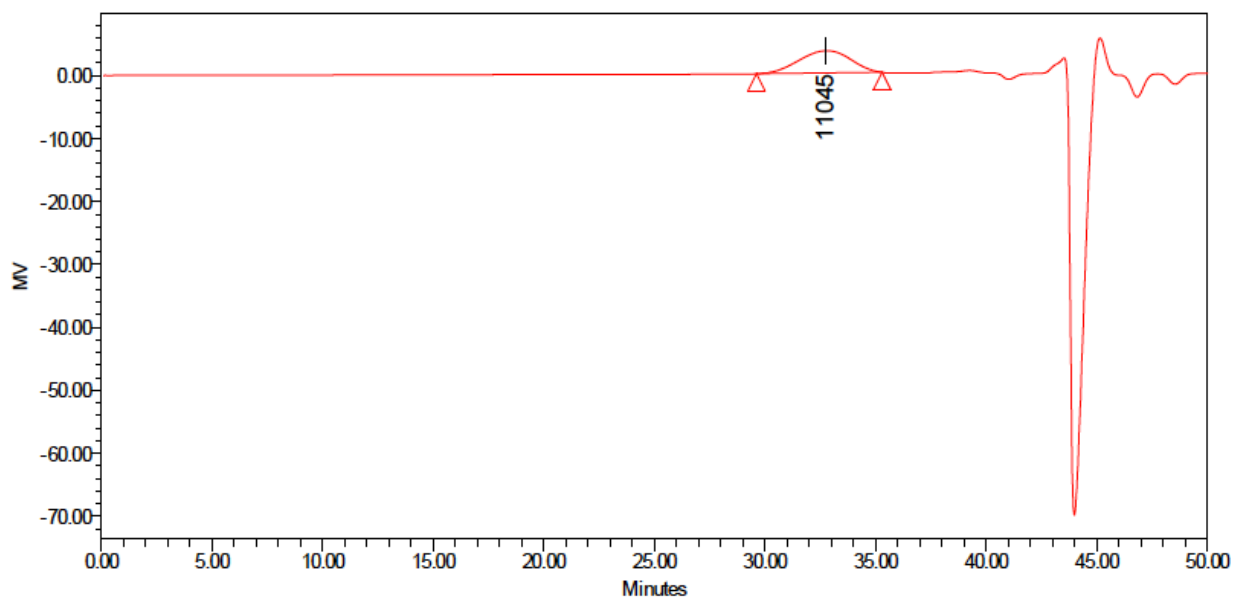


Figure B9. GPC: 25 mol% I (number value depicts $\langle M_p \rangle$).

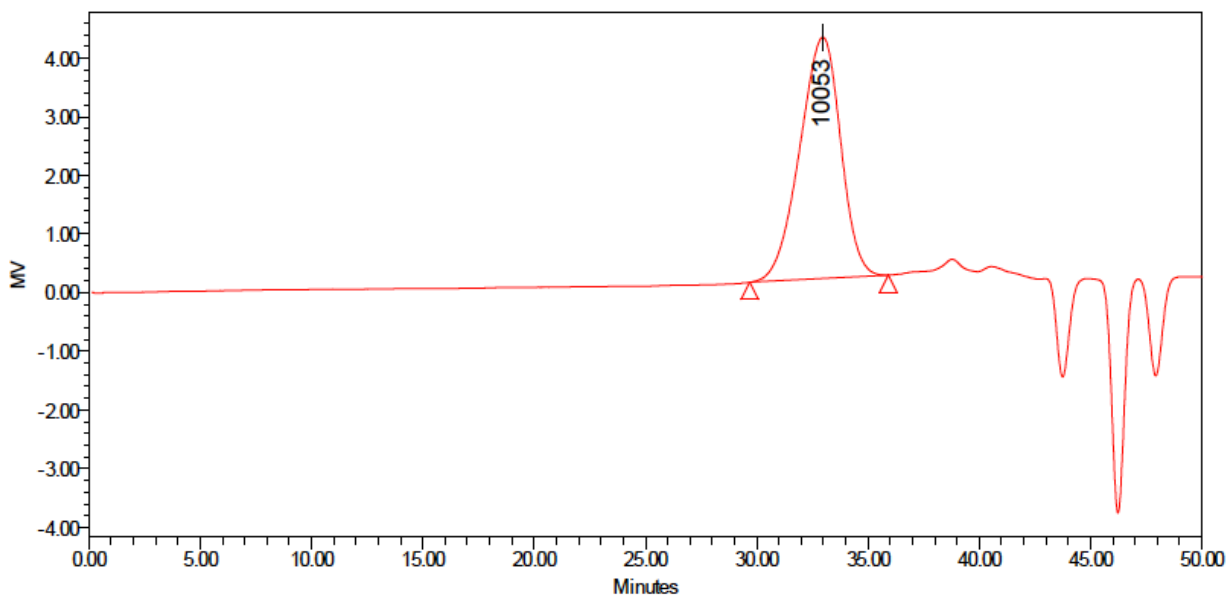


Figure B10. GPC: 35 mol% I (number value depicts $\langle M_p \rangle$).

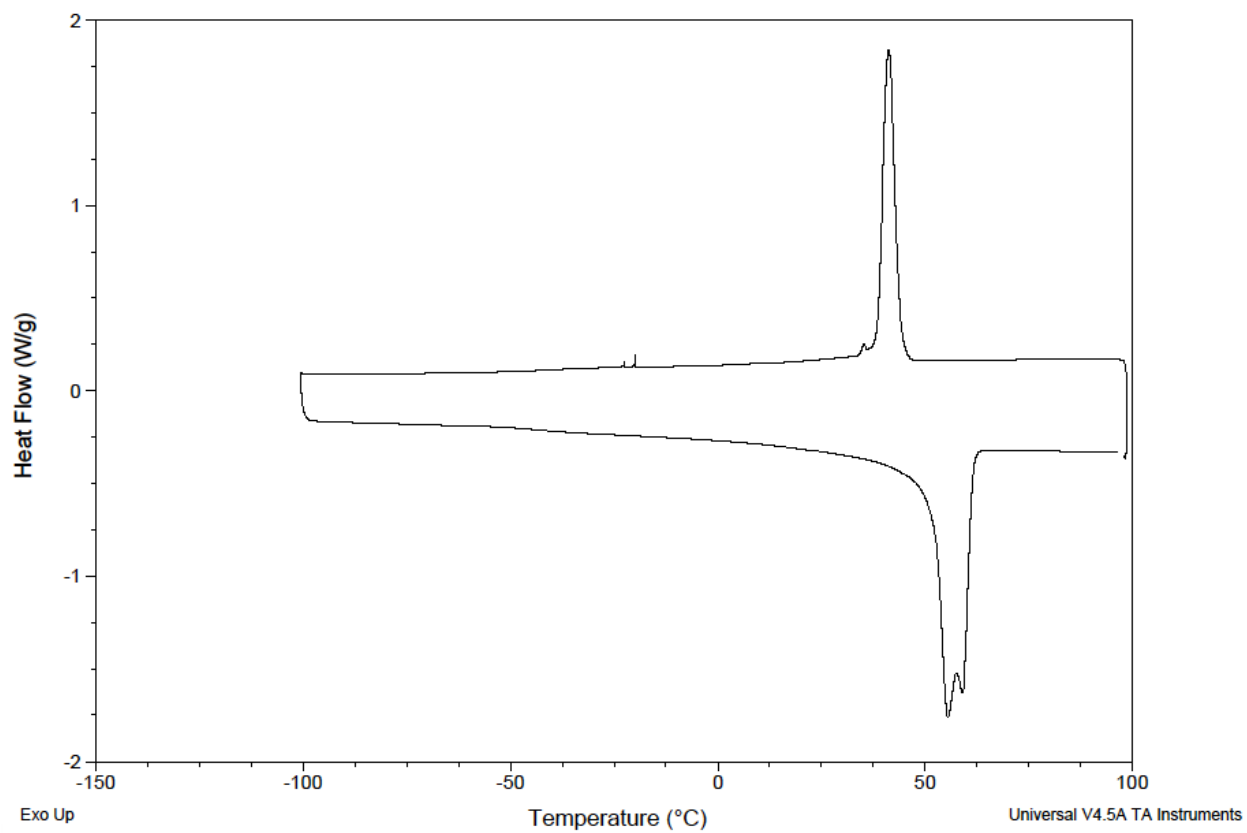


Figure B11. DSC: 15 mol% I prepolymers.

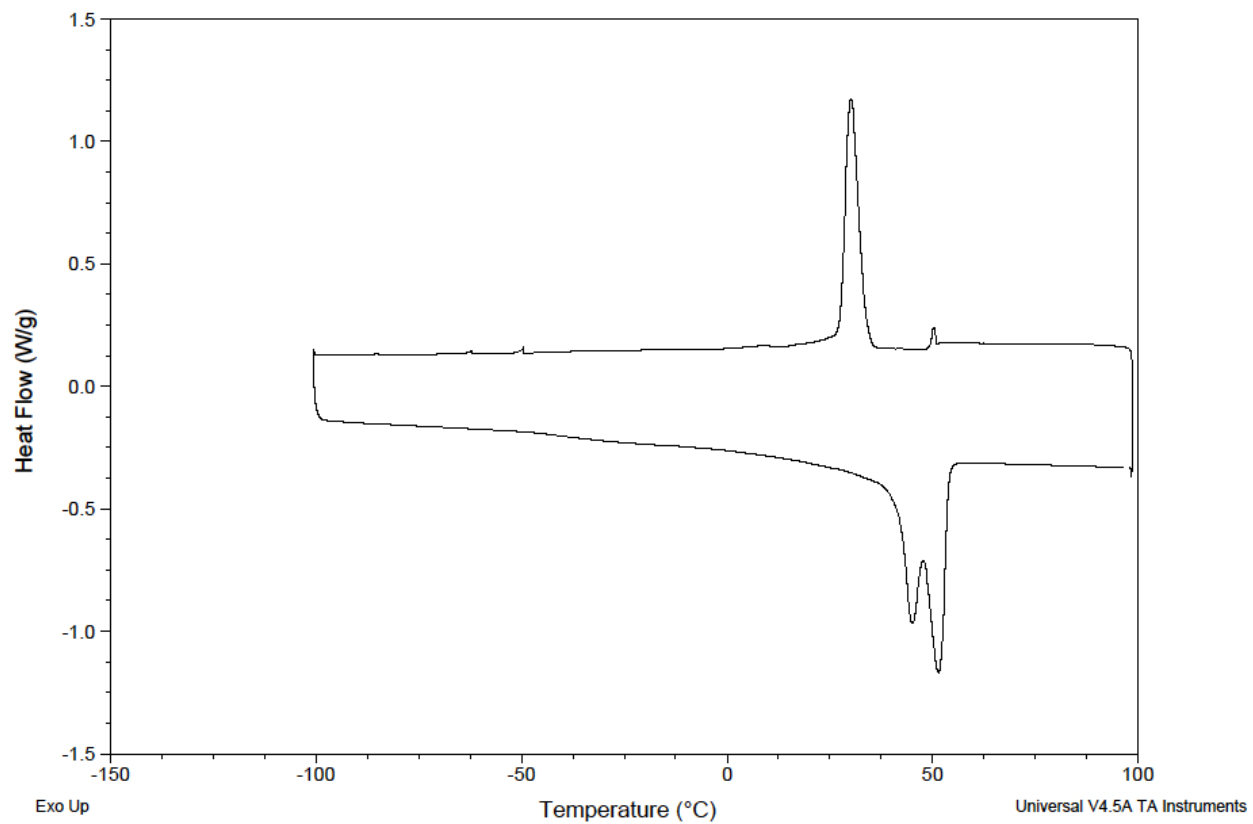


Figure B12. DSC: 20 mol% I prepolymers.

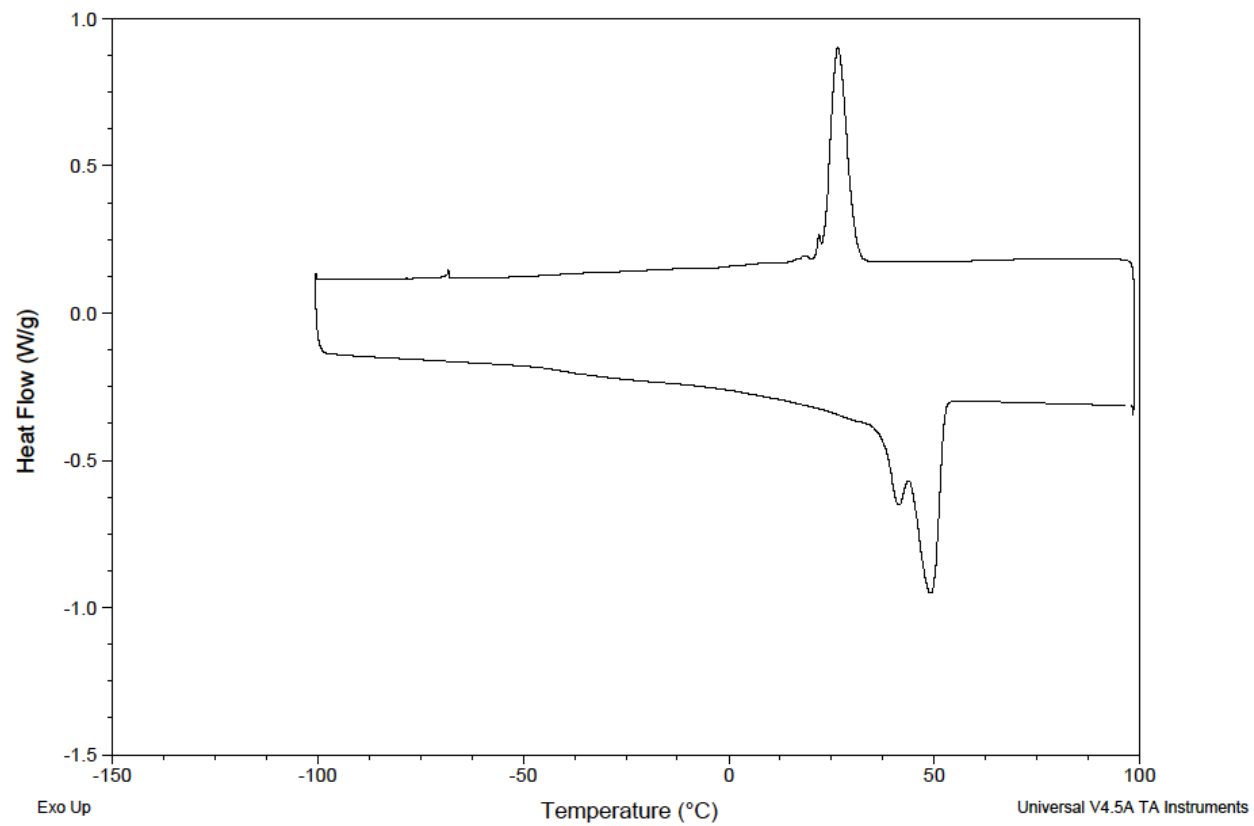


Figure B13. DSC: 25 mol% I prepolymers.

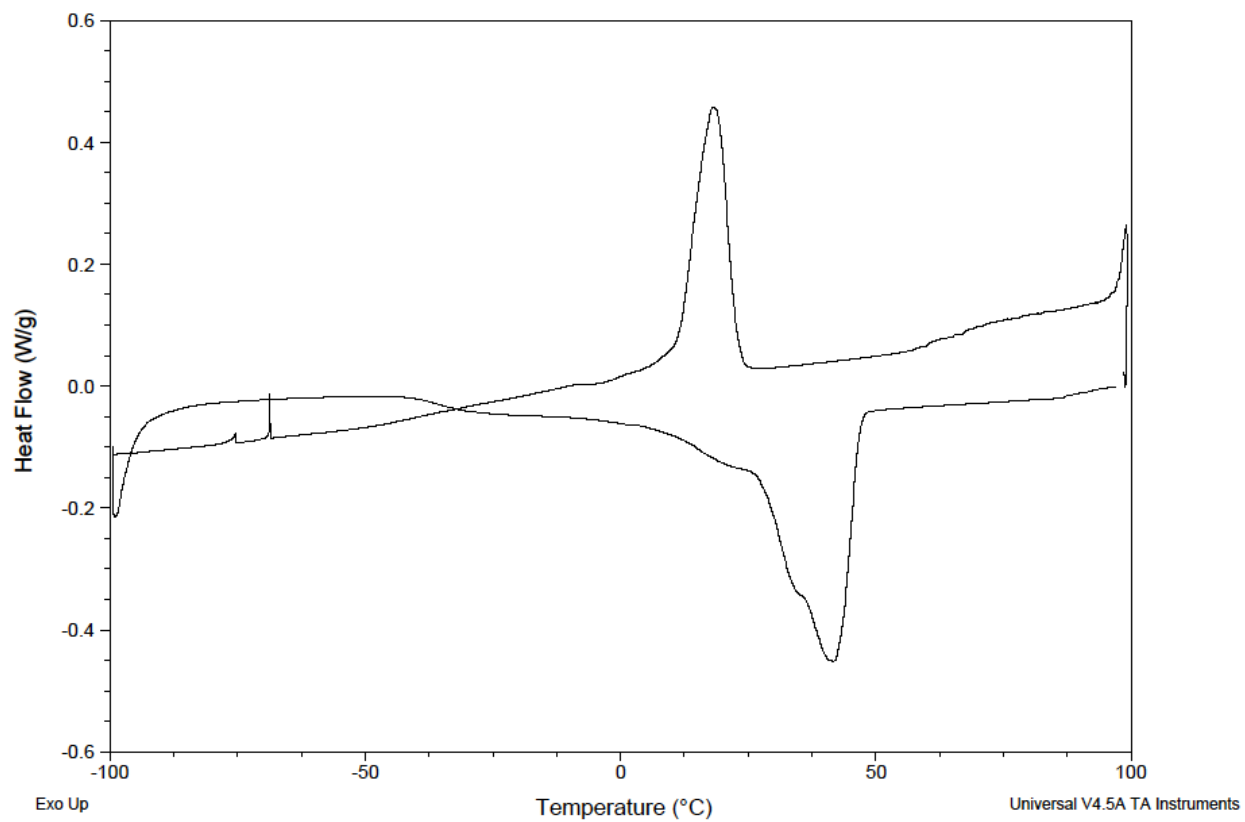


Figure B14. DSC: 35 mol% I prepolymers.

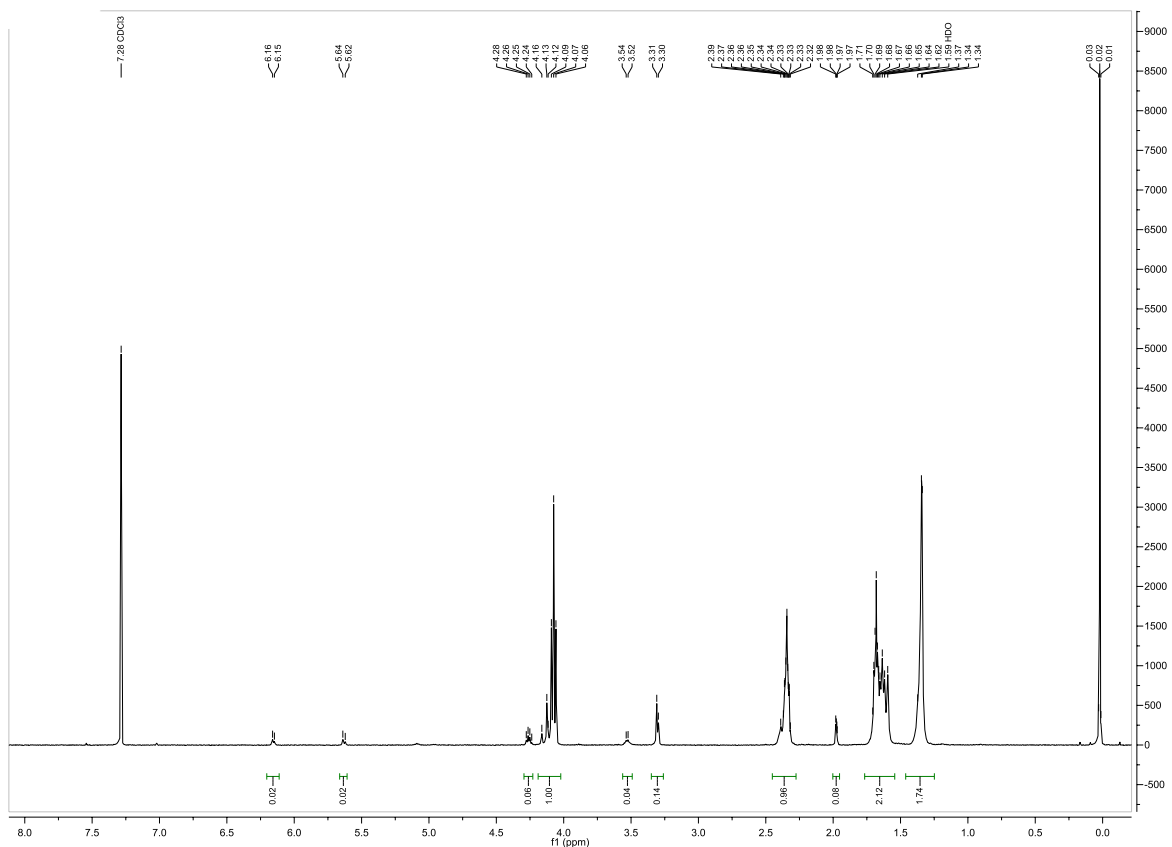


Figure B15. Example of the ^1H NMR spectrum after end-functionalizing the prepolymer with a target of 20 mole percent of the iodinated monomer. The peaks at 6.12 and 5.61 ppm indicate the addition of the methacrylate endgroup.

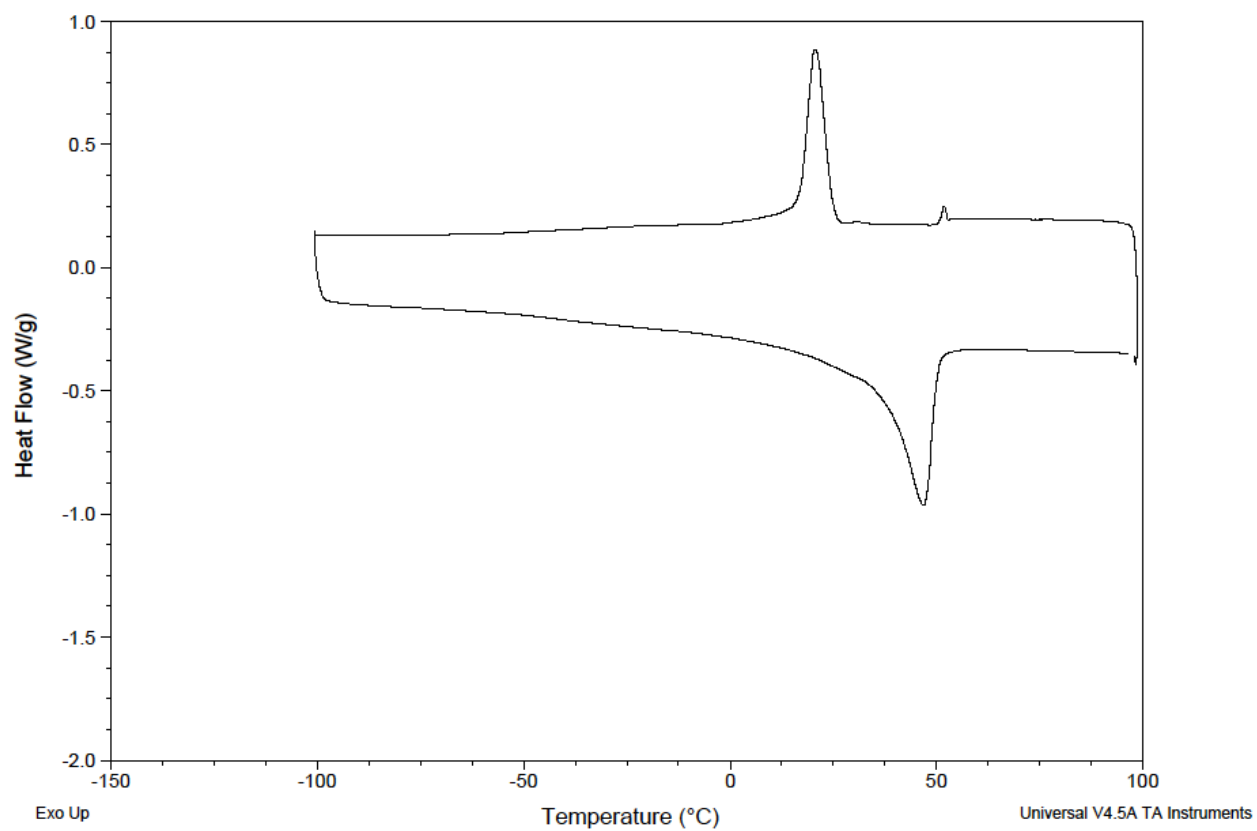


Figure B16. DSC: 15 mol% I thermoset.

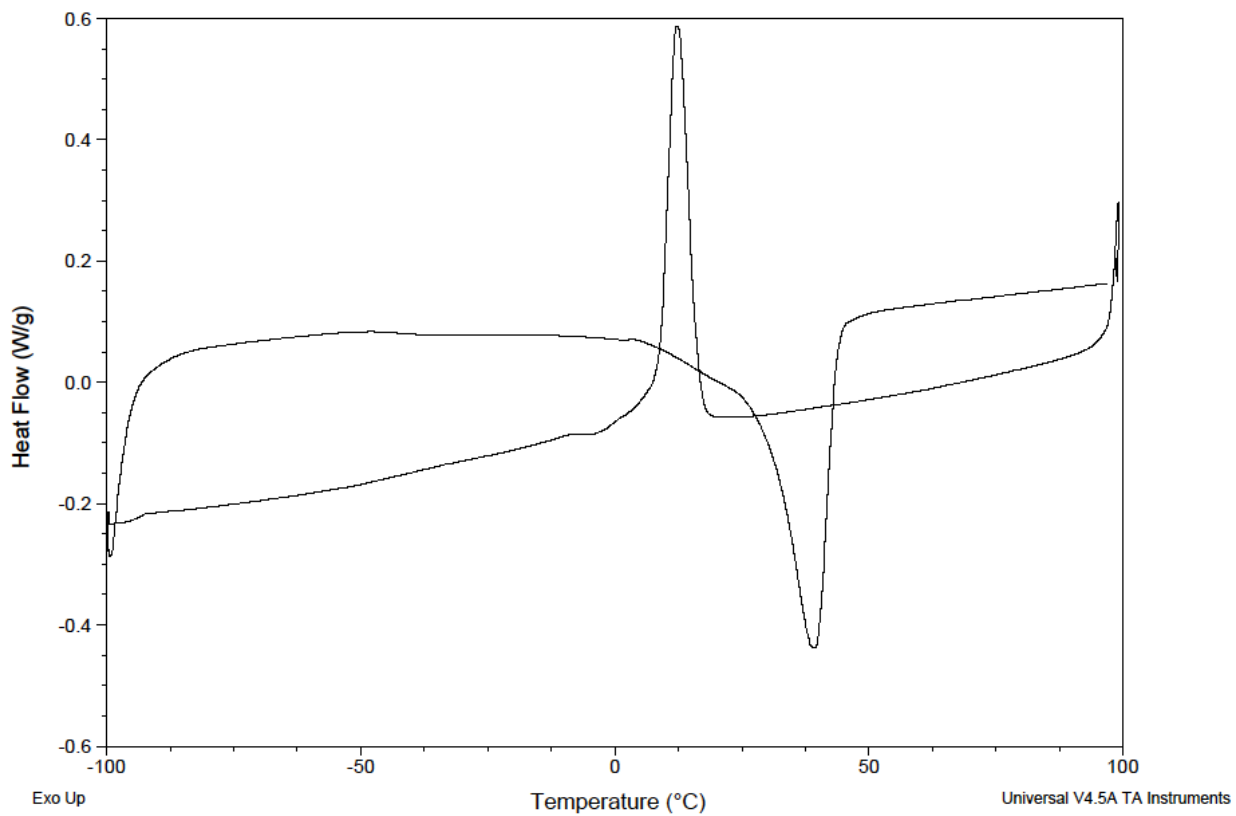


Figure B17. DSC: 20 mol% I thermoset.

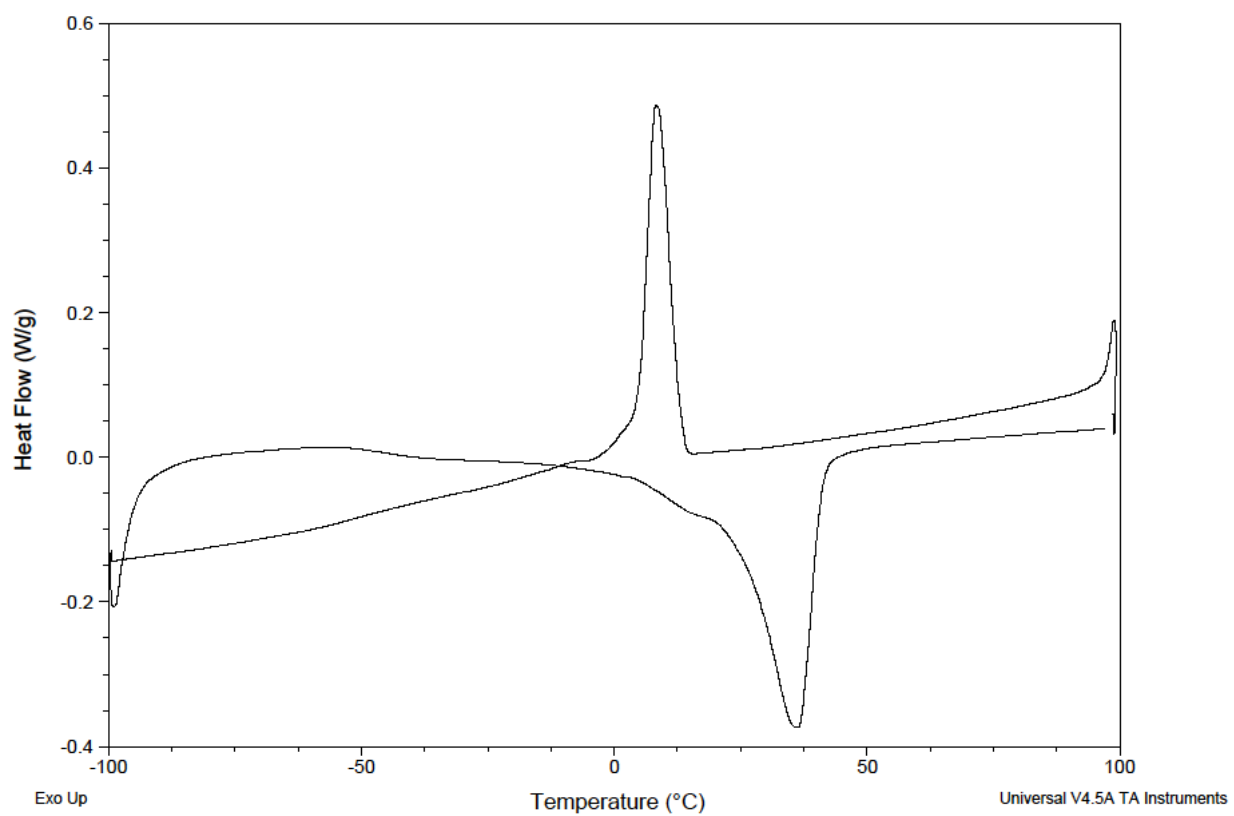


Figure B18. DSC: 25 mol% I thermoset.

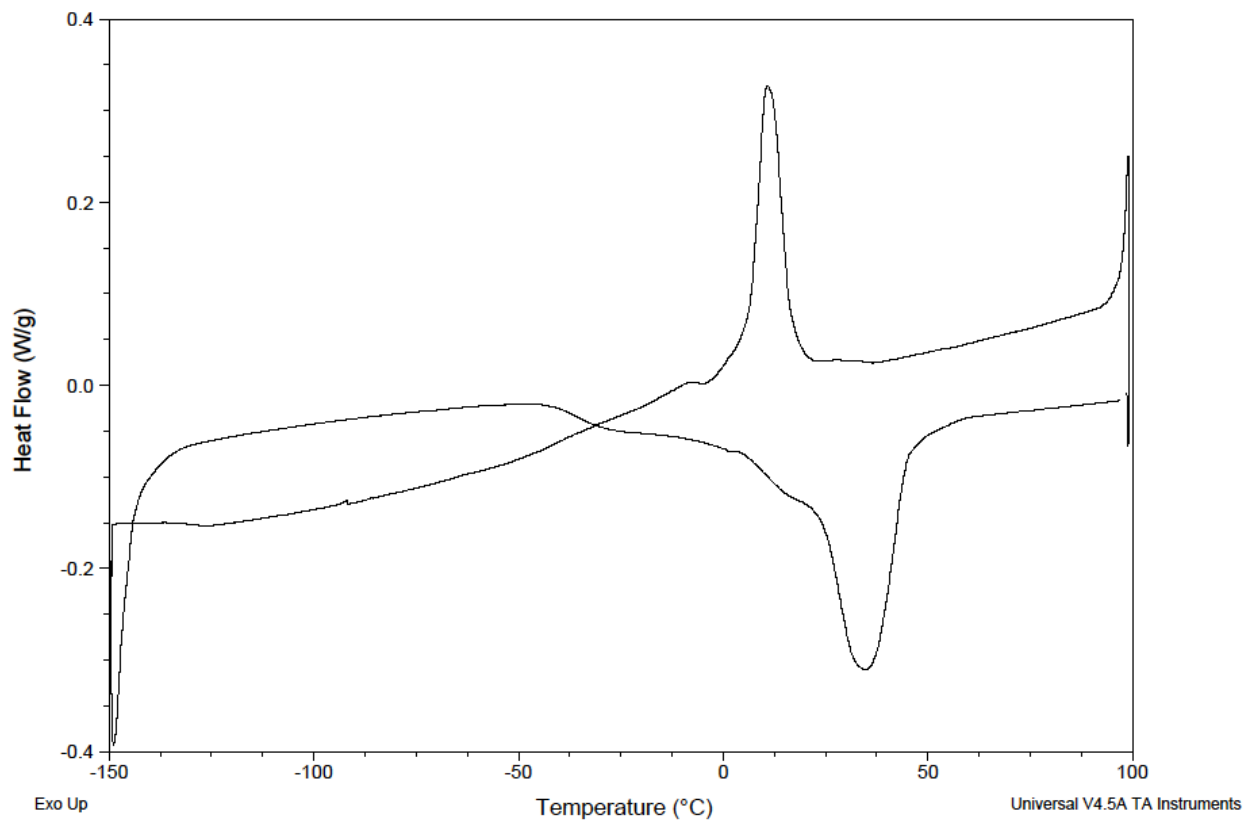


Figure B19. DSC: 35 mol% I thermoset.

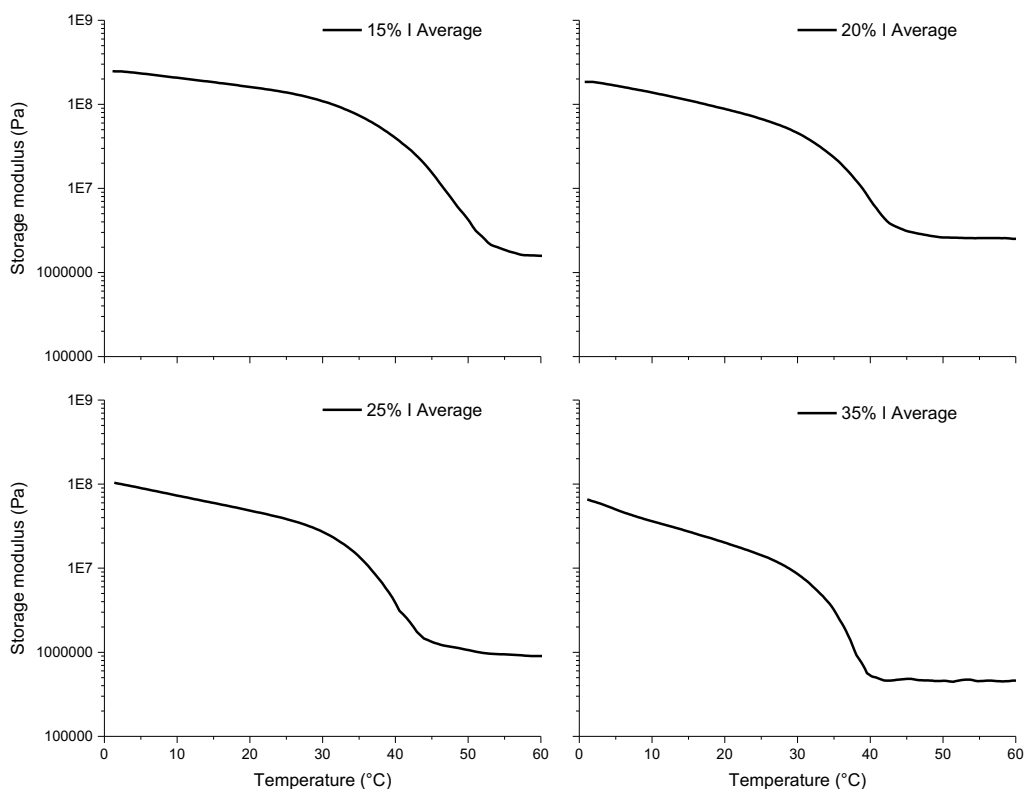


Figure B20. DMA showing the storage modulus from 0-60 °C of an average of three samples for each mole percentage of iodinated monomer incorporated into the crosslinked copolymer films.

Table B3. Weight Percent Iodine Found by EDS.

Target mole percent I monomer (%)	Prepolymer weight percent iodine (%)	Crosslinked film weight percent iodine (%)
15	37 ±3	32 ±1
20	36 ±4	30 ±2
25	48 ±2	38 ±1
35	61 ±7	55 ±2

Table B4. EDS 15 mol% I Prepolymer (3 Samples).

Atom	Weight percent (%)	Atomic percent (%)
C	40.85	71.81
O	15.88	20.96
Sn	3.15	0.56
I	40.13	6.68
C	40.93	68.39
O	20.29	25.46
Sn	1.83	0.31
I	36.94	5.84
C	41.16	67.3
O	21.96	26.96
Sn	2.42	0.4
I	34.47	5.33

Table B5. EDS 20 mol% I Prepolymer (3 Samples).

Atom	Weight percent (%)	Atomic percent (%)
C	43.58	67.96
O	23.16	27.11
Sn	1.93	0.3
I	31.34	4.63
C	40.24	69.09
O	18.79	24.22
Sn	2.37	0.41
I	38.6	6.27
C	38.67	66.56
O	20.72	26.78
Sn	3.44	0.6
I	37.17	6.06

Table B6. EDS 25 mol% I Prepolymer (3 Samples).

Atom	Weight percent (%)	Atomic percent (%)
C	30.47	62.32
O	18.03	27.68
Sn	2.52	0.52
I	48.98	9.48
C	32.71	66.73
O	15.13	23.17
Sn	2.41	0.5
I	49.75	9.61
C	34.25	66.21
O	17.13	24.86
Sn	2.55	0.5
I	46.07	8.43

Table B7. EDS 35 mol% I Prepolymer (3 Samples).

Atom	Weight percent (%)	Atomic percent (%)
C	25.23	66.69
O	8.39	16.64
Sn	3.51	0.94
I	62.87	15.73
C	21.09	62.61
O	7.78	17.33
Sn	3.68	1.11
I	67.46	18.96
C	31.34	67.55
O	13.03	21.07
Sn	2.24	0.49
I	53.39	10.89

Table B8. EDS 15 mol% I Film (3 Samples).

Atom	Weight percent (%)	Atomic percent (%)
C	47.76	74.87
O	16.52	19.45
Sn	2.35	0.37
I	32.43	4.81
C	47.02	72.9
O	18.67	21.73
Sn	2.01	0.31
I	31.49	4.62
C	48.02	74.01
O	17.87	20.68
Sn	1.88	0.29
I	31.39	4.58

Table B9. EDS 20 mol% I Film (3 Samples).

Atom	Weight percent (%)	Atomic percent (%)
C	51.1	77.59
O	15.19	17.31
Sn	2.78	0.43
I	30.33	4.36
C	47.33	73.88
O	17.87	20.95
Sn	2.71	0.43
I	32.09	4.74
C	51.96	76.26
O	17.48	19.26
Sn	2.11	0.31
I	27.84	3.87

Table B10. EDS 25 mol% I Film (3 Samples).

Atom	Weight percent (%)	Atomic percent (%)
C	45.24	75.79
O	14.1	17.74
Sn	2.61	0.44
I	38.05	6.03
C	43.93	74.65
O	14.62	18.65
Sn	2.69	0.46
I	38.76	6.23
C	45.45	75.54
O	14.53	18.13
Sn	2.63	0.44
I	37.4	5.88

Table B11. EDS 35 mol% I Film (3 Samples).

Atom	Weight percent (%)	Atomic percent (%)
C	32.15	72.38
O	8.88	15
Sn	4.15	0.94
I	54.83	11.68
C	29.67	70.17
O	9.05	16.06
Sn	3.67	0.88
I	57.61	12.89
C	32.64	72.42
O	8.98	14.95
Sn	4.35	0.98
I	53.47	11.23



Figure B21. Photo depicting minimal discoloration due to UV curing. From left to right: PCL, 35%I, 25%I, 15%I.

APPENDIX C: SUPPLEMENTARY INFORMATION FOR CHAPTER 4

SUPRAMOLECULAR ENGINEERING POLYESTERS: ENDGROUP
FUNCTIONALIZATION OF GLYCOL MODIFIED PET WITH UREIDOPYRIMIDINONE

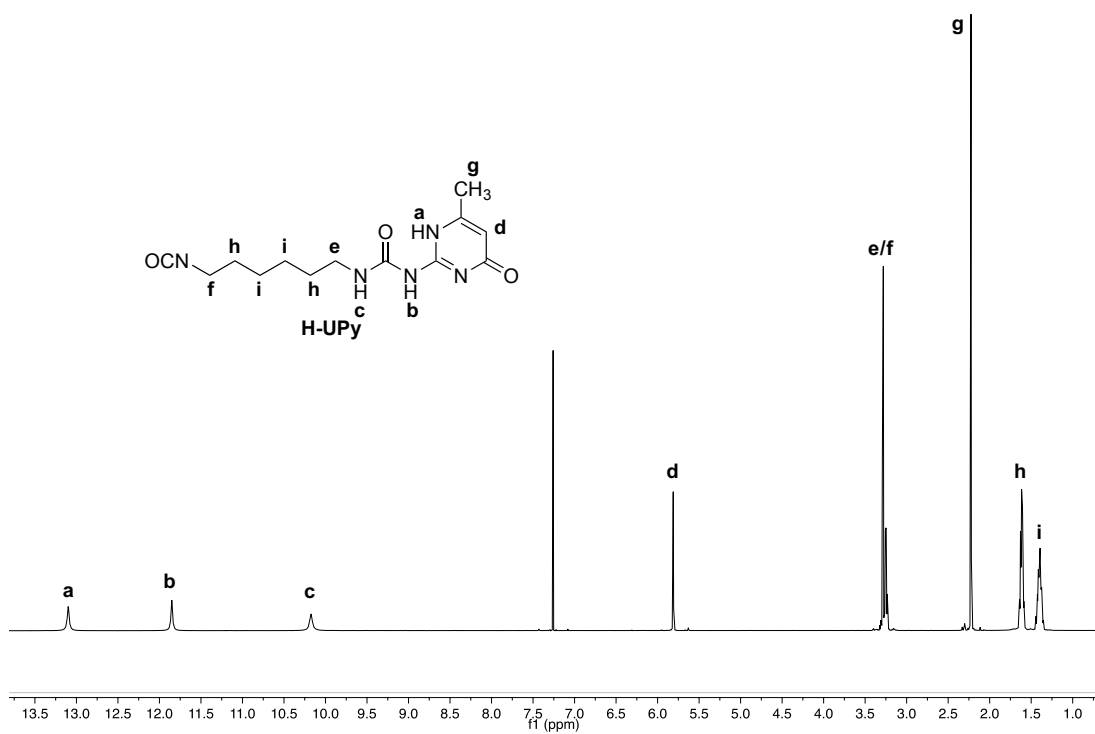


Figure C1. ¹H NMR spectrum of H-UPy in CDCl₃ at ambient temperature. ¹H NMR (400 MHz, CDCl₃) δ: 13.10 (s, 1H), 11.85 (s, 1H), 10.18 (s, 1H), 5.81 (s, 1H), 3.28 (t, 2H), 3.25 (t, 2H), 2.22 (s, 3H), 1.61 (m, 4H), 1.40 (m, 4H).

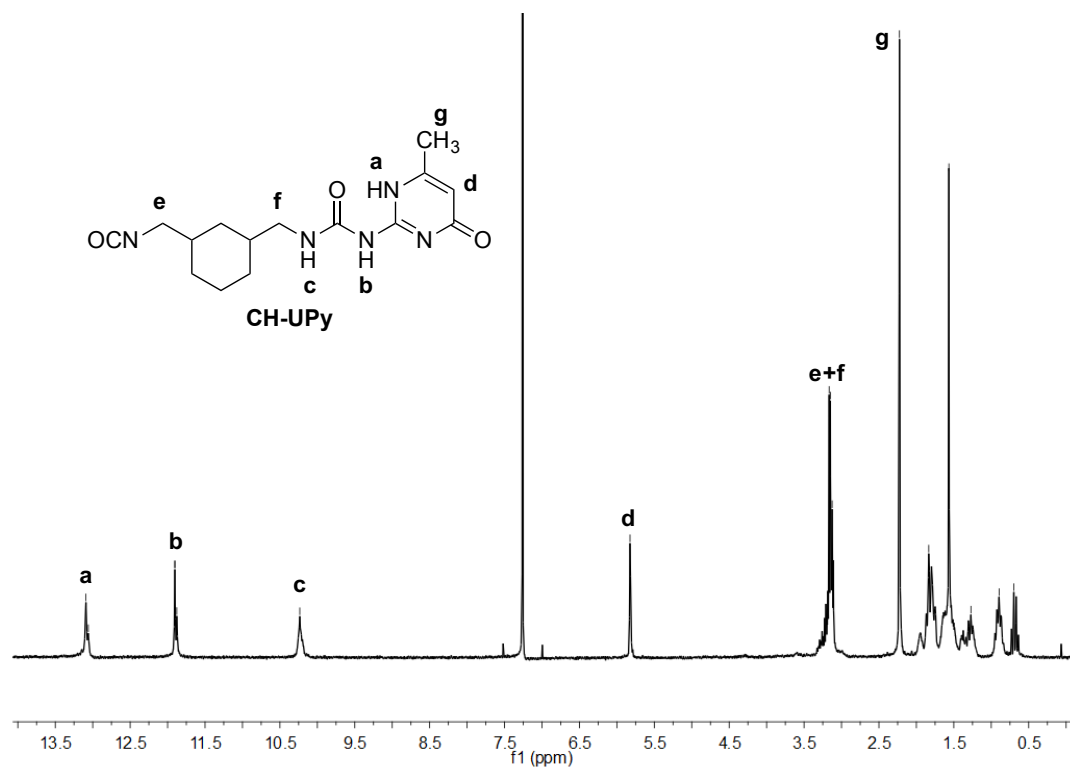


Figure C2. ^1H NMR spectrum of CH-UPy in CDCl_3 at ambient temperature.

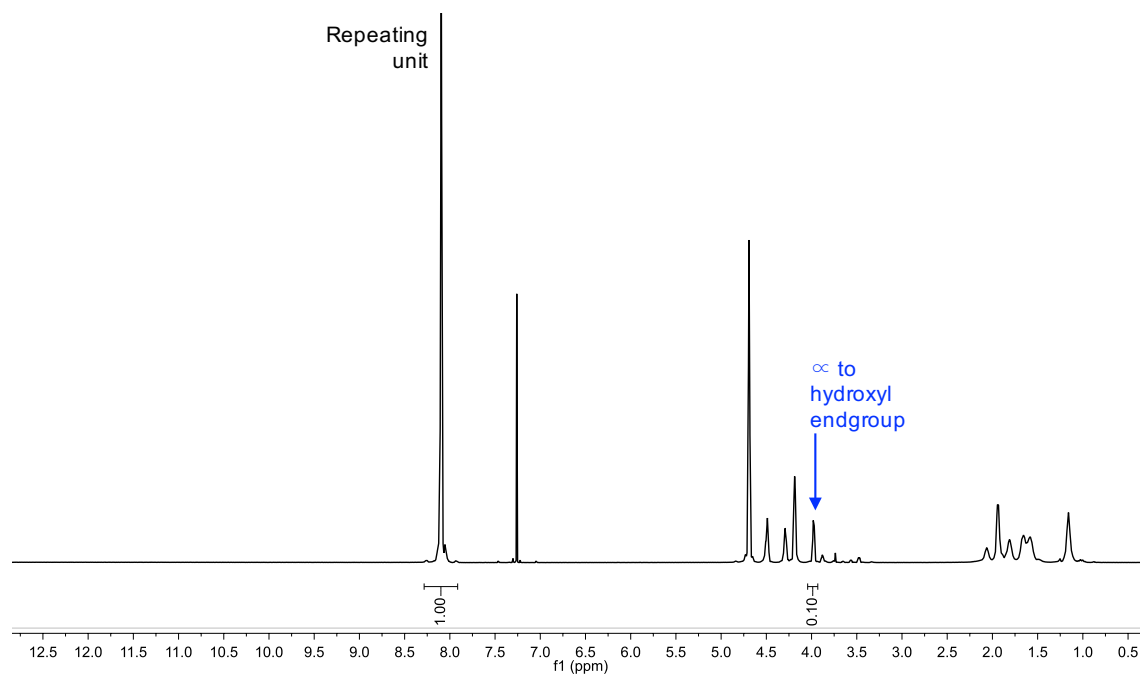


Figure C3. ^1H NMR spectrum of PETG2k in CDCl_3 at ambient temperature. The ratio of the integrals of the aromatic repeating unit (1.00) to the added integrals of the PETG peaks \propto hydroxyl endgroups (0.10) was taken to find X_n .

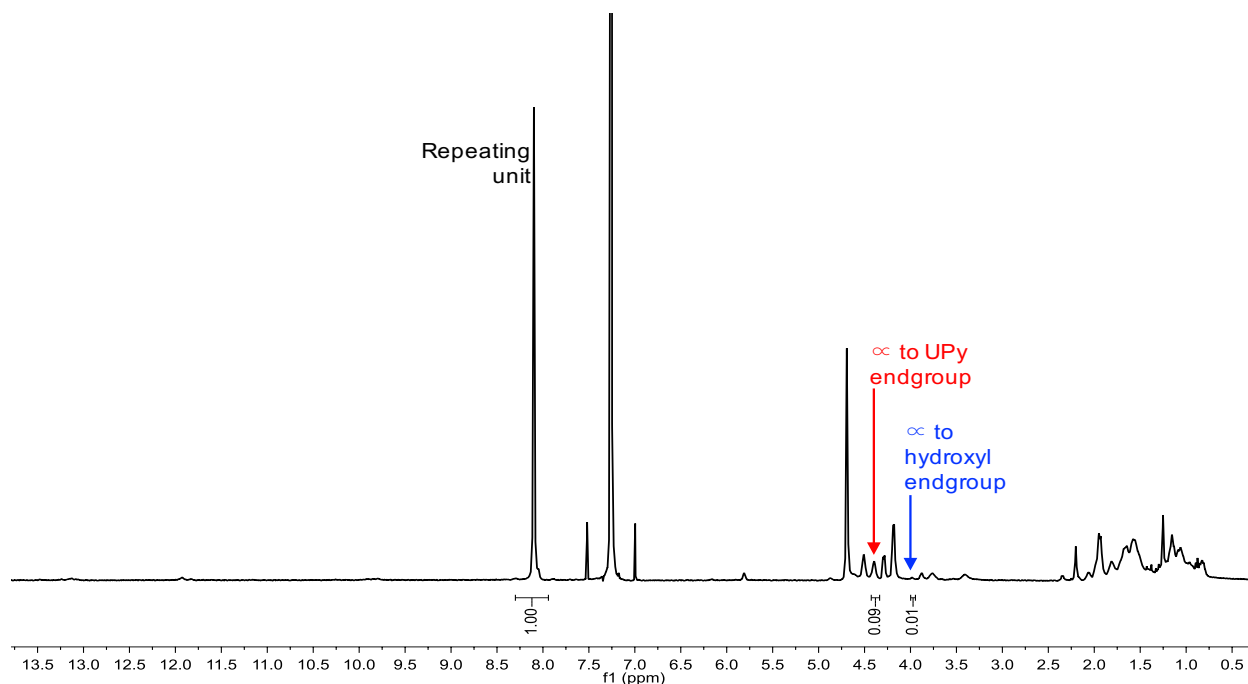


Figure C4. ^1H NMR spectrum of PETG2k-D-UPy in CDCl_3 at ambient temperature. The ratio of the integrals of the aromatic repeating unit (1.00) to the added integrals of the PETG peaks ∞ to the UPy endgroups and ∞ to existing hydroxyl endgroups (0.10) was taken to find X_n .

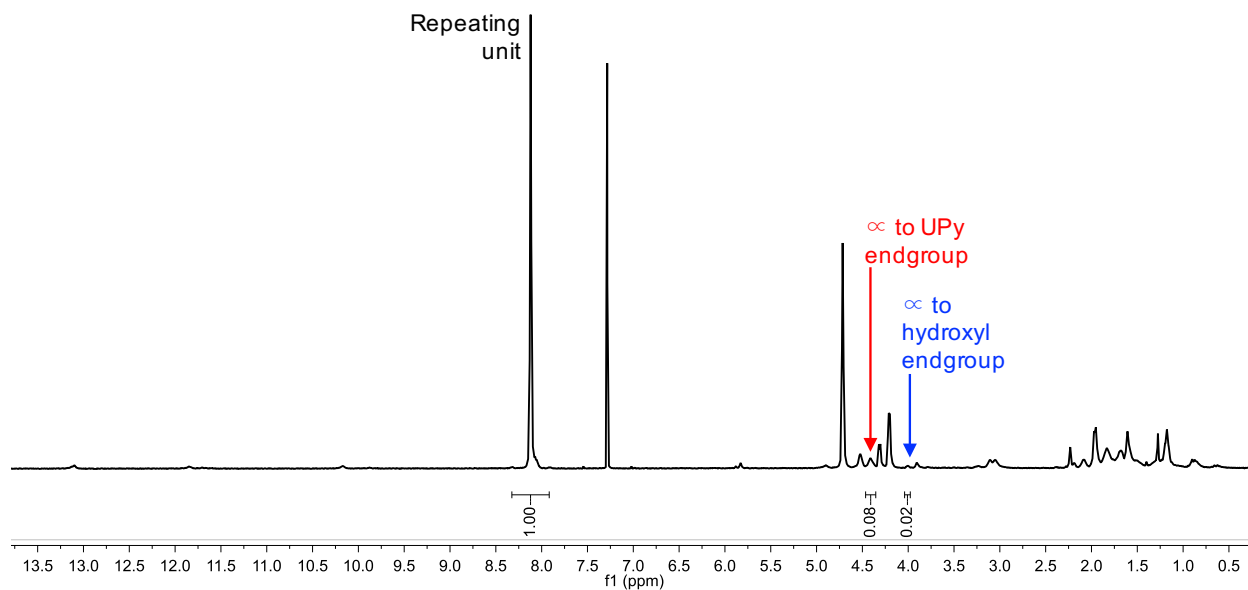


Figure C5. ¹H NMR spectrum of PETG_{2k}-CH-UPy in CDCl₃ at ambient temperature. The ratio of the integrals of the aromatic repeating unit (1.00) to the added integrals of the PETG peaks ∞ to the UPy endgroups and ∞ to existing hydroxyl endgroups (0.10) was taken to find X_n.

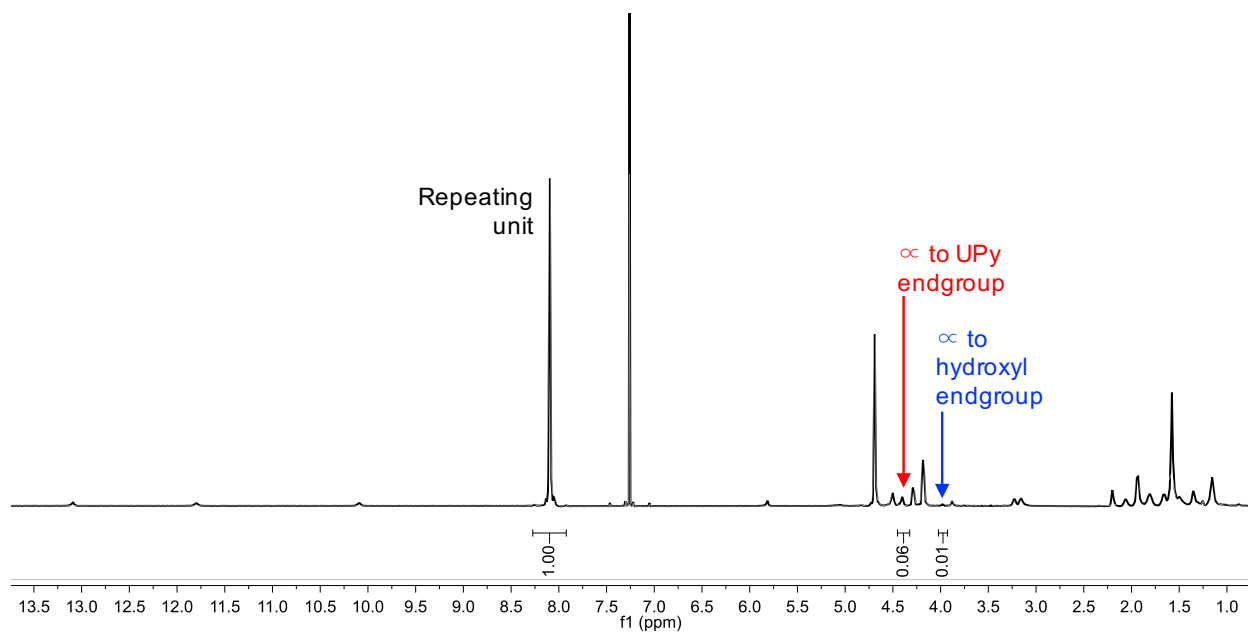


Figure C6. ^1H NMR spectrum of PETG_{2k}-H-UPy in CDCl_3 at ambient temperature. The ratio of the integrals of the aromatic repeating unit (1.00) to the added integrals of the PETG peaks \propto to the UPy endgroups and \propto to existing hydroxyl endgroups (0.07) was taken to find X_n .

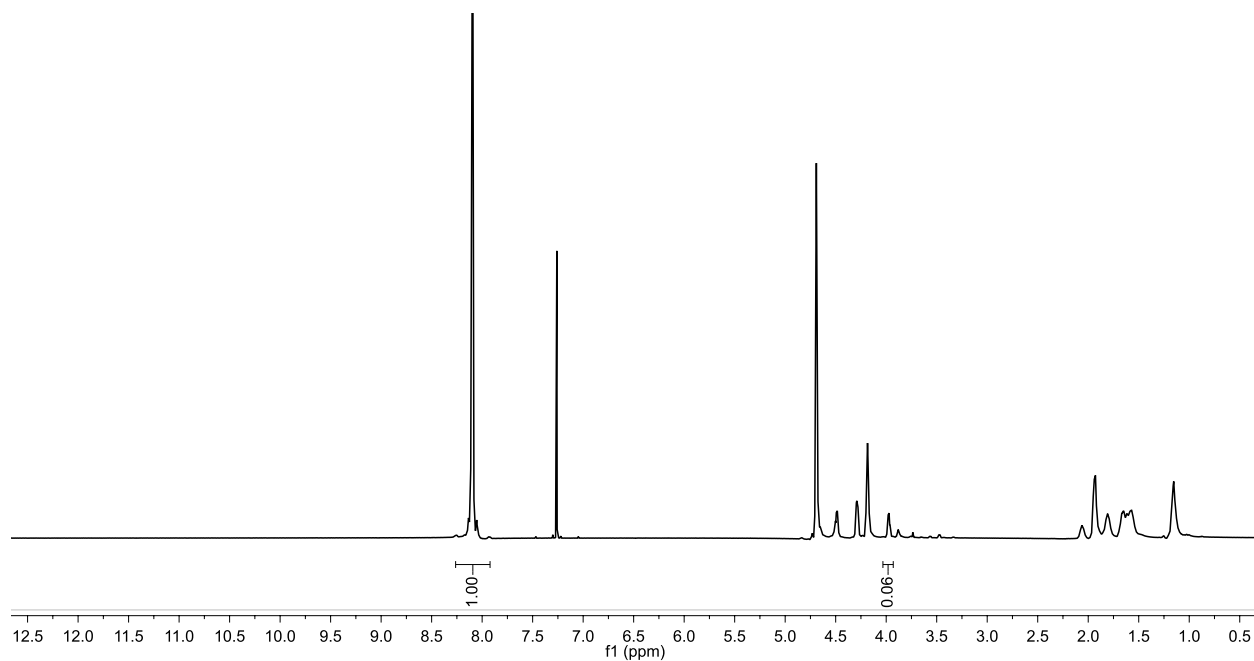


Figure C7. ^1H NMR spectrum of PETG_{3.8k} in CDCl_3 at ambient temperature.

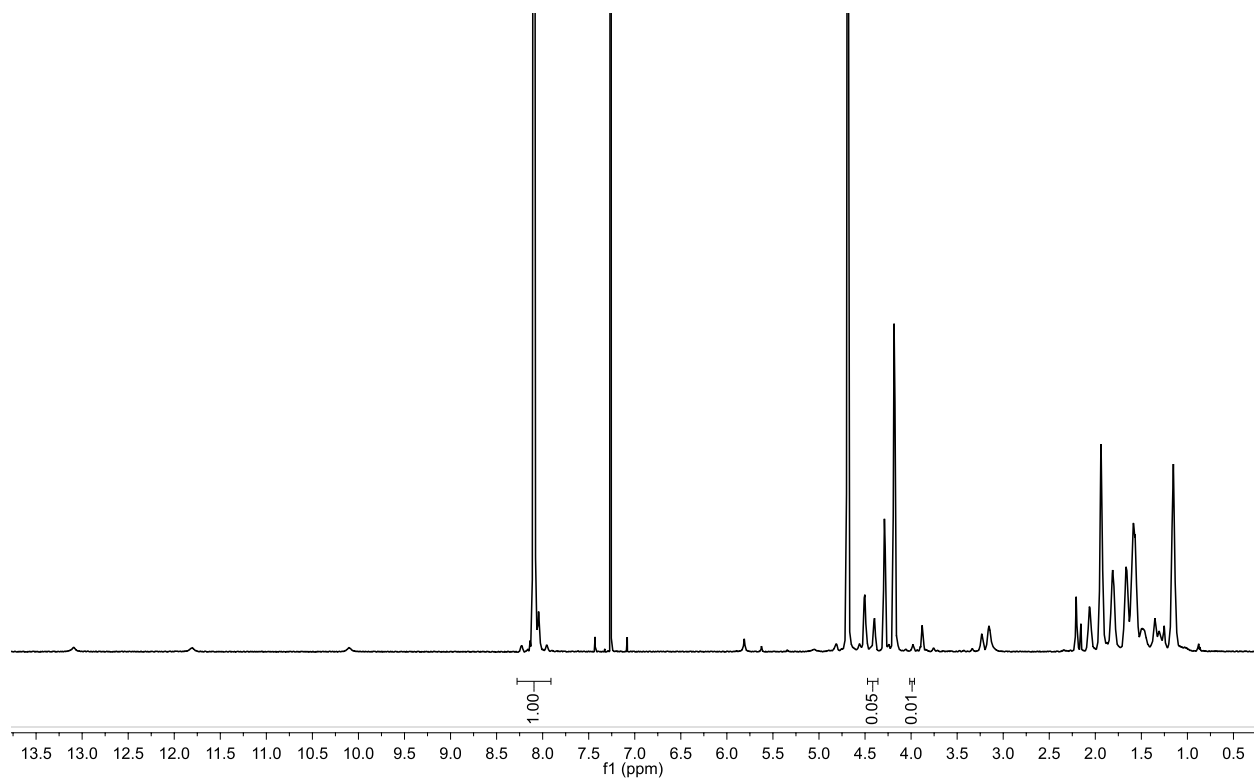


Figure C8. ^1H NMR spectrum of PETG_{3.8k}-H-UPy in CDCl_3 at ambient temperature.

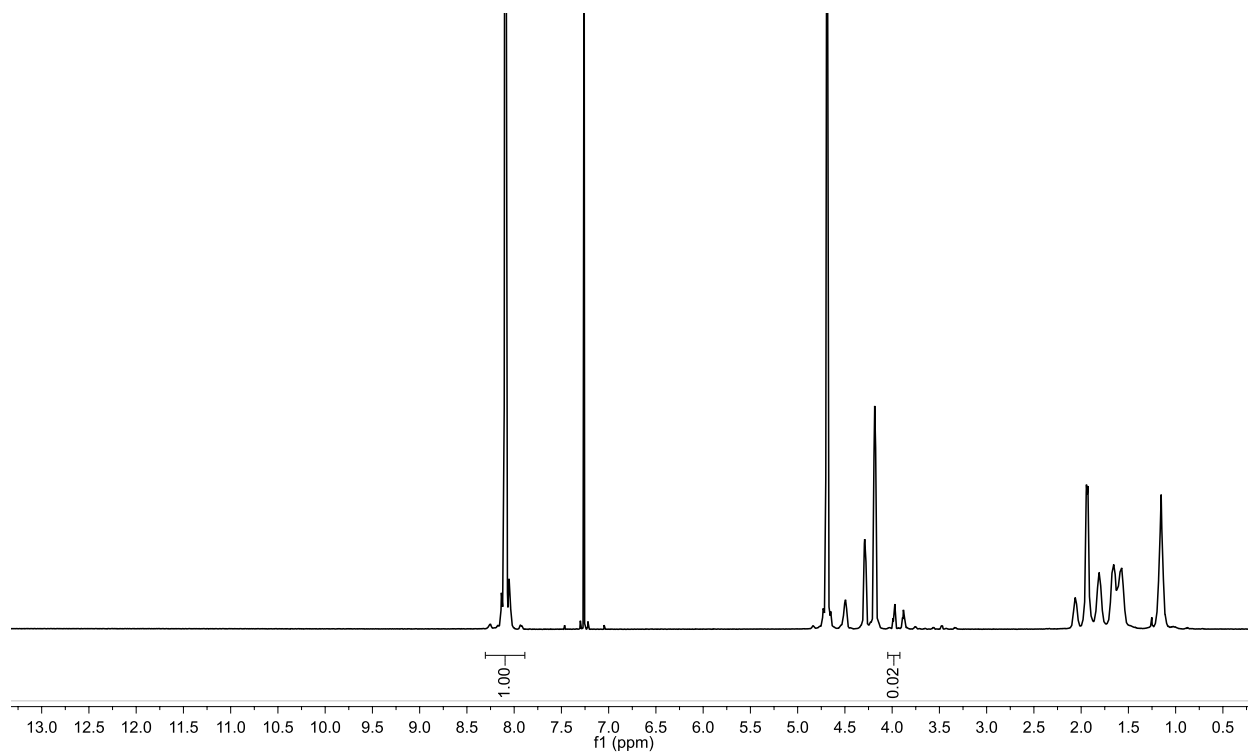


Figure C9. ^1H NMR spectrum of PETG_{6.8k} in CDCl_3 at ambient temperature.

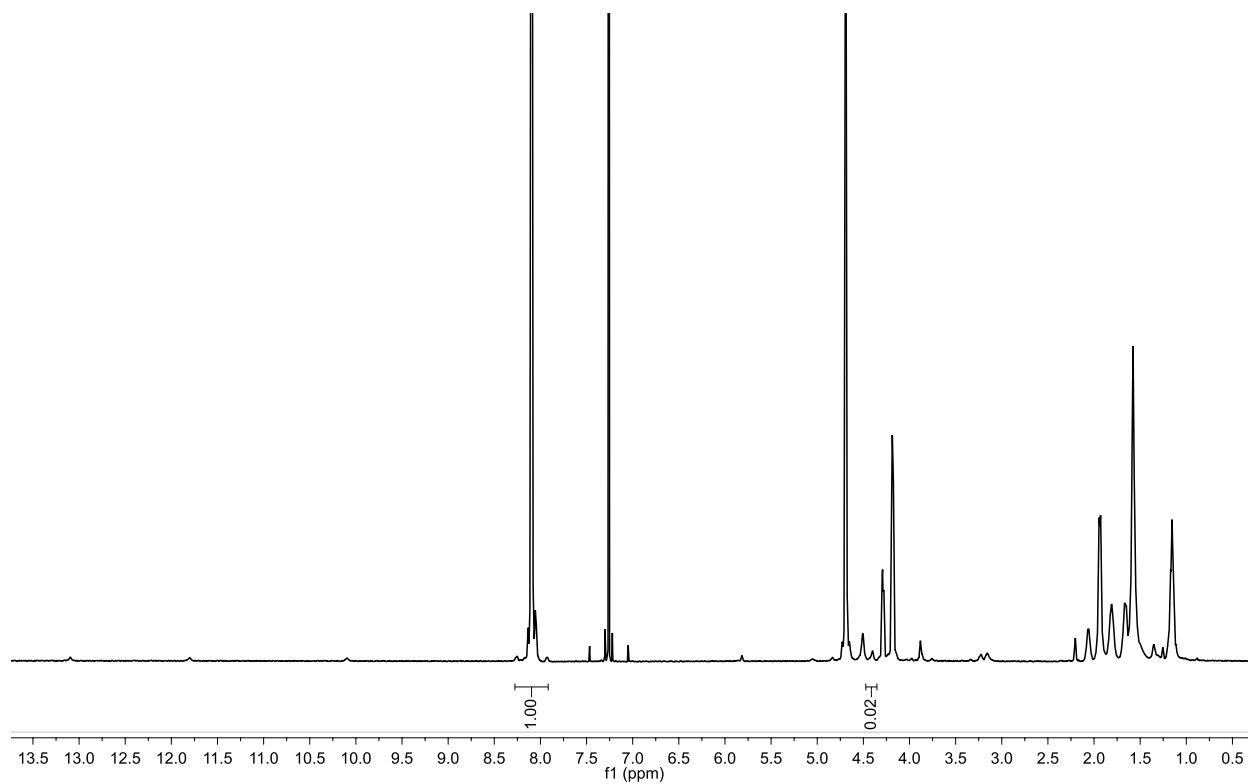


Figure C10. ^1H NMR spectrum of PETG_{6.8k}-H-UPy in CDCl_3 at ambient temperature.

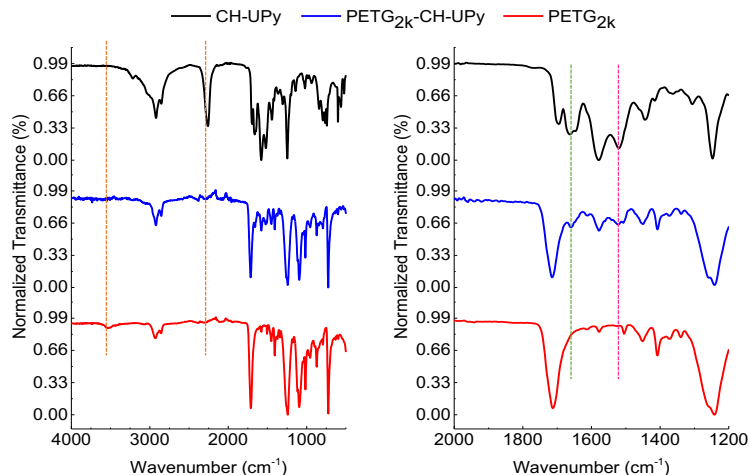


Figure C11. ATR FT-IR spectra of CH-UPy, PETG_{2k}-CH-UPy, and PETG_{2k}. The full spectra, on the left, depict the disappearance of the hydroxyl endgroup of PETG as well as the disappearance of the isocyanate functionality of CH-UPy.

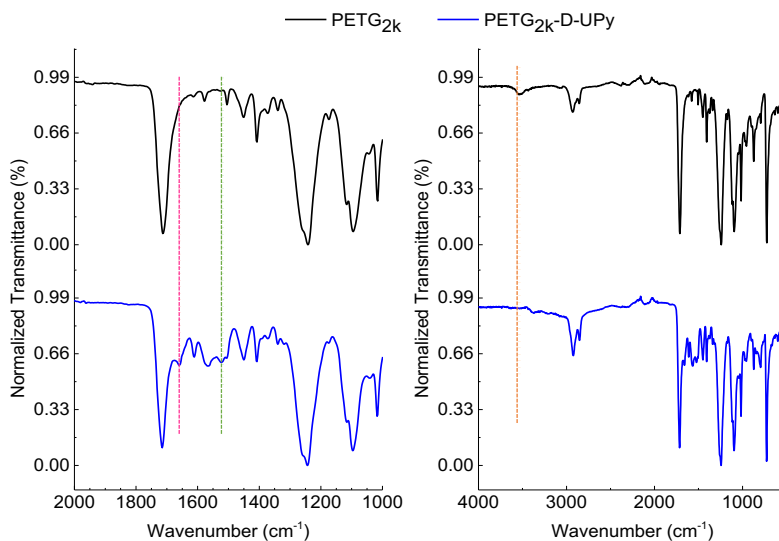


Figure C12. ATR FT-IR spectra of PETG_{2k}-D-UPy and PETG_{2k}. Peaks characteristic of the ureido endgroup are outlined in the spectra on the left. The full spectra, on the right, depict the disappearance of the hydroxyl endgroup of PETG.

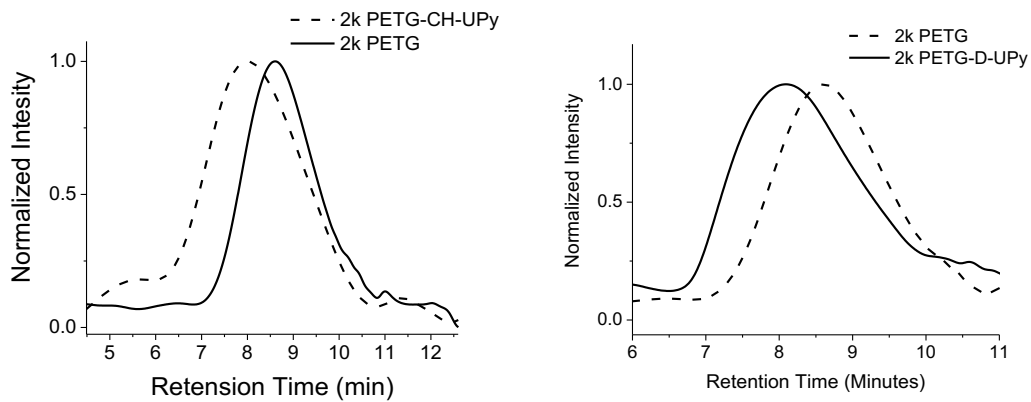


Figure C13. GPC traces of PETG_{2k}, PETG_{2k}-CH-UPy (left), and PETG_{2k}-D-UPy (right).

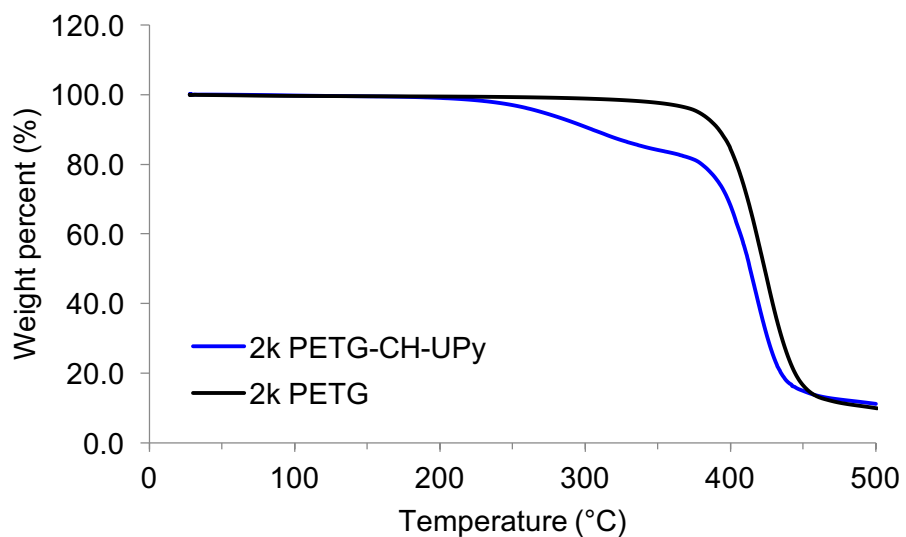


Figure C14. TGA spectra of PETG_{2k} (black) compared to PETG_{2k}-CH-UPy (blue).

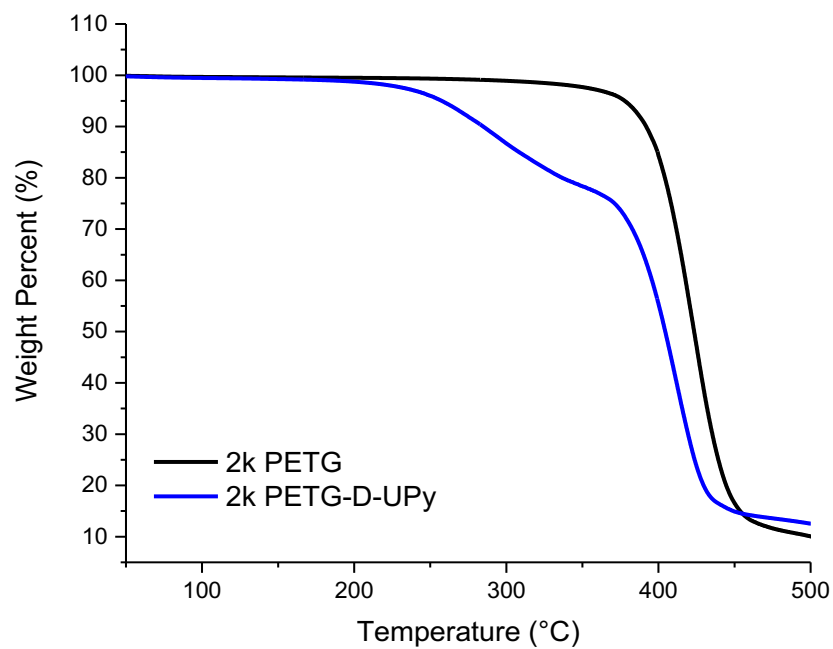


Figure C15. TGA spectra of PETG_{2k} (black) compared to PETG_{2k}-D-UPy (blue).

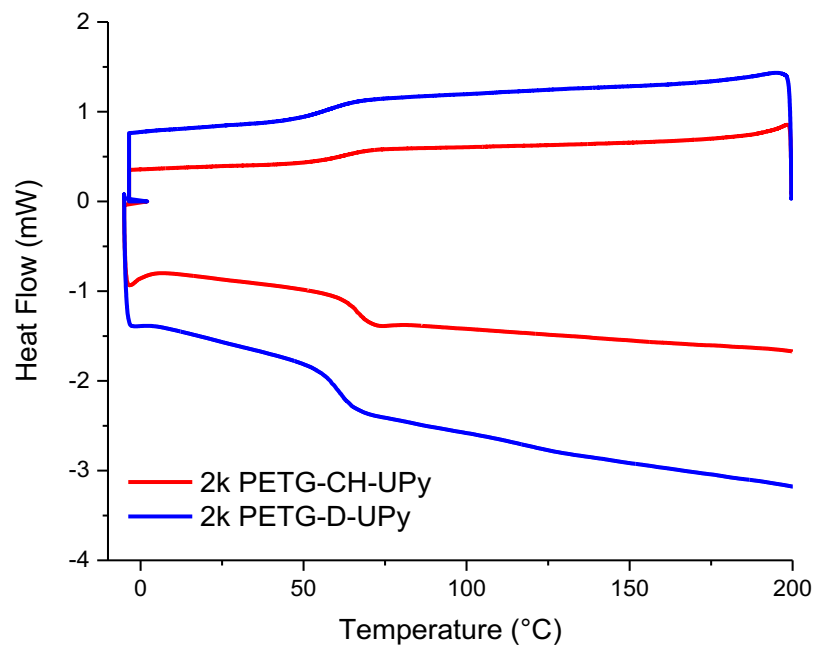


Figure C16. DSC spectra of PETG_{2k}-CH-UPy (red) and PETG_{2k}-D-UPy (blue).

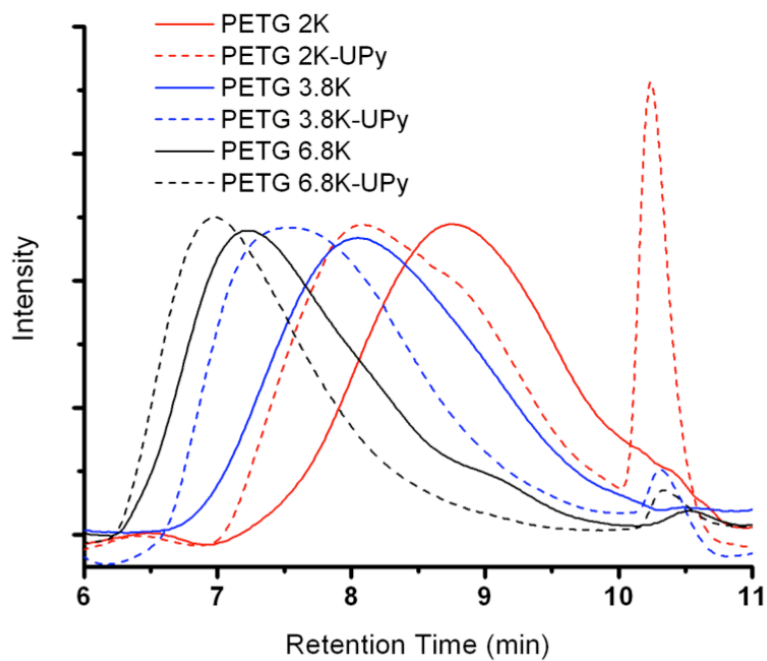


Figure C17. GPC traces of PETG before and after H-UPy functionalization.

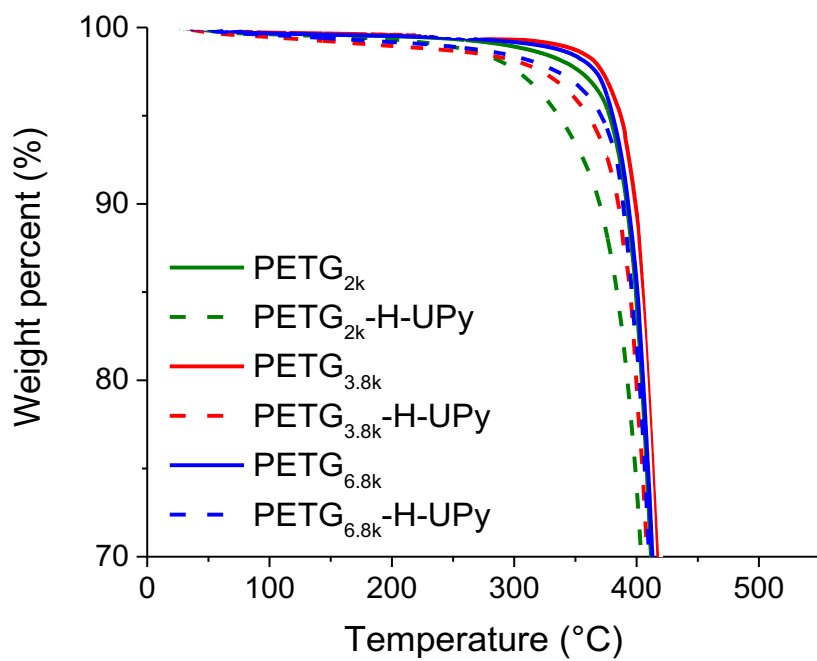


Figure C18. TGA spectra of all of the materials functionalized with H-UPy (dotted lines) compared to the unfunctionalized materials (solid lines).

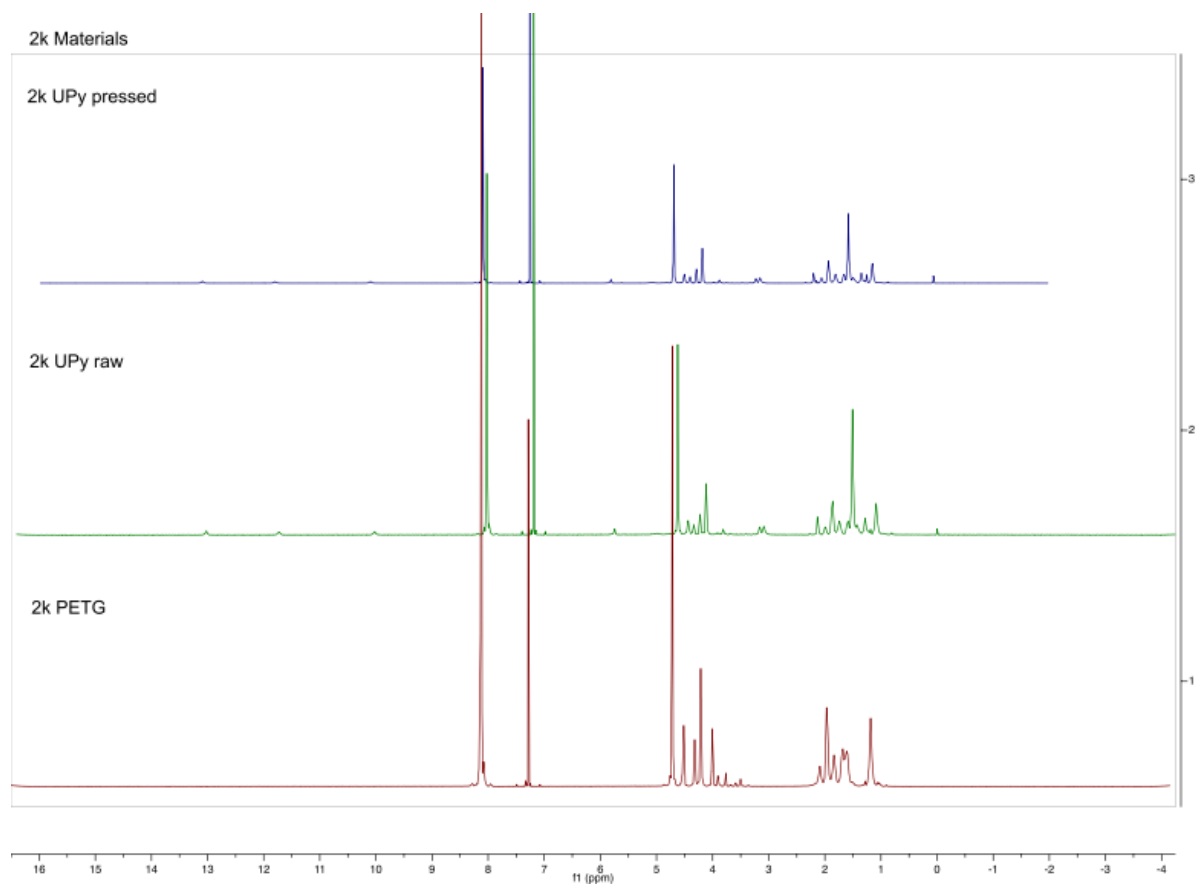


Figure C19. ¹H NMR spectrum of PETG_{2k} (red) and PETG_{2k}-H-UPy before processing (“raw”, green), and after melt pressing (“pressed”, blue) in CDCl₃ at ambient temperature.

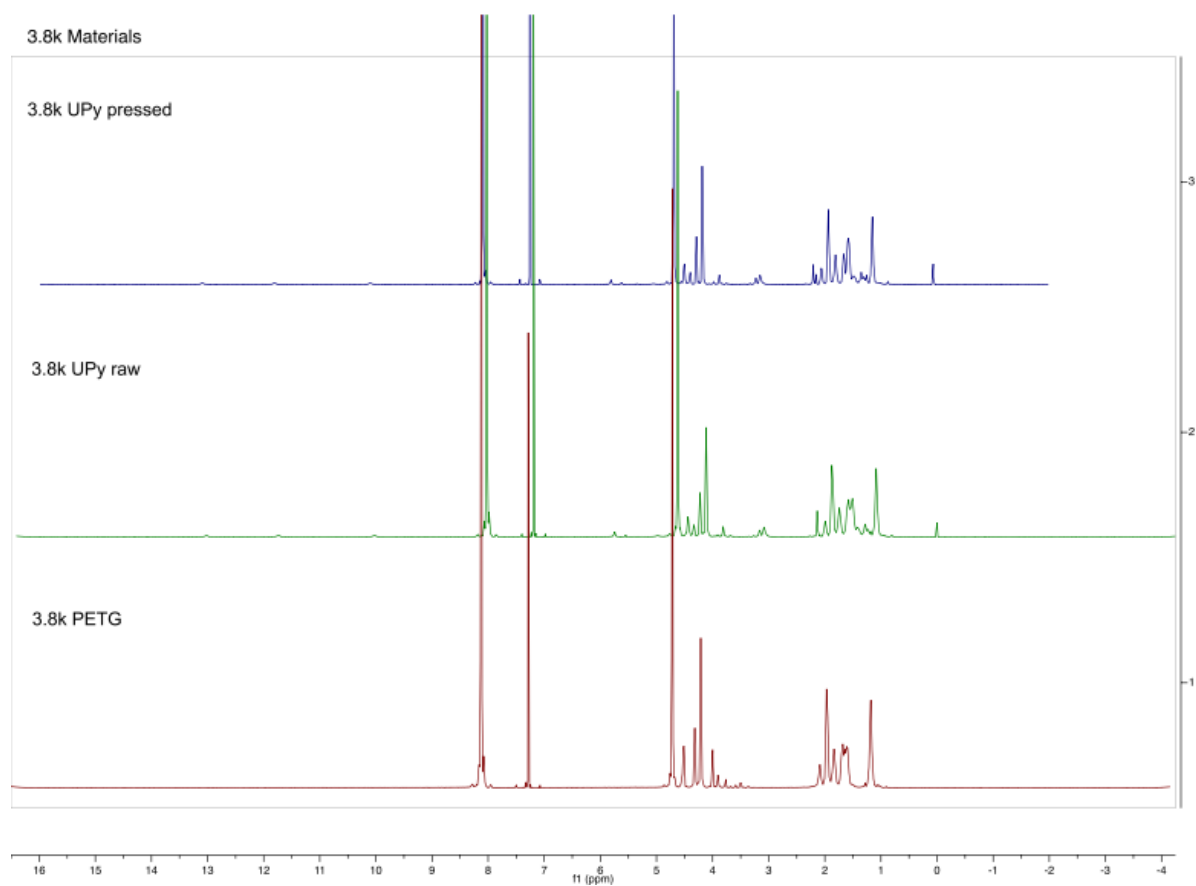


Figure C20. ¹H NMR spectrum of PETG_{3.8k} (red) and PETG_{3.8k}-H-UPy before processing (“raw”, green), and after melt pressing (“pressed”, blue) in CDCl₃ at ambient temperature.

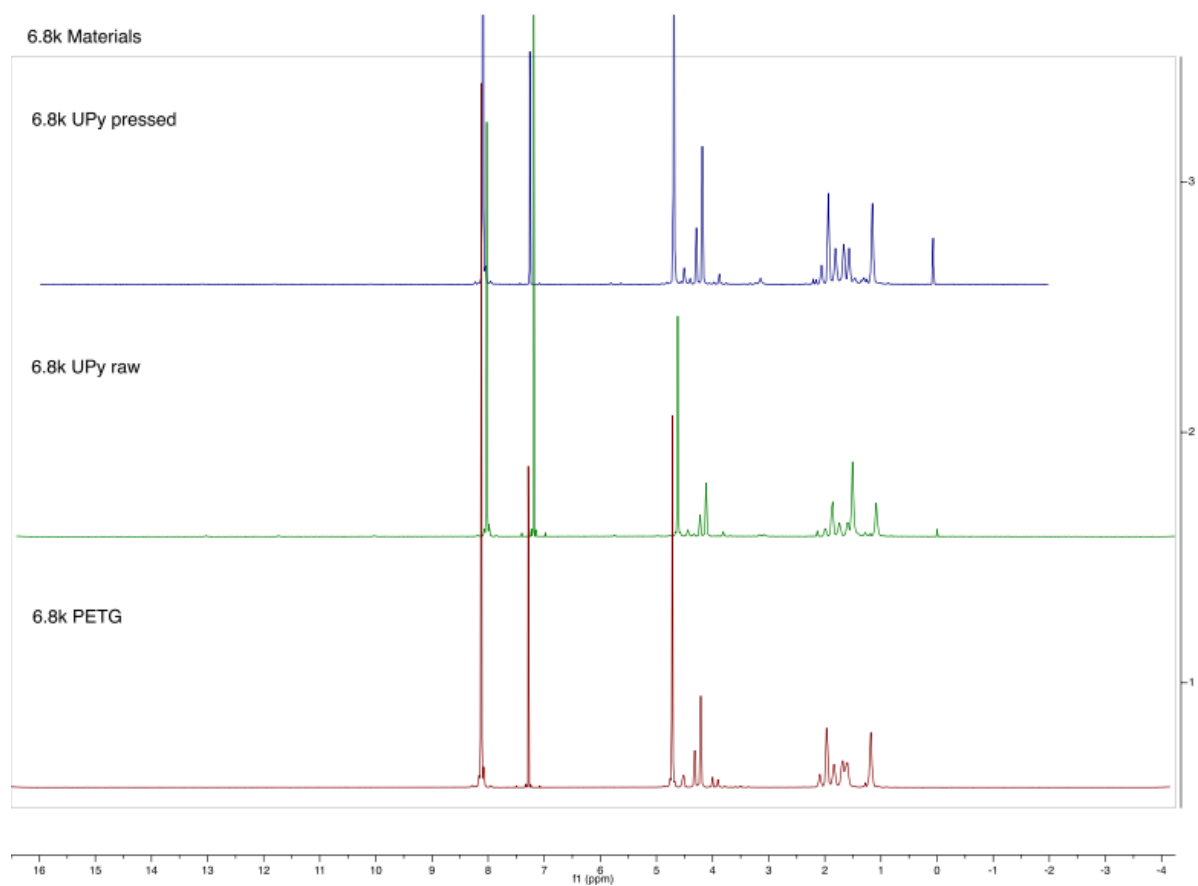


Figure C21. ¹H NMR spectrum of PETG_{6.8k} (red) and PETG_{6.8k}-H-UPy before processing (“raw”, green), and after melt pressing (“pressed”, blue) in CDCl₃ at ambient temperature.

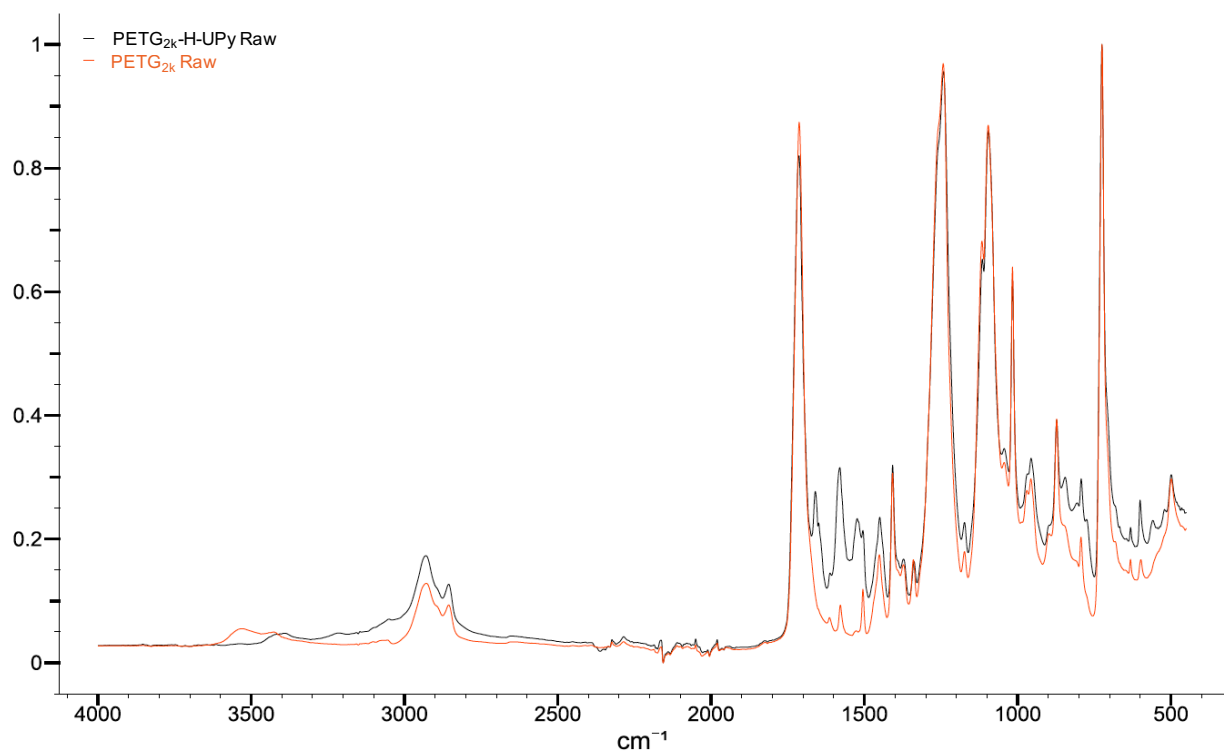


Figure C22. FT-IR Spectra comparing PETG and PETG-H-UPy of 2000 g mol⁻¹ before melt processing.

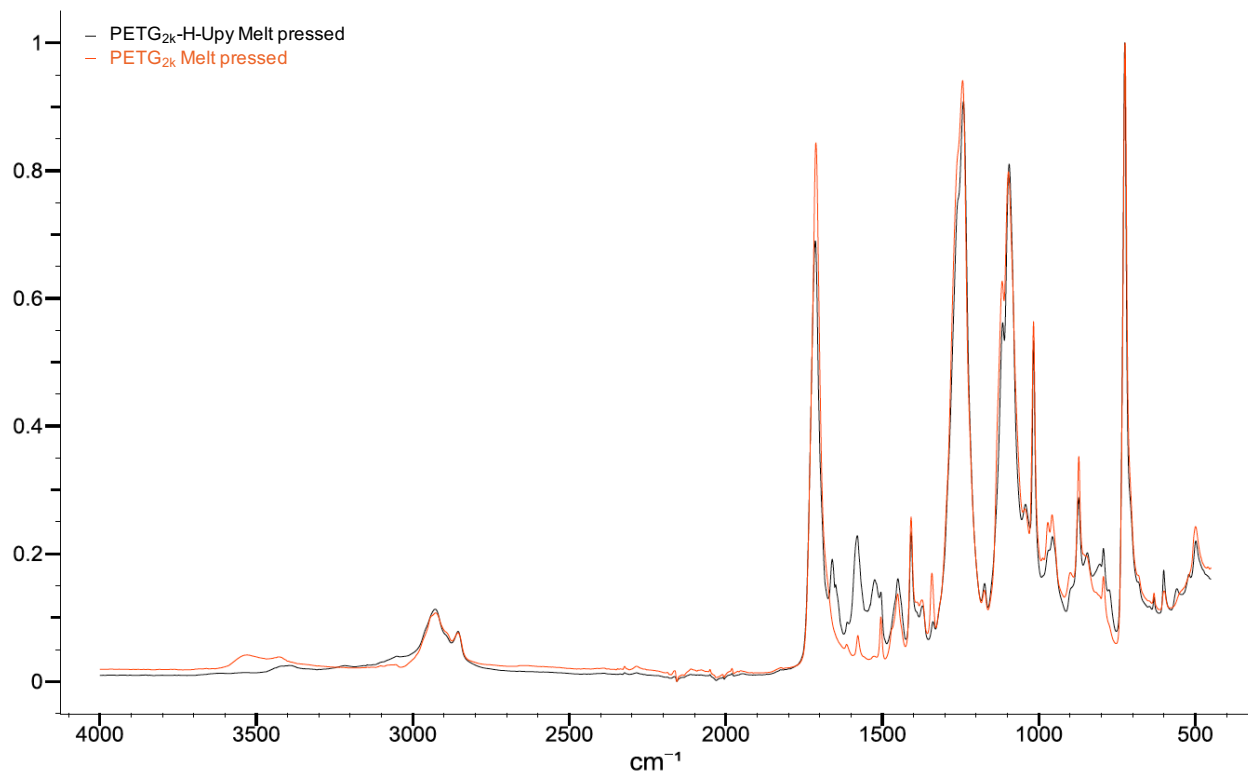


Figure C23. FT-IR Spectra comparing PETG and PETG-H-UPy of 2000 g mol^{-1} after melt processing.

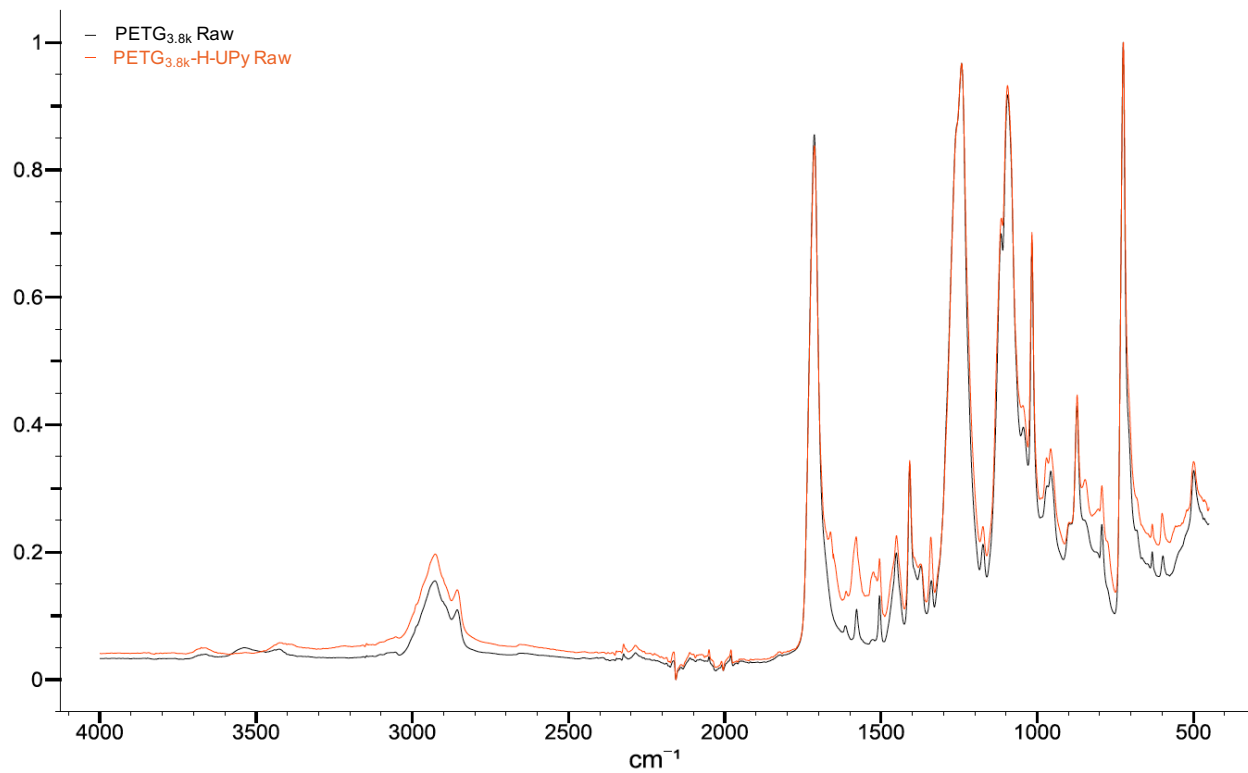


Figure C24. FT-IR Spectra comparing PETG and PETG-H-UPy of 3800 g mol^{-1} before melt processing.

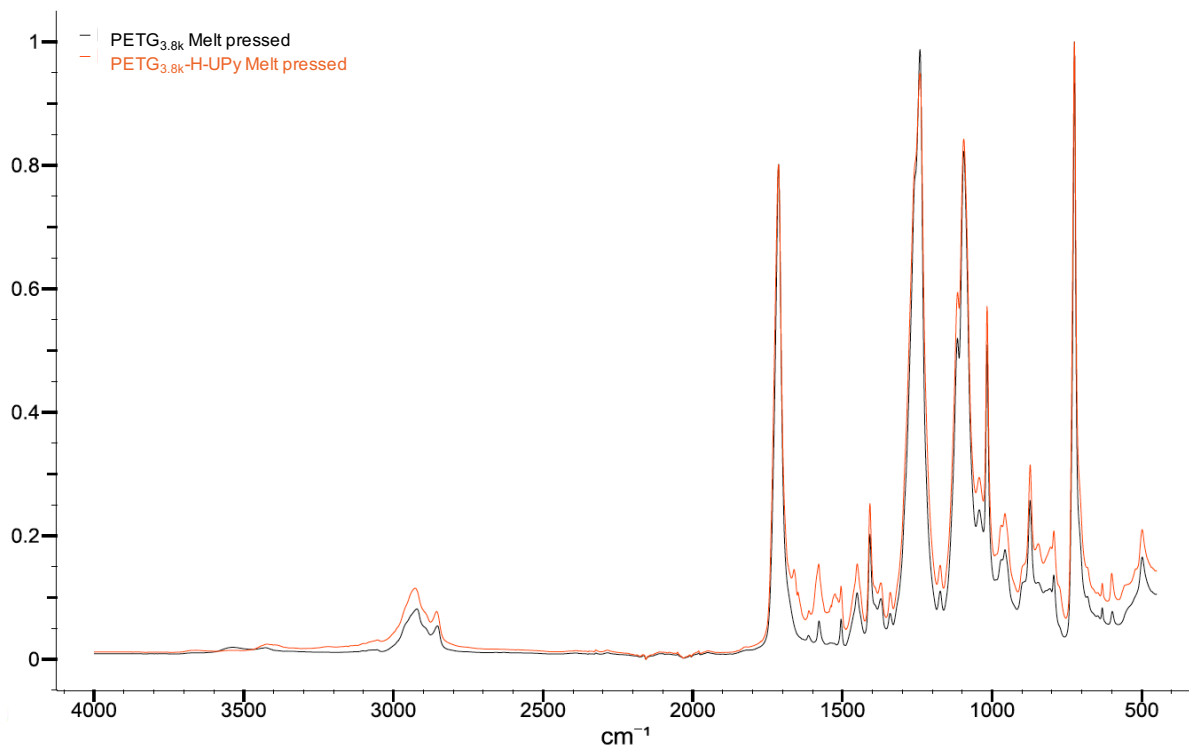


Figure C25. FT-IR Spectra comparing PETG and PETG-H-UPy of 3800 g mol^{-1} after melt processing.

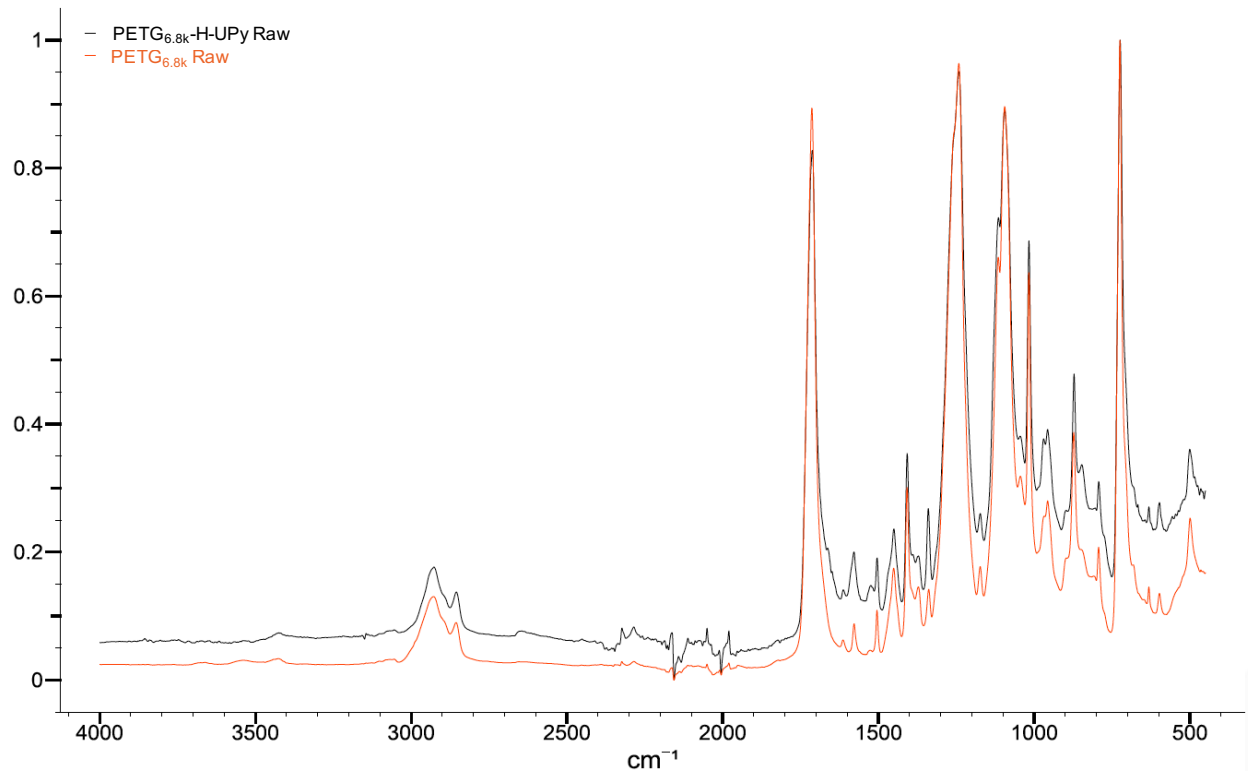


Figure C26. FT-IR Spectra comparing PETG and PETG-H-UPy of 6800 g mol^{-1} before melt processing.

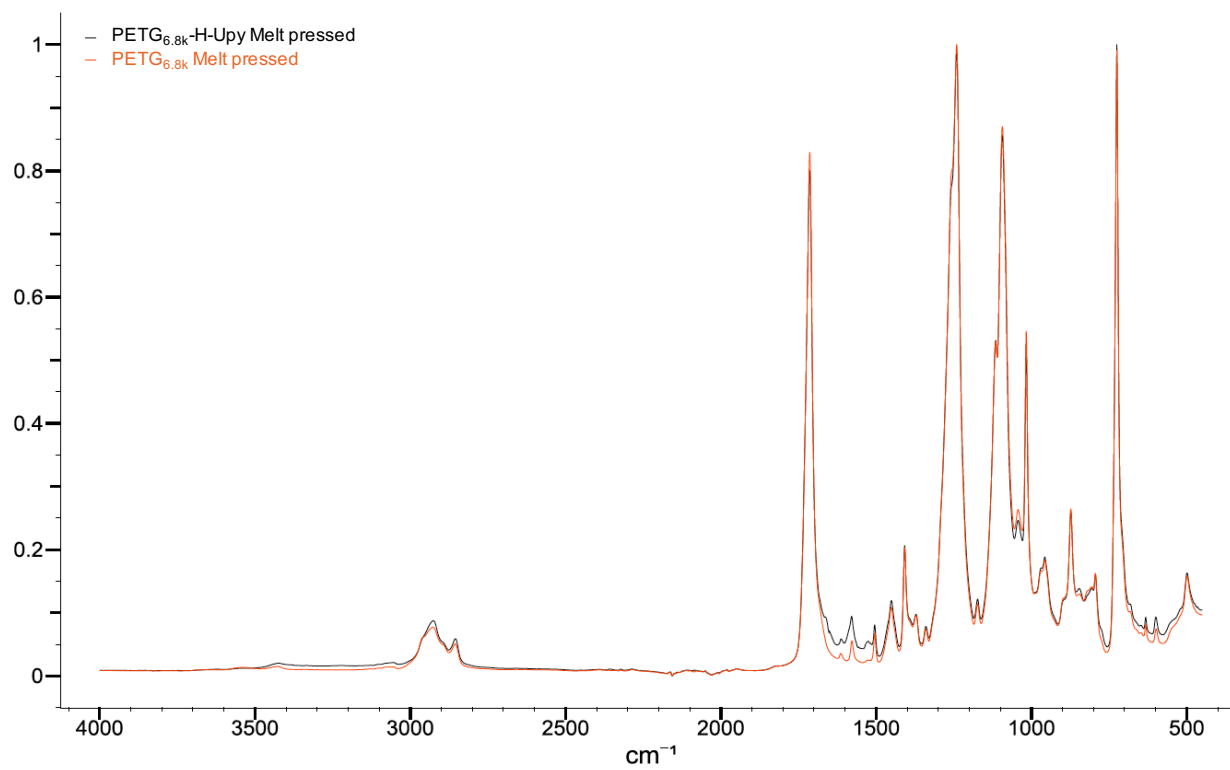


Figure C27. FT-IR Spectra comparing PETG and PETG-H-UPy of 6800 g mol^{-1} after melt processing.

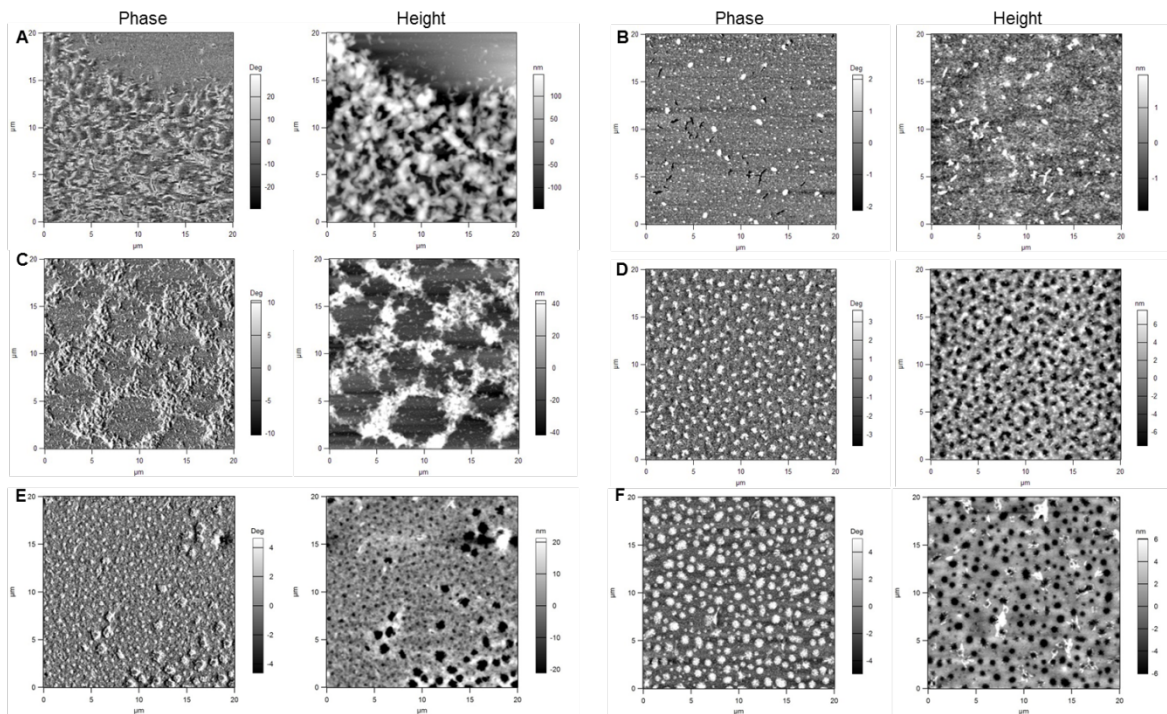


Figure C28. AFM 20x20 μm images: A) PETG_{2k}, B) PETG_{2k}-H-UPy, C) PETG_{3.8k}, D) PETG_{3.8k}-H-UPy, E) PETG_{6.8k}, F) PETG_{6.8k}-H-UPy.

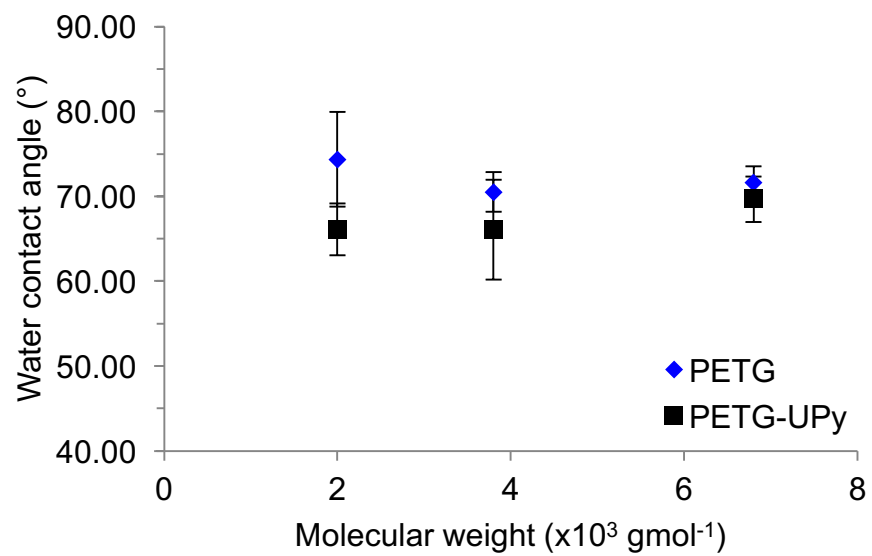


Figure C29. Contact angle of all of the materials.

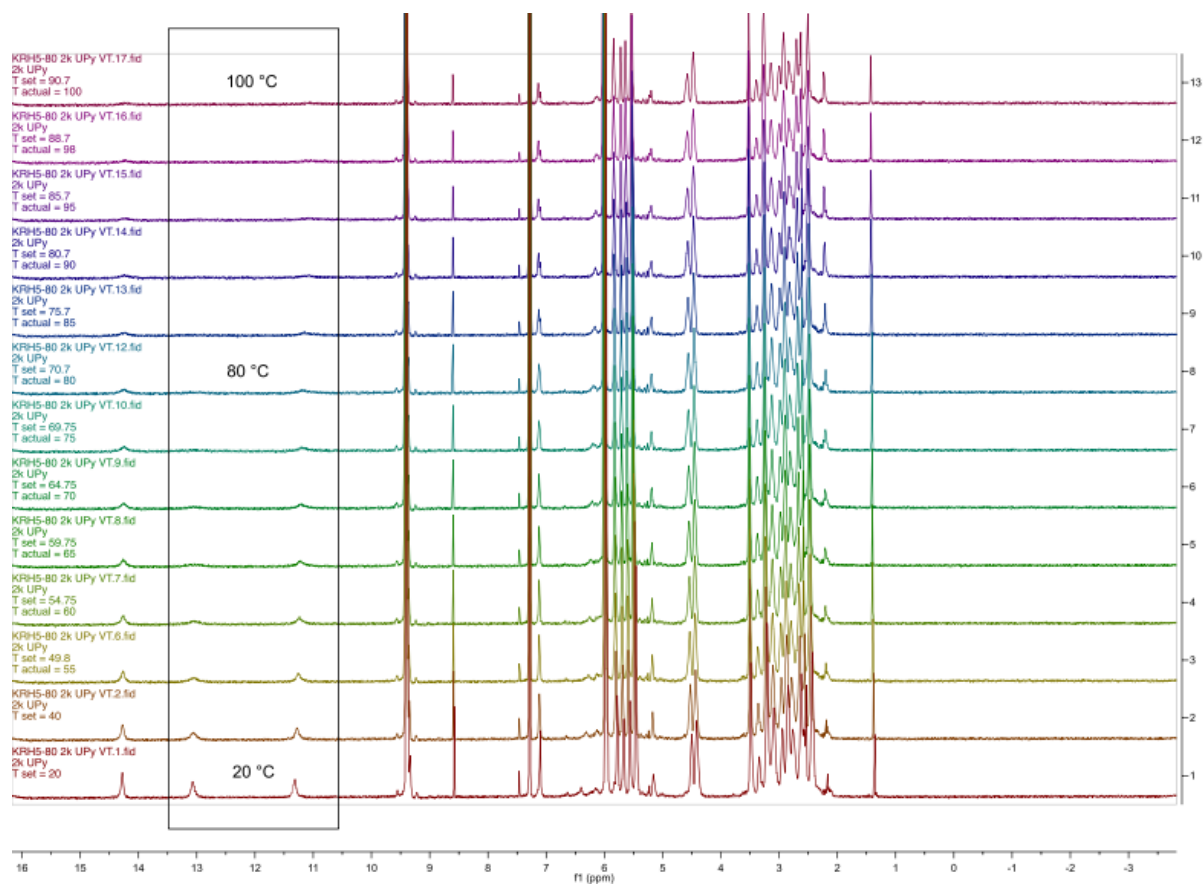


Figure C30. Variable temperature ^1H NMR spectra of PETG_{2k}-H-UPy in TCE- d_2 ($c = 5$ mM, 600 s equilibrium allowed at each temperature). The box outlines peaks that signify the presence of intermolecular H-bonding of UPy endgroups. Temperatures go from 20 °C (red, bottom spectrum) to 100 °C (purple, top spectrum).

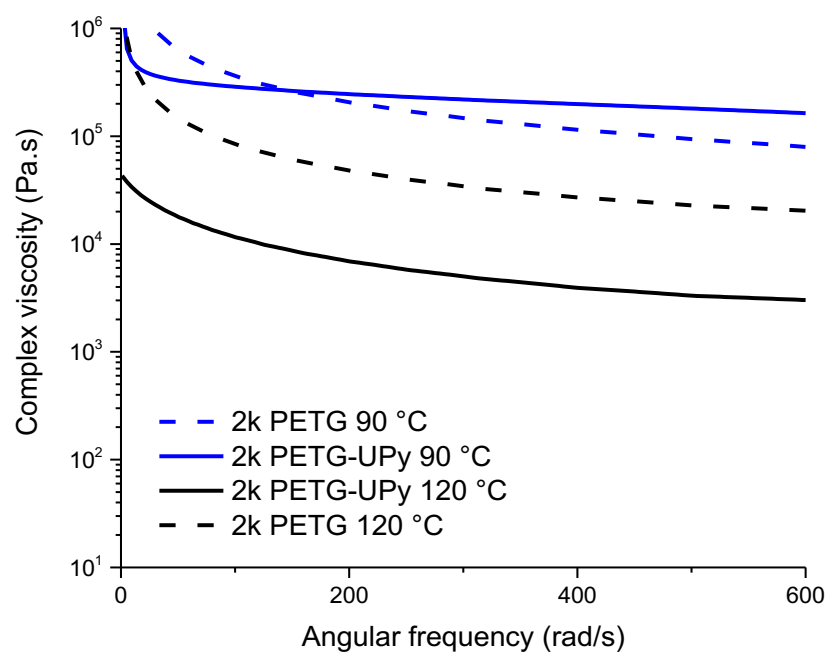


Figure C31. Frequency sweep displaying the complex viscosity of PETG and H-UPy functionalized PETG at 90 and 120 °C.

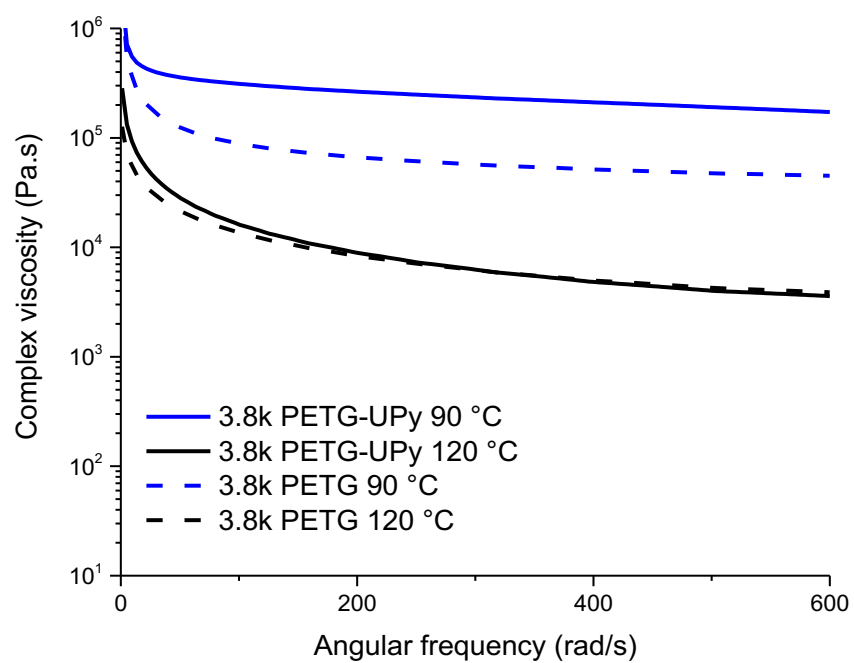


Figure C32. Frequency sweep displaying the complex viscosity of PETG and H-UPy functionalized PETG at 90 and 120 °C.

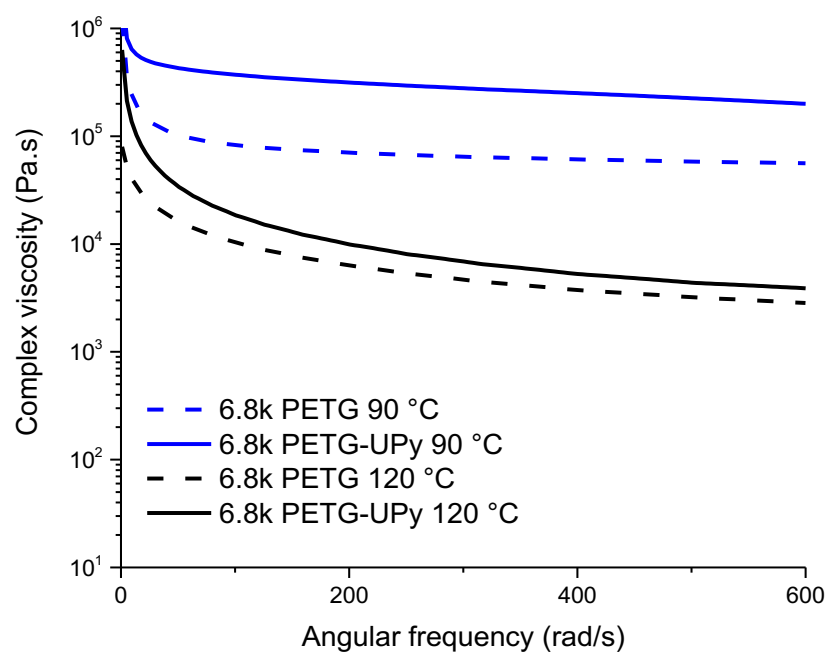


Figure C33. Frequency sweep displaying the complex viscosity of PETG and H-UPy functionalized PETG at 90 and 120 °C.

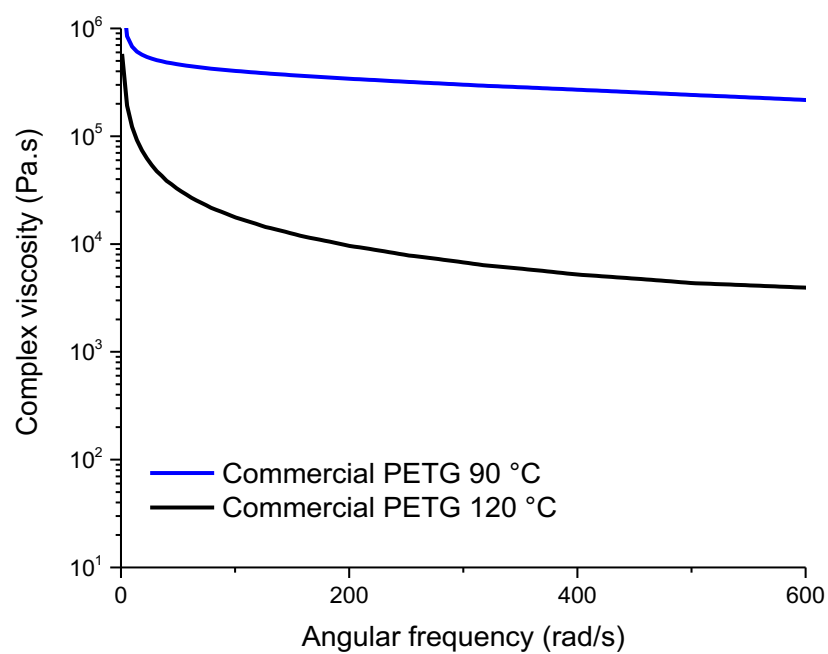


Figure C34. Frequency sweep displaying the complex viscosity of commercial-grade PETG at 90 and 120 °C.

APPENDIX D: SUPPLEMENTARY INFORMATION FOR CHAPTER 4—
COMMERCIAL COMPARISONS

SUPRAMOLECULAR ENGINEERING POLYESTERS: ENDGROUP
FUNCTIONALIZATION OF GLYCOL MODIFIED PET WITH UREIDOPYRIMIDINONE

COMMERCIAL COMPARISONS

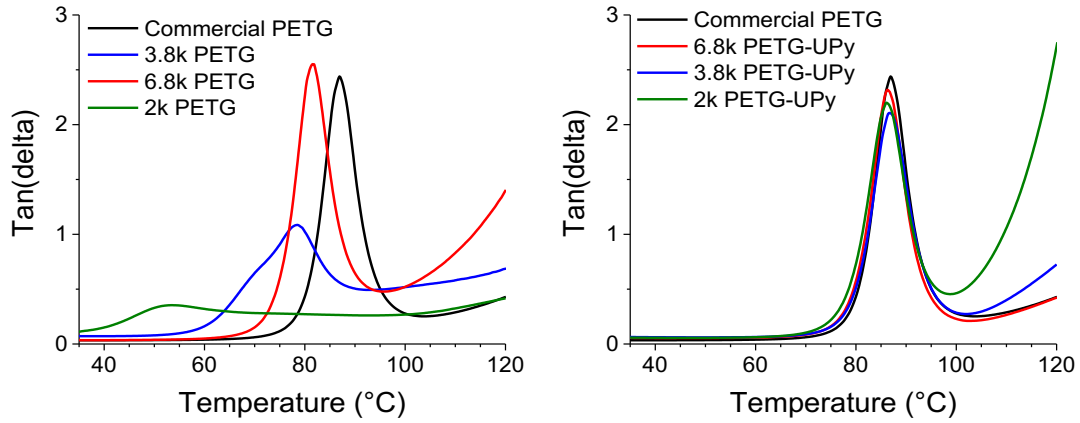


Figure D1. Comparing tan delta of low MW polymers before and after UPy functionalization with Commercial PETG.

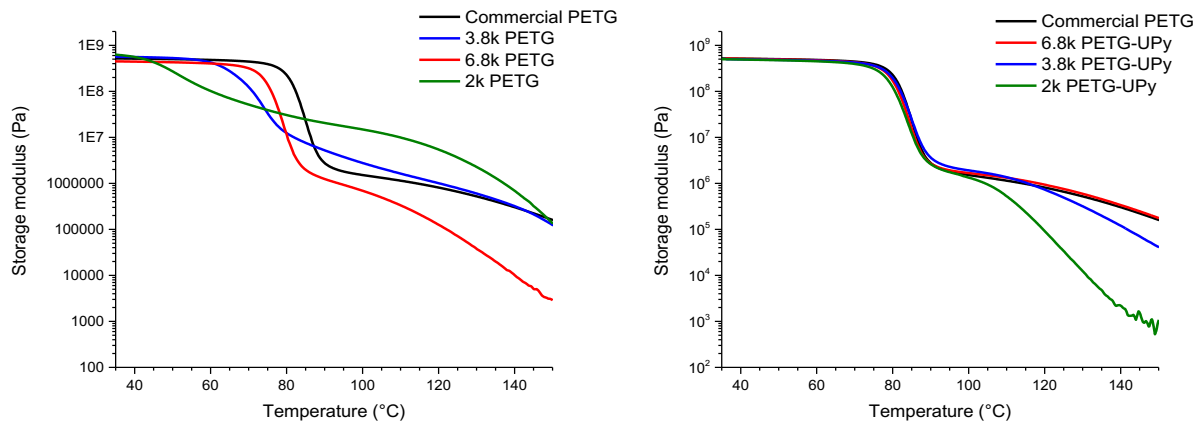


Figure D2. Comparison of G' of low MW polymers before and after UPy functionalization with Commercial PETG.

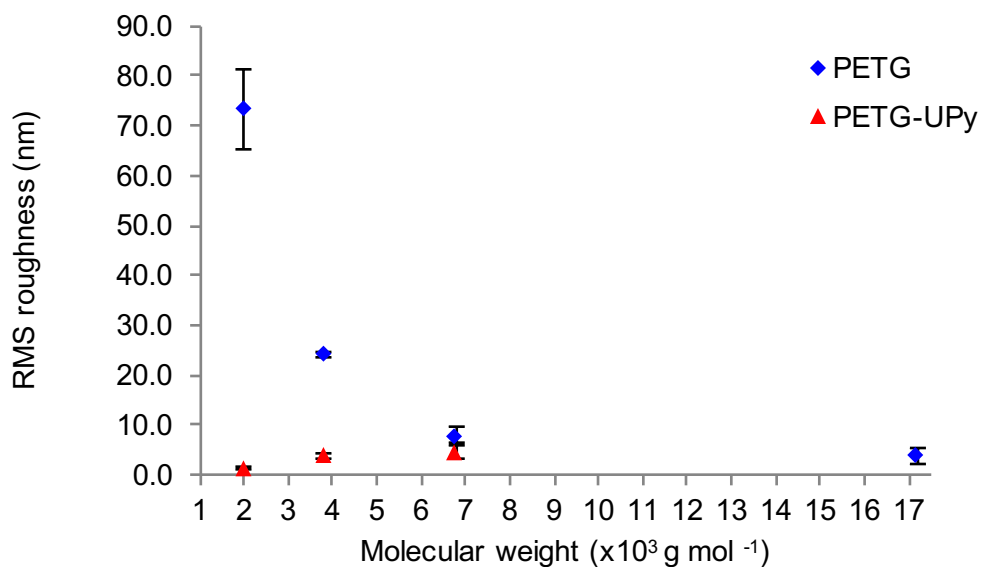


Figure D3. Comparison of the RMS surface roughness of low MW polymers before and after UPy functionalization with Commercial PETG (17.2 kg mol^{-1}).

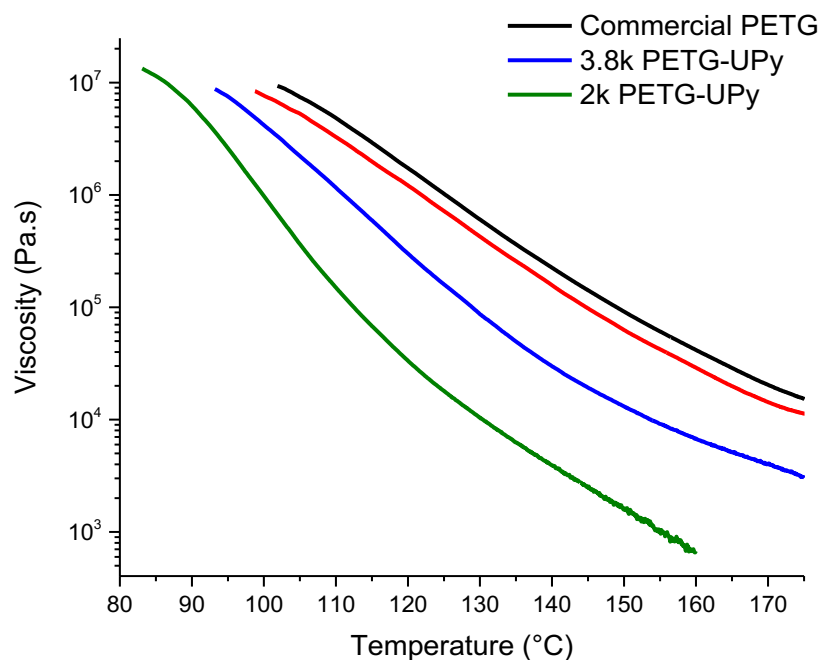


Figure D4. Comparison of melt viscosity of low MW, H-UPy functionalized polymers and Commercial PETG (Comm PETG).

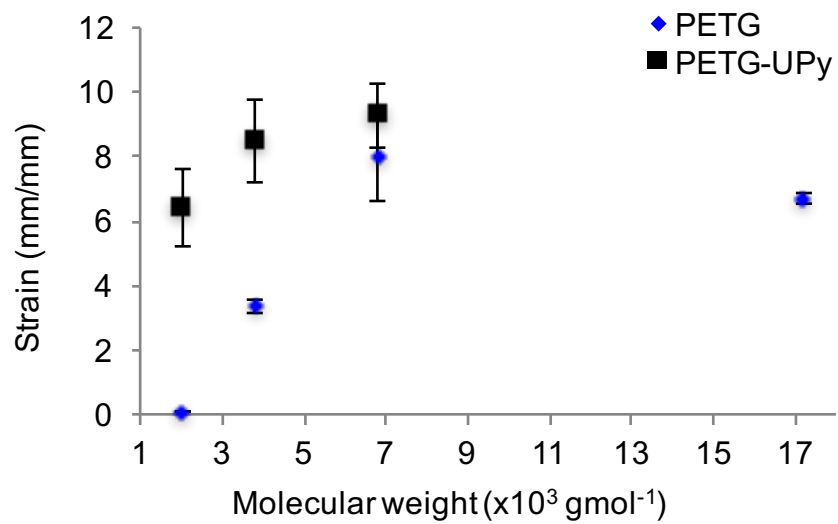


Figure D5. Comparison of the maximum strain at break of five samples of low MW polymers before and after UPy functionalization with Commercial PETG (17.2 kg mol⁻¹).